FUNDAMENTAL STUDY OF DEGRADABLE MAGNESIUM PHOSPHATE SYSTEMS FOR HARD TISSUE APPLICATIONS

by

Nicole Jean Ostrowski

B. S. Materials Science and Engineering, University of Pittsburgh, 2010

Submitted to the Graduate Faculty of

Swanson School of Engineering in partial fulfillment

of the requirements for the degree of

Doctor of Philosophy in Bioengineering

University of Pittsburgh

2015

UNIVERSITY OF PITTSBURGH

SWANSON SCHOOL OF ENGINEERING

This dissertation was presented

by

Nicole Jean Ostrowski

It was defended on

November 19th, 2015

and approved by

Dissertation Director: Prashant N. Kumta, PhD, Edward R. Weidlein Chair Professor, Departments of Bioengineering, Chemical and Petroleum Engineering, and Mechanical Engineering and Materials Science

Kacey G. Marra, Associate Professor, Departments of Plastic Surgery and Bioengineering

Ipsita Banerjee, Associate Professor, Departments of Chemical and Petroleum Engineering and Bioengineering

Alejandro J. Almarza, Associate Professor, Departments of Oral Biology and Bioengineering

Elia Beniash, Associate Professor, Department of Oral Biology

Copyright © by Nicole J. Ostrowski

2015

FUNDAMENTAL STUDY OF DEGRADABLE MAGNESIUM PHOSPHATE SYSTMES FOR HARD TISSUE APPLICATIONS

Nicole J. Ostrowski, PhD

University of Pittsburgh, 2015

Magnesium phosphate based ceramic implants and cements are currently under development and have received much attention to challenge the current standards for bone grafting materials. Compared to current calcium phosphate implants, magnesium phosphate implants display higher levels of resorption *in vivo* while maintaining high biocompatibility and osteoconductivity and low inflammatory response. The magnesium phosphate ceramics under development include dense pellets as well as cement putty, and fiber reinforced cement composite embodiments. In pellet form, amorphous tri-magnesium phosphate pellets displayed higher solubility than crystalline tri-magnesium phosphate while inducing rapid mineralization on the pellet surface which aided high osteoblast cytocompatibility of the amorphous pellet. These crystalline and amorphous tri-magnesium phosphates were therefore explored as precursor materials for a variety of cementing reactions. Amorphous, semi-crystalline and crystalline tri-magnesium phosphate precursors were correspondingly reacted with an ammonium phosphate solution to explore the effect of tri-magnesium phosphate crystallinity on the cementing reaction. The amorphous and semi-crystalline tri-magnesium phosphate powders were highly reactive, resulting in mechanically weak cements, while the crystalline tri-magnesium phosphate powder reacted efficiently with the reacting solution and were mechanically strong following reaction completion reaction while also displaying a neutral pH during incubation in saline

solution. This crystalline tri-magnesium phosphate was next evaluated with solutions of ammonium, potassium and sodium phosphate to explore the effect of each reacting salt solution on the cement reaction and product. The sodium and potassium phosphate solutions resulted in long setting times and poor mechanical resilience due to a lack of reaction completion while the ammonium phosphate solution resulted in mechanically resilient cement exhibiting clinically relevant setting times. This magnesium ammonium cement formulation was then further modified by the addition of soluble mannitol sugar crystals, or wet-spun degradable polycaprolactone fibers to evaluate the influence of added porosity or fiber reinforcement. Mannitol inclusion improved the porosity while reducing the mechanical strength. Polymeric fibers addition increased the toughness of the cement and, when removed, led to significant increase in macroporosity contributing to improved cellular infiltration. Based on the reults of the compositions studied, magnesium ammonium phosphate cements containing amounts of mannitol or more significant amounts of degradable fiber serving as initial reinforcement as well as eventual pore formers appear to be promising formulations to explore in the future.

TABLE OF CONTENTS

PREFACE ..... **XXV**

1.0 INTRODUCTION **1**

1.1 CERAMIC BONE CEMENTS **1**

1.1.1 Clinical Need **1**

1.1.2 History of Bone Cements **2**

1.1.3 Commercial Calcium Phosphate Cements and Limitations **3**

1.1.4 Magnesium Phosphate Bone Cements **4**

1.1.5 History of Magnesium Phosphate Cements **5**

1.2 MAGNESIUM CEMENT SYSTEMS **7**

1.3 MATERIALS PROPERTIES **10**

1.3.1 Chemical Composition **10**

1.3.2 Particle Size **11**

1.3.3 Cement Composition **12**

1.3.4 Setting and Handling **17**

1.3.5 Mechanical Strength and Porosity **21**

1.3.6 Adhesion **25**

1.3.7 Clinical Considerations **26**

1.4 CEMENT SYSTEM MODIFICATIONS **27**

1.4.1 Reaction Retardants 27

1.4.2 Pore Formers 28

1.4.3 Radio-opaque Additives 29

1.4.4 Combination of Systems 30

1.4.5 Composite Systems 31

1.5 *IN VITRO* PROPERTIES 32

1.5.1 Dissolution and Degradation 32

1.5.2 Cytocompatibility 35

1.5.3 Antibacterial Properties 38

1.6 *IN VIVO* STUDIES AND CLINICAL APPLICATIONS 40

1.7 DESIGNING A BETTER MAGNESIUM BONE CEMENT 42

1.8 SPECIFIC AIMS 44

2.0 SPECIFIC AIM 1: SYNTHESIS, OSTEOBLAST AND OSTEOCLAST VIABILITY OF AMORPHOUS AND CRYSTALLINE TRI-MAGNESIUM PHOSPHATE 47

2.1 INTRODUCTION 47

2.2 MATERIALS AND METHODS 50

2.2.1 Materials Synthesis 50

2.2.2 Materials Characterization 50

2.2.3 *In Vitro* Sample Preparation 51

2.2.4 *In Vitro* Dissolution and Mineralization 52

2.2.5 Cell Culture 53

2.2.6 Osteoblast Assessment 53

2.2.7 Osteoclast Assessment 55

2.2.8 Statistical Analysis 56

2.3 RESULTS 56

2.3.1 Materials Synthesis and Characterization 56

2.3.2 *In Vitro* Dissolution and Mineralization 60

2.3.3 *In Vitro* Cytocompatibility 65

2.4 DISCUSSION 70

2.5 CONCLUSION 76

3.0 SPECFIC AIM 2: SYSTEMATIC ASSESSMENT OF SYNTHESIZED TRI-MAGNESIUM PHOSPHATE POWDERS (AMORPHOUS, SEMI-CRYSTALLINE AND CRYSTALLINE) AND CEMENTS FOR CERAMIC BONE CEMENT APPLICATIONS 78

3.1 INTRODUCTION 78

3.2 MATERIALS AND METHODS 81

3.2.1 Synthesis of Magnesium Phosphate Powders 81

3.2.2 Magnesium Phosphate Powder Characterization 81

3.2.3 Cement Formation 81

3.2.4 Cement Characterization 83

3.3 RESULTS AND DISCUSSION 84

3.3.1 Magnesium Phosphate Powder Characterization 84

3.3.2 Cement Formation 88

3.3.3 Cement pH and Stability *In Vitro* 91

3.3.4 Cement Instability 100

3.4 CONCLUSION 101

4.0 SPECIFIC AIM 3: ASSESSMENT OF THE EFFECT OF REACTING SOLUTION ON THE CEMENTING REACTION WITH TRIMAGNESIUM PHOSPHATE 102

4.1 INTRODUCTION 102

4.2 MATERIALS AND METHODS 104

4.2.1 Cement Preparation 104

4.2.2 Cement Characterization 105

4.3 RESULTS AND DISCUSSION 107

4.3.1 Initial Cement Characterization 107

4.3.2 Alternative Strategies 116

4.4 CONCLUSIONS 120

5.0 SPECIFIC AIM 4: EVALUATION OF THE EFFECT OF MANNITOL POROGEN ADDITION ON A MAGNESIUM AMMONIUM PHOSPHATE CEMENT FORMULATION 122

5.1 INTRODUCTION 122

5.2 MATERIALS AND METHODS 123

5.2.1 Cement Preparation 123

5.2.2 Cement Characterization 124

5.2.3 Mechanical Properties of Cements 124

5.2.4 *In Vitro* Dissolution Characteristics 125

5.2.5 Cytocompatibility 125

5.2.6 Statistics 126

5.3 RESULTS 127

5.3.1 Cement Setting Times 127

5.3.2 Cement Characterization 128

5.3.3 Cement Strength and Porosity 135

5.3.4 Cytocompatibility 144

5.4 DISCUSSION 148

5.5 CONCLUSION 151

6.0 SPECIFIC AIM 5: EFFECT OF FIBER REINFORCEMENT OF A MANGESIUM AMMONIUM PHOSPHATE CEMENT WITH WETSPUN POLYCAPROLACTONE FIBERS 153

6.1 INTRODUCTION 153

6.2 MATERIALS AND METHODS 155

6.2.1 Fiber Generation and Characterization 155

6.2.2 Cement Generation 156

6.2.3 Cement Characterization and *In Vitro* Dissolution 157

6.2.4 Cell viability 159

6.3 RESULTS 160

6.3.1 Fiber Characterization 160

6.3.2 Cement Characterization 161

6.4 DISCUSSION 177

6.5 CONCLUSION 183

7.0 CONCLUSIONS AND FUTURE WORK 184

APPENDIX A 188

APPENDIX B 210

APPENDIX C 235

BIBLIOGRAPHY 265

LIST OF TABLES

Table 1-1 Magnesium cement related compounds 9

Table 1-2 Proposed magnesium cement chemical reactions 13

Table 1-3 Cement systems in the biomedical MPC literature 15

Table 3-1 Cement handling properties and pH in saline solution. 90

Table 4-1 Handling of cement putties and durability after drying. 109

Table 6-1 Mechanical properties of fibers at failure. 161

Table A-1 TGA/DSC mass loss and crystallization change peak temperature measurements of calcium and strontium doped TMP precipitates. 199

Table A-2 Molecular ion ratios of magensium, calcium, strontium and phosphorous measured through ICP-OES. 207

Table B-1 Coating thicknesses on magnesium substrates. 218

Table B-2 Corrosion potential (E_{corr}) and current density (i_{corr}) values for coated and uncoated substrates. 223

Table C-1 Corrosion potential (E_{corr}) and current density (i_{corr}) values for coated and uncoated substrates. 251

LIST OF FIGURES

Figure 1-1 Schematic of reaction process of chemically bonded phosphate ceramic formation, from Wagh et al [54] 6

Figure 1-2 Setting time of MgO MPCs varying with P:L (here liquid-to-solid ratio, L:S) and calcining temperature, from Wang et al [37] 19

Figure 1-3 Relationship between porosity and ln(compressive strength) calcium-magnesium phosphate cements, from Vorndran at al[87] 24

Figure 1-4 Weight loss of MPC, CPC and combination systems, from Wu et al [58] 33

Figure 1-5 MG_{63} cell growth and activity on CDHA, DCPD and Sv cements, from Ewald et al[86] 36

Figure 1-6 Effect of elevated magnesium ion concentration on hBMSCs indicating (A) increased proliferation at 10 mM Mg concentration in maintenance and osteogenic media and (B) enhanced protein expression at 10 mM Mg concentration (mean fold change compared to 0.8 mM concentration), from Yoshizawa et al[41] 37

Figure 1-7 Viable bacteria following exposure of incubation extracts of MPCs tested on three different bacteria with fresh and aged extracts, relative to PBS controls, from Mestres et al [28] 39

Figure 1-8 Results of Sv and brushite cement implantation in sheep femoral condyles for 10 months, showing a) x-ray, B) macroscopic images, C) µ-CT slices and D) histological section stained with toluidine blue and basic fuchsin, from Kanter et al [78] 41

Figure 2-1 Basic material characterization showing (a) XRD of the as synthesized powder and the powder thermally treated to 200 °C and 750 °C with reference pattern of $Mg_3(PO_4)_2$ (ICCD Card 00-033-0876) and (b) TGA/DSC of the as synthesized powder..... 58

Figure 2-2 Electron microscopy of synthesized $Mg_3(PO_4)_2$ powders displaying (a) representative SEM images of the as-synthesized and thermally treated powders (scale bar is 10µm) and (b) TEM images of the as synthesized powder at low magnification (scale bar is 40 nm) at left and images of the as-synthesized and thermally treated powders at high magnification (scale bar is 2 nm). Insets show diffraction patterns of the respective samples..... 60

Figure 2-3 *In vitro* dissolution of pellets showing (a) the released ion concentrations of magnesium (top) and calcium (bottom) into the media and (b) SEM of pellet surfaces: as-synthesized and after 14 days in media (scale bar is 10 µm)..... 61

Figure 2-4 SEM images of ATMP pellets (a) after 14 days of incubation in culture media with 0 % and 20 % fetal bovine serum (FBS, scale Bar is 5 µm) and FTIR spectra (b) of ATMP and CTMP powders, FBS, and ATMP pellet scrapings. 63

Figure 2-5 SEM image of early rosette formation (a) at 24 hours of incubation (scale bar is 1 µm), TEM images of pellet scraping at low magnification (b, scale bar is 20 nm)

and high magnification (c, scale bar is 5 nm) with inset containing the diffraction pattern for the particle, and EDS elemental analysis from the particle (d).DONE65

Figure 2-6 Live/Dead staining of MC3T3 osteoblasts, left to right are βTCP, ATMP and CTMP at days 1 and 5 post seeding (top and bottom respectively, scale bar is 200 μm)..... 66

Figure 2-7 MTT viability results of direct and indirect MC3T3 cell culture (a), SEM images of fixed MC3T3 cells on βTCP, ATMP and CTMP pellets 24 hours after seeding (b-d, scale bar is 50 μm) showing preferential attachment to surface growth particles (indicated by the arrows) on the ATMP scaffold, and ALP activity of MC3T3 cells cultured on pellets in osteogenic media (OM) (e). *Units of ALP are [(μmol/hr)/(μg protein)/cm^2 surface area] 68

Figure 2-8 SEM Images of RAW 264.7 cell morphology on pellet surfaces after 8 and 11 days of culture in media supplemented with RANKL (scale bar is 25 μm). 69

Figure 2-9 Actin-Nucleus staining of RAW 264.7 cells at days 8 & 11 of culture in media supplemented with RANKL (scale bar is 50 μm)..... 69

Figure 3-1 TGA and DSC of the synthesized $Mg_3(PO_4)_2$ powders. 84

Figure 3-2 XRD of the synthesized $Mg_3(PO_4)_2$ powders. 85

Figure 3-3 FTIR spectra of the synthesized $Mg_3(PO_4)_2$ powders. 86

Figure 3-4 BET measured surface area of the $Mg_3(PO_4)_2$ powders. 87

Figure 3-5 Scanning electron microscopy images of synthesized and thermally treated $Mg_3(PO_4)_2$ powders..... 88

Figure 3-6 Cement settings times as a function of powder crystallinity and powder-to-liquid ratios..... 89

Figure 3-7 Uniaxial compression strength of cements. 92

Figure 3-8 XRD spectra of 400 °C, 600 °C, and 800 °C cements, P:L ratios of 1:2, 1:2 and 1:1 respectively, after completion of the cement reaction. 94

Figure 3-9 XRD spectra of 400 °C, 600 °C, and 800 °C cements, P:L of 1:2, 1:2 and 1:1 respectively following 48hour PBS incubation 95

Figure 3-10 FTIR spectra of 400 °C, 600 °C, and 800 °C cements, P:L of 1:2, 1:2 and 1:1 respectively after reaction completion. 96

Figure 3-11 FTIR spectra of 400 °C, 600 °C, and 800 °C cements, P:L of 1:2, 1:2 and 1:1 respectively following 48 hour PBS incubation. 97

Figure 3-12 SEM images of 400 °C, 600 °C, and 800 °C cements, P:L ratios of 1:2, 1:2 and 1:1 respectively. The top group of images shows the fracture surface of cements, after reaction completion and after PBS incubation, while the bottom group of images shows the native (outside) surface of the same cements, after reaction completion and after PBS incubation. (Scale bar: 10 μm) 99

Figure 4-1 Setting times of cements varying with setting solution and powder-to-liquid ratios 108

Figure 4-2 pH of cements following 24 and 48 hours incubated in PBS at 37 °C. 110

Figure 4-3 True density, apparent density and porosity measurements of cements as generated and after 48 hours incubated PBS at 37 °C. 112

Figure 4-4 XRD spectra of cements as generated and after 48 hours of incubation in PBS at 37 °C Phases are (a) $Mg_3(PO_4)_2$, (b) $Mg_3(NH_4)_2H_4(PO_4)_4 \cdot 8H_2O$, (c) $MgNH_4PO_4 \cdot 6H_2O$ (d) $MgHPO_4 \cdot 3H_2O$ (e) $MgNa_3H(PO_4)_2$, (f) $Na_{1.05}Mg_{3.96}(PO_4)_3$, (g) $KMgPO_4 \cdot 6H_2O$, (h) $Mg_3(PO_4)_2 \cdot 8H_2O$, (i) $K_2Mg(PO_3)_4$, and (k) KH_2PO_4. .. 114

Figure 4-5 Cement setting times of 3M monoatomic or diatomic hydrogen salt solutions at two differnet P:L ratios of 1:1 and 2:1. 117

Figure 4-6 X-ray diffraction patters of generated seed crystals from ammonium, potassium and sodium solutions and matching phase spectra, $Mg_3(PO_4)_2$ and $MgNH_4PO_4•6H_2O$. 119

Figure 5-1 First and second setting times of mannitol-containing magnesium phosphate cements (n=4) 128

Figure 5-2 X-ray Diffraction patterns of mannitol-containing magnesium phosphate cements at (a) 0 days in PBS (as generated) and (b) 14 days in PBS. Phases present are denoted: struvite (*), newberyite (#), unreacted trimangesium phosphate (+), mannitol (>), and hannayite ($) 129

Figure 5-3 FTIR spectra of select mannitol containing cements as generated and after 14 days of incubation in PBS. 131

Figure 5-4 pH measurements (a) and weight change (b) of mannitol containing cements through 14 days of incubation in PBS (n=4) 133

Figure 5-5 Daily magnesium (a) and phosphorus (b) ion concentration measure by ICP-OES through 14 days of incubation in PBS at 37°C (n=4) 134

Figure 5-6 Compressive strength of magnesium ammonium cements, with up to 50 weight % mannitol porogen addition, through 14 days of incubation in PBS (n=4) 136

Figure 5-7 Measurements of true density (a), apparent density (b), surface area (c) and porosity (d) of mannitol containing cements through 14 days of incubation in PBS at 37 °C (n=4) 138

Figure 5-8 Mercury intrusion porosimetry measurements of mannitol supplemented cements. In (a) and (b) are the log differential intrusion volumes at 0 and 3 days of PBS incubation, respectively. In (c) and (d) are the cumulative intrusion volumes at 0 and 3 days of PBS incubation, respectively (n=1, representative only) 140

Figure 5-9 SEM images of the exposed cement surface as generated (Day 0) and after 14 days of PBS incubation (Scale bar is 50 µm). 142

Figure 5-10 SEM images of the fracture (internal) cement surface as generated (Day 0) and after 14 days of PBS incubation (Scale bar is 50 µm). 143

Figure 5-11 SEM images of internal cement surface after 1 day in PBS at 1500x magnification (Scale bar is 10 µm). 144

Figure 5-12 Live/Dead staining of MC3T3s on cements at 1 and 7 days of culture (Scale bar is 200 µm). 145

Figure 5-13 MTT (a) and cell number (b) data for MC3T3s grown on cements at 1, 3 and 7 days culture 147

Figure 6-1 Schematic of the wet spinning set up. 156

Figure 6-2 Macroscopic (a) and optical microscopy (b) image of the PCL fibers derived by wet-spinning. 160

Figure 6-3 Example Fiber Stress-Strain Curve. 161

Figure 6-4 First and second setting times of fiber containing cements 162

Figure 6-5 X-ray Diffraction spectra of cements at (a) 0 days and (b) 30 days of incubation in PBS. Phases present are denoted: struvite (*), newberyite (#), unreacted trimangesium phosphate (+), and hannayite ($). 163

Figure 6-6 FTIR spectra of cements at 0 days (a) and 30 days (b) incubation in PBS at 37 °C. 164

Figure 6-7 pH (a) and weight change (b) of cements through 30 days of incubation in PBS.... 165

Figure 6-8 Density trends of cements through PBS incubation and with the PCL fibers removed (labeled THF) showing the true density (a), envelope density (b) and porosity (c). 167

Figure 6-9 Mercury intrusion porosimetry depicting the log differential (or instantaneous) intrusion volume of cements as generated (a) and with PCL fibers removed (b) and cumulative intrusion volume of cements as generated (c) and with PCL fibers removed (d). 169

Figure 6-10 Representative force-displacement curves in 3-point bending of fiber reinforced cements. 170

Figure 6-11 3 point bend strength of cement samples at (a) the peak strength and (b) L/50 residual strength through 30 days of incubation in PBS. 171

Figure 6-12 Toughness under 3-point bending of cement samples at (a) the peak strength point and (b) L/50 residual point through 30 days of incubation in PBS. 172

Figure 6-13 Compressive strength of fiber reinforced cements through 30 days of incubation in PBS. 173

Figure 6-14 SEM images of the external (pressed) surface of fiber containing cements as generated and at 1 and 30 days of incubation in PBS at 37 °C (100μm scale bar). 174

Figure 6-15 SEM images of the internal (fracture) surface of fiber containing cements as generated and at 1 and 30 days of incubation in PBS at 37 °C (50um scale bar). 175

Figure 6-16 Live/dead staining of MC3T3 cells on magnesium ammonium cement scaffolds after fiber leaching (Scale bar is 100 µm)..... 176

Figure 6-17 SEM images of MC3T3 cells on magnesium ammonium cement scaffolds after fiber leaching (Scale bar is 50 µm). 176

Figure 6-18 Material parameters affecting mechanical behavior of FRCs (a) and representative stress-strain curves of FRCs failing through brittle, tension softening or strain hardening modalities, taken from Krueger et al. [249]. 178

Figure A-1 X-ray diffraction patterns of the as synthesized calcium and strontium doped tri-magesnium phosphate powder indicating that all the as-prepared powders were amorphous. 192

Figure A-2 X-ray diffraction results of calcium doping into tri-magnesium phosphate through aqueous co-precipitation and thermal treatment to 800 °C for 6 hours in air, phases are (a) $Mg_3(PO_4)_2$, (b) $Na_{1.05}Mg_{3.96}(PO_4)_3$, (c) $Ca_4Mg_5(PO_4)_6$, (d) $Ca_3(PO_4)_2$, and (e) $Mg_{21}Ca_4Na_4(PO_4)_{18}$ 194

Figure A-3 X-ray diffraction results of strontium doping into tri-magnesium phosphate through aqueous co-precipitation and thermal treatment to 800 °C for 6 hours in air. Phases are identified as (a) Farringtonite (f) Magnesium strontium phosphate, (g) Sodium magnesium phosphate, (h) 00-048-1855, (i) 01-076-4588, (k) 00-012-0369 and (x) for as of yet unidentified peaks. 196

Figure A-4 SEM images of calcium and strontium doped TMP powders as synthesized and after thermal treatment to 800 °C for 6h in air. Scale bar 50 microns. 198

Figure A-5 TGA/DSC plots of un-doped TMP (a), 50% calcium doped TMP (b) and 50% strontium doped TMP (c). 200

Figure A-6 XRD of calcium and strontium doped TMP thermally treated to 500 °C for 6 hours. 202

Figure A-7 XRD of calcium and strontium doped TMP thermally treated to 600 °C for 6 hours. 202

Figure A-8 XRD of calcium and strontium doped TMP thermally treated to 700 °C for 6 hours 203

Figure A-9 FTIR spectra of calcium doped TMP as synthesized and thermally treated to 500, 600 and 800 °C for 6 hours each in air 205

Figure A-10 FTIR spectra of strontium doped TMP as synthesized and thermally treated to 500, 600 and 800 °C for 6h in air. 206

Figure A-11 Live/dead staining of MC3T3 cells grown on calcium and strontium substituted TMP pellets thermally treated to 800 °C for 6 hours in air. Scale bar is 200 µm. 208

Figure B-1 FTIR spectra of Uncoated AZ31 (a), Uncoated Mg4Y (b), pure PLGA (c) and coated samples AZ31-PLGA 10 % (d), AZ31-PLGA 20 % (e), Mg4Y-PLGA 10 % (f) and Mg4Y-PLGA 20 % (g), showing clear presence of PLGA on all coated substrates. 219

Figure B-2 Polarization curves of substrates AZ31 (a) uncoated (i), PLGA 10 % (ii) and PLGA 20 % (iii) coatings and Mg4Y (b) uncoated (i), PLGA10 % (ii) and PLGA 20 % (iii) coatings. 222

Figure B-3 SEM Images of uncoated and PLGA coated AZ31 substrates post incubation in media (Scale bar is 500 μm). 224

Figure B-4 SEM Images of uncoated and PLGA coated Mg4Y substrates post incubation in media (Scale bar is 500 μm). 225

Figure B-5 ICP measurements of daily magnesium ion concentration in extracted incubation media for AZ31 coated and uncoated samples (a) and Mg4Y coated and uncoated samples (b). 227

Figure B-6 Digital Optical Images of PLGA coated AZ31 and Mg4Y substrates post incubation in media (Scale bar is 2 mm). 229

Figure B-7 Morphology of MC3T3 osteoblasts at 24 hrs post-seeding, indicating better cell adhesion for thicker PLGA coatings (Scale bar is 100 μm). 231

Figure B-8 Live/Dead Staining of MC3T3 osteoblasts on coated and uncoated substrates indicating improved biocompatibility of coated substrates over uncoated substrates (Scale bar is 100 μm) 232

Figure C-1 Simulated x-ray diffraction patterns of pure magnesium [JCPDS 35-0821] (a) and $Mg(OH)_2$ [JCPDS 7-239] (b) with glancing angle x-ray diffraction of (c) NaOH-treated AZ31 substrate showing growth of $Mg(OH)_2$ layer, indicated by the asterisk *. 246

Figure C-2 FTIR spectra of coated substrates and individual components. In each set of spectra, (a) is AZ31 with NaOH treatment, (b) is pure PEI and (c) is pure PAH

while (d) is the utilized anionic polymer and (e) is the fully coated substrate. Spectra set (i) presents the PCL coatings, (ii) presents the PLGA50:50 series and (iii) presents the PLGA75:25 series, each showing clear presence of the anionic polymers on coated substrates. The presence of the cationic polymers is obscured by thick top coating. 247

Figure C-3 SEM images of uncoated AZ31(a), PCL (b), PLGA 50:50 (c) and PLGA 75:25 (d). Scale bar is 50 μm. 248

Figure C-4 Polarization curves (a) of uncoated AZ31 (aa), PCL (ab), PLGA50:50 (ac), PLGA75:25 (ad) and $Mg(OH)_2$ (ae) showing less negative corrosion potential and reduced corrosion current for all coated substrates over the uncoated alloy. Electrochemical Impedance Spectroscopy (EIS) measurements of the coated and uncoated substrates are shown in (b). Measurements were taken in the frequency range of 1000-0.01 Hz with an amplitude of 0.005 V. 250

Figure C-5 ICP measurements of daily released magnesium ion concentration in extracted incubation media for AZ31 coated and uncoated samples. For every time point, all coated samples show statistically lower ion concentrations ($p<0.05$) than the uncoated AZ31, indicated by the *asterisk 252

Figure C-6 Cumulative hydrogen evolution in Hanks solution over a two-week period, showing a marked reduction in hydrogen release with coated samples in comparison to uncoated AZ31. 253

Figure C-7 SEM images of substrates Uncoated AZ31(a), PCL(b), PLGA 50:50 (c) and PLGA 75:25 (d) following two week incubation for hydrogen-evolution testing. Scale bar is 50 μm. 253

Figure C-8 Live/Dead staining of MC3T3 osteoblasts (a-d) and hMSCs (e-h) on day 3 of culture post seeding on uncoated AZ31 (a & e), PCL (b & f), PLGA 50:50 (c & g) and PLGA 75:25 (d & h) indicating improved biocompatibility of coated substrates over uncoated substrates. Scale bar is 200 μm. 255

Figure C-9 Cell morphology of MC3T3 osteoblasts (a-d) and hMSCs (e-h) observed at 24 hours post seeding through actin-nucleus co-staining on uncoated AZ31 (a & e), PCL (b & f), PLGA 50:50 (c & g) and PLGA 75:25 (d & h). Scale Bar is 100 μm. 255

Figure C-10 SEM morphology of fixed MC3T3 osteoblasts (a-d) and hMSCs (e-h) at 24hrs post-seeding on Uncoated AZ31 (a & e), PCL (b & f), PLGA 50:50 (c & g) and PLGA 75:25 (d & h). Scale Bar is 100 μm. 256

Figure C-11 Quantification of total DNA content, using MC3T3 osteoblasts, on substrates at various time points. On day 3 and day 7 all coated substrates showed statistically higher ($p<0.05$) levels of DNA than the uncoated substrate, indicated by the *asterisk. 257

PREFACE

To Jim, Amber, my grandparents and those friends who feel more like family.

1.0 INTRODUCTION

1.1 CERAMIC BONE CEMENTS

1.1.1 Clinical Need

Currently, autografting remains the primary solution of many clinicians for the repair of dental, craniofacial and orthopedic boney critical-sized defects. However autografting requires a painful secondary surgery site which increases the risk of patient pain, infection and complications. The use of synthetic bone void filling materials eliminates the need to resect boney tissue from a secondary location in the body and also does not carry the same risk of disease transmission as allografting materials [1-3]. Synthetic materials also do not have same risk of low supply or high cost associated with autografts and allografts nor do these materials suffer from inconsistency which occurs due to variability in donor bone quality [4]. For these reasons, the market for synthetic bone filling materials is expected to continue to increase as surgeons and dentists move away from autograft and allograft materials favoring synthetic substitutes [5]. Bone grafting substitutes utilize synthetic materials, typically polymers or ceramics, to fill routine, chronic or traumatic voids along with non-degradable metal based fixation devices [6]. Applications of bone void fillers are widespread, ranging from filling holes left by routine tooth removal, to space filling during spinal fusions to maxillofacial reconstruction of wounded soldiers after

traumatic combat and battlefield injuries [7-9]. Degradable materials provide the additional benefit of resorbing over time to be replaced by native tissue, avoiding the long-term rejection issues seen in non-degradable materials systems [3]. Based on the US Food and Drug Administration (FDA), calcium and magnesium implants of this type are formally termed 'bone void fillers', separating them from the poly (methyl methacrylate) (PMMA)-type polymeric cements. It should be noted however 'cement' is colloquially used to refer to these materials in the literature, thus 'cement' will be used throughout this discussion and the subsequent chapters of this thesis.

1.1.2 History of Bone Cements

Calcium phosphate (CaP) scaffolds have been the preferred choice for bone repair scaffold because these materials mimic the chemical composition of hydroxyapatite ($Ca_{10}(PO_4)_6(OH)_2$, HA), the mineral found in human bone [10]. Due to this similarity in chemistry, CaPs show excellent biocompatibility. However, the commercial products now available, such as particulate fillers and bone cements, are less than ideal in other aspects. Ceramic bone cements are generally consisting of two component systems, a powder containing calcium phosphate salts and an aqueous solution. Upon mixing the powder and liquid results in the formation of freely moldable slurry with a paste-like consistency. This undergoes a chemical reaction, transitioning from a viscous, injectable liquid, requiring less invasive surgery, to a solid implant by entanglement of the crystals precipitating within the paste [11, 12]. While the use of a ceramic bone substitute was initially explored more than 100 years ago, research and development into CaP cements (CPC) as they are currently understood began in the early 1980s with LeGeros, 1982, and Brown and Chow, 1983 [13-15]. Not long after, CPCs were commercialized, and at present, myriad

commercial formulas are available for a wide variety of applications, including the repair of craniofacial, dental, and fracture defects [8, 16-18].

1.1.3 Commercial Calcium Phosphate Cements and Limitations

Commercially available CPCs exhibit two main formulations: brushite, or dicalcium phosphate dihydrate, ($CaHPO_4 \cdot 2H_2O$, DCPD) forming and hydroxyapatite (HA) forming. Within these two classifications, there are numerous additives and reacting solutions, including reaction accelerants, cohesion promoters, fillers, plasticizers and radiological contrast agents [16, 18]. DCPD cements resorb well and set rather rapidly but exhibit low mechanical strengths and are acidic during the setting reaction [19]. HA forming cements on the other hand, achieve higher strengths however the reaction proceeds very slowly, risking early failure of the implant [20]. However, it should be noted that the formed HA by cement setting reactions is micro-structurally and chemically similar to natural inorganic component of bone (apatite) rendering CPCs biologically more active than the bulk ceramic related sintered blocks of HA [21, 22]. Additionally, the most popular HA grafts currently in use today may remain unchanged and only partially resorbed in the patient's body for an extended period of time due to the sintered nature of HA, potentially resulting in tissue inflammation and poor integration with the patient's bone [23-25]. Even brushite cements may display slower than expected degradation rates *in vivo*, as some researchers have found re-precipitation of apatite within the brushite cements, slowing the cement resorption [26, 27]. For these reasons, it is important to explore more bioactive, faster-degrading grafts with suitable mechanical properties for orthopedic, craniofacial and dental implantation which is the focus of the current study.

1.1.4 Magnesium Phosphate Bone Cements

The use of magnesium phosphate (MgP) based materials, particularly cements, have been proposed for clinically adoptable implants as an alternative to the options discussed earlier [28-33]. The first published instances of research into MgP cement (MPC) for biomedical applications occurred in the mid-1990s, with Driessens et al exploring CPC/MPC cement mixtures (CMPC) [34, 35]. The majority of MPC research however has been completed in the past decade. Nevertheless, the body of published research regarding MPCs for biomedical applications is still limited in both, variety as well as depths of fundamental study. A PubMed search (http://www.ncbi.nlm.nih.gov/pubmed) for "magnesium phosphate cement" yielded 19 results while a similar search for "calcium phosphate cement" yielded 856 results. Similarly, a search of the same terms in ISI Web of Science (http://www.webofknowledge.com/) yielded 65 and 1826 results, respectively. While these searches are not completely exhaustive or mutually exclusive, the results do give an indication of the depth of MPC research conducted to date. Some researchers have also observed that MPCs can achieve a more ideal combination of strength, setting time and resorption rate than calcium phosphate cements while remaining biocompatible *in vitro* [28, 29, 34, 36-39].

In addition to calcium, many other ions such as magnesium, silicon, zinc, potassium and copper play important roles in bone regeneration, from regulating metabolic processes and genes pertaining to osteoblastic differentiation to promoting angiogenesis and increasing bone cell adhesion [40, 41]. Magnesium has been shown to play a vital role in calcification and increasing bone density, mineral metabolism, HA crystal formation and increased bone cell adhesion and stability [19, 34, 42]. The specific role of magnesium in bone regeneration is still under investigation but has been shown to be dependent upon the local concentration as well as the

differentiation stage of the bone cells [41, 43]. While a high level of magnesium increases osteoblast proliferation, it has been shown to have the opposite effect on osteoclast formation and function, temporarily suspending the formation of polynucleated osteoclast cells *in vitro* [44-46]. The utilization of magnesium-based implants is arguably acceptable from a biological standpoint. However, high concentrations of any of these ions, including calcium, can significantly impede the viability of cells [47]. The goal of the present study is to review the scientific development and achievements of magnesium cements to date. Furthermore, the objective is to assess how these cements compare with calcium phosphate competitors and to analyze the future directions and outlook for the research, development and clinical implementation of these cements.

1.1.5 History of Magnesium Phosphate Cements

While the research work in the field MPCs is relatively young, similar formulations have witnessed a longer history of study in the fields of structural engineering and waste remediation [48-52]. These cements, often called chemically bonded phosphate ceramics or cold-setting ceramics, undergo a defined series of reaction steps, including an exothermic acid-base reaction, to form a hard product [52, 53]. Typically, MPCs are formed by reacting the solid magnesium oxide with an acid phosphate solution, resulting in the dissolution of the oxide into the solution, forming a solution of cations with water termed aquosol. These aquosols then react with the phosphate salts, forming a gel. As more dissolution occurs, aquosol formation and gelation occur leading to thickening of the mixture and eventual solidification causing crystallization to occur around any unreacted core of the remaining oxide [54]. This process is depicted in Figure 1-1 [54]. The rate at which this reaction proceeds depends primarily on the dissolution

step [12, 53]. If more than one solid precursor is involved in the cement setting reaction, the rate of the reaction will be controlled by the precursor with the least solubility and therefore, can significantly alter the cement handling, setting characteristics as has been similarly observed for CPCs [55]. While the traditional industrial applications are different, the base knowledge surrounding select cementing properties, including setting time, mechanical strength and workability of these industrial cements may be useful for the development of magnesium based bone cements.

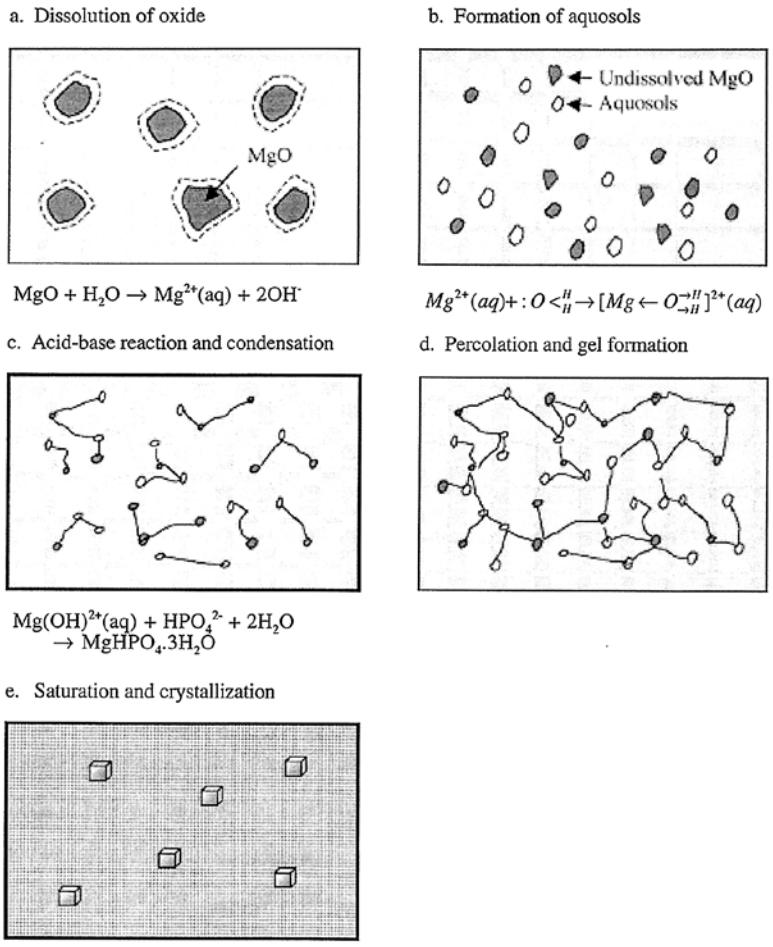

Figure 1-1 Schematic of reaction process of chemically bonded phosphate ceramic formation, from Wagh et al [54]

1.2 MAGNESIUM CEMENT SYSTEMS

Magnesium cement systems are typically generated using a matrix of two ceramics, magnesium oxide (MgO) and trimagnesium phosphate anhydrous ($Mg_3(PO_4)_2$, TMPA), with a variety of soluble phosphate salt solutions such as phosphoric acid (H_3PO_4, PA), monoammonium hydrogen phosphate ($NH_4H_2PO_4$, MAHP), disodium hydrogen phosphate (Na_2HPO_4, DNaHP) and dipotassium hydrogen phosphate (K_2HPO_4, DKHP) [36-38, 56-59]. Table 1-1 shows the possible magnesium cement precursor and product phase chemical formulas, common names and acronyms as well as commonly utilized calcium phosphate phases for comparison.

The bulk of research, both in the biomedical application as well as other applications mentioned above, involve use of magnesium oxide as the starting ceramic, typically reacted with ammonium or potassium phosphate salts, including the work of Mestres, Yang and Wu [29, 38, 52, 58]. To a lesser extent, trimagnesium phosphate has been explored with similar reacting salts, such as the work done by Klammert and Moseke, [31, 32, 60-62]. In the patent landscape, filings for magnesium cements and fillers for biomedical applications are evenly split between MgO and TMPA based formulations, with an additional large body of patents based on MgO formulations optimized for non-biomedical purposes [63-72]. While in the academic landscape, research has spanned basic science to product development, the work covered under patent landscape primarily involves two formulation embodiments: magnesium oxide plus potassium phosphate and calcium-substituted trimagnesium phosphate plus ammonium phosphate [66, 67, 71]. Of particular interest is the work by Mr. Thomas Lally focusing on the magnesium oxide and potassium phosphate formulation which has led to the OsteoCrete^{TM} product from Bone Solutions, Inc. (BSI) [67]. This is the only magnesium based cement formulation that has been approved by the FDA, having proceeded through the Section 510(k) substantial equivalence

route. OsteoCrete™ has been approved as a bone void filler for long-bone and pelvic applications, which should be ready to be commercially launched in 2015. BSI President Drew Diaz plans to pursue additional applications with the product, including the use as an adhesive and in spinal surgeries (personal communication, January 30th, 2015). The success, or lack thereof, of this BSI product could likely set the stage clinically for other researchers and companies to follow, as this class of products finds its place in the medical community.

Table 1-1 Magnesium cement related compounds.

Chemical Formula	Phase Name(s) (*Most Common)	Acronym
MgO	Magnesium Oxide, Magnesia*, Periclase	MgO
$Mg_3(PO_4)_2$	Trimagnesium phosphate*, Farringonite*, Trimagnesium phosphate anhydrous, Magnesium phosphate tribasic	TMPA
$Mg_3(PO_4)_2 \cdot 8H_2O$	Bobierrite*, trimagnesium phosphate octohydrate	TMPO
$Mg_3(PO_4)_2 \cdot 22H_2O$	Cattiite*, trimagnesium phosphate hydrate	Ct
$MgHPO_4$	Dimagnesium phosphate, Magnesium biphosphate, Magnesium hydrogen phosphate*	MHP
$MgHPO_4 \cdot 3H_2O$	Newberyite*, Magnesium phosphate dibasic trihydrate,	Nb
$MgNH_4PO_4 \cdot 6H_2O$	Struvite*, Magnesium Ammonium Phosphate Heptahydrate	Sv
$Mg(NH_4HPO_4)_2 \cdot 2H_2O$	Schertelite*	Sh
$MgKPO_4 \cdot 6H_2O$	Magnesium potassium phosphate hexahydrate, k-struvite*	KSv
$Mg_3(NH_4)_2(HPO_4)_4 \cdot 8H_2O$	Hannayite*	Hn
$Mg_2PO_4OH \cdot 4H_2O$	Holtedahlite*	Ho
$Mg(OH)_2$	Magnesium hydroxide*, Brucite	MH
$5Mg(OH)_2 \cdot MgCl_2 \cdot 8H_2O$	Magnesium oxychloride*	MOc
$MgCl_2$	Magnesium Chloride*	MC
$Ca_{10}(PO_4)_6(OH)_2$	Hydroxyapatite*	HA
$Ca_3Mg_3(PO_4)_4$	Stanfieldite*	Sf
$Ca_9Mg(PO_4)_6(HPO_4)$	Whitlockite*	W
$Ca_9(PO_4)_5HPO_4OH$	Calcium deficient hydroxyapatite*	CDHA
$CaHPO_4 \cdot 2H_2O$	Brushite*, Dicalcium phosphate dehydrate	DCPD
$CaHPO_4$	Dicalcium phosphate anhydrous*	DCPA
$Ca(H_2PO_4)_2 \cdot H_2O$	Monocalcium phosphate monohydrate*	MCPM
$\alpha, \beta\text{-}Ca_3(PO_4)_2$	Alpha, Beta-Tricalcium phosphate*	αTCP/ βTCP
$Ca_4(PO_4)_2O$	Tetracalcium phosphate*	TTCP
$Ca_8H_2(PO_4)_6 \cdot 5H_2O$	Octocalcium phosphate*	OCP
$NH_4H_2PO_4$	Monoammonium hydrogen phosphate*, Ammonium dihydrogen phosphate	MAHP
$(NH_4)_2HPO_4$	Diammonium hydrogen phosphate*, Diammonium phosphate	DAHP
KH_2PO_4	Monopotassium hydrogen phosphate* Potassium dihydrogen phosphate	MKHP
K_2HPO_4	Dipotassium hydrogen phosphate*	DKHP
NaH_2PO_4	Monosodium hydrogen phosphate*, Sodium dihydrogen phosphate	MNaHP
Na_2HPO_4	Disodium hydrogen phosphate*	DNaHP
$CaSO_3 \cdot {}^1/_2H_2O$	Calcium sulfate hemihydrate*	CSH
$CaSO_3 \cdot 2H_2O$	Calcium sulfate dehydrate	CSD
$Na_4P_2O_7$	Sodium Pyrophosphate*	SPP
$(NH_4)_2C_6H_6O_7$	Diammonium citrate*, Citric acid diammonium salt	DAC
$C_6H_8O_7$	Citric Acid*	CA
H_3PO_4	Phosphoric Acid*, Orthophosphoric acid	PA

1.3 MATERIALS PROPERTIES

The variety and extent to which raw material characteristics and resulting cement product properties affect the biochemical and biomechanical properties of bone putties is the basis for the vast majority of research and development that is much needed to advance this field. Cement properties which should be controlled or well understood include the following listed in no particular order of importance or preference: phase composition; setting time and handling characteristics; injectability and cohesion; exothermicity; setting pH; strength and porosity; adhesion; biocompatibility and toxicity; osseointegration and osseoinduction; solubility and cell-mediated degradation.

1.3.1 Chemical Composition

Precursor material properties which are important to consider include powder phase(s), particle size and shape, which affect the particle solubility and reactivity, liquid chemical composition and concentration, as well as the material source and level of purity. The phases used in a cementing reaction affect the reaction products, as discussed in the previous section. The size and shape of the powder particles expectedly affect the kinetics of the ensuing reaction and thus have an effect on the majority of subsequent properties including setting time and mechanical strength, such as increasing surface defects to increase wetting and nucleation sites [73]. The cement may be composed of ceramic powder with the reacting salt in aqueous solution or it may contain both the ceramic and salt in powder form, with reaction occurring following the addition of water [29, 62]. In some instances, the reacting salt(s) may be delivered in both powder and solution [74]. The control of particle size and reactivity are typically achieved through ball

milling, which reduces the particle size and increases the surface area therefore increasing the reactivity, and thermal treatment, or dead-burning, which decreases the surface reactivity. Dead-burning is very common for MgO powder.

1.3.2 Particle Size

The size of particles, and thus the surface area of the stating precursors, in MPCs affects not only the reaction rate of the cement but the handling characteristics such as injectability which ultimately may or may not affect the final strength of the cement [49]. The size or surface area of the starting powders is not frequently reported in the MPC literature. When reported, typical particle sizes for MgO and TMPA in MPCs range between 5-100 μm. For example, Mestres et al reported the use of MgO and MAHP or monosodium hydrogen phosphate (NaH_2PO_4, MNaHP) in powder form with mean (D_{50}) particle sizes of 5 μm (MgO), 7 μm or 185 μm (MNaHP), and 14 μm, 33 μm or 275 μm (MAHP) [29, 38]. Klammert et al tested a series of $Mg_xCa_{3-x}(PO_4)_2$ cements, where the magnesium-calcium phosphate powder was ground repeatedly several times, altering the D_{50} between 15 μm and 56 μm [60]. The grinding time was found to directly affect the setting time, with more grinding resulting in lower D_{50} and lower set times. Yu et al and Wu et al used MgO that were sieved between 200-300 meshes, to yield particle sizes in the 0.05-0.075 mm range particle diameters [36, 58]. Beyond this, many researchers report synthesis and post-processing protocols, which are easily followed, but do not report final raw powder size, shape or surface area. For example, Grossardt et al used TMPA that was sieved through -125 μm mesh then ball-milled for 1 hour and Moseke et al sieved TMPA through a -355 μm mesh then ball milled for 2 hours, Wang et al calcined MgO at various temperatures (1100 °C to 1500 °C)

for 3 hours [37, 62, 74]. A final particle size or surface area is however not reported in these publications, hence it is difficult to compare results with the information provided.

1.3.3 Cement Composition

As discussed above, the typical starting materials for MPCs is MgO or TMPA ceramic powder reacted with water soluble monoatomic or diatomic phosphate salts of ammonium, potassium or sodium. These precursors typically result in newberyite ($MgHPO_4 \cdot 3H_2O$, Nb), struvite ($MgNH_4PO_4 \cdot 6H_2O$, Sv), Sv analogs, or amorphous products with unreacted precursors. A variety of proposed chemical reactions between MgO or TMPA and phosphate salts can be seen in Table 1-2. A few less stable phases, such as schertelite ($Mg(NH_4HPO_4)_2.2H_2O$, Sh) and hannayite ($Mg_3(NH_4)_2(HPO_4)_4 \cdot 8H_2O$, Hn) may be formed as well. Table 1-3 contains a summary of cement compositions noted in the field of biomedical magnesium cements. Most researchers note varying levels of unreacted MgO or TMPA powder within the resulting cement structure. This tends to disappear, either through transformation or dissolution, following incubation in aqueous solutions. Some authors also note the formation of less stable phases, such as Sh and Hn which transition to more stable Sv and Nb phases after exposure to aqueous solutions [29, 38, 75]. As Moseke, Wang and many others note, the amount of unreacted ceramic powder increases with increasing powder to liquid ratio (P:L), attributed to the lack of phosphate salt available for continued reaction as well as physiochemical constraints due to water consumption and reaction progression [37, 57, 62]. Additionally, the ratio of ceramic powder to salt plays a role in the final composition and MPC properties. The molar ratio of ceramic to salt is typically kept at greater than 3:1, as excess ceramic contributes to moving the acid-base

reaction forwards towards completion [76, 77]. However, this ratio, if controlled by the P:L, may affect the materials strength and other properties, not just the degree of completion of the reaction [57]. When assessing trends in mechanical strength or cytocompatibility, it is not often possible to separate the effects of phase composition from the effects of microstructure and porosity. For this reason, it is best when authors provide a comprehensive documentation of the cement properties, such as reported in Kanter et al, which allows for a holistic review of the research results [78].

Table 1-2 Proposed magnesium cement chemical reactions.

Possible Chemical Reactions in the Magnesium Cement Systems	Reference
$MgO + 2H_3PO_4 \rightarrow Mg(H_2PO_4)_2 \cdot H_2O$	Wagh 2004 [79]
$MgO + H_3PO_4 + 2H_2O \rightarrow MgHPO_4 \cdot 3H_2O$	Wagh 2004 [79]
$3MgO + 2H_3PO_4 \rightarrow Mg_3(PO_4)_2 + 3H_2O$	Wagh 2004 [79]
$MgO + NH_4H_2PO_4 + 5H_2O \rightarrow MgNH_4PO_4 \cdot 6H_2O$	Yang 2014 [52]
$MgO + 2NH_4H_2PO_4 \rightarrow Mg(NH_4)_2(HPO_4)_2 \cdot 4H_2O$	Sugama 1983 [80]
$MgO + (NH_4)_2HPO_4 + 5H_2O \rightarrow MgNH_4PO_4 \cdot 6H_2O + NH_3 \uparrow$	Sugama 1983 [81]
$MgO + KH_2PO_4 + 5H_2O \rightarrow MgKPO4 \cdot 6H_2O$	Qiao 2012 [82]
$MgO + H_3PO_4 \rightarrow Mg(H_2PO_4)_2 \cdot 2H_2O + Mg(H_2PO_4)_2 \cdot 4H_2O$ *	Finch 1989 [83]
$MgO + (NH_4)_2HPO_4 \rightarrow Mg_3(PO_4)_2 \cdot 4H_2O + Mg(OH)_2 + MgNH_4PO_4 \cdot 6H_2O$ *	Sugama 1983 [80, 81]
$MgO + NH_4H_2PO_4 \rightarrow MgNH_4PO_4 \cdot 6H_2O + Mg(NH_4)_2(HPO_4)_2$ *	Sugama 1983 [80, 81]
$6MgO + 3Ca(H_2PO_4)_2 \cdot H_2O \rightarrow 2Mg_3(PO_4)_2 + Ca_3(PO_4)_2 + 6H_2O$	Jia 2010 [84]
$2Mg_3(PO_4)_2 + 3(NH_4)_2HPO_4 + 36H_2O \rightarrow 6MgNH_4PO_4 \cdot 6H_2O + H_3PO_4$	Klammert 2010 [32]
$Mg_3(PO_4)_2 + (NH_4)_2HPO_4 + 15H_2O \rightarrow 2MgNH_4PO_4 \cdot 6H_2O + MgHPO_4 \cdot 3H_2O$	Moseke 2011 [62]
$Mg_3(PO_4)_2 + NH_4H_2PO_4/(NH_4)_2HPO_4 \rightarrow Mg_3(NH_4)_2H_4(PO_4)_4 \cdot 8H_2O$ *	Ostrowski 2015 [75]
	* Not Balanced

Less common formulations include the use of magnesium hydroxide ($Mg(OH)_2$, MH) and PA to create cement of pure Nb, the use of MgO and monocalcium phosphate monohydrate ($Ca(H_2PO_4)_2 \cdot H_2O$, MCPM) to create TMP and TCP, and recently the creation of magnesium

oxychloride ($5Mg(OH)_2 \cdot MgCl_2 \cdot 8H_2O$, MOc) cement by combining MgO and magnesium chloride($MgCl_2$, MC) with PA [39, 84, 85].

There are however, two dominant MPC precursor ceramic powders, MgO and TMPA, which both have shown appropriate working properties namely, high initial compressive strength and high levels of cytocompatibility. This has led to significant segmentation between research groups, with a group focusing solely on one of the two MPC styles. However, there has not been a direct comparison of analogous cements from each category in order to assess the two types of products directly. For example, a study comparing each powder reacted with the often studied 3.5 M diammonium hydrogen phosphate ($(NH_4)_2HPO_4$, DAHP) solution, while controlling the powder surface area and P:L, could yield insight into the degree of reaction completion, cement strength morphology, and cytocompatibility. Additionally, while many researchers report cement morphology, and correlations can be drawn between morphology and cement properties, particularly strength, there is no systematic research reported in the MPC field into controlling the reaction parameters to achieve control of morphology or regulating morphology to control the cement properties.

Table 1-3 Cement systems in the biomedical MPC literature.

Author/Reference	Reactants: Powder/ Solution/ Additive (*Retardant, #Radiopacity, ^Other)	Product Matrix	P:L	Set Times (min) $1^{st}/2^{nd}$	Compressive Strength (^{C} Compacted, ^{H} Humid/ Wet Setting, ^Other)	Porosity (%)	Density g/cm^3
Magnesium Cement Systems							
Ewald (2011) [86]	TMPA+Sv / 3.5M DAHP	Sv+TMPA	2:1	-	6.6 MPa^{H}	-	-
Grossardt (2010) [74]	TMPA+Sv / 3.5M DAHP	Sv + TMPA	2:1	-	-	-	-
Kanter (2014) [78]	TMPA / 3M DAHP+0.5MAHP / -	TMPA+Sv	2:1 and 3:1	- / 3.3-6	57.5 to 65.5 MPa^{H}	5-7	-
Klammert (2010) [60]	TMPA+MCPM / 0.5M CA / -	Nb+DCPD	3:1	- / 21	10-45MPa^{H}	-	-
Mestres (2013) [28]	MgO+MAHP / Water / Borax*	Sv+Sh+MgO+Borax	7.7:1	13/14	43.4 MPa^(7 days *in vitro*) 22 MPa^(dentin pushout)	-	-
Mestres (2013) [28]	MgO+MNaHP / Water / Borax*	MgO+Amorphous+Borax	7.7:1	6.5/7	30.8 MPa^(7 days *in vitro*) 21 MPa^ (dentin pushout)	-	-
Mestres (2013) [28]	MgO+MAHP+MNaHP / Water / Borax*	Sh+Sv+MgO+Borax	7.7:1	7.5/8.5	46.1 MPa^(7 days *in vitro*) 20 MPa^ (dentin pushout)	-	-
Mestres (2014) [38]	MgO+MAHP/ Water / Borax*, Bi_2O_3#	Sv+Sh+Mgo+Borax+Bi_2O_3	7.7:1	7.2/8.8	17MPa^{H}, 41MPa^(7 days *in vitro*)	11	-
Mestres (2014) [38]	MgO+MNaHP/ Water / Borax*, Bi_2O_3#	MgO+Amorphous+Borax+ Bi_2O_3	7.7:1	5.8/7.4	12MPa^{H}, 40MPa^(7 days *in vitro*)	5.0	-
Mestres (2014) [38]	MgO+MNaHP+MAHP/ Water / Borax*, Bi_2O_3#	Sv+Sh+MgO+Borax+Bi_2O_3	7.7:1	9.0/11.4	15MPa^{H}, 32MPa^(7 days *in vitro*)	4.2	-
Mestres (2011) [29]	MgO+MAHP/Water/Borax*	Sv+Sh+MgO+Borax	7.7:1	15/16	30 MPa^{H}, 47MPa^ (7 days *in vitro)*	-	-
Mestres (2011) [29]	MgO+MNaHP/ Water / Borax*	MgO+Amorphous+Borax	7.7:1	8/9	28 MPa^{H}, 45 MPa^ (7 days *in vitro)*	-	-
Mestres (2011) [29]	MgO+MNaHP+MAHP/ Water / Borax*	Sh+Sv+MgO+Borax	7.7:1	12/13	30 MPa^{H}, 18MPa^ (7 days *in vitro)*	-	-
Moseke (2011) [62]	TMPA / 3.5M (DAC+DAHP)	Sv+TMPA	2.5:1	2-90+ / -	3.7-64.6 MPa^{H}	-	1.48-1.88
Ostrowski (2015) [75]	TMPA/ 3.0 M (MAHP+DAHP) / -	Hn+TMPA	2:1 to 1:3	<1 - >60	2-30 MPa, 0-15 MPa^ (2 days *in vitro*)	-	-
Tan (2015) [85]	MgO/MC+PA/ -	MOc	1.7:1 to 1:1	-	19-27 MPa, 5-32 MPa^ (21 days in vitro)	-	-
Vorndran (2011) [87]	TMPA / 3.5M DAHP / -	Sv+Nb+TMPA	3:1	- / 4	45-65 MPa^{H}	14-19	-

Table 1-3 (Continued).

Wang (2013) [37]	MgO+MKHP / Water / -	MgO+KSv	4:1 to 1.5:1	- / 2.5-17	11-23 MPa^{H}	7-22	-
Wu (2008) [58]	MgO+DAHP/Water/ -	Sv+MgO	8:1	- / 11	58 $MPa^{C,H}$	-	-
Yang (2014) [88]	MgO+MAHP / Water / -	Sv+MgO	-	-/ 3	18 MPa^{H}, 36 MPa^ (4 weeks *in vitro*)	-	-
Yu (2010) [89]	MgO+MAHP/ Unknown / Unknown*	-	-	-	85MPa^{H}, 28MPa^ (3 months in vivo)	-	-
Zhou (2013) [39]	MH/PA/ -	Nb	1.25:2	3.5/11.8	13MPa^{H}	-	-
Zhou (2013) [39]	Nb/water/-	Nb	2.5:1	2.8/6.7	30 MPa^{H}	-	-
Combination Systems							
Driessens (1995) [15, 34]	DCPD +MgO+Nb / Water / -	$CaMg_2(PO_4)_2$	-	-	11 MPa, 3 MPa^ (8 weeks in vivo)	-	-
Jai (2010) [84]	MgO+MCPM / Water / -	TMPA+TCP	5:1 to 1.9:1	- / 5-12	30-75 $MPa^{C,H}$	-	-
Klammert (2011) [31]	$Mg_{2.25}Ca_{0.75}(PO_4)_2$ / 0.05M CA / -	DCPD+Nb, transformed to W after implantation	3:1	-	10 MPa, 4 MPa^ (15 months *in vivo*)	-	-
Klammert (2011) [31]	$Mg_{2.25}Ca_{0.75}(PO_4)_2$ / 3.5M DAHP / -	TMPA+Sv, transformed to TMPA+W (implanted)	3:1	-	12 MPa, 1 MPa^ (15 months *in vivo*)	-	-
Wu (2008) [58]	MgO+MAHP+TTCP+DCPA / Water / -	HA+MgO+Sv+TTCP	8:1 to 4:1	- / 6-12	33-83 $MPa^{C,H}$	-	-
Klammert(2010) [60]	$Mg_xCa_{x-3}(PO_4)_2$+MCPM / 0.5M CA / -	DCPD+TCP+Nb (with Mg)	3:1	- / 8-60<	10-45MPa^{H}	-	-
Pijocha (2011) [90]	MgO+MAHP+HA/ Water / SPP* or CSH*	-	3.85:1 to 1.4:1	-	-	-	-
Vorndran (2011) [87]	$Mg_xCa_{3-x}(PO_4)_2$ / 3.5M DAHP / -	Sv+(Nb or DCPD)+(Sf or TMPA)	3:1 to 1.5:1	- / 3.5-32	20-80 MPa^{H}	17-32	-
Wu (2008) [58]	MgO+DAHP+TTCP+DCPA/Water/ -	Sv+MgO+HA+TTCP	8:1	- / 6-9	68-91 $MPa^{C,H}$	-	-
Yang (2014) [88]	MgO+MAHP+CSH / Water / -	Sv+MgO+CSH	-	- / 6-12	15-26MPa^{H}, 25-70MPa^ (4 weeks *in vitro*)	-	-
Other Notable Systems							
Klammert (2010) [32]	TMPA+DAHP / 0.75M DAHP+0.75M MAHP	TMPA+Sv+Nb	3:1	- / 2.5-26	0.23-7.01 MPa^ (3D Printed Scaffolds)	-	-
Kumar (2009) [91]	MgO+MKHP / Water / SiO_2^ (filler) Note: Cast cement, thermally treated	MgO + KSv + $K_2MgSi_5O_{12}$	-	-	-	-	2.15-2.50

1.3.4 Setting and Handling

Setting times are a critical aspect of bone cement design. The cement must set slowly enough to allow the clinician to mix, handle and make adjustments to the material. However it must also set rapidly enough to ensure fast completion of surgery as well as provide the needed mechanical support or rigidity to handle the cement. First (or initial) and second (or final) set times, as defined by ASTM C266-13, are the times at which the cement can withstand 0.25 and 1.0 pounds (113 and 454 grams) of weight without indentation [7]. Practically, the cement can no longer be manipulated after the first set time and is not truly functional until after the second set time. In general, first and second set times of 8 and 15 minutes are regarded as ideal for most clinical applications [92]. However, too short a first setting time is not suitable for most clinical application as the handling of the cement can be progressively difficult as it approaches the first setting time and therefore, can be unworkable before completion of the proper implantation [21, 93]. Another important aspect, which has often been neglected in the cement literature, is the setting of the cement in the presence of blood and serum [94]. It is inevitable that the cement paste will be in contact with the blood during implantation which can considerably delay the setting of the cement as well as affect the final mechanical strength of the implant [94]. Thus it is important to formulate the cement with a setting time that allows the surgeon to perform implantation fast enough to prevent delaying the operation or creating unpredictable problems due to interaction of the cement with the excess blood leading to incomplete reaction and slow setting leaving the cement as a slurry or paste with no perceivable rigidity.

Setting times are affected by the material and environmental conditions including powder size, surface area and reactivity, setting solution or reacting salt concentration, P:L, temperature

and humidity. One of the great advantages of MPCs is the significant control over setting time which researchers are able to command, as revealed in Table 1-3. For example, Wang et al observed that both the calcining temperature as well as the P:L ratio affected the setting time of cement from MgO and monopotassium hydrogen phosphate (KH_2PO_4, MKHP) powders, ranging from 2 minutes (1100 °C, 4:1) to 17 minutes (1500 °C, 1.5:1), as shown in Figure 1-2 [37]. They demonstrated robust control over the setting time by controlling these two parameters, which would allow for set time optimization. Similarly, Moseke et al reported that cements of TMPA and 3.5 M DAHM resulted in set times of 1.5 to 16 minutes, with set time increasing with decreasing P:L [62]. On more extreme ends, Klammert et al found that grinding of the reacting precursors significantly reduced the setting times for cements of MCPM + $Mg_xCa_{3-x}(PO_4)_2$, reducing the setting time from greater than 1 hour to only 9 minutes with 2 hours of grinding [60]. Similar ranges of setting times, from 1 minute to 1 hour, have been observed by the vast majority of researchers through the control of P:L and particle surface area [29, 78, 84].

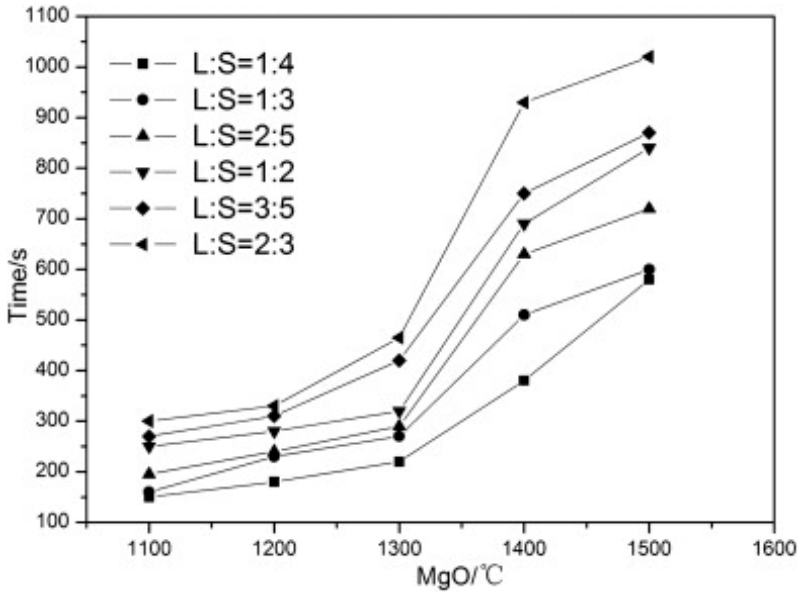

Figure 1-2 Setting time of MgO MPCs varying with P:L (here liquid-to-solid ratio, L:S) and calcining temperature, from Wang et al [37].

From the CPC literature it is well known that most CPCs disintegrate upon early contact with aqueous solution or body fluids such as blood [92]. Cohesion time, defined as the time from which the cement paste no longer disintegrates when immersed in a specific solution or fluid, becomes a critical property for these cements [92, 93]. While not frequently discussed in the MPC literature, it is important clinically to ensure the cement putty remains intact during application. For clinical use the cement paste must have a shorter cohesion time than the first setting time. Along with the cohesion time, "anti-washout-ability" is another parameter which is also frequently used in the field of CPCs [93]. Although definition of anti-washout-ability is very similar to the cohesion time, the former is the time required for disintegration of the paste under dynamic aqueous conditions whereas a static environment is used to measure the latter. The "anti-washout-ability" time is generally much longer than the cohesion time, although cohesion time is typically reported [12]. Although there are no specific procedures to measure the

cohesion time for bone cements, a modified version of the test method for determining the resistance of freshly mixed concrete to washing out in water or test method used by Bohner et al can be employed [95]. Despite the importance of cohesion time, only one author, Mestres, has reported the cohesion of MPC, determining time of cohesion visually to be less than 6 minutes for both MAHP and MNaHP cement formulations [28]. In the CPC literature, there is not always agreement upon the definition or metrics for cohesion determination. Bohner has reviewed the CPC literature, determining that cohesion may be improved through enhancing van der Waals forces, decreasing electrostatic forces or through increasing the cement viscosity [16, 18]. This may be achieved through decreasing the mean particle size and increasing the ionic strength of the solution or adding hydrogels to the liquid [16, 18].

Though not frequently reported in the MPC literature, injectability is clinically important to allow for minimally invasive surgeries or the filling of complicated defect sites. It is typically measured by the volume which can be extruded by a predetermined level of force, and can be affected by the time between mixing and testing as well as the maximum force, injection speed and aperture size of the injection needle. Filter pressing is a concern related to injectability, where the force of injection ejects proportionally more liquid than the solids in the mixture [76]. This results in an 'in-use' product which may vary quite significantly from the anticipated properties.

Cohesion is intricately related to injectability, and many of the additives which improve injectability may also improve cohesion. Typical methods to promote cohesion and injectability include additives, such as glycerol, chitosan, carboyxmethyl cellulose (CMC) or nanoparticles, and increasing the viscosity or altering the wetabillity of the particle surfaces [13, 14, 17, 18, 26, 62, 96]. Mestres et al observed injectability of 89 % for MgO+MNaHP cements but only 36 %

for MgO+MAHP cements [38]. Moseke et al determined for a cement of TMPA with 3.5 M DAHP solution an injectability of 78 % at a P:L 2.0 but only 20% at a P:L of 2.5 [62]. The supplementation of the reacting solution with diammonium citrate ($(NH_4)_2C_6H_6O_7$, DAC) greatly improved the injectability at the same P:L, with 2.0 achieving 88 % at 3.0 M/0.5 M phosphate/citrate ratio and 99 % at 2.0 M/1.5 M phosphate/citrate ratio. The effect is more dramatic at P:L 2.5, increasing to 47 % at 3.0 M/0.5 M and 98 % at 2.0 M/1.5 M phosphate/citrate ratios. The improved injectability was not due to increased zeta potential as had been anticipated, but instead was attributed to the fact that the citrate ions are not consumed during the setting reaction [62]. Although the majority of additives to improve injectability negatively affect other cement properties, the addition of certain chemicals, such as the polymerized aminosalicylic acid explored by Ginebra et al, which would contribute additional positive cement properties, are likely the best to explore moving forward [26].

1.3.5 Mechanical Strength and Porosity

Due to the hierarchical structure of HA mineral and collagen, natural bone displays high strengths, on average 130-190 MPa for cortical bone and 3.6-9.3 MPa for cancellous bone [97]. When clinicians utilize bone implants, the mechanical properties of those implants must therefore be taken into serious consideration, depending upon the application and necessary properties for the application. For example, highly load baring applications will require a material which is capable of bearing load. While ceramics can handle high loads in compression, they are brittle and perform poorly in tension and torsion. For this reason, MPC and CPCs are primarily used in low- semi-load or non-load bearing applications. The clinical success of bone cements so far has been governed by the setting and handling characteristics as well as by the

mechanical strength of the scaffolds following setting. Therefore, the level of strength achieved by MPCs is one of the greatest attractions, with researchers frequently reporting strengths greater than 50 MPa (Table 1-3). The most common mechanical test for bone cements is uniaxial compression testing performed on cylindrical or cuboidal samples. It is sometimes difficult to compare compressive strengths reported by various researchers because additional factors, such as compaction, dry or wet setting environment, and dry or wet testing conditions drastically affect the strength of cements. Compaction will increase the strength of the product by reducing the porosity and is not advised for bone cement research because similar compaction is not realistic in a clinical setting [98]. Setting under a humid environment or when immersed in aqueous solution will reduce the strength in comparison to a dry environment, but is advisable because humidity more closely mimics *in vivo* conditions. When conducting direct comparisons, many researchers find higher initial compressive strengths for MPCs than CPCs. Highly dense sintered HA ceramics may achieve strengths up to 150 MPa under laboratory conditions. On the other hand, macroporous HA cements and commercially available HA cements generally display strengths below 30 MPa at 40 % or more porosity [6, 93]. Brushite cements rarely display strengths above 20 MPa without the incorporation of macropores [93]. Comparatively, MgP cements have routinely demonstrated strengths between 40-85 MPa [36, 37, 56, 57, 99]. Frequently, this advantage is not retained with extended incubation *in vitro* or *in vivo*, which is likely due to the higher solubility of the crystalline phases present in MPCs [31, 34, 36, 85]. However, others note an increase in strength following *in vitro* incubation, which may be attributed to further completion of the cementing reaction [29, 38, 88]. Factors which may affect the strength evolution of bone cements include the ceramic to salt ratio, P:L, particle size, additives and porosity [52]. Klammert et al reported that grinding time, and thus D_{50}, of

TMPA powder when mixed with monocalcium phosphate monohydrate ($Ca(H_2PO_4)_2 \cdot H_2O$,MCPM) affected the wet compressive strength of the resulting cement increasing from 10 MPa to a maximum of 40 MPa [60]. However, other research indicates that while the particle size may affect the rate of strength evolution, it does not play a large role affecting the final strength [52]. It is well recognized that the strength of MPC is sensitive to the P:L used in the cement [52]. Within the bounds of workable putty viscosities, a decrease in P:L results in decreased strength of the cement, a trend which is observable in the analysis of compression data in Table 1-3. Moseke et al found that P:L of a 3.5 M DAHP solution with TMPA powder moderately affected the cement strength: cements at 1:1 had a compressive strength of only 20 MPa, while cements the strongest cement, at 56 MPa, were those at 2:1 [62].

In 2014, Kanter et al created Sv cements from TMPA powder mixed with a solution of 3.0 M DAHP/0.5 M MAHP [78]. The cements achieved strengths of 57-65 MPa, significantly greater than HA cements (27 MPa) or DCPD cements (10-34 MPa) assessed in the same study. It is important to note that the MPCs had porosity less than 10 % while CPCs had porosities between 30-45 %. Similarly, Wang et al determined that P:L affected the strength of a cement comprising of MgO + MKHP powders, reducing it from 22 MPa at 4:1 to 7 MPa at 1.5:1 while simultaneously increasing the porosity increased from 11 % to 23 % under the same range [37].

Porosity plays a complicated role in the bone cement field. For many biomaterial applications, the inclusion of cell-sized open porosity is highly encouraged because it is shown to improve implant integration, increase degradation rates and reduce the rate of implant rejection [12, 22, 100]. However, particularly for ceramics, the inclusion of large pores, historically seen as defects, drastically reduces the mechanical strength of the product [12, 93, 101]. This makes the design of porous bone cements a delicate balance of desired properties. Additionally, the

level of porosity preferred may vary depending upon the application. For example, Mestres et al, in developing MPCs for endodontic applications, desired low open porosity because this yields lower degradation and leakage rates [38]. The porosity of MPCs is frequently lower than DCPD cements, ranging from 5-25 % [37, 38, 74]. Vorndran et al assessed the porosity of cements in a series of $Mg_xCa_{3-x}(PO_4)_2$ with 3.5 M DAHP approximately following a linear curve fit of ln(strength), with increasing strength with decrease in porosity as shown in Figure 1-3 below [87]. The trend was not perfectly predictive, and some differences observed were attributed to differences in the microstructure at the same porosity levels.

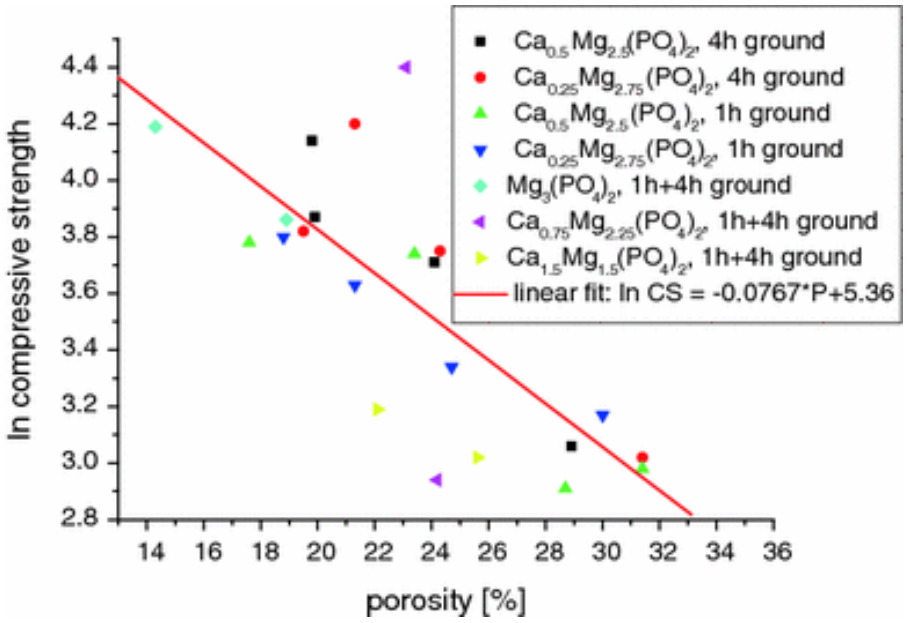

Figure 1-3 Relationship between porosity and ln(compressive strength) calcium-magnesium phosphate cements, from Vorndran at al [87].

While uniaxial compression testing is the predominant strength measurement method accepted for MPCs, and ceramics in general, other measures of cement mechanical resilience may be important to consider. When implemented clinically, bone cements do not undergo

strictly compressive loading. Instead, the cement may be expected to perform adequately under compression, tension and shear forces, the magnitude and importance of which are determined by the defect site [13]. For this reason, testing for screw pullout strength, stiffness or elastic modulus, or push-out strength in dental applications may become crucial to understanding the performance of the cement. Ideally, both the strength and elastic modulus of the cement implant would be in agreement with the surrounding bone or tooth tissue. Mestres et al observed the push-out strength of magnesium cement formulations (MgO with MAHP or MNaHP) in explanted teeth to be higher than that of commercial mineral trioxide aggregate (MTA), a widely used commercial Portland cement derivative [28, 38].

1.3.6 Adhesion

One of the greatest innate attributes of some MPCs which is not perceived spontaneously in CPCs are their adhesive capabilities, a clinical need which is currently filled with polymer formulations, particularly PMMA [102]. Indeed, this property helped launch the OsteoCrete^{TM} formulation, from Bone Solutions Inc., through FDA approval which built interest in MPCs according to BSI President Drew Diaz (personal communication, January 30th, 2015). OsteoCrete^{TM} MPC has been investigated in tendon-to-bone fixation, bone flap securing, screw fixation and bone-to-bone adhesion, showing improved adhesion and healing in nearly all circumstances [73, 103-106]. Research comparing the OsteoCrete^{TM} formulation with other common MPC formulations has not been completed to determine whether most MPCs indeed display this adhesive capability or if this aspect is unique only to the OsteoCrete^{TM} system.

1.3.7 Clinical Considerations

For clinical implementation an MPC must achieve more than adequate mechanical strength and *in vivo* response. The commercial product must be manufactured, packaged, sterilized and implanted under realistic conditions. The cement materials need to be stable for extended shelf life. Because MPCs undergo acid-base reactions, the reacting components should ideally be kept separate, such as delivering the salt in solution form upon mixing. For formulations which this salt is delivered in powder form, it is imperative that the product remain dry until it is ready for use, else the components react prior to opening the package. Sterilization is another critical clinical concern often not assessed in academic research. All cement components must undergo stringent, often destructive, sterilization methods, such as γ irradiation. Although ceramics and salts are likely to be inert to these destructive sterilization methods, additives such as polymers or drugs may not be so resilient. Zeng et al used cobalt 60 irradiation for sterilization of cement pieces after reaction, while Kanter et al used γ irradiation to sterilize cement powders and autoclaving to sterilize reacting liquids prior to *in vivo* implantation, each with no negative effects reported [78, 107].

Thermal evolution during the cementing reaction is an additional clinical concern. A high temperature exothermic reaction observed during the setting reaction can result in tissue necrosis and implant failure. Clinically accepted maximum temperatures are expected to be in the 45°C and below range [108]. For MPCs, controlling the maximum temperature frequently means controlling the reaction rate. Mestres et al inferred that while a finer salt powder did not necessarily result in earlier temperature evolution during the setting reaction, the finer salt powder resulted in higher maximum temperature levels, up to 80 °C [29]. Moseke et al on the other hand, observed a maximum temperature 54 °C for a cement of TMPA+ 3.5 M DAHP while

Wang et al determined that decreasing P:L and increasing calcining temperatures reduced the maximum temperature reached, in the range of 35-65 °C for a cement of MgO + MKHP [37, 62]. Zhou et al decreased the setting temperature of a cement of MH+PA by pre-reacting the cement under microwave irradiation, grinding the resulting cement, and then mixing that powder with deionized water. The setting temperature for the cement following this process was reduced from 60 °C to room temperature [39].

1.4 CEMENT SYSTEM MODIFICATIONS

Modifications to basic cements systems are very common, in both the civil engineering applications as well as biomedical engineering applications of magnesium cements. Modifications to basic formulas may include combination of systems, typically with calcium-containing compounds for biological reasons, composite systems, or the addition of reaction retardants and pore formers.

1.4.1 Reaction Retardants

Acid-base reactions may be rapid at times and thus resulted in very short setting times (Table 1-3). When other processing controls, such as changes in particle size and P:L, are not sufficient to slow the reaction, retardants such as Borax and citrates may be added, with borax being the most common. Mestres et al confirmed that increasing additions of borax decreased the maximum temperature evolution and delayed the setting reaction for MgO+MAHP or MNaHP, but was more effective with the MAHP [29]. The addition of 3 % borax was determined optimal based

on the maximum temperature and setting times for this series of cements. In later studies, Mestres et al utilize 1 and 6 % borax easily tailoring the setting time of their cement system as desired [28].

Some researchers have also inferred that adding retardants reduces the maximum temperature reached while others have found that it may increase the maximum temperature. Moseke et al utilized the supplementation of DAC as a reaction retardant in a TMPA+ 3.5 M DAHP solution MPC [62]. The increase in setting time was proportional to the citrate content, with proportions of 2.0M and greater (of the 3.5 M total salt concentration) resulting in setting times longer than 60 minutes. Proportions of 0.5 M, 1.0 M and 1.5 M improved the setting time, within clinical constraint, as well as improving the injectability of the cement. However, these same additions increased the maximum setting temperature, from 54 °C up to 73 °C as well as decreasing the compressive strength of the cement. Pijocha et al analyzed the addition of calcium sulfate hemihydrate ($CaSO_3 \cdot {}^1/_2H_2O$, CSH) or sodium pyrophosphate ($Na_4P_2O_7$, SPP) as reaction retardants, effectively reducing the maximum temperature from 88 °C to 38 °C and below. The effect of these retardants on other cement properties was not however reported [90].

1.4.2 Pore Formers

Porosity is a double-edged sword in ceramic bone cements: it is necessary for biodegradation, cellular infiltration and implant integration; however the strength of a ceramic or cement is inversely proportional to its largest defects [12, 93, 100]. Some level of porosity is always present in MPCs, as discussed above, however the addition of intentionally constructed macroporosity could prove beneficial to MPC implants. There are numerous ways to create porosity in a cement scaffold, including the use of 3D printing for pre-constructed (non-

injectable) cements and water soluble porogens [109, 110]. Klammert et al used 3D printing to create porous MPC scaffolds, utilizing TMPA powder and 0.75 M MAHP/ 0.75 M DAHP solution as the binder [32]. Including DAHP salt in the powder phase as well as incubation of the scaffold in reacting solution after printing increased the compressive strength of the printed scaffold. However, the porosity of the structures was not reported nor correlated with other cement properties [61]. Beyond this report, the addition of pore formatting agents has not been explored in MPCs. In the CPC field, a wide variety of pore formation methods has been used, including the addition of sugar crystals such as mannitol, salt crystals and gas pore evolution [111-114]. Although considerable amounts of macropores can be formed using these processes, some techniques, such as 3D printing and gas evolution, may not be suitable for use with an injectable cement paste. Moreover, the rapid dissolution of highly water soluble pore formers, prior to the complete setting of the cement, can result in mechanically inferior implant or fragmentation of the partially set putty. Therefore, the use of slowly degrading biocompatible polymeric microspheres and fibers as pore formers have been proposed for CPCs [115-119]. These pore-forming agents have been successful in improving CPC integration and resorption *in vivo* and may be utilized in MPCs as well [120-122].

1.4.3 Radio-opaque Additives

The ability to non-destructively, non-invasively track the progress of cement implants is highly desirable for clinicians. Radiographic evaluation is a tool to achieve this goal, but in order for a clinician to track the implant it must be radio-opaque [123]. This analysis is particularly common in the dental field to track the state of procedures such as root canals. Barium sulfate and zirconium dioxide are common radiopacifiers in bone cements but their addition may be

detrimental to other cement properties [77, 124]. For this reason, some attempts have been made at utilizing more biologically neutral radiopacifiers, such as strontium carbonate [124]. Mestres et al add up to 15 % Bi_2O_3 to an MPC of MgO+MAHP or MNaHP in order to increase the radiopacity, and determined that 10 % addition displayed sufficient contrast, in comparison to 16 % currently contained in commercial dental MTA [38].

1.4.4 Combination of Systems

The most common combination systems with magnesium phosphate cements are CMPCs, or combinations with well-known calcium phosphate cements, both because of the known bioactivity of CaPs as well as the more extensive knowledge of CPCs in research and development. CMPCs are created by generating substituted ceramic powders, particularly in the $Mg_xCa_{3-x}(PO_4)_2$ system, or by simply mixing together an MPC formula with a CaP filler or CPC formula, such as the addition of HA to an MPC cement [87, 90]. Frequently, CMPCs are found to have a better combination of mechanical strength and cytocompatibility or biocompatibility than MPC or CPC formulations. Klammert et al found a cement of $Mg_xCa_{3-x}(PO_4)_2$ and MCPM mixed with 0.5 M citric acid ($C_6H_8O_7$, CA) resulted in the formation of DCPD and Nb, with the amounts varying based on X [60]. Vorndran et al made a series of cements of $Mg_xCa_{3-x}(PO_4)_2$ with 3.5 M DAHP solution. The cement of $Mg_{2.25}Ca_{0.75}(PO_4)_2$ displayed the highest compressive strength, up to 80 MPa, as well as the greatest cell number, but cement of TMPA had the highest cell activity [87]. Wu et al generated combination systems of MgO + DAHP mixed with TTCP + DCPA. They found that 1:1 combination of the two systems, at a P:L of 8:1, resulted in the highest compressive strength, of 91 MPa [58]. Other combination systems explored include reacting MgO + MCPM, which yields TMPA + TCP as cementing products instead of reactants,

or the addition of CSH which both contributes to the cementing reaction, converting to calcium sulfate dehydrate ($CaSO_4 \cdot 2H_2O$, CSD) as well as acts as a reaction retardant [84, 88, 90]. Zeng et al assessed porous granules of MPC, CPC and MCPC for cell proliferation and osteogenic differentiation of bone marrow stromal cells as well as the functionality of maxillary sinus floor surgery on rabbits [107]. They determined that the MCPC enhanced cell proliferation and differentiation over MPC as well as formed more bone than either CPC or MPC.

Another option to alter cement properties and improve bioactivity of the resulting cement is through the substitution of alternative anions and cations in the MgO and TMPA. Many trace elements such as Sr, Cu, Zn, and Si are present in the human body and are known for their role in bone metabolism [40, 125]. Release of these ions from the scaffold after exposure to a physiological environment favorably affects both osteogenesis and angiogenesis. The inclusion of such additives has been widely studied in the calcium phosphate field but has not been explore in MPCs.

1.4.5 Composite Systems

Composite systems of MPCs are a particularly under-explored area of MPC development. Based on the extensive knowledge gathered surrounding CPCs and related cements, a variety of MPC composite systems can be envisioned and should be explored. Composite systems, particularly composites with biopolymers and biological macromolecules are of particular interest because the addition of such materials has the potential to improve cement properties, such as degradation rate or elastic modulus, which are not ideal in MPCs alone. Combination of systems which would be of interest to explore include composites with bio-glasses and metals, composites with synthetic degradable polymers or natural biopolymers such as collagen, silk,

alginate, in fiber or microparticulate forms, composites with growth factors (GFs), biomolecules and drugs, and multi-level composites with growth factors (GFs), biomolecules or drugs entrapped microparticles or reinforcing fibers of biopolymers [126-134].

1.5 *IN VITRO* PROPERTIES

1.5.1 Dissolution and Degradation

Biodegradability, through dissolution, cell-mediated resorption, or a combination of these two mechanisms, is often considered a mandatory requirement for bone cements. Many researchers report dissolution at 37 °C in aqueous solution, such as phosphate buffered saline or Ringer's solution, as an indication of solubility-mediated dissolution. While this measure does not directly translate to degradation rate *in vivo* it is a good indication of comparative rate of dissolution between compositions or in comparison to calcium phosphate controls. It can also be used to draw correlations between ionic concentrations in solution and cellular response to the scaffold. Because the higher dissolution rates of MPCs than CPCs is one of the greatest advantage of MPCs, most researchers report MPC dissolution as it compares to the HA or DCPD CPCs. Relative dissolution of cements typically follow the decreasing trend of HA < DCPD < MgP cements [58, 59]. MPCs may degrade more slowly than other calcium-based formulations, such as calcium sulfate cements [88]. In the case of CMPCs, the ratio of CaP to MgP is assessed as it relates to the degradation rate, where again the dissolution follows the decreasing trend of CPC < CMPC (High CaP) < CMPC (High MgP) < MPC [84]. For example, Wu et al generated combination systems forming Sv and HA [58]. The *in vitro* degradation of these systems,

measured by weight loss, was dependent upon the ratio of MPC to CPC, with increasing MPC increasing the weight loss over a 3 month period, as shown in Figure 1-4 [58]. Both of these trends are easily attributed to the respective solubility of magnesium and calcium phosphate phases [30]. The inclusion of other additives, such as reaction retardants and pore formers, may alter the dissolution profile of MPCs [85, 135, 136]. In some instances, such as the dental MTA replacement analyzed by Mestres et al, there is a desire for lower dissolution rates [38]. It is important to note that the formulations studied by Mestres et al were relatively of low porosity which contributed to the low dissolution rates.

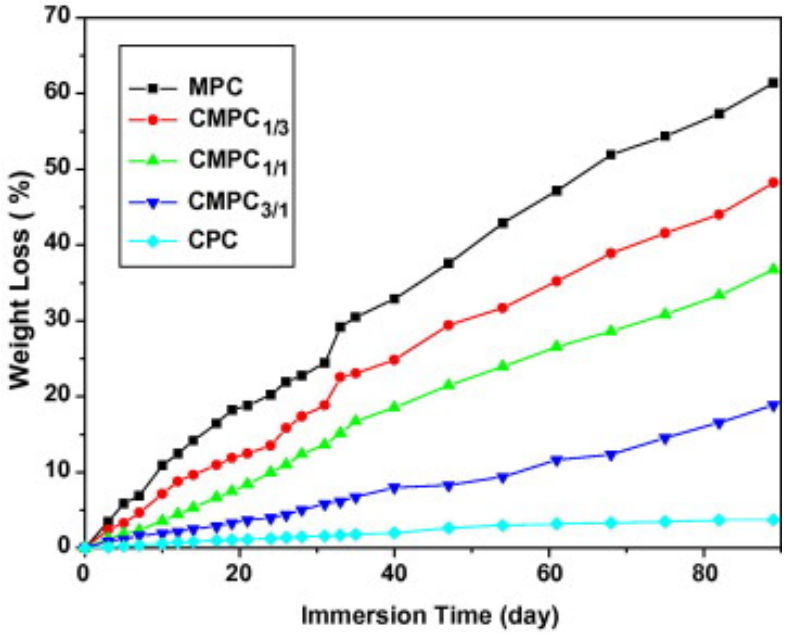

Figure 1-4 Weight loss of MPC, CPC and combination systems, from Wu et al [58].

For the resorption of DCPD CPCs, dissolution-mediated degradation is combined with cell-mediated degradation, while for HA CPCs, cell-mediated degradation is the primary source of implant resorption [137, 138]. Grossardt et al analyzed both dissolution and cell-mediated resorption of a TMPA+Sv cement created with 3.5 M DAHP with RAW 264.7 monocytes,

which would form osteoclasts *in vivo* [74]. These samples were incubated with and without RAW cells, and the ion concentrations in media were assessed as a measure of dissolution. Results indicated that Sv MPCs resorbed three fold faster than DCPD CPCs; however this resorption was mainly dissolution-mediated while DCPD CPC resorption is a mix of dissolution and cellular activity and HA CPC underwent almost strictly cell-mediated resorption. When discussing the desired dissolution rate of bone cements, there is not a true 'correct' rate of degradation, as the desired rate is dependent upon the defect site as well as other clinical considerations, such as patient age and additional trauma at the implant site. However, it is a mandatory requirement that the degradation and resorption kinetics of the degradable scaffolds have to be controlled in such a way that the bioresorbable scaffold retains its physical properties and strength until the tissue engineered transplant is remodeled by the host tissue [139, 140].

Another consideration for bone cements is the pH of the cement *in vitro* or *in vivo* because it can affect the viability of the surrounding cells. MPCs are typically neutral to slightly basic *in vitro*, a notable advantage over acidic DCPD cements [19, 29, 84]. Klammert et al observed that cements of $Mg_{2.25}Ca_{0.75}(PO_4)_2$ + MCPM reacted with citric acid displayed a physiological pH throughout the 21 days of testing [60]. Kanter et al also perceived that Sv cements during setting exhibited an approximate pH of 7.5 but reduced over 30 minutes to around 4.5 pH [78]. In addition to a variety of other properties, a physiologic setting pH is often desired to enable the viable incorporation of biologics or drugs, which tend to be unstable at higher and lower pH values [24, 141, 142].

1.5.2 Cytocompatibility

Cytocompatibility of MCPs with osteoblastic and osteoclastic cells is frequently completed in conjunction with material physiochemical evaluations. Most common are assessments of MPCs with osteoblast cell lines, MC3T3-E1 and MG_{63}, or bone marrow stromal cells. Osteoblasts predominantly display higher proliferation and cellular activity on MPCs or CMPCs in comparison to CPCs [58, 60, 84, 87, 91]. Ewald et al found that MG_{63} cells displayed high cell number and cellular activity on Sv cements in comparison to CDHA or DCPD cements, as shown in Figure 1-5 [86]. Determination of osteogenic response to MPCs is not consistent, with some authors reporting higher expression of alkaline phosphatase (ALP) and osteogenic genes while others report lower expression in comparison to CPC or other control substrates [84]. For example, in the same study as above, Ewald et al studied protein production for several osteogenic proteins, including ALP, collagen, and osteocalcin, on Sv, DCPD and CDHA cements. They ascertained that protein production on Sv cements were higher than the polystyrene controls but lower than DPCD and CDHA cements [86]. Klammert et al also observed that cements of $Mg_{2.25}Ca_{0.75}(PO_4)_2$ + MCPM + CA displayed slightly inferior ALP activity than titanium controls with MC3T3-E1 cells [60]. Zeng et al assessed extracts from porous granules of MPC, CPC and CMPC for cell proliferation and osteogenic differentiation of bone marrow stromal cells [107]. They determined that cell proliferation was highest on MPC but that CMPC had higher ALP and osteocalcin (OCN) expression. Similarly, Jia et al confirmed that a cement of MgO + MCPM supported higher proliferation of MG_{63}, as well as higher ALP expression after 4 days, than CPC controls [84]. Importantly, Yu et al determined that cements of MgO+MAHP displayed no carcinogenicity or mutagenicity in a variety of tests including unscheduled DNA synthesis, Ames mutagenicity test and micronuclei test [36].

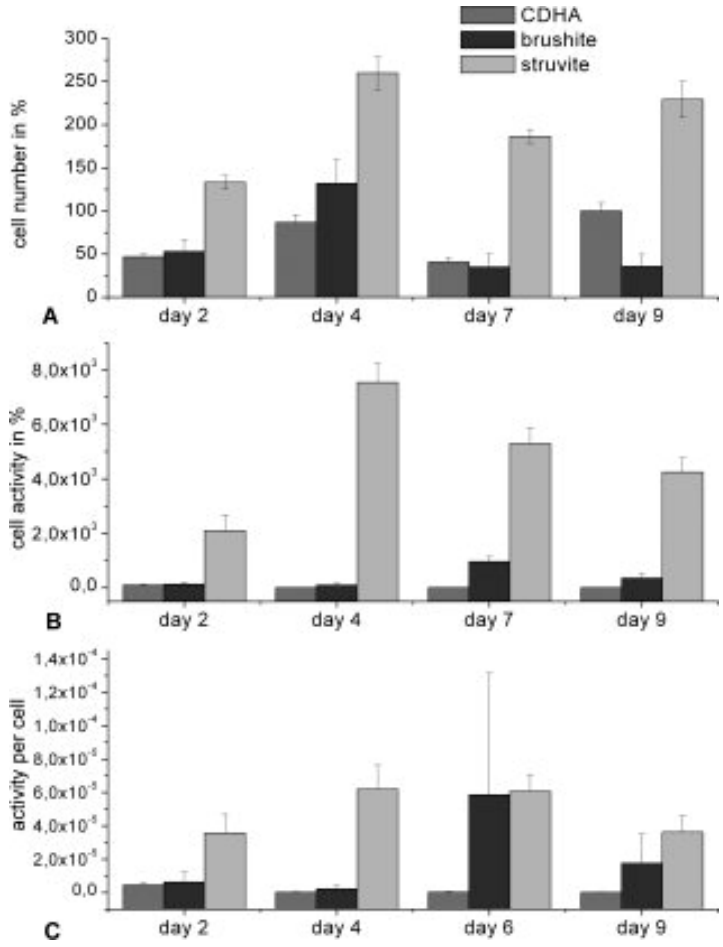

Figure 1-5 MG_{63} cell growth and activity on CDHA, DCPD and Sv cements, from Ewald et al [86].

Observing a wider body of work, the role on magnesium or magnesium substrates on osteogenic differentiation and gene expression may be explored in the MPC context. Research indicates that magnesium may stimulate osteogenic expression, matrix production and mineral deposition, however these results are concentration dependent [41, 43]. Yoshizawa et al studied the effect of $MgSO_4$ concentration, thus free magnesium ions, on human bone marrow stromal cells (hBMSCs) in maintenance and osteogenic media, shown in Figure 1-6 [41]. The authors showed that cell number was concentration, time and media dependent (Figure 1-6a) with

increasing magnesium ion concentration increasing cell number [41]. They also showed that an elevated magnesium ion concentration (10 mM over 0.8 mM controls) enhanced collagen X, VEGF, PGC-1α, HIF-1α and HIF-2α protein expression (Figure 1-6b) [41]. The high cytocompatibility combined with possibility of elevated osteogenic activity likely indicates that the presence of a CaP scaffold is not needed in order to effectively rebuild boney tissue.

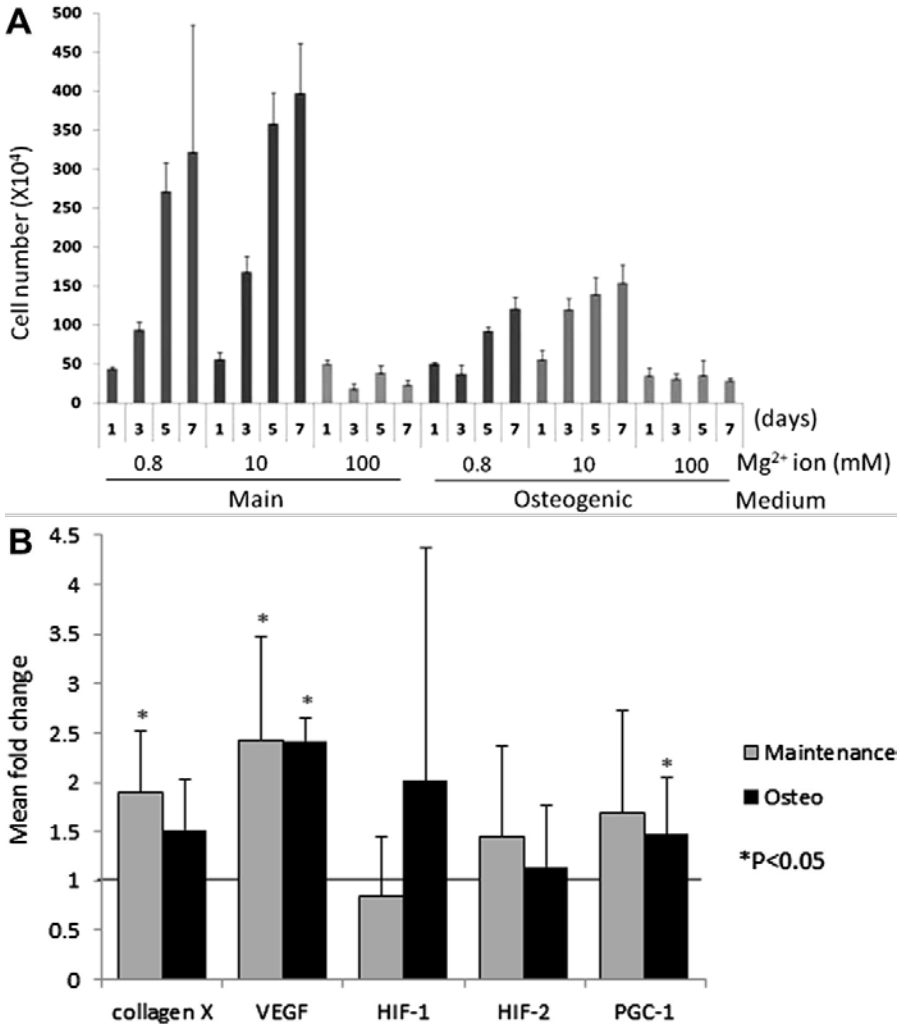

Figure 1-6 Effect of elevated magnesium ion concentration on hBMSCs indicating (A) increased proliferation at 10 mM Mg concentration in maintenance and osteogenic media and (B) enhanced protein expression at 10 mM Mg concentration (mean fold change compared to 0.8 mM concentration), from Yoshizawa et al [41].

As mentioned above, elevated levels of magnesium have been shown to temporarily suspend the formation of osteoclasts from monocytes [44-46]. Grossardt et al observed that with RAW 264.7 monocytes that Sv cements supported higher cell number and cell activity than DCPD cements [74]. Grossardt also determined that RANKL-supplemented RAW 264.7 cells on Sv surfaces did not stain positive for TRAP, but did express CT-R, an osteoclast-specific protein. These are contradictory results, indicating that while the cells were very active, they have not formed mature polynucleated osteoclast cells as anticipated. The implications of suspended osteoclast formation on bone tissue scaffolding of any sort are not immediately obvious. Although a scaffold interrupting the natural bone growth process may not be ideal, many patients currently take medications in order to slow bone resorption to decrease their rate of fractures and some research has been conducted to assess the delivery of such a medication in a CPC formulation [143]. Janning et al inferred that locally restricting osteoclast proliferation increased bone formation [44]. Given the resorption properties of MPCs, osteoclast activity is not required from MPC degradation, nor is it an absolute requirement for new bone growth. Thus it is likely that the temporary suspended osteoclast formation may ultimately be beneficial to MPC implants, allowing for a more rapid rate of new bone ingrowth.

1.5.3 Antibacterial Properties

Another possible property inherent to MPCs which is desired, and often added to CPCs, is antibacterial activity. While CPCs have antibiotics such as vancomycin added to the cement formulation, some MPCs may be naturally antibiotic [144, 145]. Mestres et al observed cements of MgO + MNaHP salt or MNaHP/MAHP salt mixture exhibited bactericidal effects on *S. sanguinis* bacteria, while cements reacted with only MAHP salt exhibited growth inhibition but

no bactericidal effects [29]. The bactericidal effects were attributed to a combination of pH increase (up to 9.91) while the growth inhibition was attributed to acidic conditions and the release of Mg^{2+} ions and reactive oxygen species from the remaining MgO. In a later study Mestres et al determined the antibacterial activity against three strains of bacteria: *E. coli, P. aeruginosa* and *A. actinomycetemcomitans* [28]. As shown in Figure 1-7, the authors observed that incubation extracts from both cement formations were most effective against *A. actinomycetemcomitans* and least effective against *E. coli*, with only aged MNaHP being effective against *E. coli [28]*. These results again were attributed to the change in pH and osmolarity of the solution. For comparison, in dental applications $Ca(OH)_2$ is frequently used, which displays a pH of 12.5, so the alkalinity is not likely to be a concern in this field. If the alkalinity and ion release from MPCs is not detrimental to the implant performance, innate antibiotic nature of MPCs may be particularly useful in high bacterial density prone sites such as dental reconstruction.

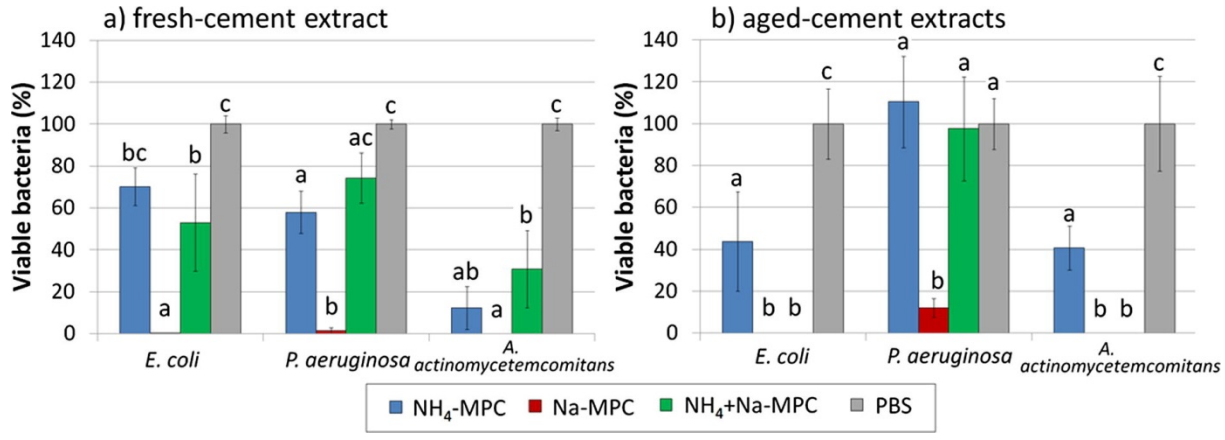

Figure 1-7 Viable bacteria following exposure of incubation extracts of MPCs tested on three different bacteria with fresh and aged extracts, relative to PBS controls, from Mestres et al [28] .

1.6 *IN VIVO* STUDIES AND CLINICAL APPLICATIONS

Current *in vivo* assessments of MPCs or CMPCs are somewhat limited, but the results are highly encouraging. When implanted in boney sites such as the femur condyle defects in rabbits, MPCs consistently show higher ingrowth of new bone than CPCs, with little to no inflammation or foreign body response. Yu et al implanted fully reacted plugs of cement of MgO + MAHP in the muscle and femur condyle of rabbits [36]. In the condyle defect, they observed that within 1 month or less, the interface of the implant and bone was clear, but after 3 months, the interface was not clear, and by 6 months the implant was replaced by new woven bone which was partly transformed into lamellar bone. They also measured the blood levels of magnesium phosphate and calcium and observed that the cement did not change the metabolic levels of these ions. Wu et al implanted preset samples HA CPC and Sv+HA CMPC into holes drilled in the femur of rabbits [58]. They reported substantially greater degradation of the CMPC implant, as well as higher new bone volume, 85 % for the Sv+HA system versus less than 10 % for the HA system. Zeng et al also assessed porous granules of Sv MPC, HA CPC and Sv+HA CMPC systems for the functionality of maxillary sinus floor surgery on rabbits [107]. They observed that the CMPC formed more bone than CPC or MPC. The addition of bone marrow stromal cells with the cement granules resulted in even greater bone growth and scaffold dissolution. Kanter et al on the other hand, implanted Sv cements from TMPA + 3.0 M DAHP / 0.5 M MAHP in the femoral condyle of adult sheep, the CT results of which are depicted in Figure 1-8 [78]. They determined that after 10 months the porosity of Sv cements increased above 20 % but underwent a substantial reduction in strength. The Sv cement was determined to be more favorable for bone regeneration than DCPD or HA cements, degrading more substantially and resulting in more new bone growth than the CPC cements. The loss of mechanical strength following implantation *in*

vivo is however, a consistent trend but has not negatively affected the functionality of the MPC implants [31, 34, 78]. For example, Yu et al implanted the same MPC scaffolds intramuscularly in rabbits, which displayed significant surface changes with time as well as reductions in compressive strength, from 85 MPa initially to 25 MPa after 3 months [36]. In addition to these formulations, the OsteoCrete^{TM} MPC formulation has been studied in a variety of animal models and defects, including cranial defects in rabbits, securing dental implants in dogs, and metacarpal and metatarsals in horses [103, 105, 146]. OsteoCrete^{TM} has demonstrated improved adhesion and healing in nearly all surgical sites explored.

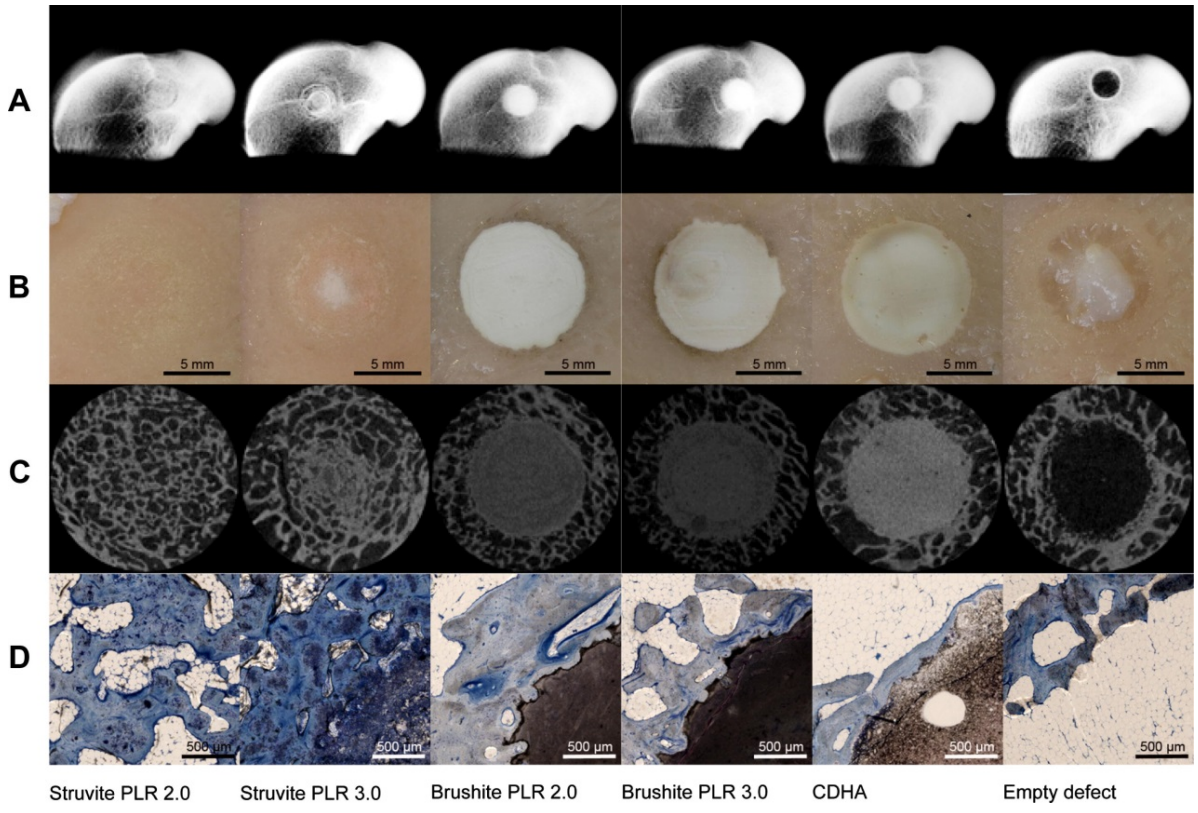

Figure 1-8 Results of Sv and brushite cement implantation in sheep femoral condyles for 10 months, showing a) x-ray, B) macroscopic images, C) µ-CT slices and D) histological section stained with toluidine blue and basic fuchsin, from Kanter et al [78].

There thus is a broad range of potential uses for ceramic bone cements, including dental filling, adhesion, and void filling. Clinical applications for ceramic bone cements may include orthopedic, vertebroplasty, maxillofacial surgery, endodontic treatments, filler agents in dental pulp capping and root canals. The implementation of MPCs for these applications depends upon a wide variety of property performance metrics. Some applications have been demonstrated to be successful with MPCs, as signified by the FDA clearance of OsteoCrete™ for long bone and pelvic applications.

1.7 DESIGNING A BETTER MAGNESIUM BONE CEMENT

Although MPCs display greater mechanical strength than CPCs, the strength and elastic modulus of MPCs at this time remains inferior to native bone. For this reason, clinical use of MPCs is expected to remain predominately relegated to semi-load or non-load bearing applications, similar to commercial CPC products. With this in mind, the commercial viability of MPCs hinges on their unique advantages over CPCs. In addition to the increased mechanical strength, MPCs have shown more rapid degradation and subsequent bone in-growth *in vivo* than CPCs counterparts, a propensity for inherent antibiotic ability, and significantly finer control over setting times than CPCs, as well as the adhesive capabilities demonstrated by the Osteocrete™ formulation demonstrating the slight positive edge of MPCs over the ubiquitous CPCs [29, 36, 78, 104].

From a clinical perspective, certain characteristics are crucial for ease of use and product performance that all need to be addressed for commercial implementation, including injectability, porosity and dissolution. The adhesive capabilities of MPCs, which are not inherent

to CPCs, can be extremely useful for simple or compound fracture manipulation. These situations, as well as many others, require an injectable formulation. However the injectability of MPCs, inherent or additive-induced, has not been thoroughly explored. Many additives which improve injectability also act as cohesion promoters, and may therefore improve the cement paste stability in the presence of bodily fluids, another crucial requirement for clinical implementation [14, 17].

An added unique advantage of MPCs are their higher solubility than CPCs, resulting in more rapid *in vivo* resorption and cellular infiltration than CPCs. This may be improved further through the addition of pore formers which promote rapid cellular infiltration and fluid transport. Although a variety of pore forming techniques have been explored with CPCs, there is still no clinically available CPC which is both porous and injectable, and very few FDA approved CPC formulations are indeed injectable. This lack of clinical accessibility may be due to poor handling characteristics of porous CPCs, including long setting times and insufficient mechanical integrity. As MPCs have shorter setting times, higher mechanical strengths and greater dissolution than CPCs, the development of porous, injectable MPCs formulations have the opportunity to gain clinical favor for many difficult applications wherein CPCs may be considered inadequate.

The formation of new bone on and around an implant can be strongly dependent on the release of ions from the degrading implant. A high level of magnesium is known to stimulate new bone growth *in vitro* and *in vivo*, with several recent studies on magnesium alloy implants demonstrating enhanced bone growth around the corroding implant [41, 43, 147]. In addition to magnesium, various other cations and anions are implicated in new bone formation, and the study of ion-doped MPCs has the potential to show even greater bone growth while maintaining

suitable handling, setting and mechanical characteristics clinically necessary for implementation [40, 97, 125].

In addition to the scientific rigors of product development, MPCs will face societal hurdles entering the market place. The market is conservative in many respects. Although the limitations of CPCs are widely known and criticized, clinicians are often reluctant to use a new product which differs significantly from what is currently used. When this difference is manifested in the chemical make-up of the implant, a large body of clinical study evidence is required to build trust in a new product's safety and efficacy. With time however, the unique capabilities of magnesium phosphate cements, including adhesive and antibacterial features, can overcome these hurdles, ultimately improving clinical care in applications wherein calcium phosphate cements may not be deemed capable of performing.

1.8 SPECIFIC AIMS

Ceramic granules and cements for dental and craniofacial applications have been primarily developed with the intent to fill voids in bony tissue and prevent additional bone recession while promoting new bone growth. The primary series of materials studied thus far are composed of hydroxyapatite. In many cases, apatite implants are considered non-resorbable and thus suffer from similar maladies as other permanent foreign implants.

Bone cements based on magnesium oxide and magnesium phosphate have the potential to fill the needs not satisfied by these calcium phosphate implants, demonstrating higher mechanical integrity and greater resorbablilty *in vivo* than apatite cements. However, the body of knowledge related to these materials is scant and undeveloped in comparison to the calcium

phosphate literature. It is hypothesized that magnesium phosphate substrates and cements will be simple and straight forward to generate in a laboratory environment and will demonstrate cytocompatibility comparable to calcium phosphate controls, while maintaining adequate strength under aqueous conditions thus demonstrating increased bone-forming capacity.

Accordingly, five specific aims have been formulated to evaluate this hypothesis.

Specific Aim 1

Synthesize trimagnesium phosphate cement precursors and perform materials characterization and cytocompatibility assessment to determine viability of the base materials. Specific Aim 1 is the subject of Chapter 2.

Specific Aim 2

Evaluate the effect of trimagnesium phosphate crystallinity (amorphous, semi-crystalline and crystalline) on the cementing reaction and the materials characteristics of the resulting cement. Specific Aim 2 is the subject of Chapter 3.

Specific Aim 3

Assess the effect of reacting solutions of potassium phosphate, sodium phosphate and ammonium phosphate with crystalline trimagnesium phosphate on the ensuing cement forming reactions and evaluate cytocompatibility of the resulting cement. Specific Aim 3 is the subject of Chapter 4.

Specific Aim 4

Evaluate the effect of porogen addition to a model cement system to investigate alteration of the mechanical behavior, increase the porosity and improve the cellular interaction with the resulting cement. Specific Aim 4 is the subject of Chapter 5.

Specific Aim 5

Evaluate the effect of biodegradable polymer fiber reinforcement addition to a model cement system to explore the improvement in fracture toughness while also providing cell sized porosity. Specific Aim 5 is the subject of Chapter 6.

2.0 SPECIFIC AIM 1: SYNTHESIS OF AMORPHOUS AND CRYSTALLINE TRI-MAGNESIUM PHOSPHATE AND OSTEOBLAST AND OSTEOCLAST VIABILITY ASSESSMENT

2.1 INTRODUCTION

Historically, for patients in need of bone repair or replacement, synthetic substitutes may be chosen over naturally derived materials, such as allografts and autografts, due to the mass production capacity and lower immunogenicity of synthetic materials [1, 148]. Ceramic implants are often the primary choice simply for their mechanical durability similar to bone. These materials include bioglasses, zirconium oxides, aluminum oxides, and calcium oxides or phosphates; however the implementation of ceramic scaffolds may be hindered a variety of considerations [149-151]. 3D printed implants require extensive planning and invasive surgical procedures, particulate fillers offer limited mechanical stability, while bone cements, which require less invasive surgery either exhibit low strengths or are too slow to achieve desired strengths, risking premature failure [11, 20, 109, 152]. With many of these implant options a major concerns is the lack of resorbability which may result in implant rejection or chronic infection, as well as poor integration with host tissue. A common choice of synthetic implant are calcium phosphate (CaP) based grafts since these materials are chemically similar to the mineral component of native bone tissue, however even these implants are less than ideal [10]. CaP

implants resorb too slowly, necessitating extremely long periods of time for the implant to be replaced by native bone [23, 24].

In addition to calcium, many other ions such as magnesium, silicon, zinc, potassium and copper play important roles in bone regeneration. These include regulating metabolic processes, modulating osteoblastic differentiation, increasing osteoblastic cell adhesion, and promoting angiogenesis [40]. Magnesium has been shown to play a role in calcification, mineral metabolism, HA crystal formation and increased bone cell adhesion, proliferation and differentiation, thus the utilization of magnesium-based implants is acceptable from a biological standpoint, however only recently have the mechanisms behind the effect of magnesium ion levels on osteoblast viability been investigated, and this work is still in the early stages [19, 34, 41].

Due to the promising results of magnesium for bone regeneration, the use of magnesium phosphate (MgP) based materials has been proposed for clinically adoptable implants [29-31]. Currently, the body of published research regarding magnesium phosphates for biomedical applications is limited both in variety and depth of study. The majority of current studies of individual magnesium phosphate phases tend to focus solely on materials synthesis and characteristics without thorough *in vitro* evaluation of cell response to the material [33, 153, 154]. Studies which do focus on cytocompatibility often have little detail regarding materials characteristics and are frequently combined with calcium phosphates which convolute the implications of the presence of magnesium phosphate [55, 58, 155-157]. In two recent studies, researchers have synthesized MgPs and amorphous magnesium phosphate nanoparticles for biomedical applications [30, 39]. In each study, the non-toxicity of MgPs on relevant cell lines was demonstrated. However, neither of

these studies demonstrated the capability of MgPs to support osteogenic differentiation on bulk samples or explored osteoclastic resorption directly on the MgP scaffolds.

The study explores the materials characteristics and inherent cytocompatibility of amorphous magnesium phosphate and crystalline tri-magnesium phosphate, $Mg_3(PO_4)_2$. The comparison of amorphous and crystalline embodiments of magnesium phosphate is of particular interest due to the anticipated differences in stability, solubility and reactivity resulting from varying the crystallinity of the scaffold, which may result in differences in cellular viability on the substrates. The focus of the current work was to explore the synthesis and cytocompatibility of amorphous and crystalline MgPs, the spontaneous mineralization of the amorphous MgP *in vitro* and the mineralization-assisted increase in cytocompatibility of the amorphous MgP material. The mineralization of biomaterial surfaces in aqueous solutions, such as cell culture media, has been widely observed to improve the *in vitro* cytocompatibility and *in vivo* biocompatibility and osseointegration of a variety of materials including hydrogels, electrospun polymers, glass fiber composites and metallic implants, including the mineralization of magnesium phosphate on gellan gum hydrogel [158-164]. This study thus evaluates the synthesis of MgPs and aims to characterize the materials properties as well as *in vitro* mineralization of the amorphous MgP pellet surfaces. Cytocompatibility with osteoblast-forming and osteoclast-precursor cell lines is also assessed in order to evaluate whether amorphous magnesium phosphate or crystalline tri-magnesium phosphate are favorable candidate materials for bone void repair applications.

2.2 MATERIALS AND METHODS

2.2.1 Materials Synthesis

Magnesium phosphate (MgP) powders were synthesized through an aqueous precipitation reaction between magnesium chloride and tri-sodium phosphate (Sigma Aldrich). The reactants were dissolved separately in deionized water at concentrations of 0.3 M and 0.2 M respectively. The magnesium containing solution was then pipetted into the phosphate containing solution, at room temperature, resulting in precipitation of magnesium phosphate following the reaction in Equation 2-1:

Equation 2-1

$$3Mg^{+} + 2PO_4^{3-} \rightarrow Mg_3(PO_4)_2$$

The solution was centrifuged at 19,500 rcf for 5 minutes and the supernatant liquid was discarded. The resulting precipitate was rinsed in deionized water and then centrifuged in triplicate to remove the excess sodium and chloride ions. Finally, the precipitate was rinsed in acetone, centrifuged and the solid was collected. The precipitate was dried overnight at 60 °C and stored in sealed containers under ambient conditions before further testing.

2.2.2 Materials Characterization

Crystalline phases were identified using X-ray diffraction (XRD, Philips X-Pret PRO diffractometer) equipped with Cu Kα radiation and a Si-detector (X'celerator). The X-ray

generator was operated at 45 kV and 40 mA at a 2θ range of 10-90 degrees. Thermogravimetric analysis and differential scanning calorimetry (TGA and DSC, Netzsch STA 409 PC Luxx) were used to identify the level of hydration and temperature of crystallization. The as-synthesized powder was heated at a rate of 10 °C/min to 1000 °C under argon. The particles formed were observed via scanning electron microscopy (SEM, JEOL, JSM-6610LV). Samples were sputter coated with palladium (Cressington sputter coater 108A) prior to imaging. Energy dispersive spectroscopy (EDS) was used to identify the relative atomic content of the synthesized powder. Fourier transform infrared spectroscopy (FTIR, Nicolet 6700 spectrophotometer, Thermo Electron Corporation) with a diamond ATR Smart orbit was used to identify the differences in molecular chemical linkages between amorphous and crystalline precipitates. FTIR spectra were obtained at a resolution of 1.0 cm^{-1} averaging 64 scans in the 400 – 40000 cm^{-1} frequency range. High-resolution transmission electron microscopy (HRTEM, JEOL JEM-2100F with Gatan GIF-Tridiem) was operated at 200 kEV to obtain high-resolution images to confirm the crystallinity and assess the individual particles. For HRTEM, the particles were suspended in ethyl alcohol and pipetted on copper grids with holey carbon film. The sample grids were subsequently air-dried before imaging.

2.2.3 *In Vitro* Sample Preparation

To prepare samples for *in vitro* testing, MgP powders were thermally treated, pressed into pellets, and then sintered through additional thermal treatment to circumvent extensive weight and volume changes during thermal treatment. To create amorphous magnesium phosphate pellets, the powder was heated to 200 °C for 6 hours in air, pressed into pellets and then again heated to 200 °C for 6 hours in air to sinter the pellets, termed as “ATMP” pellets. To create

crystalline TMP pellets, the as-prepared powder was heated to 750 °C for 4 hours in air, pressed into pellets and then again heated to 750 °C for 4 hours in air to sinter the pellets, termed as "CTMP" pellets. The pellet size was 13 mm diameter x 2 mm thick and were pressed using a Carver hand press set to 10,000 psi. . For a positive control β-tricalcium phosphate (β-TCP, HIMED Inc, Old Bethpage, NY) powder was also pressed into pellets of the same size and sintered at 1000 °C for 4 hours.

2.2.4 *In Vitro* Dissolution and Mineralization

Substrates were sterilized by rinsing in ethanol for 15 minutes then drying under exposure to UV light for 1 hour per side. Each substrate was soaked in 2 mL of α-MEM growth media (MEM α, Gibco, Grand Island, NY) containing 0 %, 10 %, and 20 % fetal bovine serum (FBS) and 1 % penicillin/streptomycin (P/S) antibiotics, under standard growth conditions of 37 °C, 5 % CO_2 and 95 % relative humidity. The different concentrations of FBS in media were used to assess the role that FBS may play on the surface changes and mineralization. The *in vitro* dissolution characteristics of ATMP, CTMP and β-TCP substrates were characterized by assessing ionic concentrations of magnesium and calcium within the collected supernatant cell culture media through inductively coupled plasma optical emission spectroscopy (ICP-OES, iCAP duo 6500 Thermo Fisher). The media was collected at numerous time points through 7 days of incubation. All media was removed at each time point and media was not changed between time points to allow for sequential and cumulative release measurements. Collected media was diluted in 0.03 M Tris buffer solution and analyzed by ICP-OES with the culture media used as standard to compare against. Calcium ion concentrations were measured in order to compare the TMP substrate ion release to the ion release from the β-TCP control. Following incubation in cell

culture media, the substrates were dried for observation under SEM. The mineral formed was characterized by collecting the particles grown on the surface and analyzing them using SEM coupled with EDS, FTIR and HRTEM, as described above.

2.2.5 Cell Culture

Murine MC3T3 –E1 pre-osteoblast cells and RAW 264.7 macrophage cells were utilized for cell culture studies. Cells were cultured at 37 °C, 5 % CO_2 and 95 % relative humidity in α-MEM (MC3T3-E1 cells) or DMEM (RAW264.7 Cells) growth media containing 10 % FBS and 1 % P/S. The substrates were sterilized as previously described, soaked in culture media for 24 hours, then seeded with MC3T3 cells at a density of 40,000 cells/well or RAW cells at a density of 50,000 cells/well in 24-well plates. The media was changed every other day throughout testing.

2.2.6 Osteoblast Assessment

Cell viability was assessed using Live/Dead staining (Invitrogen, Live/Dead Staining Kit). The Live/Dead assay was performed on days 1 and 5 post seeding according to the manufacturer's protocol. Imaging was performed using fluorescence microscopy (Olympus CKX41). Following imaging, cells were fixed using a 2.5 % glutaraldehyde solution and subjected to alcohol dehydration and mounted for SEM imaging under the previously stated conditions.

Cell viability directly cultured and indirectly cultured was assessed using the MTT activity assay (Vybrant® MTT Cell Proliferation Assay Kit). For the MTT assay, the cells were subjected to fresh media, 500 μL each, with 50 μL of 12 mM MTT (3-(4,5-Dimethylthiazol-2-

yl)-2,5-diphenyltetrazolium bromide) solution and incubated for 4 hours. After incubation, 500 μL of sodium dodecyl sulphate was added and incubated for 18 hours to lyse cells and solubilize formazan. After solubilization, 200 μL of solution from each sample was transferred to a 96 well plate and the absorbance of the sample was measured using Synergy2 Multi-Mode Microplate Reader (Biotek, USA) at an emission wavelength of 570 nm. Due to concerns surrounding Mg^{2+} interaction with MTT as reported in the literature, the reported values are normalized by background readings for each material [165]. However, significant differences between backgrounds were not observed. An indirect method of culture was also employed to distinguish between the effects of ions dissolved from the samples in media and surface morphology on the osteoblast viability. The pellets were incubated in 2 mL of culture media supplemented with FBS and P/S for 48 hours. This supernatant media was then collected and MC3T3 cells cultured on tissue culture plastic (96 well plates) were exposed to this media for 1 and 5 days, replacing with new supernatant every 48 hours. Cells were exposed to the fully concentrated supernatant as well as supernatant diluted into fresh culture media to 25% of the original concentration. MTT activity assay were then completed similar to the protocol above.

Osteoblast maturation was assessed by measuring alkaline phosphatase (ALP) activity. MC3T3-E1 cells were cultured on substrates for 7 days in growth media (α-MEM with FBS and P/S). After 7 days cells were cultured in osteogenic media. Osteogenic media was prepared by supplementing the growth media with 100 nM dexamethasone, 50 μM ascorbic acid and 10 mM β-glycerophosphate and cultured for an additional 3, 7 and 14 days. After culture for these time points, samples were rinsed with PBS then incubated in CellLytic cell lysis buffer, 0.5ml per well, for 30 minutes on a shaker to lyse the cells. The supernatant was collected, centrifuged and stored at -20°C until testing. For determination of ALP activity, Sigmafast p-nitrophenyl

phosphate (pNPP) and Tris Buffer tablets were used. 200 µL of pNPP buffer solution was mixed with 20 µL of lysis extract and incubated for 2 hours at 37°C. 0.3 N NaOH solution was added to stop the reaction, and the absorbance was read at 405 nm using the plate reader. The total protein concentration was determined, utilizing a Pierce BCA Protein Assay kit according to the manufacturer's protocol. The ALP activity was normalized by the total protein content for each sample.

2.2.7 Osteoclast Assessment

The proliferation, maturation, and activity of RAW 264.7 monocytes into osteoclast-like cells were assessed through SEM imaging and fluorescent staining of cellular actin and nuclei. RAW cells were seeded on substrates in 24 well plates with 1 mL of media per well. The cells were cultured for 24 hours after seeding in growth media, after which cell culture media was supplemented with 50 ng/mL RANKL (BioLegend, San Diego, CA) to induce differentiation into poly-nucleated osteoclast-like cells. The media containing RANKL was replenished every other day. The cells were rinsed with PBS and fixed using a 4 % paraformaldehyde solution. F-actin was stained using phalloidin–Tetramethylrhodamine B isothiocyanate (phalloidin-TRITC, Sigma Aldrich) and the nuclei were stained using 4',6-diamidino-2-phenylindole (DAPI) (Applichem) according to the manufacturer's instructions. Imaging was completed using fluorescence microscopy as previously described. Subsequently, the cells were subjected to alcohol dehydration and mounted for SEM imaging, under the previously stated conditions.

2.2.8 Statistical Analysis

Statistical calculations were performed using IBM SPSS Statistics 20 statistical analysis program. For TGA/DSC the mean and standard deviation was expressed for a total of seven independent samples. For all other quantitative assessments, including ionic content via ICP-OES, MTT viability assay and ALP activity assay, the mean and standard deviation was assessed for a sample size of three per sample. Statistically significant differences were assessed through one-way ANOVA with Tukey's post hoc testing where significance was set at $p<0.05$.

2.3 RESULTS

2.3.1 Materials Synthesis and Characterization

The purpose of this study was to synthesize crystalline and amorphous magnesium phosphate phases, characterize the synthesized powders, and evaluate their biological response *in vitro.* For the majority of the materials testing, a total of seven batches of synthesized materials were analyzed in order to ensure repeatability. The x-ray diffraction results of the as-synthesized powder and thermally treated powders can be seen in Figure 2-1a. Diffraction data indicates that the native as-synthesized powder is indeed amorphous. Similar to the as-synthesized material, the material thermally treated to 200 °C for 6 hours in air was also shown to be amorphous in the bulk. The material heat treated to 750 °C for 4 hours in air, above the exothermic reaction temperature seen in DSC, was however as expected was identified to be crystalline $Mg_3(PO_4)_2$ (TMP, ICCD Card 00-033-0876). To understand the crystalline phase evolution during thermal

treatment of the amorphous phase, TGA/DSC was also conducted, the results of which are shown in Figure 2-1b. DSC analysis conducted in argon indicates a broad endothermic reaction with an average reaction onset and end between 90-212 °C and a sharp exothermic peak with an average onset and end temperatures between 657-689 °C. The TGA plot shows an average weight loss of 30.4 % with approximately 24.2 % occurring within the bounds of the endothermic peak seen between 90-212 °C and the remaining weight loss occurring gradually throughout the temperature range of thermal treatment.

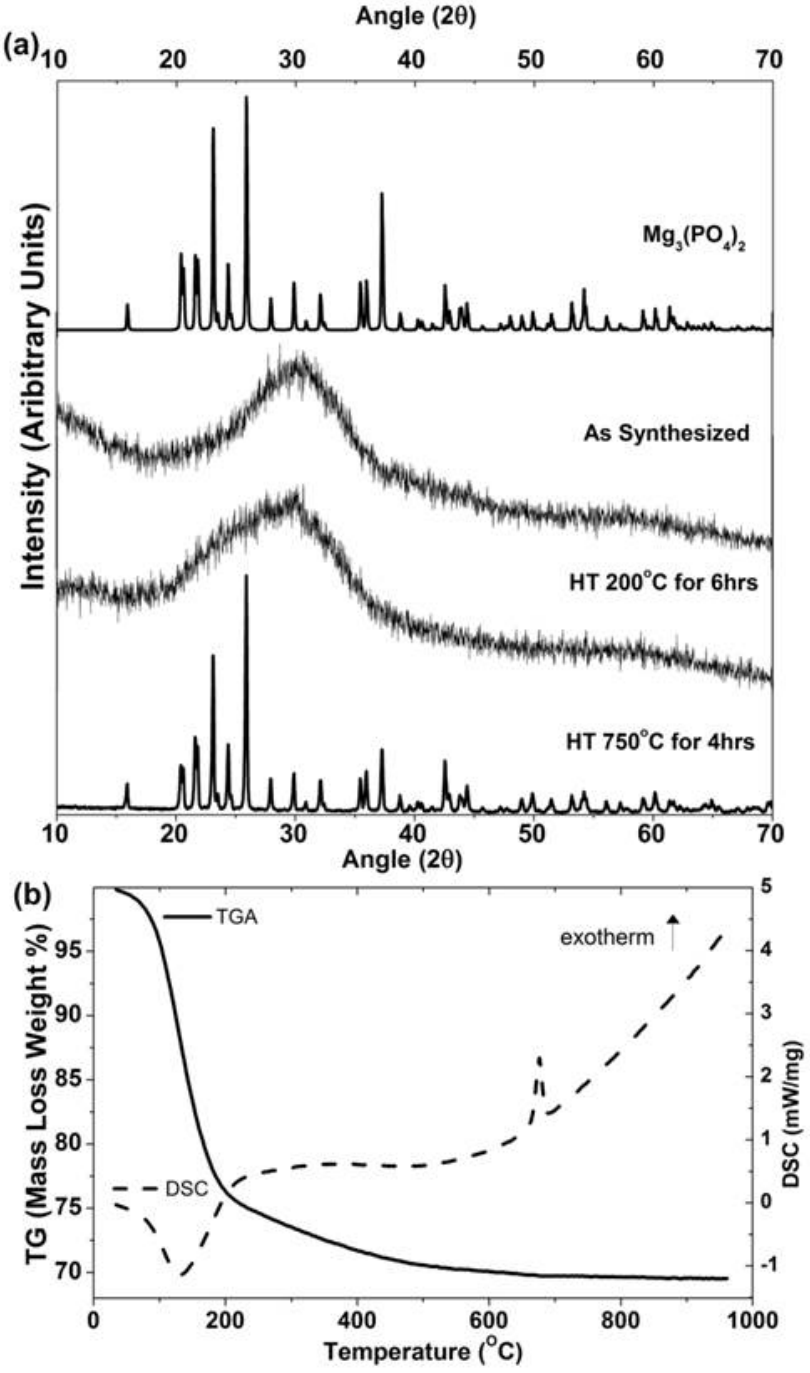

Figure 2-1 Basic material characterization showing (a) XRD of the as synthesized powder and the powder thermally treated to 200 °C and 750 °C with reference pattern of $Mg_3(PO_4)_2$ (ICCD Card 00-033-0876) and (b) TGA/DSC of the as synthesized powder.

In Figure 2-2a are shown representative SEM images of the native, as-synthesized precipitate and the precipitate after thermal treatment to 750 °C for 4 hours in air. No qualitative difference can be seen in the particle size and geometry between the as-synthesized and the crystallized particles, with both native and thermally treated powders showing the flat, plate-like particles with a wide distribution of particle sizes. An EDS spectrum was used to identify the elemental composition of the powders (data not shown). The measurements showed an average Mg/P ratio of 1.48 ± 0.04, confirming the nearly stoichiometric nature of the tri-magnesium phosphate present in the as-synthesized amorphous material. Representative HRTEM images of the as-synthesized and thermally treated powders are shown in Figure 2-2b. The low-magnification image of the as-synthesized powder indicates that the particles seen in SEM are in fact, agglomerates of much smaller spheres of amorphous material. High magnification images of the as-synthesized and thermally treated powders and fast Fourier transform (FFT) pattern insets (2-2b center and right, respectively) confirm that the precipitated TMP is amorphous and forms a highly disorganized crystalline material under the thermal treatment parameters. Given this characterization information, subsequent *in vitro* testing was completed on powders treated to 200 °C (ATMP) and 750 °C (CTMP). XRD of sintered pellets confirmed that pellets thermally treated to 200 °C remained amorphous and pellets thermally treated to 750 °C retained the same crystalline TMP form (data not shown), confirming the stability of the amorphous and crystalline powders under the extended thermal treatment required for pellet generation.

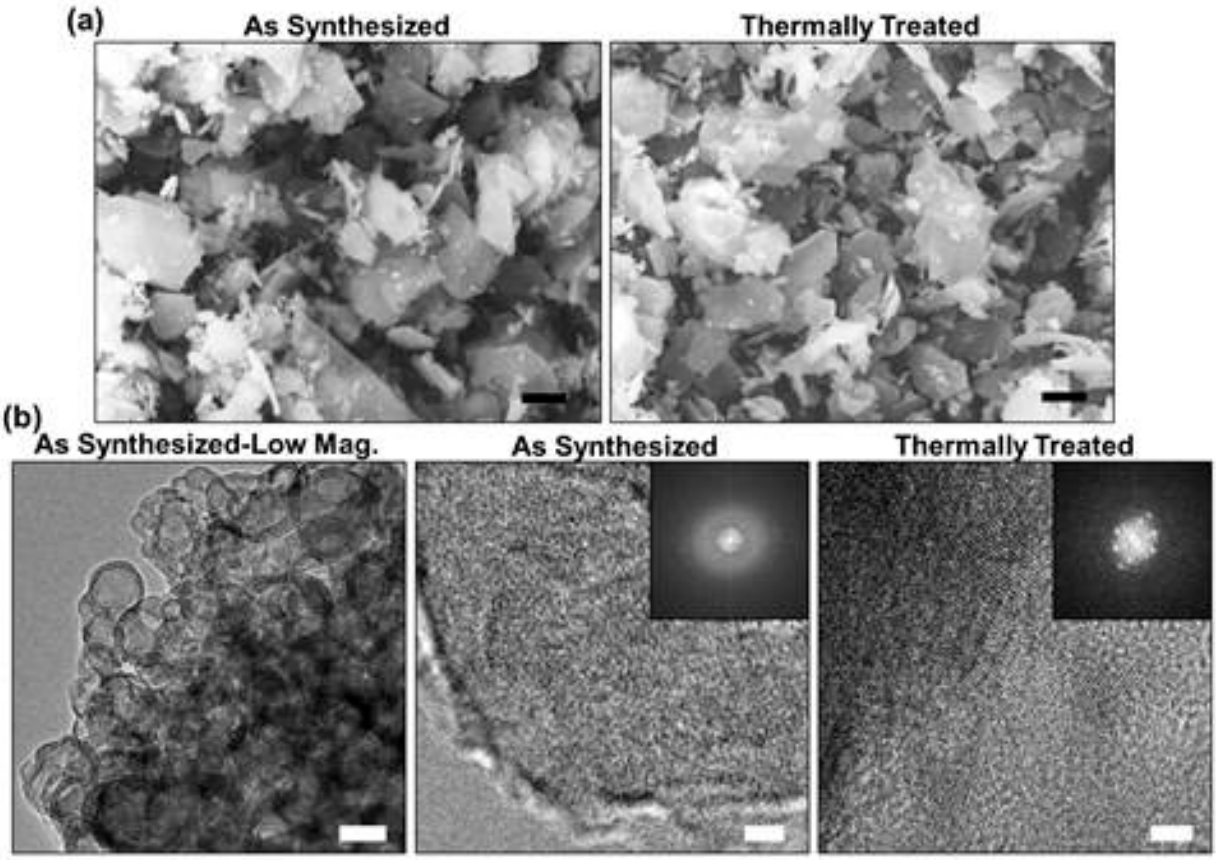

Figure 2-2 Electron microscopy of synthesized $Mg_3(PO_4)_2$ powders displaying (a) representative SEM images of the as-synthesized and thermally treated powders (scale bar is 10μm) and (b) TEM images of the as synthesized powder at low magnification (scale bar is 40 nm) at left and images of the as-synthesized and thermally treated powders at high magnification (scale bar is 2 nm). Insets show diffraction patterns of the respective samples.

2.3.2 *In Vitro* Dissolution and Mineralization

In vitro dissolution and surface mineralization of the pellets was studied in order to understand the media and surface environment to which cells are exposed to. Pellets of ATMP, CTMP and β-TCP were immersed in the growth media and the media was collected at numerous time points. ICP-OES was then used to determine the ionic concentrations of magnesium and calcium in the

media in order to evaluate the dissolution of substrates under *in vitro* conditions. ICP-OES measurements show that the ATMP released much higher levels of magnesium ions than CTMP, up to 9 mM with ATMP versus 3 mM with CTMP (Figure 2-3a, top) after 125 hours of immersion, while magnesium ion concentrations in β-TCP controls remained the same as the media samples ($p<0.001$). Measurements of calcium ion concentration (Figure 2-3a, bottom) showed an interesting trend of calcium ion level reduction over time. All three materials showed some calcium level reduction in media ($p<0.01$ beyond 1 hour for ATMP and CTMP, $p<0.01$ for β-TCP beyond 12 hours), however the reduction in Ca levels for ATMP was significantly higher than CTMP or β-TCP ($p<0.01$ beyond 1 hour).

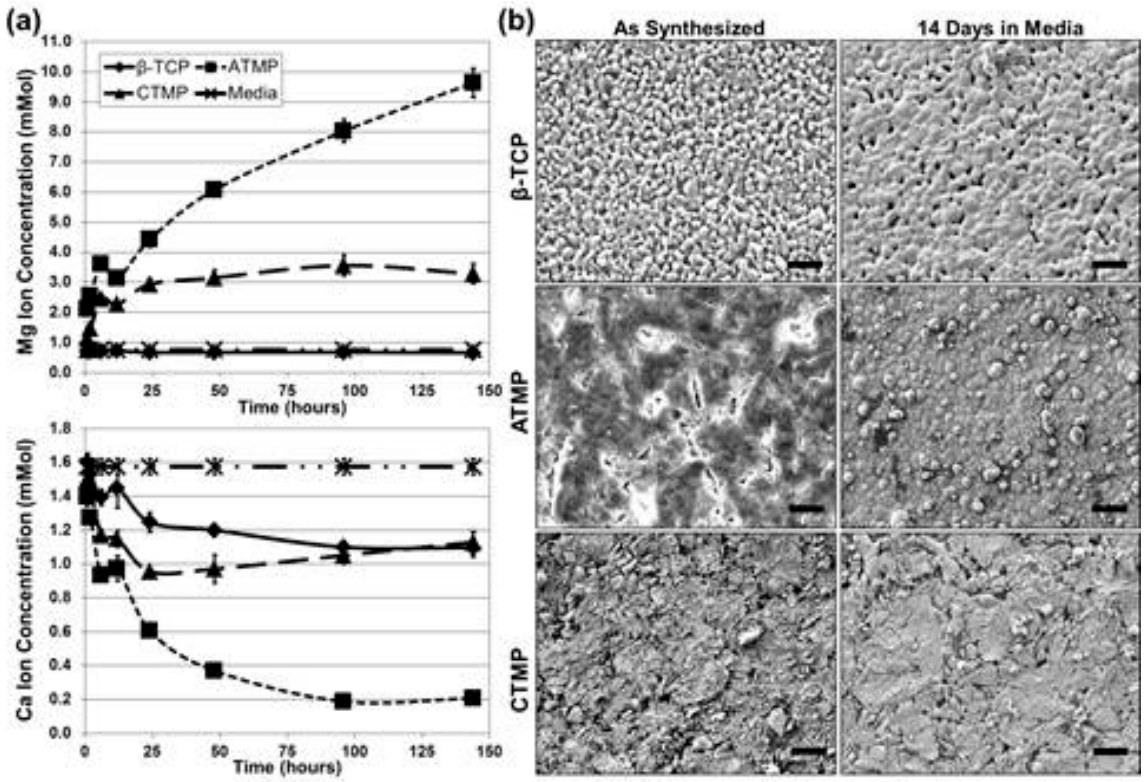

Figure 2-3 ***In vitro*** **dissolution of pellets showing (a) the released ion concentrations of magnesium (top) and calcium (bottom) into the media and (b) SEM of pellet surfaces: as-synthesized and after 14 days in media (scale bar is 10 μm).**

SEM images of the pellet surfaces prior to media exposure and after two weeks of media incubation can be seen in Figure 2-3b. The images indicate that the surface of β-TCP and CTMP remain relatively unchanged throughout this time period while the ATMP surface undergoes significant morphological changes. The ATMP surface promotes the growth of rosette-like crystal features. Images of the surface of ATMP pellets incubated for 14 days in culture media with 0 % and 20 % FBS, shown in Figure 2-4a, also show significant changes in morphology. The change in ATMP surface morphology when incubated in 0 %, 10 % and 20 % FBS are quite different, indicating the critical role FBS may play in the dissolution and formation of the rosette type morphology. In order to determine the nature of the surface growth, granules of the rosette shaped growths were scraped from the surface and analyzed. FTIR spectra of the ATMP powder, CTMP powder, FBS and the scrapings of the rosette growth collected from the surface of the ATMP can be seen in Figure 2-4b.

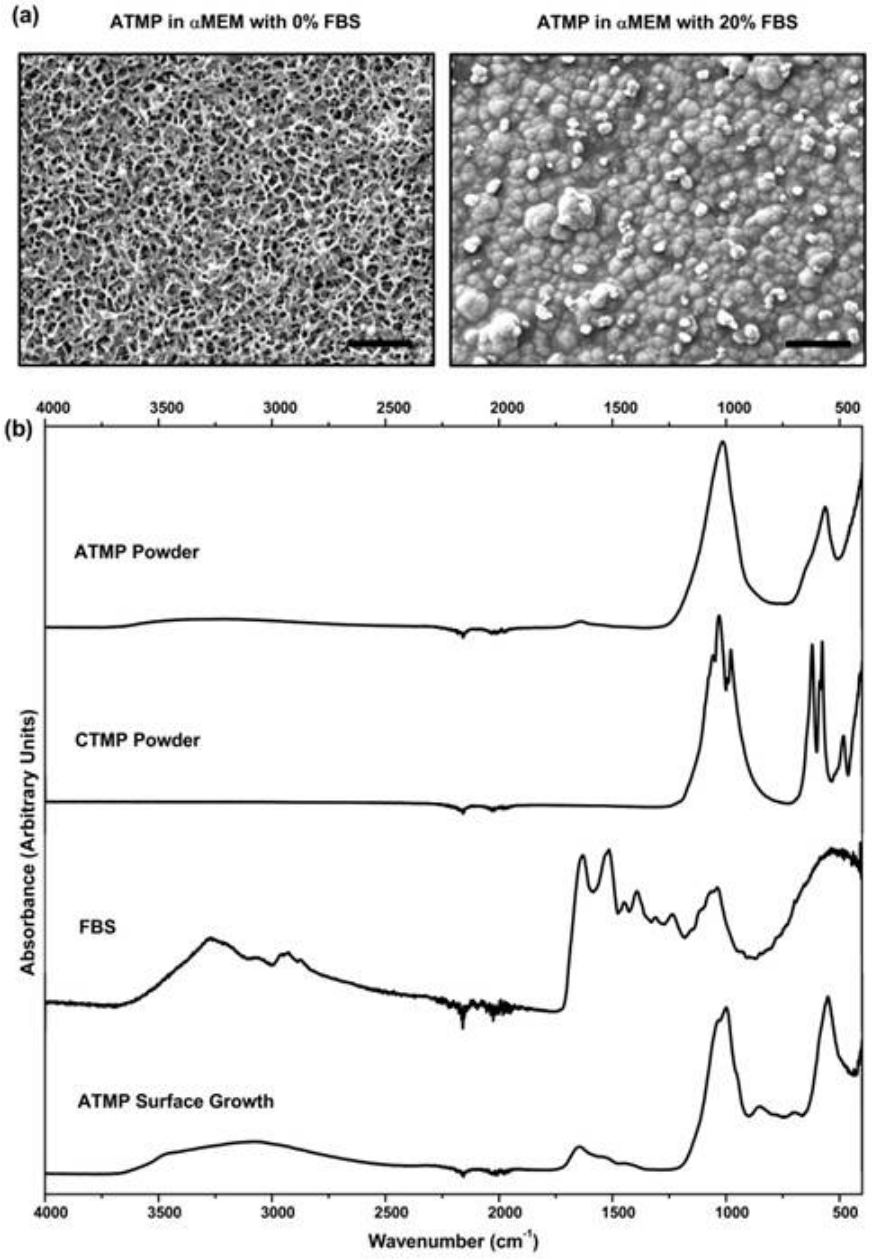

Figure 2-4 SEM images of ATMP pellets (a) after 14 days of incubation in culture media with 0 % and 20 % fetal bovine serum (FBS, scale Bar is 5 µm) and FTIR spectra (b) of ATMP and CTMP powders, FBS, and ATMP pellet scrapings.

FTIR spectra of the CTMP powder shows numerous sharp peaks between 900-1200 cm^{-1} and 450-700 cm^{-1} which correspond with various PO_4^{3-} adsorption bands; υ2 (480 cm^{-1}), υ4

(575 & 590 cm^{-1}), $\upsilon 1$ (960 cm^{-1}) and $\upsilon 2$ (1000 cm^{-1}), respectively [166]. ATMP powder spectra show broad peaks around 1000 cm^{-1} and 600 cm^{-1}. These bands are the result of the various PO_4^{3-} bands which lack the splitting and definition of specific bonds corresponding to the crystalline state due to the amorphous nature of the TMP powder. Scrapings of the rosette growth show that there appears to be minor increased organization of phosphate bonds around 1000 cm^{-1} but the linkages do not achieve distinguishable states corresponding to the various conformations (bending and stretching) which are seen in the fully crystallized CTMP material and are not truly indicative of crystallization. The spectra also show adsorbed water (broad peak 2700-3500 cm^{-1}) as well as numerous broad bonds associated with carbon-oxygen bonds. These carbon-oxygen bands can be attributed to the carbonate ions substituted into the phosphate structure, wherein bonds at 850 cm^{-1} and between 1400-1650 cm^{-1} could represent the carbonate substitution for hydroxide or phosphate typically seen in the apatite structure [166]. The broad peaks between 3000-3500 cm^{-1} is attributed to the adsorbed water. Finally, the weak peak seen at 3500 cm^{-1} as well as the peak observed at 700 cm^{-1} may be attributed to OH^- stretch which would be indicative of the formation of the characteristic apatite-like structure [166]. The amorphous nature of the surface growth requires the use of additional characterization techniques to further distinguish the specific role of various ions or compounds contributing to the growth of the final product.

Figure 2-5a shows the SEM image of the ATMP pellet surface during the early stages of the rosette structures formation. This image shows that the rosette structures indeed grow onto the surface of the pellet as opposed to growing within the culture media and depositing on the pellet surface. In Figure 2-5b and c are low and high magnification HRTEM images (respectively) of collected rosette scrapings from an ATMP pellet surface after incubation. The image in Figure 2-5c and corresponding FFT pattern (insert) indicate that although the habitual

rosette morphology would imply the formation of a crystalline product, the structures in fact is amorphous. EDS measurements shown in Figure 2-5d, while not reliably quantitative, indicate that the isolated products are composed of phosphorous, oxygen and magnesium with a significant amount of calcium, suggesting that these rosette morphologies are likely calcium-substituted magnesium phosphates.

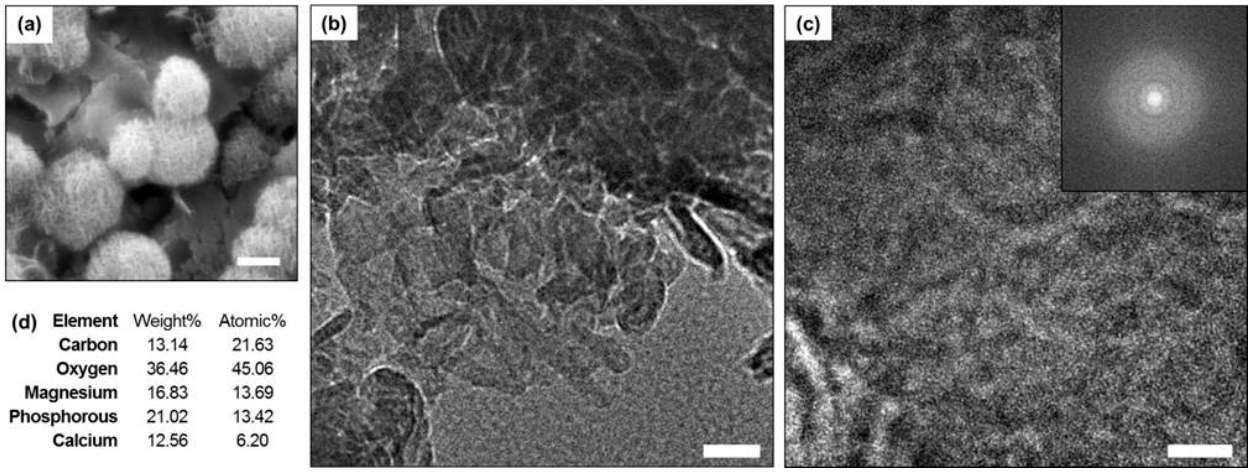

(d)

Element	Weight%	Atomic%
Carbon	13.14	21.63
Oxygen	36.46	45.06
Magnesium	16.83	13.69
Phosphorous	21.02	13.42
Calcium	12.56	6.20

Figure 2-5 SEM image of early rosette formation (a) at 24 hours of incubation (scale bar is 1 µm), TEM images of pellet scraping at low magnification (b, scale bar is 20 nm) and high magnification (c, scale bar is 5 nm) with inset containing the diffraction pattern for the particle, and EDS elemental analysis from the particle (d).

2.3.3 *In Vitro* Cytocompatibility

Viability of MC3T3-E1 murine pre-osteoblasts was characterized using Live/Dead staining as well as the MTT viability assay. Live/Dead staining at days 1 and 5 post seeding can be seen in Figure 2-6. The cellular attachment on ATMP and CTMP substrates qualitatively showed cell densities similar to the β-TCP control at day 1. At day 5 however, ATMP and β-TCP substrates showed significant proliferation from day 1. In contrast, the CTMP substrates showed only

minor changes in live cell density after day 5. MTT assay results of direct and indirect cell cultures, seen in Figure 2-7a, showed that there are differences in cell activity levels between substrates, similar to the trends visualized in the Live/Dead staining. Day 1 results show that with direct cell seeding, ATMP and CTMP are significantly lower than β-TCP and not statistically different from each other ($p<0.05$) while with the indirect culture the ATMP surface exhibits viability that is lower than the CTMP. Day 5 analysis shows that with direct seeding, β-TCP is slightly higher than ATMP ($p=0.061$) while CTMP is now much lower than both β-TCP and ATMP ($p<0.05$). Day 5 indirect cultures show an even greater difference between ATMP, and the CTMP and β-TCP ($p<0.05$). Dilution of the extract appears to negate the cellular activity differences observed in the cultures.

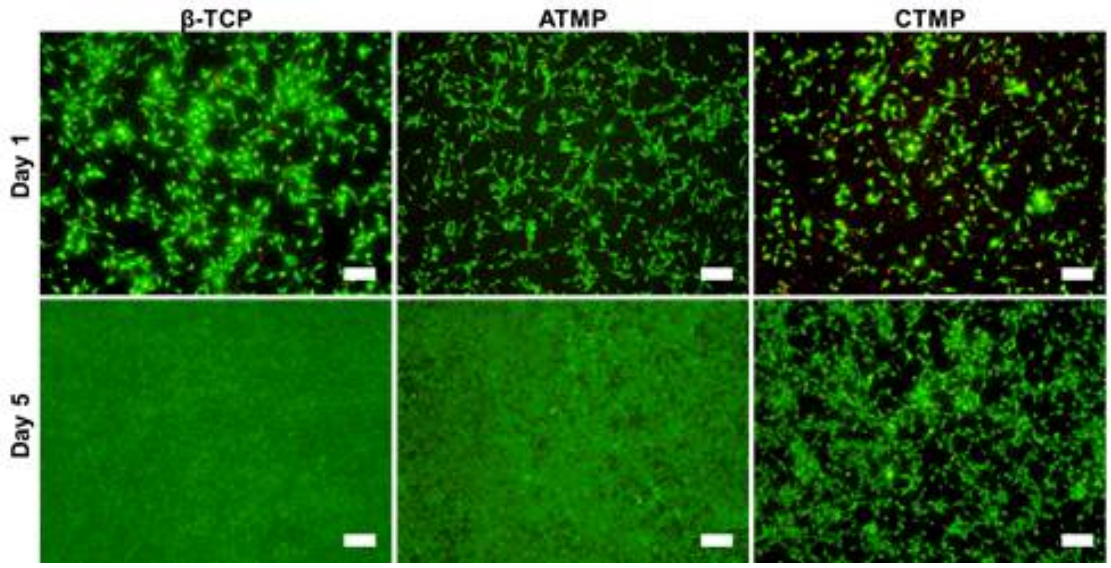

Figure 2-6 Live/Dead staining of MC3T3 osteoblasts, left to right are βTCP, ATMP and CTMP at days 1 and 5 post seeding (top and bottom respectively, scale bar is 200 μm).

In Figure 2-7b-d can be seen representative SEM images of fixed cells on the surface of βTCP, ATMP and CTMP pellets. Figure 2-7c shows that the MC3T3-E1 cellular cytoplasmic

extensions appear to be preferentially attached to the rosette formations on the surface of the ATMP pellet, as indicated by the arrows in the images. Alkaline phosphatase activity is shown in Figure 2-7e. Results indicate that MC3T3 cells show an earlier increase in ALP activity on the ATMP pellets than on the β-TCP or CTMP pellets. At 7 days of culture in osteogenic media, a total of 14 days of culture, ALP activity presented on ATMP pellets was statistically higher than the β-TCP ($p=0.004$) and CTMP ($p=0.001$). By 14 days of culture in osteogenic media, β-TCP achieved ALP levels similar to ATMP and the tissue culture control ($p>0.5$) while the CTMP substrates never achieved increased ALP activity levels ($p<0.05$).

SEM images of RAW 264.7 cells fixed on substrates after 8 and 11 days of culture in media supplemented with RANKL can be seen in Figure 8. β-TCP substrates show significant proliferation of monocytes and the formation of polynucleated cells at Day 8 with pseudopodia extensions of these cells at Day 11. After 8 and 11 days of culture both ATMP and CTMP show substantial proliferation and attachment of monocytes to pellet surfaces but the samples give no indication of the formation of polynucleated cells. In Figure 2-9 are displayed images of actin and nucleus staining of RAW cells. Images indicate that monocytes grown on tissue culture plastic controls rapidly form polynucleated cells, as seen in the Control, Day 8 image. The Control Day 11 image shows strong actin ring formation surrounding polynucleated cell, which is indicative of true osteoclast cell formation. β-TCP substrates show formation of some polynucleated cells at Day 8 and pseudopodia extensions of these cells at Day 11. Similar to SEM image results collected after 8 and 11 days of culture both ATMP and CTMP show significant proliferation of monocyte and although there are clusters of monocytes, there is no indication of the formation of polynucleated osteoclast-like cells.

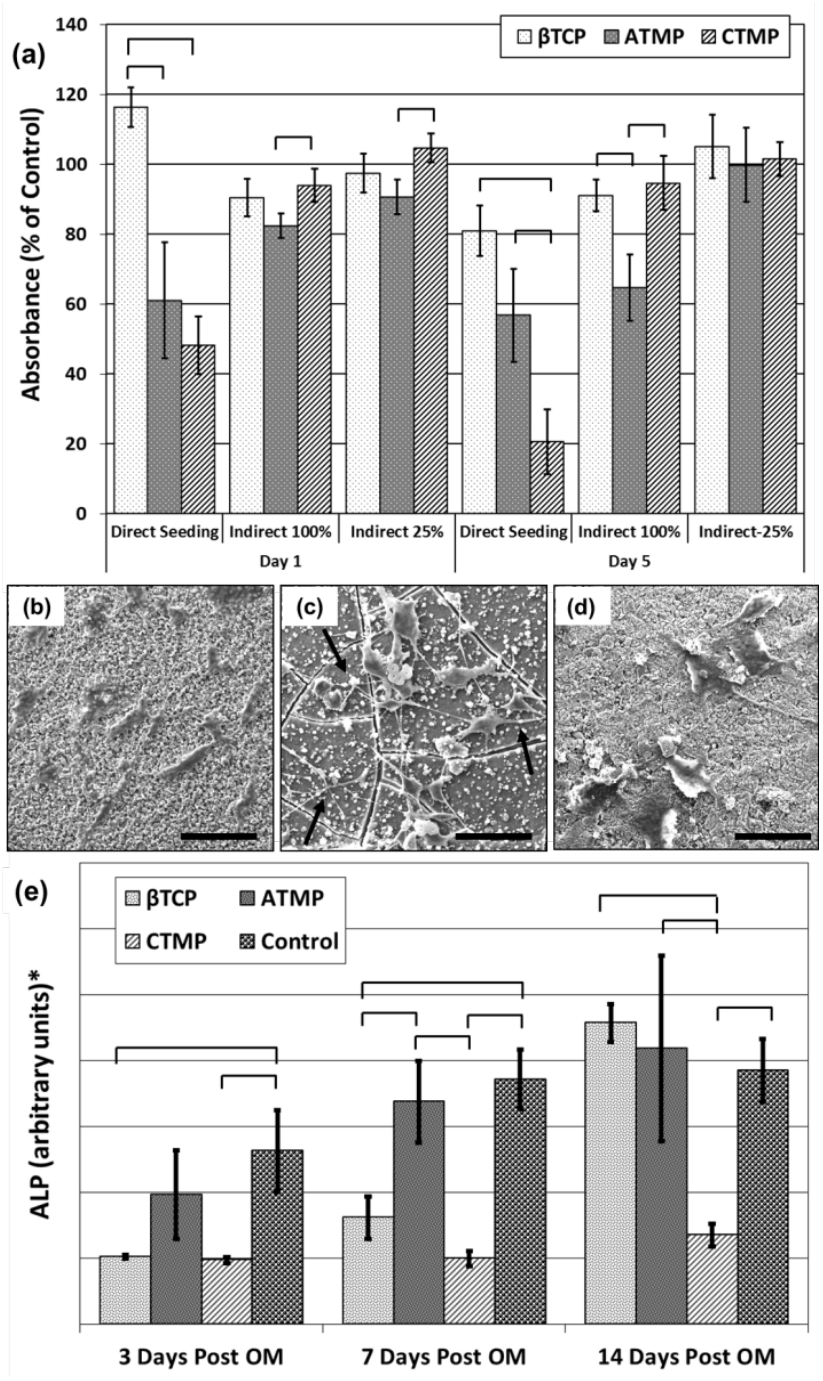

Figure 2-7 MTT viability results of direct and indirect MC3T3 cell culture (a), SEM images of fixed MC3T3 cells on βTCP, ATMP and CTMP pellets 24 hours after seeding (b-d, scale bar is 50 µm) showing preferential attachment to surface growth particles (indicated by the arrows) on the ATMP scaffold, and ALP activity of MC3T3 cells cultured on pellets in osteogenic media (OM) (e). *Units of ALP are [(µmol/hr)/(µg protein)/cm^2 surface area].

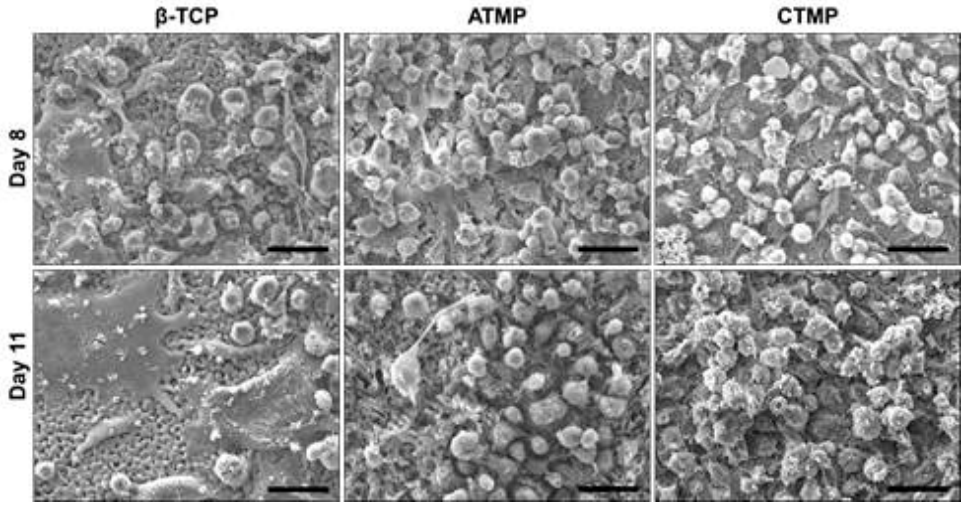

Figure 2-8 SEM Images of RAW 264.7 cell morphology on pellet surfaces after 8 and 11 days of culture in media supplemented with RANKL (scale bar is 25 µm).

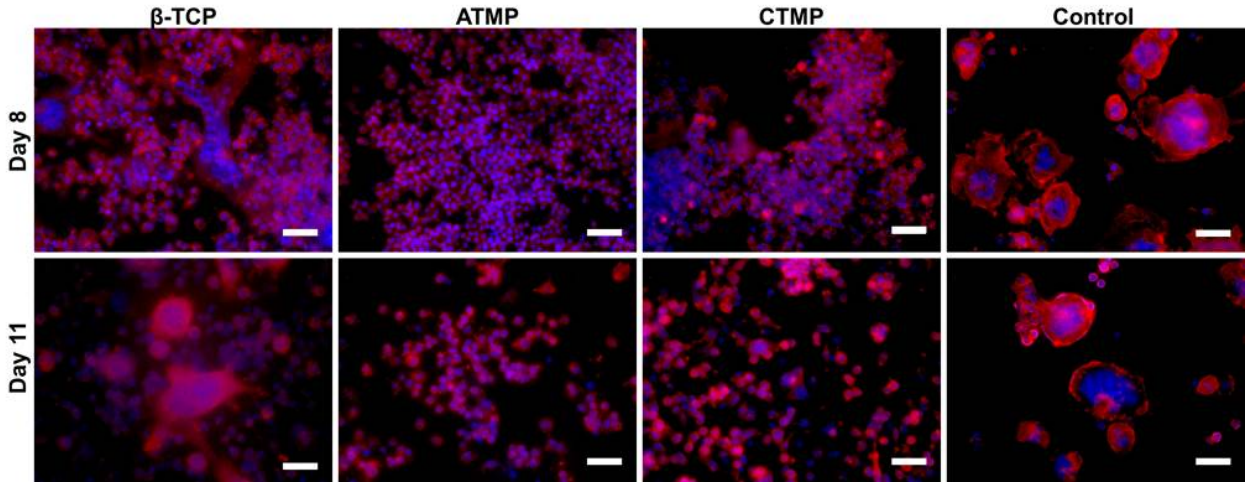

Figure 2-9 Actin-Nucleus staining of RAW 264.7 cells at days 8 & 11 of culture in media supplemented with RANKL (scale bar is 50 µm).

2.4 DISCUSSION

Magnesium, one of the most common metals in the body, is implicated in more than 300 enzymatic reactions, and shares many chemical similarities with calcium [167-169]. For this reason, many researchers have begun assessing the potential benefit of partially or fully substituting magnesium in calcium phosphate based implants intended for bone regeneration, since 50-60 % of the body's magnesium is stored in bone [167]. The work in this paper operates on the notion that calcium phosphates or biologics such as BMP-2 are not necessary for an effective bone repair scaffold. All necessary chemical and mechanical signaling for bone repair can be achieved through strong constructs with ion-based cell regulation; in particular the use of magnesium phosphate is attractive as magnesium is known to upregulate cellular proliferation and osteoblast activity [34, 40, 41]. As research in this field progresses, new embodiments, synthesis methods, and insight into the biological activities of magnesium phosphates are being discovered which will increase the breadth and depth of knowledge of these lesser studied materials. The aqueous precipitation of magnesium phosphates is not a new phenomenon, [40-41] but has recently been revisited by a few authors including Tamimi et al with the purpose of relating the spontaneous precipitation to biologically relevant conditions [30, 170, 171]. Tamimi et al found that, at 37 °C and pH below 8.0, under physiological concentrations with 10x physiological concentrations of magnesium and phosphate ions, mineral precipitation did not occur. Under other pH, temperature and ion concentration ranges, copious precipitation however occurred, most frequently resulting in the formation of crystalline tri-magnesium phosphate with various levels of bonded water. These minerals where shown to be non-toxic. More recently, Zhou et al reported a method of microwave synthesis of amorphous magnesium phosphate nanoparticles, which transformed to $Mg_3(PO_4)_2 \cdot 8H_2O$ when incubated in cell culture media

while Douglas et al reported the formation of a mixture of amorphous magnesium phosphate and $Mg_3(PO_4)_2 \cdot 8H_2O$ on a hydrogel scaffold which showed improved cytocompatibility over calcium phosphate mineralization on the same hydrogel [33, 164]. However, beyond this recent study, no studies characterizing amorphous magnesium phosphate have been published.

The aqueous precipitation method used in this study is at higher ionic concentrations than those utilized by either Tamimi or Zhou. This high concentration, room temperature aqueous precipitation of magnesium phosphate powder was demonstrated to be a simple, reliable method of formation of the phosphate. Spontaneous precipitation of amorphous magnesium phosphate (ATMP) from $MgCl_2$ and Na_3PO_4 solutions occurred in a highly basic environment. The precipitate remains amorphous while in solution, and rapid rinsing and drying of the powder is deemed necessary to stabilize the amorphous material. Once dried, the amorphous powder is stable under ambient conditions, similar to amorphous calcium phosphate (ACP) [172]. Thermal treatment above 600 °C in air for extended time however, is required to transform the material into crystalline $Mg_3(PO_4)_2$. The combination of TGA, DSC and XRD results shown in Figure 2-1a and 2-1b indicate that the low-temperature endothermic reaction seen in DSC corresponds to the loss of water from the precipitate structure while the high temperature exothermic reaction corresponds to the transition of the TMP precipitate from amorphous to crystalline phase of TMP. The loss of water and the corresponding temperature induced phase transition results in the formation of crystalline anhydrous $Mg_3(PO_4)_2$ after thermal treatment.

While the SEM images of the TMP powder, Figure 2-2a, show flat, plate-like particles, HRTEM images in Figure 2-2b (left) indicates that the as-synthesized bulk particles are agglomerates of much smaller, spherical particles which appear to be in the range of 50 nm. The thermal treatment of these agglomerates results in numerous randomly oriented microcrystalline

regions within a single particle, Figure 2-2b (right). The agglomeration of nanoparticle sized precipitates into larger particles has been the subject of thorough study by Matijević et al as well as many others [173, 174]. Matijević et al's work indicates that the agglomeration of nanoparticle precipitates into micron-sized particles of seemingly crystalline shapes is not unusual and may be controlled by synthesis parameters such as ion concentrations, pH and agitation rate [173, 174]. Such parameters could be further controlled during the TMP synthesis and result in greater control over the size, morphology and polydispersity of the as-synthesized TMP particles. Powder characteristics of particle size and morphology have direct implications towards the reactivity and stability of the bulk material and would be of high interest to study moving forward.

Many implanted materials are designed to be replaced by native tissue through dissolution and degradation. This rate of implant removal is controlled by numerous material and implant properties. While these mechanisms are often desired, overly-aggressive reactions may result in implant failure and localized or systemic toxicity. The *in vitro* dissolution patterns (Figure 2-3a) shown by the ATMP and CTMP indicate sustained release of magnesium from both substrates during incubation as well as calcium removal from the media. The higher magnesium release shown by the ATMP over the CTMP is as expected, as amorphous materials are generally more soluble than their crystalline counterparts due to the disordered nature of the amorphous structure [175]. It should be noted that in measuring the dissolution of the pellets *in vitro*, the intention is to draw connections between relative dissolution rates and cellular activity, and not to predict clinical dissolution rates. Though the ion concentrations are not at median lethal dose 50 % (LD50) levels, it could be anticipated that the high level of magnesium concentration in ATMP cell culture should result in lower osteoblast viability in comparison to

the CTMP culture [47, 176]. However the direct opposite is observed: the ATMP displays markedly better MC3T3 viability over time than the CTMP. Live/Dead staining (Figure 2-6) and MTT viability tests (Figure 2-7a) indicate that ATMP is more cytocompatible over time than CTMP. To test the hypothesis that the increased magnesium ion concentration in ATMP should be detrimental to osteoblast viability, the indirect method of culture was employed, utilizing media extracted after pellet incubation. The indirect culture shows the anticipated results, with fully concentrated extracts from ATMP showing statistically lower viability than the CTMP extracts, especially after 5 days of culture (Figure 2-7a).

The differences seen between ATMP and CTMP in the direct versus indirect cultures imply that there is some other factor, such as surface chemistry or mechanotransduction, modulating the osteoblast cell viability on the ATMP. Herein the effect of the surface morphological changes observed on the ATMP which are not observed on the CTMP is concluded to be this modulating effect. The surface growth documented on ATMP (Figures 2-3b, 2-4a and 2-5a) is seen in the SEM images of fixed MC3T3 cells (Figure 2-7c). These representative images appear to show that the osteoblast cellular cytoplasmic extensions are preferentially elongated and attached to the rosette nodules grown on the ATMP surface. This indicates that the surface mineralization on the ATMP is directly affecting the osteoblast viability. It is difficult to elucidate beyond this whether the improved viability is due to physiochemical or mechanical cues, although it is likely due in part to both.

This spontaneous mineralization, and resulting increase in cytocompatibility, is of particular interest because past studies have shown that *in vitro* mineralization of synthetic biomaterials' surfaces results in increased cytocompatibility *in vitro* and biocompatibility *in vivo* [158, 160, 162, 163, 177-180]. Many researchers purposely mineralize the surface of

biomaterials and spontaneous mineralization is seen by many as inherently valuable [177, 180]. The rosette formations seen on ATMP pellet surfaces are nearly identical to calcium phosphate and hydroxyapatite mineralization habits seen on a wide variety of biomaterials [177, 181]. The visualized rosette morphology classically resembling apatite, in addition to the ICP results, showing calcium ion consumption from the media, and the EDS observations, showing calcium ion presence in the rosette structure all indicate that the rosette formations can be anticipated to have a hydroxyapatite framework highly substituted with magnesium. However, the formations were shown to be amorphous in nature. Magnesium, especially at high substitution levels, is known to stabilize amorphous calcium phosphate during synthesis and under *in vitro* conditions, suspending the formation of crystalline hydroxyapatite [155, 168, 182-184]. Additionally, results show that the level of fetal bovine serum plays a role in stabilizing the rosette morphology of the ATMP surface growth (Figure 2-4a). Though the presence of FBS-provided compounds, such as amino acids and growth factors, may contribute to the development of a particular growth morphology of the substrate, it is not specifically resolved in the FTIR spectra (Figure 2-4b). It is possible that there are proteins adsorbed to the surface of the mineralized growth but that the concentration is too low for proper detection with the methodology utilized.

The effect of this rosette growth on osteoblast cells may be significant. Not only does the cytocompatibility of the amorphous magnesium phosphate pellets improve over the CTMP pellets, the early stage of differentiation of MC3T3 cells into osteoblasts, as measured by the increased ALP activity on ATMP substrates (Figure 2-7e) at earlier time points than β-TCP controls maybe both attributed in part to the rosette growth. The result is that the ATMP material achieves high levels of cellular proliferation and more active differentiation than even the β-TCP control. This is in contrast to what has been seen in some cell culture on magnesium

phosphate minerals and cements, which displayed decreased osteoblast gene expression, including ALP, in comparison to calcium phosphate analogs [30, 86]. Studies have shown that magnesium doping into calcium phosphates or magnesium ion supplementation *in vitro* can increase osteoblast differentiation, and it is likely that the calcium rich surface mineralization is reducing the effect of direct magnesium phosphate interaction [60, 185-187]. In contrast, the lack of differences in viability and differentiation of RAW 264.7 monocytes into osteoclast-like cells on the ATMP and CTMP indicates that the differentiation appears to be affected by only the presence of a high level of magnesium and not the surface mineralization. Though the mineral layer may restrict physical contact with magnesium phosphate substrate, the magnesium ion concentration which the RAW cells are exposed to is high with both the ATMP and CTMP substrates. SEM images of RAW cells grown on substrates with RANKL supplementation (Figure 2-8) indicate that all substrates facilitated active monocyte proliferation. However, while RAW cells actively form osteoclast-like polynucleated cells on β-TCP, there is almost no indication of polynucated cells observed on ATMP or CTMP substrates during the period studied. Previous studies have shown that magnesium ions appear to temporarily suspend the formation and differentiation of precursor monocytes into mature osteoclasts but that magnesium does not affect the viability and function of mature osteoclasts [44, 45, 74, 188]. Because of the number of factors affecting osteoclast studies, osteoclast-substrate studies are often controversial and more precise, controlled studies would be highly beneficial to understanding the relationship between magnesium ions, magnesium phosphates, effects of surface composition, microstructure and particle size on osteoclast cells [189].

The early differentiation of osteoblasts and suspended formation of osteoclasts may have a positive effect on the integration of the material into bone. Due to the reactive nature of the

amorphous magnesium phosphate, and the resulting spontaneous mineralization of ATMP *in vitro,* this material is likely to generate implant substrates which are more bioactive and osteoconductive than the more common inert materials. The high solubility but lower anticipated cell-mediated resorption of the amorphous magnesium phosphate, along with the increased osteoblast activity, could result in more rapid formation of new bone tissue *in vivo*. Future work exploring the *in vivo* reactivity, degradation and bone formation would be interesting to determine whether *in vitro* results presented here correspond well with *in vivo* mineralization of similar amorphous, apatite-like formations as well as possibly demonstrating a favorable effect of the amorphous magnesium phosphate and surface mineralization on osteoblast and osteoclast activity. These studies are currently being planned and will be reported in the near future.

2.5 CONCLUSION

Amorphous magnesium phosphate was successfully generated through an aqueous precipitation method and subsequent thermal treatment resulted in crystalline tri-magnesium phosphate. Pellet substrates of the amorphous magnesium phosphate were significantly more soluble *in vitro* and showed higher levels of osteoblast viability and differentiation than the crystalline tri-magnesium phosphate phase. Under *in vitro* cell culture conditions, the amorphous magnesium phosphate substrate induced spontaneous growth of calcium-rich amorphous phosphate rosettes morphologically similar to crystalline hydroxyapatite mineralization on the pellet surface. The increased osteoblast viability is attributed to the synergistic effects of high solubility of the material, the high magnesium concentration seen by the osteoblasts, and the serum protein mediated apatite-like mineralization on the material. Both amorphous magnesium phosphate

and crystalline tri-magnesium phosphate supported extensive monocyte proliferation but suspended osteoclast formation. The combination of high solubility, spontaneous mineralization, increased osteoblast proliferation and differentiation and suspended osteoclast formation indicates that amorphous magnesium phosphate may be a unique material to explore for bone repair implant applications, in particular acid-base reacting bone cement style applications.

3.0 SPECFIC AIM 2: SYSTEMATIC ASSESSMENT OF SYNTHESIZED TRI-MAGNESIUM PHOSPHATE POWDERS (AMORPHOUS, SEMI-CRYSTALLINE AND CRYSTALLINE) AND CEMENTS FOR CERAMIC BONE CEMENT APPLICATIONS

3.1 INTRODUCTION

Bone substitutes are widely used in patients who require implantation to repair or remodel bone defects. These bone substitutes can range from synthetic materials such as metals and polymers to natural polymeric and biologic materials including allografts and autografts [1, 3]. Calcium phosphate based synthetic grafts are an excellent choice of bone replacement systems because these implants mimic the chemistry of the mineralized portion of human bone and have shown excellent biocompatibility [10, 24]. Currently, there are calcium phosphate based bone cements clinically available; however these products are less than ideal. Optimal bone cements should display high biocompatibility and osteoconductivity, strengths similar to natural bone, resorption rates in line with rapid bone remodeling, and clinically appropriate mix-ability, injectability, and setting times [10, 141, 190]. Brushite ($CaHPO_4$) based calcium phosphate bone cements, although readily resorbable, tend to display prohibitively fast setting rates and compressive strengths lower than natural bone. Hydroxyapatite ($Ca_5(PO_4)_3(OH)$) based calcium phosphate bone cements are capable of achieving higher strengths, but set very slowly and require several years to resorb and allow for bone remodeling [23, 24].

Recently it has been proposed that magnesium phosphate cements may pose a more clinically favorable option to traditional calcium phosphate cements [29]. Preliminary studies have shown that magnesium phosphate based cements display higher strengths, better setting times and faster resorption rates than calcium phosphates, while maintaining a high level of biocompatibility [28, 29, 31, 34, 36, 38, 39, 62, 191]. However, in contrast to calcium phosphates, the intensity and depth of study into these cement systems is still limited to only a few phases and remains to a large extent unexplored with inconsistent evaluation.

The following study explored the cementing characteristics of amorphous and crystalline tri-magnesium phosphate (TMP), $Mg_3(PO_4)_2$ ceramic which was synthesized and assessed in Chapter 2. Trimagnesium phosphate is a potential bone cement precursor material critical to the cementing reaction. It is important to study the precursor reactants as these material properties correlate to the final cement product since the material properties affect reaction kinetics, cement formulation and final product properties. Recent studies into magnesium phosphate cements have developed due to higher strengths and faster resorption rates of these cements. Magnesium phosphate cement or ceramic compositions explored to date include $MgHPO_4 \cdot 3H_2O$, $MgKPO_4 \cdot 6H_2O$, $Mg_3(PO_4)_2 \cdot 8H_20$, $MgNH_4PO_4 \cdot 6H_2O$, and $Ca_3Mg_3(PO_4)_4$ [29, 32, 36, 60, 74, 86].

The use of amorphous calcium phosphates (ACPs) in bone scaffolds and cements is known, however there is not the same level of understanding regarding the potential of amorphous magnesium phosphates for biomedical applications. ACPs are often regarded as highly useful as scaffolds or scaffold precursors because of the highly reactive and soluble nature of the ACP [9]. ACP is a critical part of the natural bone formation process, a transient phase which is a precursor to HA [192-194]. These ACPs have been used in bone cements to increase

the cement reactivity or bioresorbability. ACPs have also been shown to increase osteoconductivity of implant coatings as well as increase the mechanical properties of composites [192]. Magnesium has been widely shown to stabilize calcium phosphate in the ACP stage over conversion to HA [182, 195]. However, the analogy between ACP and amorphous magnesium phosphate is not clear as the synthesis of amorphous magnesium phosphate has only recently been reported [33]. In the previous study (Chapter 2), a comparison of the cytocompatibility of dense substrates of amorphous magnesium phosphate and crystalline tri-magnesium phosphate showed increased proliferation and differentiation of murine pre-osteoblast cells on the amorphous TMP substrates over the crystalline CTMP counterpart substrates [196]. It is however unclear whether the use of amorphous tri-magnesium phosphates is feasible to generate a functional bone cement product, or more importantly, how this cement may compare to cement made with a crystalline tri-magnesium phosphate. In this study therefore, the functionality of these amorphous and crystalline tri-magnesium phosphate powders, as well as the semi-crystalline tri-magnesium phosphates powders, and their propensity for cement formation in cement forming reactions with a concentrated, neutral pH ammonium phosphate solution particularly, for use in bone cement applications is explored and systematically assessed.

3.2 MATERIALS AND METHODS

3.2.1 Synthesis of Magnesium Phosphate Powders

Magnesium phosphate powders were synthesized via an aqueous precipitation reaction between 0.3 M $MgCl_2$ and 0.2 M Na_3PO_4, in deionized water, as described in Equation 2-1. The synthesized powders were then thermally treated to 400 °C, 600 °C or 800 °C for 6 hours at each temperature in a box furnace in air to form amorphous, semi-crystalline or fully crystalline dehydrated TMP, respectively. Powders were lightly ground and sieved to below 500 μm to remove large agglomerated clusters.

3.2.2 Magnesium Phosphate Powder Characterization

The as-synthesized and thermally treated magnesium phosphate powder samples were characterized utilizing a number of techniques: thermogravimetric analysis and differential scanning calorimetry (TGA and DSC), x-ray diffraction (XRD), Fourier transform infrared spectroscopy (FTIR), specific surface area (SSA) and scanning electron microscopy (SEM). The detailed specifics regarding controls and parameters used for these characterization methods can be found elucidated in Chapter 2.

3.2.3 Cement Formation

Series of cements were compared by combining the amorphous, semi-crystalline and crystalline $Mg_3(PO_4)_2$ powders with a pH 7.0, 3 M solution of ammonium phosphate. The solution was

made by combining monobasic ammonium phosphate ($NH_4H_2PO_4$) and dibasic ammonium phosphate ($(NH_4)_2HPO_4$) salts in deionized water at a ratio to obtain pH 7.0. The ratio of monobasic to dibasic ammonium phosphate to yield neutral pH 3 M solution is approximately 2:7 monobasic:dibasic, which would yield X and Y of approximately 16 and 11, respectively. Assuming an ideal complete reaction, this would yield a final product of approximately, 60 % $MgNH_4PO_4$ and 40 % $MgHPO_4$, as described below.

The powders were mixed with the ammonium phosphate solution at a variety of powder-to-liquid ratios (P:L), and thus the effect of the powder state on the cement reactivity was assessed. The cementing reaction should proceed per the reaction below for crystalline, semi-crystalline and amorphous $Mg_3(PO_4)_2$ according to Equation 3-1.

Equation 3-1

$$Mg_3(PO_4)_2 + (NH_4)_x(H)_yPO_4 = x\bullet MgNH_4PO_4 + y\bullet MgHPO_4$$

where x and y are based on the mole balance of the monobasic and dibasic ammonium phosphate salts in solution. In addition, with the given P:L ratios, a molar ratio of magnesium phosphate to ammonium phosphate greater than one is always maintained. This is because for the acid-base reacting cements such as these, an excess of magnesium phosphate ensures that the reaction proceeds further in the forward direction towards completion, which should yield greater strength and reduce the leaching of remaining soluble salts into the media. The P:L ranges tested in this study is shown in Table 1. The cement nomenclature used is dictated by the thermal treatment temperature of the powder, namely 400°C, 600°C or 800°C cement. Additional details, such as powder-to-liquid ratio is expressly stated.

3.2.4 Cement Characterization

Cements were made with powders heat treated at 400°C, 600°C and 800°C after a soak time of 6h at each temperature, using a variety of powder-to-liquid ratios, as indicated in Table 3-1. The setting times of the cement pastes were determined with the Gilmore needle test discussed earlier in Chapter 1 following the ASTM standard C266-13 at room temperature. Amorphous, semi-crystalline and crystalline tri-magnesium phosphate powders were mixed with the specified volume of solution and stirred for 60 seconds before filling into 10 mm circular molds. The handling characteristics will be qualitatively assessed based on consistency and injectability. The set cements were stored overnight at 37 °C before subsequent testing. The compressive strength of cement cylinders, nominally 6 mm x 12 mm, was analyzed using a 2 kN load cell (Instron, Norwood, MA) and a cross head speed of 1.0 mm/min, with 3 samples per condition. XRD and SEM analysis were used to assess the cements following completion of the reaction, utilizing the same procedures and equipment specified above. Pellets of the reacted cement were soaked in phosphate buffered saline (PBS) for 48 hours at 37 °C. At this point the pH and strength of each formulation was recorded. XRD and SEM analyses were again completed on the cements following PBS incubation to determine if any, changes occurring due to the extended saline incubation.

3.3 RESULTS AND DISCUSSION

3.3.1 Magnesium Phosphate Powder Characterization

Thermogravimetric analysis and the differential scanning calorimetry results of the as-synthesized TMP powder can be seen in Figure 3-1, showing the vast majority of weight loss occurring at temperatures lower than 200 °C, shown in TGA. The exothermic peak observed at temperatures less than 700 °C in the DSC scan, without any noticeable corresponding weight change, is attributed to the bulk crystallization of the material. These results confirmed the selection of temperatures of 400 °C, 600 °C and 800 °C used for obtaining the dehydrated amorphous, semi-crystalline and fully crystalline TMP for subsequent cementing reactions.

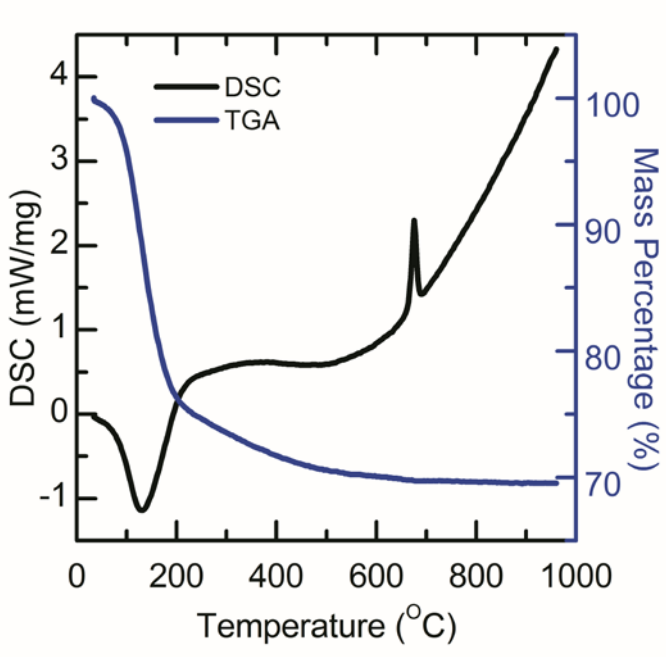

Figure 3-1 TGA and DSC of the synthesized $Mg_3(PO_4)_2$ powders.

X-ray diffraction of the synthesized and heat treated powders, shown in Figure 3-2, indicates that the synthesized powder is amorphous when generated, and retains the amorphous structure following thermal treatment at 400 °C. At 600 °C, crystalline peaks appear but a definitive amorphous hump is still retained, and finally at 800 °C, as expected following the thermal analysis results, complete conversion to fully crystalline $Mg_3(PO_4)_2$ (ICCD Card 00-033-0876) is observed.

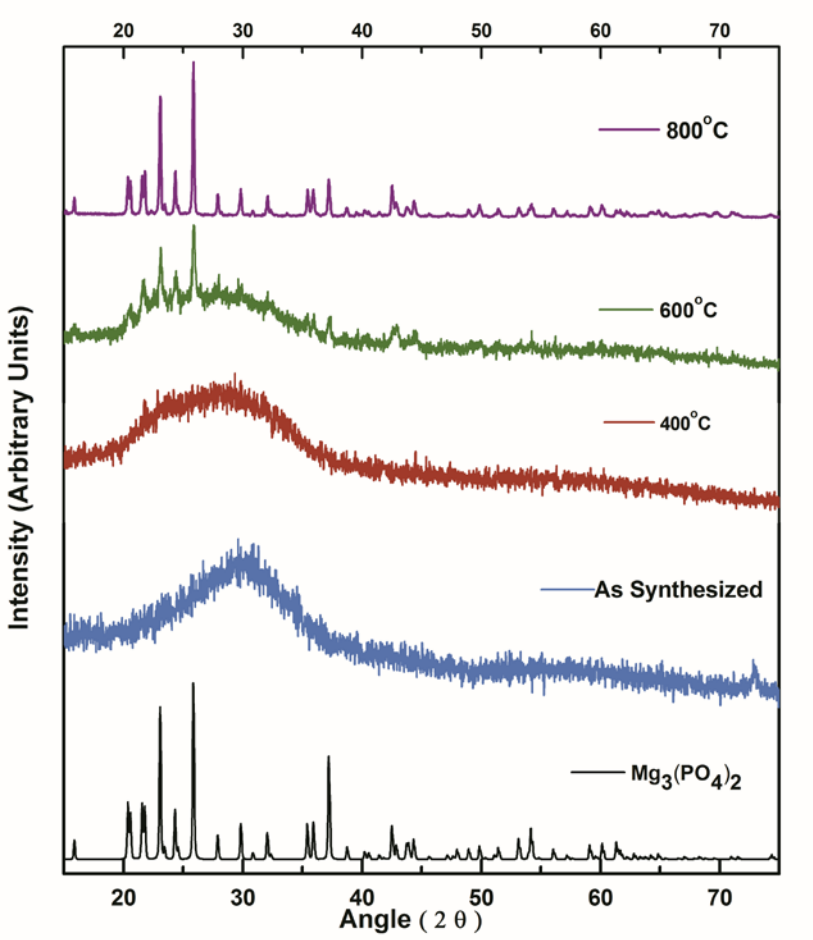

Figure 3-2 XRD of the synthesized $Mg_3(PO_4)_2$ powders.

Fourier transform infrared spectroscopy, seen in Figure 3-3, corroborates the TGA/DSC and XRD results. FTIR shows increased crystallinity with thermal treatment indicated by the more defined peak separations, from the as-synthesized material through the 800 °C thermal treatment, in the 1200 to 900 cm^{-1} and 700 to 450 cm^{-1} ranges which correspond to PO_4^{3-} adsorption bands [166]. Additionally, the 600 °C and 800 °C thermally treated powders show an absence of a broad hump in the 3500 to 2700 cm^{-1} range and the band at 1650 cm^{-1} which are indicative of adsorbed water and OH stretching bonds, respectively [166].

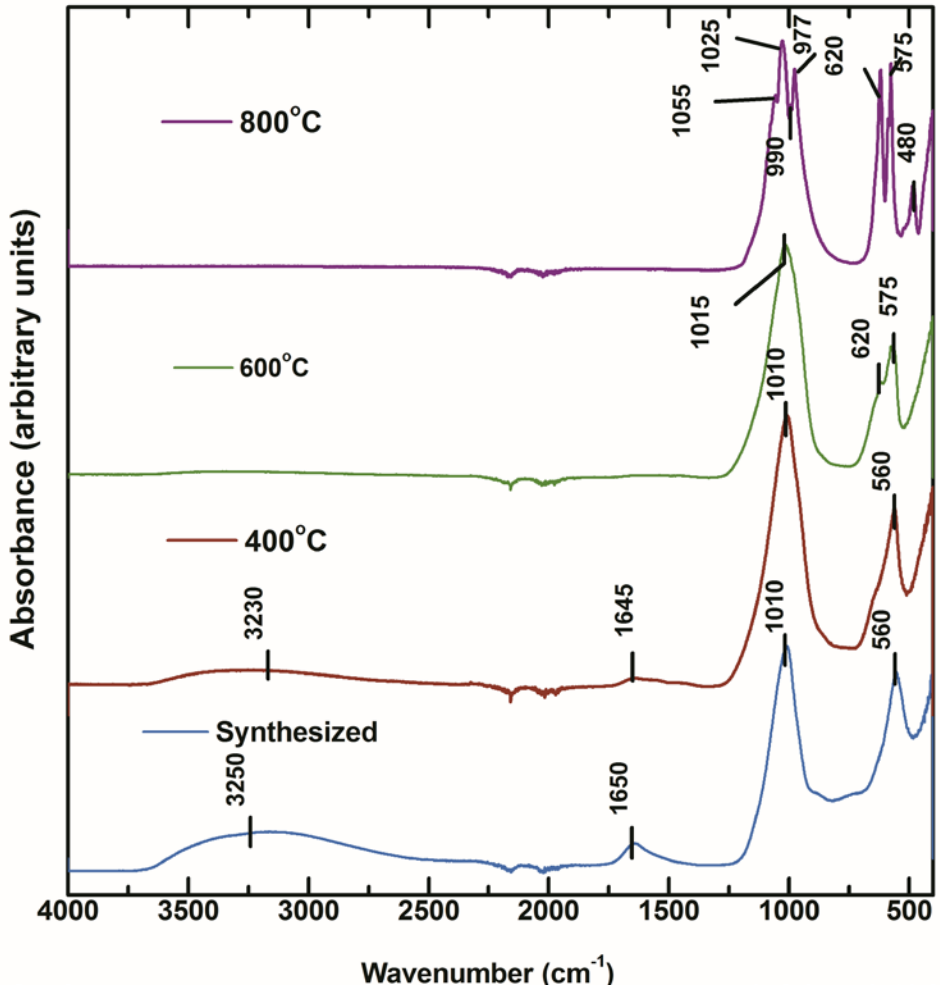

Figure 3-3 FTIR spectra of the synthesized $Mg_3(PO_4)_2$ powders.

Specific surface area measurements, shown in Figure 3-4, of the powders indicate that the as-synthesized material displays a high surface area of ~170 m^2/g, with subsequent thermal treatment significantly reducing the surface area. The initial surface area indicates that the particles are likely in the nanometer size range. However, the SEM images shown in Figure 3-5, demonstrates that the powders comprise much larger particles. Previous work from our laboratory indicate that these particles are in fact, agglomerates of much smaller, nanometer-sized particles, resulting in the large macroscopic particle clusters contributing to the surface area measured values [196].

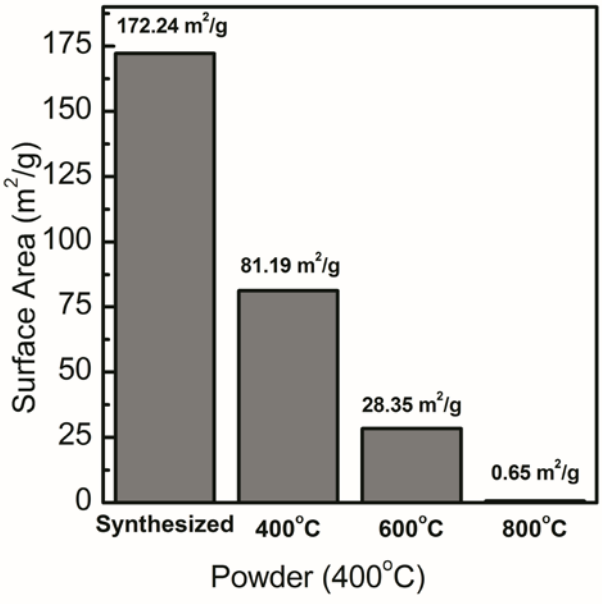

Figure 3-4 BET measured surface area of the $Mg_3(PO_4)_2$ powders.

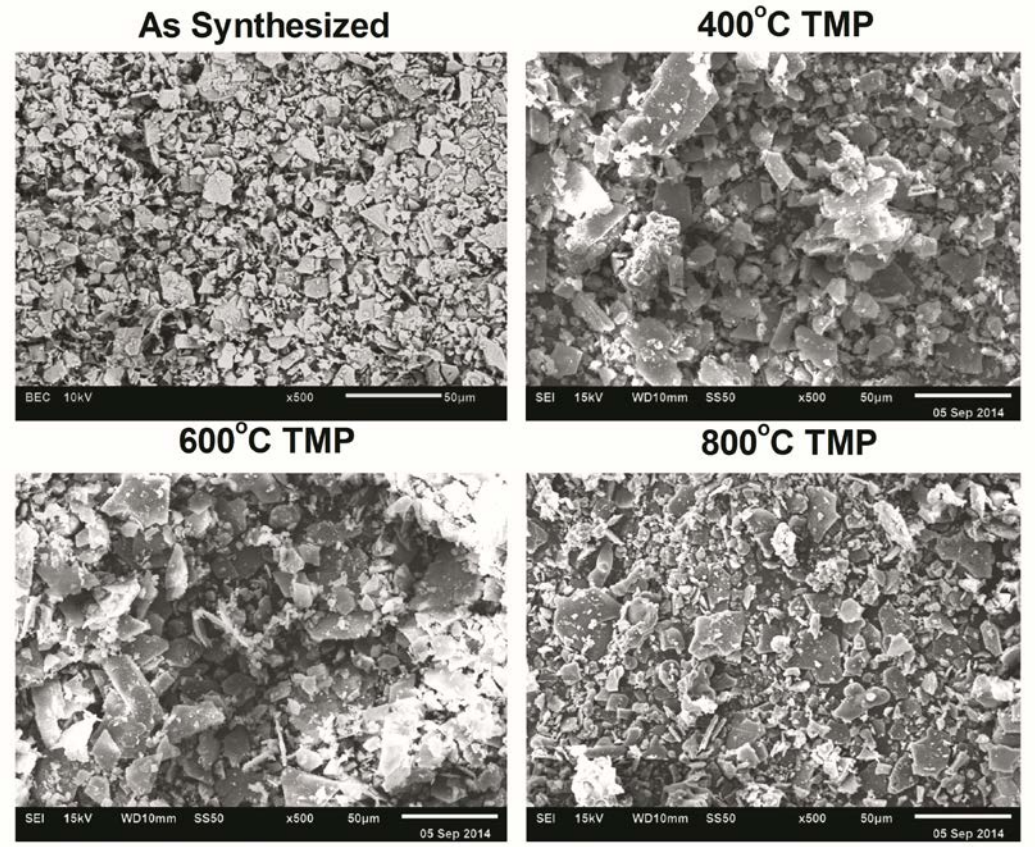

Figure 3-5 Scanning electron microscopy images of synthesized and thermally treated $Mg_3(PO_4)_2$ powders.

3.3.2 Cement Formation

A variety of P:L ratios for each heat treated powder was tested, with the goal of achieving a viscous paste consistency with set times of 10 and 15 minutes. Table 3-1 contains the P:L ratios and the cement setting properties of the 400 °C, 600 °C, and 800 °C heat treated powders. The 400 °C and 600 °C powders were perceived to be highly reactive, requiring large amounts of solution to wet the powder and create a paste. There was no P:L ratio tested for 400 °C and 600 °C powder which was perceived to be within the ideal parameters for a cement, namely forming a moldable paste with setting times of 10 and 15 minutes, as demonstrated in Figure 3-6. The

800 °C heat treated powder on the other hand, created a more viable cement, with P:L ratios of 1:1 creating a low viscosity paste with the most ideal set times (8:53 min and 14:47 min).

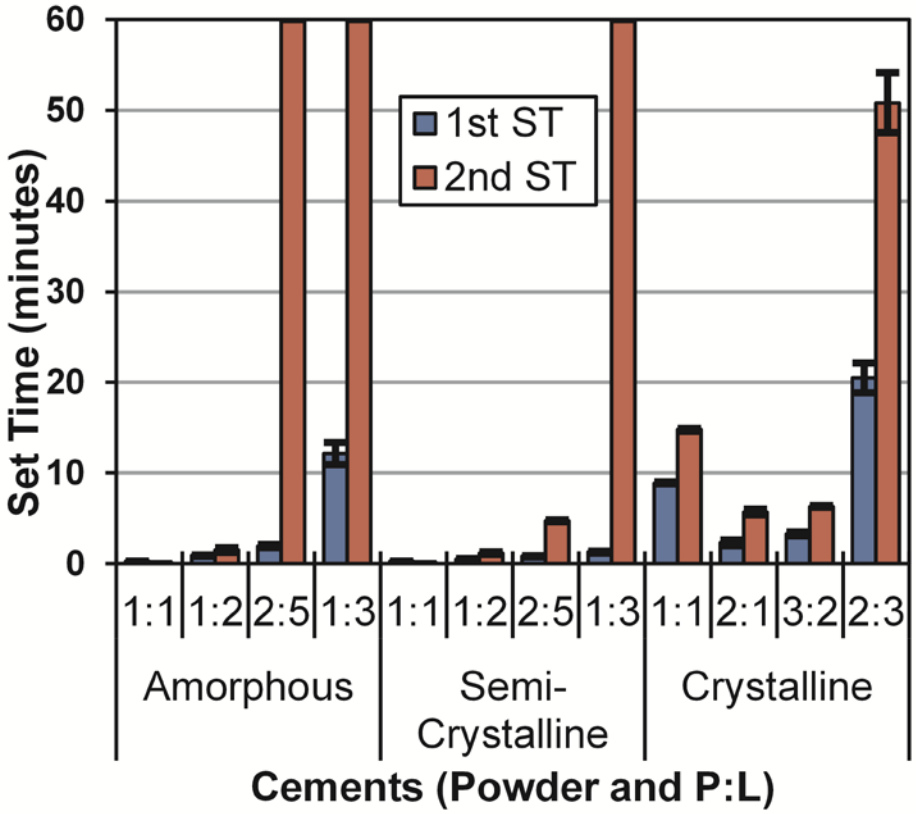

Figure 3-6 **Cement settings times as a function of powder crystallinity and powder-to-liquid ratios.**

Table 3-1 Cement handling properties and pH in saline solution.

Powder	P:L Ratio	Handling	pH in PBS
400°C	1:1	Reacts too quickly, cannot be stirred and molded to form a cement pellet	N/A
	1:2	Reacts very quickly, forms a dry, crumbled mixture which could be molded, but does not form a paste.	6.02
	2:5	Reacts quickly, but contains excess liquid to form a chunky paste that does not set.	5.99
	1:3	Reacts more slowly, forms a liquid paste that does not set.	5.96
600°C	1:1	Reacts too quickly, cannot be stirred and molded to form a cement pellet	6.87
	1:2	Reacts very quickly, forms a dry, crumbled mixture which could be molded, but does not form a paste.	6.35
	2:5	Reacts very quickly, forms a dry, crumbled mixture which could be molded, but does not form a paste.	6.27
	1:3	Reacts quickly, but contains excess liquid to form a chunky paste which does not set.	6.15
800°C	1:1	Forms a nice putty, with desirable set times.	7.47
	2:1	Mixture is dry, forms a crumbled material, but packable into a mold and sets too quickly.	7.58
	3:2	Mixture is dry, forms a dry putty, packable into a mold and sets too quickly.	7.77
	2:3	Forms a very thin putty, set time is too slow.	6.57

The high reactivity of the amorphous and semi-crystalline powders and the perceived increase from very short to long set times in these cements with increasing liquid content, is likely due to the complex interplay of the physicochemical properties of the powders and the resulting cements. TMP powders mixed with the reacting solution undergo a dissolution-precipitation type reaction to generate the cemented product, wherein the TMP is partially dissolved into the solution, and then re-precipitates the product phase(s). Hurle et al. have recently shown that, for calcium phosphate cements, the amount of amorphous calcium phosphate plays a strong role in increasing the reactivity of the cement [197]. The authors deduced that the high reactivity with amorphous calcium phosphate is due to high, instantaneous

dissolution of the amorphous phase into solution, resulting in supersaturated concentrations of ions in solution and earlier precipitation of calcium-deficient hydroxyapatite. Additionally, the authors determined that the cement crystallite size was reduced when cements were made with amorphous calcium phosphate, due to the high super-saturation conditions. Super-saturation increase the nucleation probability and number of crystal nucleation sites, ultimately resulting in more, smaller crystals [197]. It is possible that for the amorphous and semi-crystalline TMP cements considered herein for this study, similar conditions and reactivity can be expected, with the amorphous TMP content quickly dissolving, causing super-saturation of the dissolved ion in the reacting solution, leading to rapid precipitation of the crystals, giving the cements the less than 15 second setting times. With higher liquid volumes as expected, the second setting time increases to greater than 1 hour while the first set time remains less than 2 minutes. This is likely due to the sheer volume of excess phosphate liquid used that cannot be completely consumed in the ensuing cement reaction since the formation of the crystals and the crystal growth alone combined with the exothermic nature of the reaction cannot on its own lead to complete solid phase formation. Evaporation of the excess cementing liquid is required to bring the crystals into contact and giving the cement mechanical resilience.

3.3.3 Cement pH and Stability *In Vitro*

The pH of the cements generated with 400 °C and 600 °C heat treated TMP were lower than the cements from 800 °C TMP, also seen in Table 3-1. Additionally, the mechanical resilience of the cements from 400 °C and 600 °C heat treated TMP in PBS was quite low, demonstrated in Figure 3-7. These cements were observed to be soft or easily friable after incubation in the saline solution, showing mechanical strengths of less than 5 MPa for all the P:L

ratios, with strengths less than 2 MPa following PBS incubation. All the cement samples demonstrated a loss of mechanical resilience with PBS exposure. In contrast to this however, the 800 °C TMP cements demonstrated much higher strengths, above 20 MPa, with P:L ratios of at least 1:1. These cements showed marginal decrease in strength following PBS incubation, and moreover, remained significantly stronger than the native, as-reacted 400 °C and 600 °C TMP cements.

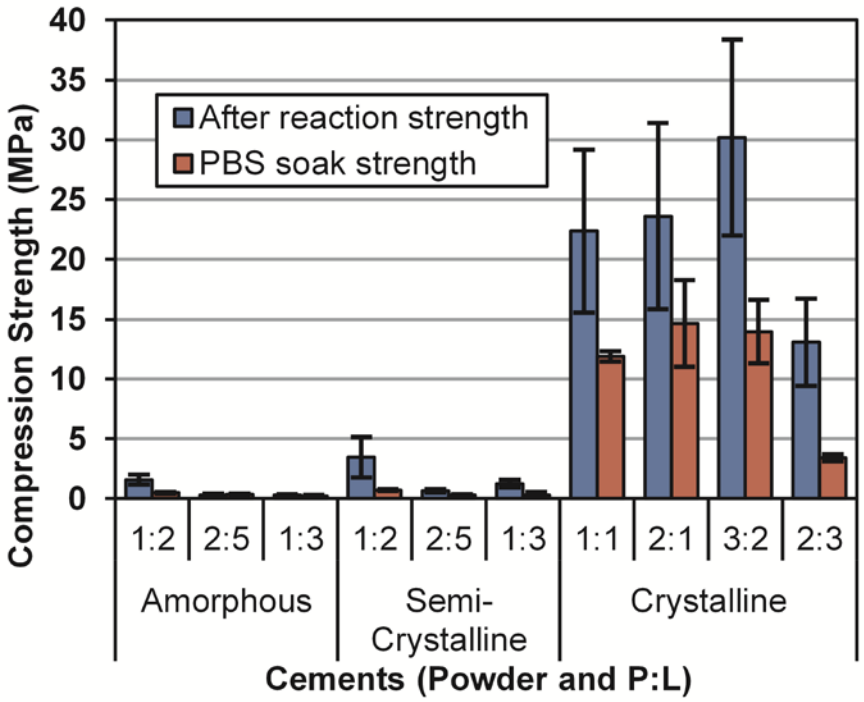

Figure 3-7 Uniaxial compression strength of cements.

In Figures 3-8 and 3-9 are seen the XRD results of the select 400 °C, 600 °C, and 800 °C heat treated TMP cements corresponding to P:L ratios of 1:2, 1:2 and 1:1 respectively, as generated (Figure 3-8) and after PBS soaking (Figure 3-9). The diffraction patterns of each cement after the final cement setting time shows the formation of, instead of the predicted $MgNH_4PO_4$ and $MgHPO_4$, an intermediate phase, $Mg_3(NH_4)_2H_4(PO_4)_4{\bullet}8H_2O$ (hannayite, ICCD

98-000-6099). The intensity of the peaks differs slightly between the starting TMP powders. In addition to this, the 800 °C precursor shows remaining $Mg_3(PO_4)_2$ while the 400 °C and, to a lesser extent the 600 °C heat treated TMP, show an underlying amorphous hump indicating remaining amorphous phase, most likely the unreacted amorphous TMP. Following incubation in PBS, all the cements transformed into the anticipated $MgNH_4PO_4 \cdot 6H_2O$ (ICCD 98-002-2086) and $MgHPO_4 \cdot 3H_2O$ (ICCD 00-035-0780), without any visible remaining crystalline or amorphous TMP, as shown in Figure 3-9. This likely indicates that the cements, after setting, are not fully reacted, and the exposure to PBS allows for further reaction of the unreacted amorphous TMP phase as well as the accompanying transformation of the less stable hannayite phase to form the desired $MgNH_4PO_4$ phase.

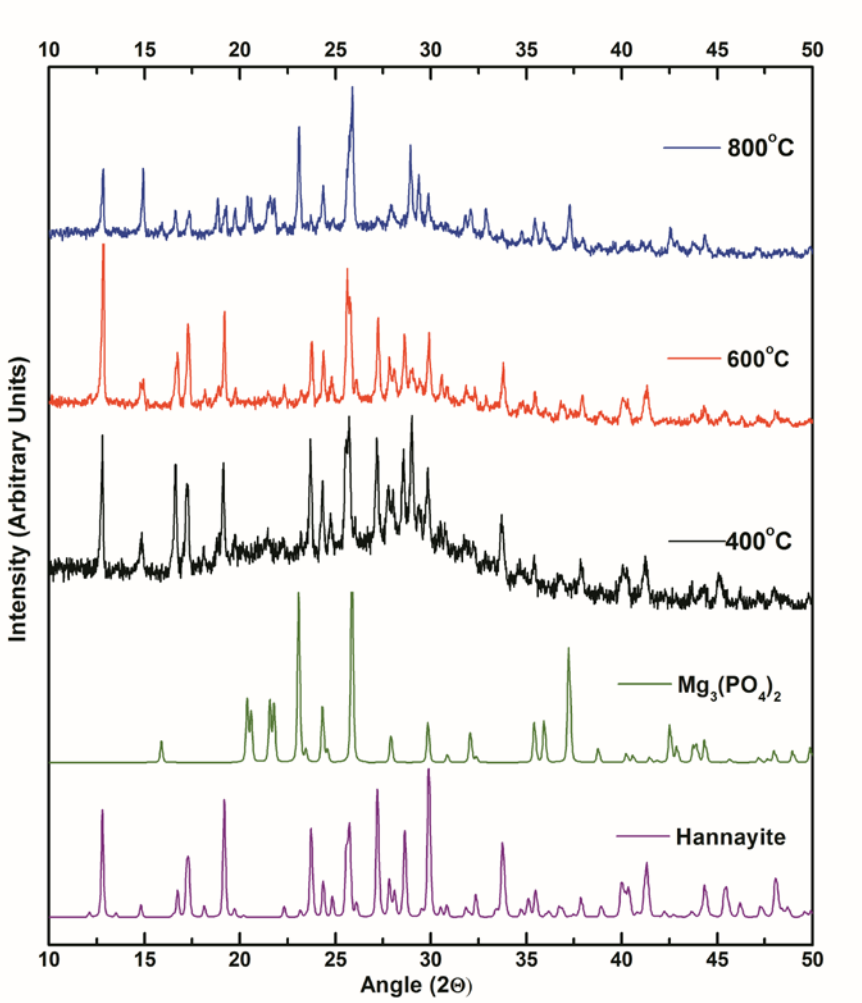

Figure 3-8 XRD spectra of 400 °C (P:L 1:2), 600 °C (P:L 1:2), and 800 °C cements (P:L 1:1), after completion of the cement reaction.

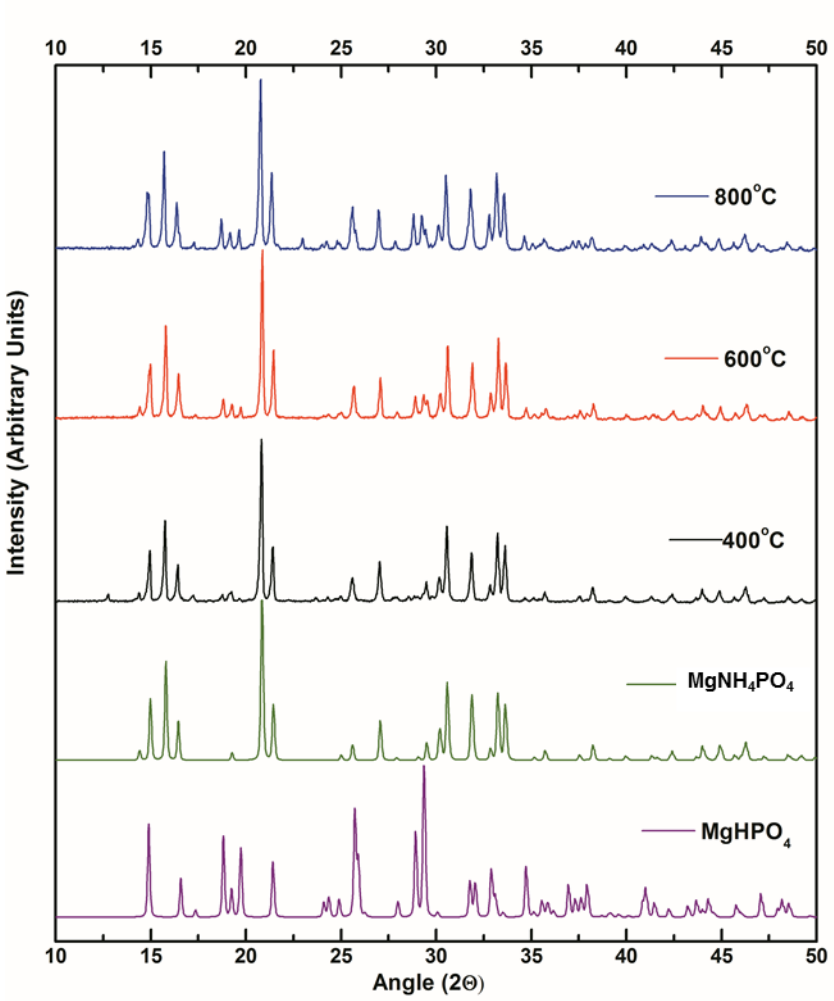

Figure 3-9 XRD spectra of 400 °C (P:L 1:2), 600 °C (P:L 1:2), and 800 °C cements (P:L 1:1) following 48hour PBS incubation.

In Figures 3-10 and 3-11 are shown the FTIR results of the select 400 °C, 600 °C, and 800 °C heat treated TMP precursor cements, corresponding to P:L ratios of 1:2, 1:2 and 1:1 respectively, as generated (Figure 3-10) and after PBS immersion (Figure 3-11). Similar to the powder FTIR spectra, the cement FTIR spectra show peaks surrounding the PO_4 vibration frequencies (1200 to 900 cm^{-1} and 700 to 450 cm^{-1}) and OH/HOH vibration regions, as well as NH_4 vibration bands. As seen in previous studies, the poorly defined bands under the broad adsorbed water hump correspond to OH stretching vibrations (3250 cm^{-1}) and NH_4 stretching

vibration (2900 cm^{-1}) [166, 198]. The bands between 1600 cm^{-1} and 1400 cm^{-1} are also corresponding to NH_4 vibrations, while the additional bands 650-750 cm-1 are attributed to H bonding of water [198]. Unlike the XRD, the FTIR analysis shows no significant change in the cements after incubation in PBS. This is likely due to the fact that FTIR assesses vibrational frequencies, and the P-O, H-O, and N-H bonds' vibrational frequencies which are inherently present in the structure and do not change significantly within the crystallographic and molecular structure.

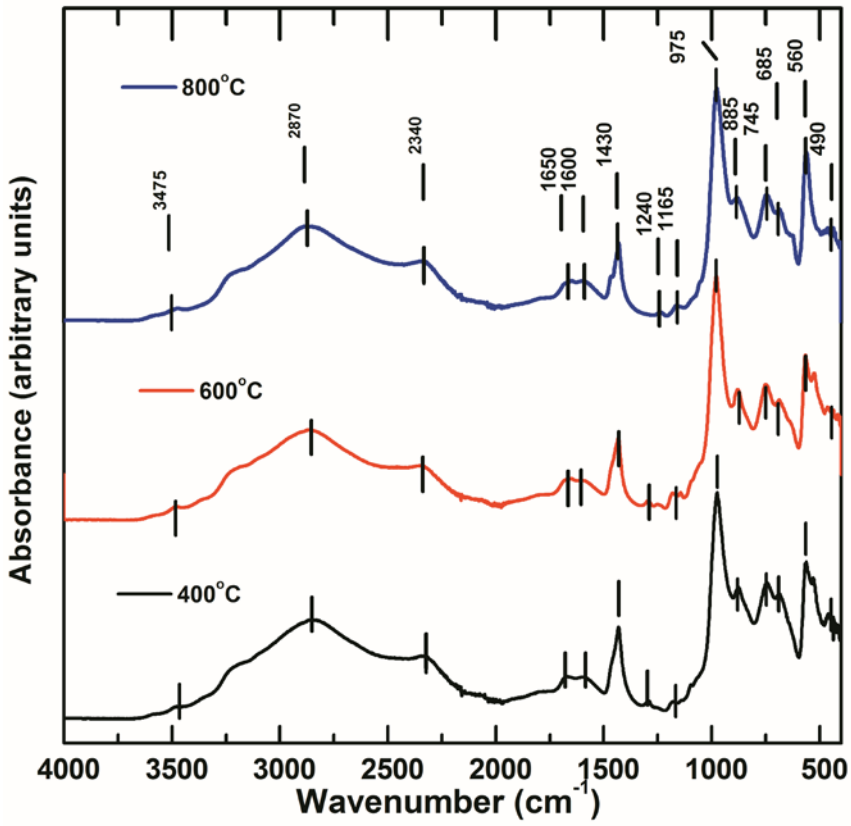

Figure 3-10 FTIR spectra of 400 °C (P:L 1:2), 600 °C (P:L 1:2), and 800 °C cements (P:L 1:1) after reaction completion.

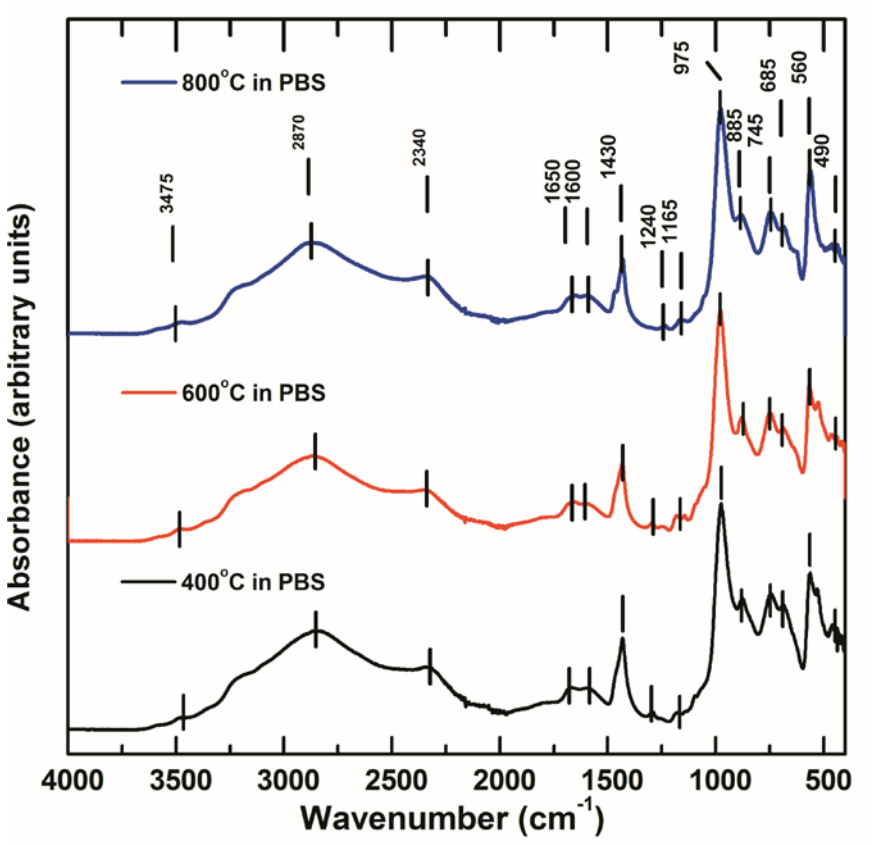

Figure 3-11 FTIR spectra of 400 °C (P:L 1:2), 600 °C (P:L 1:2), and 800 °C cements (P:L 1:1) following 48 hour PBS incubation.

Figure 3-12 displays the SEM images of the cements after setting and following PBS incubation. Both native (external) surface and fracture surface images are shown. It can be seen that that the internal and external surfaces of the 400 °C and 600 °C heat treated TMP precursor cements were perceived to be quite different following setting. The native, external surfaces of these cements appear featureless, with almost wave-like topology containing embedded crystallites at 1500x magnification particularly, for the 400 °C derived TMP cement, while the internal fracture surface displays more block shaped cuboidal shaped crystals. It is likely that this featureless surface of the cements is contributed by the amorphous content with precipitated extremely small crystallites embedded, as previously discussed, with no presence of any

noticeable crystalline facets emerging due to the rapid nature of the reaction. The fracture surface of the 400 °C and 600 °C TMP cements are similar to the 800 °C TMP cement, although the crystalline TMP appears to have resulted in a wider distribution of crystallite sizes in the cement structure. Unlike the amorphous and semi-crystalline TMP cements, the crystalline TMP resulted in cement with an external surface which is very similar to the internal fracture surface, showing block and elongated crystal growth, indicating a slower dissolution-precipitation reaction and more controlled crystal growth, as supported by the likely observed reaction rates. Following the incubation in PBS, the external morphology of the 400 °C and 600 °C heat treated TMP cements changed drastically, with the formation of a smaller cuboidal to spherical particles. These same shaped particles are seen in the fracture surface images as well. The 800 °C TMP cement appears to have undergone some formation of additional smaller particles at the expense of larger crystallites similar to Ostwald's ripening, but the change is however, not as drastic. The significant changes seen in the 400 °C and 600 °C heat treated TMP cements likely plays a role in the observed changes in the observed mechanical strength as well as the changes in XRD.

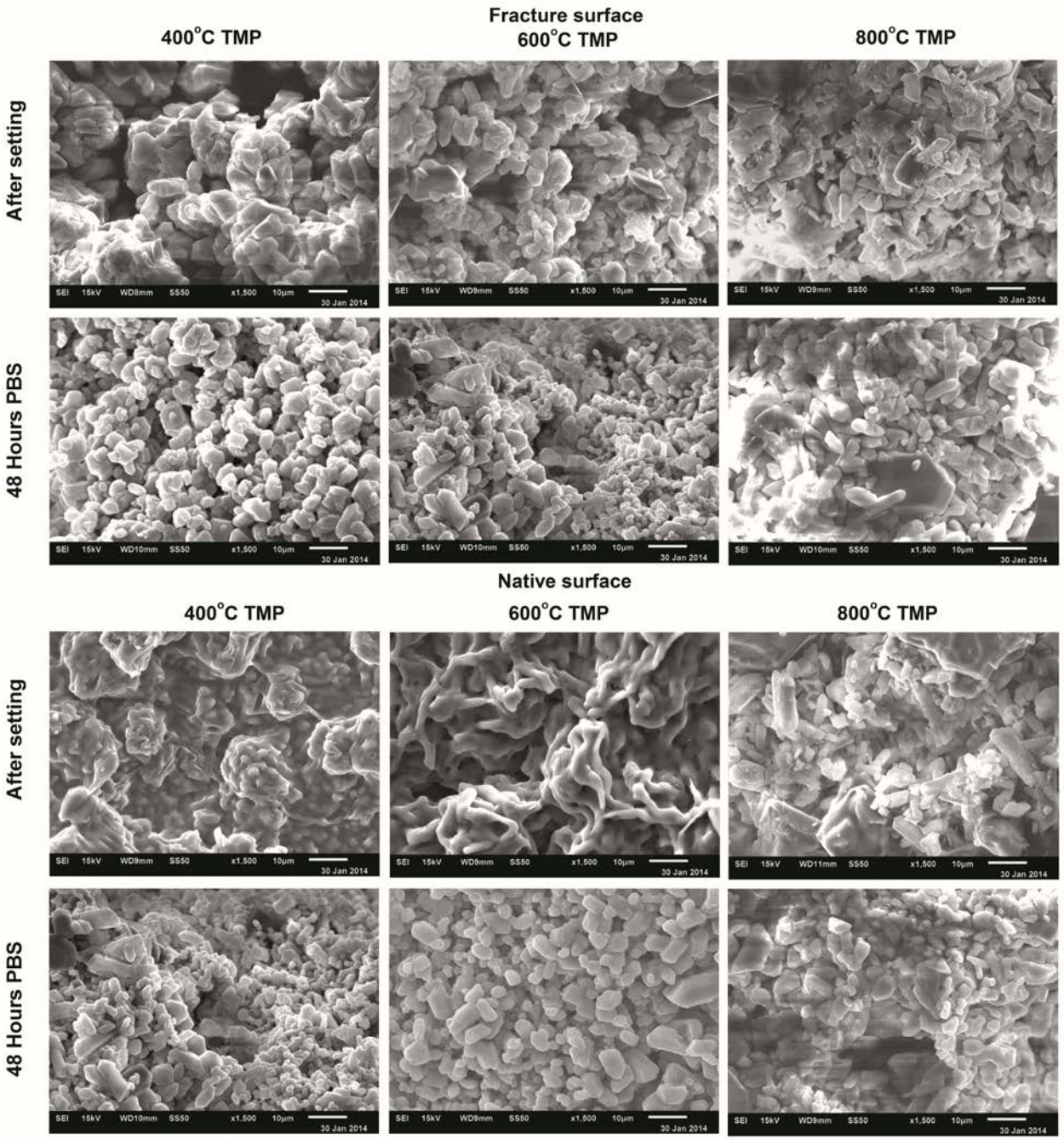

Figure 3-12 SEM images of 400 °C (P:L 1:2), 600 °C (P:L 1:2), and 800 °C cements (P:L 1:1). The top group of images shows the fracture surface of cements, after reaction completion and after PBS incubation, while the bottom group of images shows the native (outside) surface of the same cements, after reaction completion and after PBS incubation. (Scale bar: 10 µm)

3.3.4 Cement Instability

In all of these tests, it is not possible to separate the effect of powder crystallinity and the effects of powder surface area on the cement viability. However, in this study an attempt is made to correlate the physicochemical properties of the powders with the ensuing cementing reaction reactivity and the cement functionality. XRD results show similar final product formation for all the cement products while SEM and SSA results of reacted cements indicate differences in the cement crystallite size with the different starting precursor powders. Thus far, the mechanical stability of the cements appears to depend on the rate of initial cementing reaction and the cement bond formation, which in turn, appears to be controlled by the physicochemical properties of the tri-magnesium phosphate powder. Although there are advantages and desirable properties achievable in the amorphous precursor materials, viable cement could not be created within the tested parameters of this study. Recently Bhaduri et al. utilized microwave-assisted aqueous synthesis of amorphous tri-magnesium phosphate, as well as microwave synthesis of magnesium hydroxide cements to alter the exothermicity of the cements [39, 199]. These synthesis techniques may be a potential solution to combat the high reactivity of amorphous tri-magnesium phosphate powders. Additional methods to reduce the reactivity of the amorphous TMP in cementing reactions include reduction in specific surface area through thermal treatment as well as the formation of densified agglomerates, through pressing of dense pellets and subsequent pulverization of these pellets, as well as the utilization of reaction retardants. Although not reported here, the first and third alternatives have been recently attempted in our laboratory although yielding similar results with no significant improvements in the mechanical resilience of the cements. The densification and pulverization method as well as a microwave synthesis method are still to be explored. However, moving forward from the results presented

here, future studies under these parameters will focus on the fully crystalline, low surface area tri-magnesium phosphate cement due to the simplicity and the observed overall efficiency of the approach.

3.4 CONCLUSION

Crystalline, semi-crystalline and amorphous tri-magnesium phosphate powders were tested with a neutral 3 M ammonium phosphate solution in order to assess the cementing reactions of the various powders. Under the available parameters, the fully crystalline, low surface area 800 °C derived tri-magnesium phosphate powder resulted in cements which demonstrated much better workability, more neutral pH and higher strengths than the amorphous or semi-crystalline TMP derived cements. Further studies will thus focus on optimizing the cementing reaction, microstructure, and studying the cytocompatibility of this particular cement formulation which will be reported in the subsequent chapters to follow.

4.0 SPECIFIC AIM 3: ASSESSMENT OF THE EFFECT OF REACTING SOLUTION ON THE CEMENTING REACTION WITH TRIMAGNESIUM PHOSPHATE

4.1 INTRODUCTION

As discussed in Chapters 1 and 3, there is strong motivation to utilize magnesium phosphate cements for bone void filling and repair. While a large number of studies have focused on the use of ammonium phosphate salts reacting with TMP or MgO to yield the cement product, other reactants may also be explored. Monopotassium hydrogen phosphate (KH_2PO_4) has been used as the reacting salt for the Osteocrete^{TM} formulation and phosphoric acid is also occasionally employed [79, 83, 105, 146]. Mestres et al have utilized monosodium hydrogen phosphate in antibacterial cement formulations [28, 29, 38]. Similarly, the use of phosphate solutions particularly, dilute sodium phosphate solutions are frequently employed in calcium phosphate cement generation [35].

While magnesium and phosphorous are recognized as necessary to healthy bone development and maintenance, the role or implications of other ions such as sodium, potassium and ammonium are less understood. Although high levels of sodium intake are implicated in low bone density and osteoporosis, both sodium and potassium have physician recommended dosage intakes which can be found stored in low levels in mature bone [200]. Furthermore, it is recommended that an individual consume 1500mg of sodium, 4700mg of potassium and 420 mg

of magnesium on a daily basis, indicating systemic toxicity resulting from cement implants would be unlikely [201]. Localized toxicity at the site of the implant may still be a concern. Dietary potassium has been found to modulate the interaction of interstitial fluid surrounding bone mineral [202]. Some researchers have observed that an increase in dietary ammonium sulfate improved bone phosphate content in calves while others observed decreased bone density when diets were supplemented with ammonium chloride. However, in either of these cases the bone metabolic balance is tied to acid/base balance within the body and is not directly tied to the presence of ammonium ion [203, 204]. Ammonium ion is routinely cleared from the body through the urea cycle [205]. Thus the utilization of any of these ions within a cementing reaction is not anticipated to cause significant negative effects on the biocompatibility of the cement product.

The goal of this chapter is thus to assess the effect of various cement reacting solutions comprising potassium phosphate, sodium phosphate and ammonium phosphate with the starting solid reacting precursor of crystalline trimagnesium phosphate on the cement forming reactions. Although several authors have utilized one or more of these salts and the use of solutions is not common, direct comparisons of all three types of salts have not been evaluated. While in Chapter 3 the ammonium phosphate solution resulted in an encouraging cement product, cements resulting from potassium or sodium phosphate solutions may be more desirable as sodium and potassium ions are necessary for numerous biological processes while ammonium ions are merely a waste product to be cleared by the body. As in Chapter 3, neutral pH solutions of these salts will be created through a balanced use of monoatomic and diatomic salts. By maintaining a neutral pH of the reacting solution and in the final cement product, the opportunity

exists to utilize the solutions directly for drug or biologic delivery as well as attempt the incorporation of cells for multifunctional scaffold delivery in future studies.

4.2 MATERIALS AND METHODS

4.2.1 Cement Preparation

Crystalline $Mg_3(PO_4)_2$ was synthesized according to the protocol described in Chapter 2. The powder was thermally treated to 800 °C for 6 hours to ensure a specific surface area (SSA) of approximately 1.0 m^2/g, as described in Chapter 3.

The TMP powder was mixed with pH 7.0 solutions of ammonium phosphate, sodium phosphate or potassium phosphate, at a 3 M concentration. Three different solution embodiments were tested. The solutions were based on potassium, sodium and ammonium phosphate salts. The ratio of mono-atomic ammonium, sodium or potassium to diatomic ammonium, sodium or potassium soluble phosphate salts is determined such that the solution is at pH 7.0, as described for the ammonium solution in Chapter 3.

In the simplest form, the theoretical reactions employed for the cementing reactions are identical to Equation 3-1 with the sodium and potassium phosphate analogs:

Equation 4-1

$$Mg_3(PO_4)_2 + (Na)_x(H)_yPO_4 = x\bullet MgNaPO_4 + y\bullet MgHPO_4$$

Equation 4-2

$$Mg_3(PO_4)_2 + (K)_x(H)_yPO_4 = x\bullet MgKPO_4 + y\bullet MgHPO_4$$

where X and Y are based on the mole balance of the monobasic and dibasic ammonium phosphate salts in solution discussed in Chapter 3. For example, the ratio of monobasic to dibasic ammonium phosphate to yield neutral pH 3M solution is approximately 2:7 to 3:10 (range of 0.286-0.3) monobasic/dibasic, which would yield X and Y of approximately 23 and 16, respectively. Assuming perfect reaction, this would give final product of nearly 59 % $MgNH_4PO_4$ and 41 % $MgHPO_4$. For potassium phosphate, the salt ratio is 9:10, or 51 % $MgKPO_4$ and 49 % $MgHPO_4$, and for sodium phosphate the salt ratio is 2:5 monobasic to dibasic for 3M solutions, or 57 % $MgNaPO_4$ and 43 % $MgHPO_4$. These appropriate salt ratios were determined experimentally. The 3M sodium phosphate salt solution is super-saturated at room temperature, and was stored at 37 °C prior to testing to ensure accurate concentrations during cement formation. For simplicity, these solutions are referred to as NH_4H (ammonium), NaH (sodium), and KH (potassium) solution during subsequent discussion and in all the figures.

Cements were synthesized as in Chapter 3 as mentioned above. The powders were mixed with the phosphate solution at a variety of powder-to-liquid ratios (P:L), and thus the effect of the powder state on the cement reactivity was assessed. As in Chapter 3, with each of the tested P:L ratios, a molar ratio of magnesium phosphate to phosphate solution greater than one is always maintained to force the forward reaction towards completion and consumption of TMP. Additional details such as the powder-to-liquid ratio is expressly stated.

4.2.2 Cement Characterization

The setting times of the cement pastes were determined with the Gilmore needle test following the ASTM standard C266-13 at room temperature, as previously described. Crystalline tri-magnesium phosphate powders were mixed with the specified volumes of potassium, sodium

and ammonium solution and stirred for 60 seconds before filling into 10 mm circular molds. The handling characteristics will be qualitatively assessed based on consistency and injectability. The set cements were stored overnight at 37°C before subsequent testing. True density, apparent density and porosity as well as XRD analysis were used to assess the cements following completion of the reaction, utilizing the same procedures and equipment specified above. Pellets of the reacted cement were soaked in 2 ml of phosphate buffered saline (PBS) for 48 hours at 37°C and the pH was systematically recorded. Density and XRD analyses were again completed on the cements following PBS incubation to determine if any changes occurred due to the saline incubation.

The % porosity of cements following PBS incubation was determined according to Equation 4-3.

Equation 4-3

$$\% \text{ porosity} = 1 - \rho_A/\rho_T$$

The true density (ρ_T) was measured using helium pycnometry (AccuPyc II 1340, Micrometrics) and the apparent density (ρ_A) was determined through Equation 4-4.

Equation 4-4

$$\rho_A = \text{weight}/(\pi r^2 h)$$

4.3 RESULTS AND DISCUSSION

4.3.1 Initial Cement Characterization

Crystalline $Mg_3(PO_4)_2$ was created according the protocol described above and subsequently mixed with 3.0 M reacting solutions of ammonium, potassium or sodium phosphate at Ph 7.0. A variety of powder-to-liquid (P:L)ratios were evaluated to determine the optimal solution content for each cement formulation. In Figure 4-1 is displayed the first and second setting times of the cements with varying powder-to-liquid ratios tested. Corresponding to this in Table 4-1 are the descriptive assessment of the putty handling characteristics during cement creation and strength after setting and drying are complete. It was observed, as in Chapter 3 that varying the P:L ratios of ammonium phosphate solution results in significant control over the setting time of the magnesium ammonium cement. The setting times of the 3M 1:1 ammonium solution are quite similar to those measured for the same embodiment, though with higher variation, indicating good reliability with the cement generation.

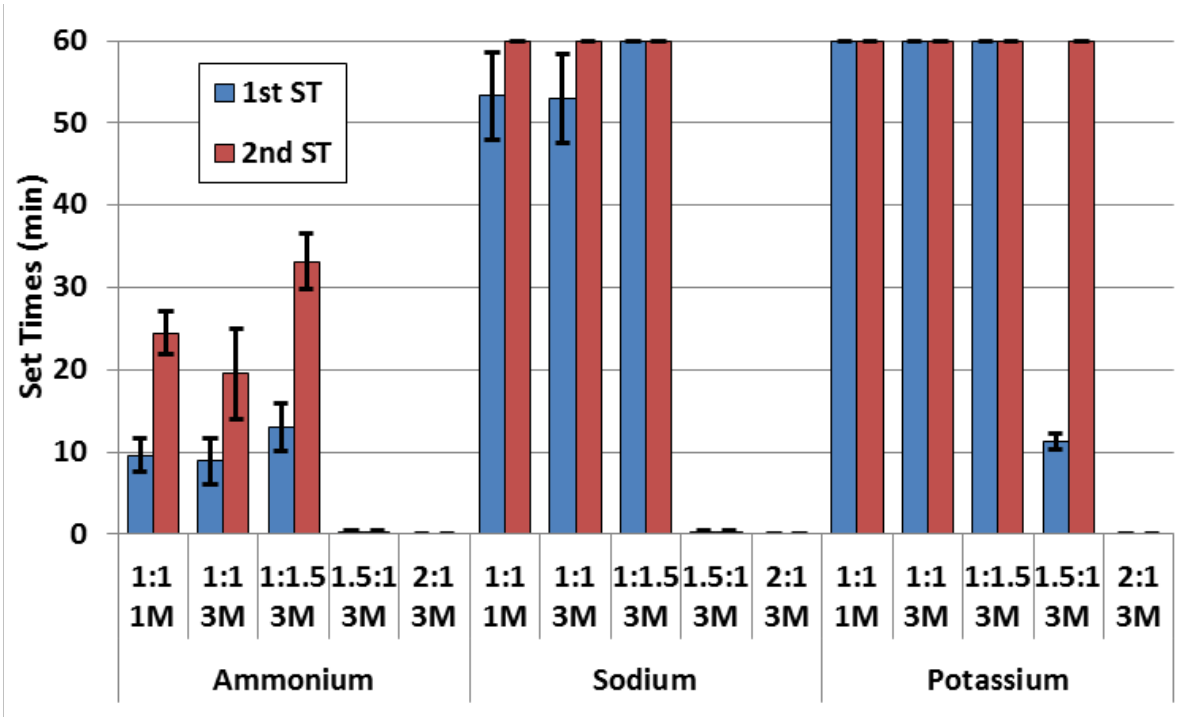

Figure 4-1 Setting times of cements varying with setting solution and powder-to-liquid ratios.

However, the same control over setting time is not observed with the sodium and potassium phosphate solutions. The setting times are exaggerated, displaying no 'set' time at all or set times that are far greater than one hour at room temperature. Similar results were observed when testing at 37 °C (data not shown). Following overnight incubation at 37 °C, cements were removed from the molds and the durability of the cement product was determined. For most cements made with the ammonium phosphate solutions, a durable product resulted.

In comparison, the majority of the cements made with sodium and potassium containing cement reacting solutions were perceived to be not strong, often cracking or crumbling apart during this process. Reducing the solution concentration to 1 M slowed the 2nd set time of the cement made with the ammonium phosphate solutions only slightly compared to the P:L of 1:1 for 3M concentration, but did not appear to affect the setting time of the cements made with

sodium or potassium phosphate solutions. The lower concentration however, resulted in slightly less durable products after drying.

Table 4-1 Handling of cement putties and durability after drying

Solution	P:L	Handling	Durability
1M NH_4H	1:1	Good putty viscosity	Durable, did not crumble when handled
3M NH_4H	1:1	Good putty viscosity	Durable
	1:1.5	Liquid, low viscosity	Durable, did not crumble when handled
	1.5:1	Viscosity high, not flowable, must be pressed into mold	Durable, did not crumble when handled
	2:1	Too dry, does not form putty	Crumbles when handled
1M NaH	1:1	Liquid, low viscosity	Breaks easily when handled
3M NaH	1:1	Viscosity is good, putty-like.	Mostly holds together, edges may crumble
	1:1.5	Liquid, very low viscosity	Breaks easily when handled
	1.5:1	Viscosity high, not flowable, must be pressed into mold	Breaks easily when handled
	2:1	Too dry, does not form putty	Crumbles when handled
1M KH	1:1	Liquid, very low viscosity	Breaks easily when handled
3M KH	1:1	Viscosity like a putty	Mostly holds together
	1:1.5	Liquid, very low viscosity	Breaks easily when handled
	1.5:1	Viscosity high, not flowable, must be pressed into mold	Breaks easily when handled
	2:1	Too dry, does not form putty	Crumbles when handled

Resulting cement pellets or pieces were incubated in PBS for up to 48 hours at 37 °C. The pH was recorded at 24 hours and the PBS was replaced following which the pH was measured again at 48 hours, the results of which can be seen in Figure 4-2. For the ammonium phosphate derived cements at a concentration of 3M, the pH after 24 hours was slightly acidic (6.6-7.0) but neutralized (7.4-7.6) following replenishing of PBS and additional incubation time of 48h. High liquid content, at P:L of 1:1.5, resulted in more acidic cements (6.6-6.7) while

lower liquid content, at P:L ratios of 1.5:1 and 2:1, resulted in more neutral cements (6.9-7.0). As seen in the previous chapter, use of higher liquid contents results in more struvite formation than newberyite, likely leaving unreacted hydrogen ions which serve to lower the media pH initially. Reducing the solution concentration to 1 M resulted in a more basic pH (7.6) at both 24 and 48 hours of incubation. Conversely, the pH of all sodium and potassium derived cement products was slightly basic, generally 7.5-7.7, at both 24 and 48 hour PBS incubation for the 1 M 1:1 cements as well as the 3 M cements at every P:L ratio tested. The sodium phosphate derived cements were very slightly more basic at 24 hours than at 48 hours while the potassium phosphate solution based cements were slightly more basic at 48 hours than 24 hours. Following incubation in PBS, the more durable sodium and potassium phosphate derived cements were however, observed to break into pieces.

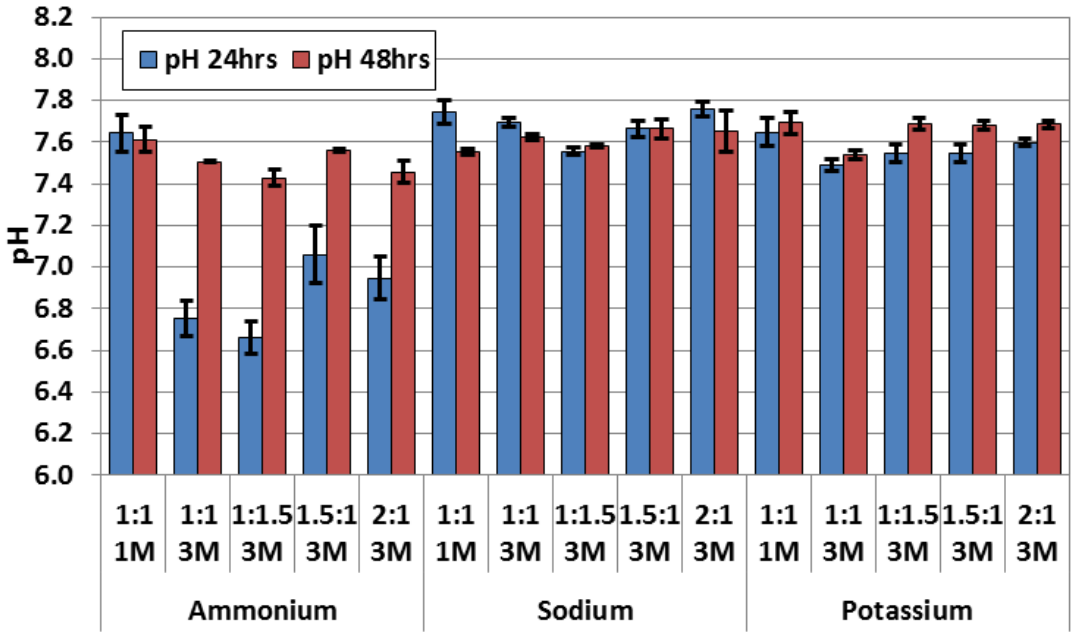

Figure 4-2 pH of cements following 24 and 48 hours incubated in PBS at 37 °C.

As the cements created with 3 M solutions at a 1:1 powder-to-liquid ratio resulted in a moderately durable product for all three solutions, these samples were further tested to examine the materials properties of the resulting cement products. In Figure 4-3 is displayed the true density (a), apparent density (b) measurements and calculated porosity (c) of these cement embodiments. The true density measurements are of n=1 and the true density and porosity measurements are of n=2. The true density measurements indicate that the ammonium phosphate derived cement has a similar true density in the as generated form and after 48 hours incubation in PBS with a value of 2.1 g/cm^3, while the sodium and potassium derived cements undergo a marked decrease in true density following PBS incubation with density values reducing from 2.6 to 2.0 g/cm^3 for the sodium phosphate containing cement and 2.5 to 2.2 g/cm^3 for the potassium phosphate derived cement.

Apparent density of the as generated cements was much higher for the ammonium phosphate derived cements (1.55 g/cm^3) than potassium phosphate containing cements (1.40 g/cm^3), which were higher still than the sodium phosphate containing cements (1.05 g/cm^3). Following incubation in PBS the apparent density of the ammonium and potassium phosphate containing cements decreases (1.40 g/cm^3 and 1.10 g/cm^3) but that of sodium phosphate containing cements remains the same (1.05 g/cm^3).

Porosity calculations indicate the ammonium phosphate derived cements have much lower porosity than the sodium or potassium phosphate solution derived cements, both as generated and after PBS incubation. The ammonium and potassium phosphate derived cements had marginal increases in porosity following PBS incubation, 30 to 38% and 43 to 50% respectively, while the sodium phosphate derived cement had a large decrease in porosity from 60 to 46%.

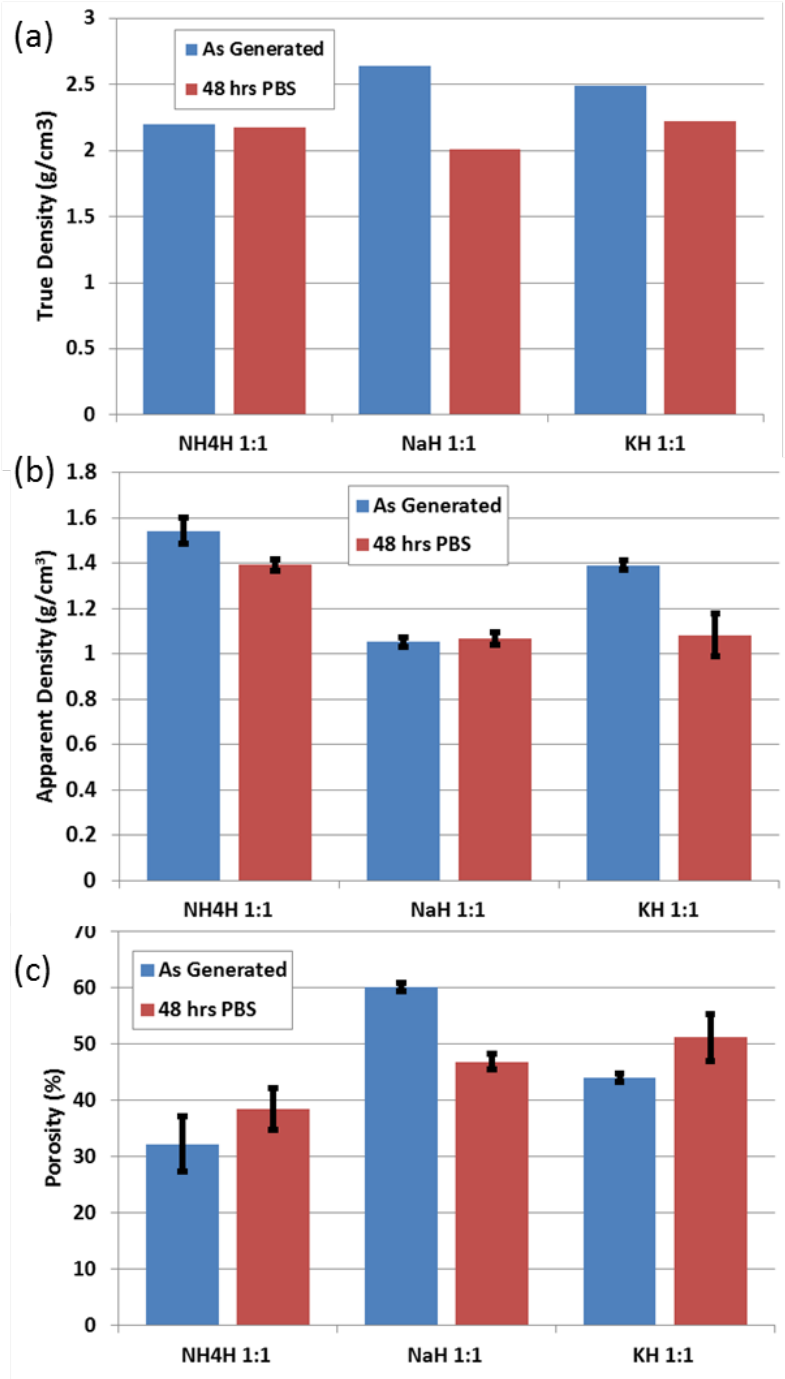

Figure 4-3 True density, apparent density and porosity measurements of cements as generated and after 48 hours incubated PBS at 37 °C.

X-ray diffraction measurements and phase identification of all the cements in both, as generated and after PBS incubation can be seen in Figure 4-4. As seen in Chapter 3, the ammonium phosphate derived cement is initially comprised of the anticipated $MgNH_4PO_4•6H_2O$ (c) and $MgHPO_4•3H_2O$ (d) as well as unreacted $Mg_3(PO_4)_2$ (a) and the same temporary phase (b) $Mg_3(NH_4)_2H_4(PO_4)_4•8H_2O$, and following incubation, the $MgNH_4PO_4•6H_2O$ (c) phase is the dominant one along with $MgHPO_4•3H_2O$ (d) and a small amount of $Mg_3(PO_4)_2$ (a). The as generated sodium phosphate made cement displaces mostly $Mg_3(PO_4)_2$ with a small amount of (e) $MgNa_3H(PO_4)_2$ (ICCD Card 00-035-0811) and (f) $Na_{1.05}Mg_{3.96}(PO_4)_3$ (ICCD 00-054-0072). Following PBS incubation the diffraction pattern is quite similar, with the addition of $MgHPO_4•3H_2O$ (d) and a slight reduction in maximum peak high of (e) and (f). Similarly, potassium phosphate derived cements show a majority of unreacted $Mg_3(PO_4)_2$ (a). The as generated potassium phosphate containing cement also has small amounts of $MgHPO_4•3H_2O$ (d), (g) $KMgPO_4·6H_2O$ (ICCD 00-035-0812), (h) $Mg_3(PO_4)_2·8H_2O$ (ICCD 00-033-0878) and (k) KH_2PO_4 (ICCD 00-031-1030). Following PBS incubation the soluble KH_2PO_4 and the hydrated trimagnesium phosphate (h) are completely removed following dissolution. In addition to the unreacted trimagnesium phosphate (a) in the final structure are $K_2Mg(PO_3)_4$ (I, ICCD 00-024-0877) (i) and the anticipated phases $KMgPO_4·6H_2O$ (g) and $MgHPO_4•3H_2O$ (d).

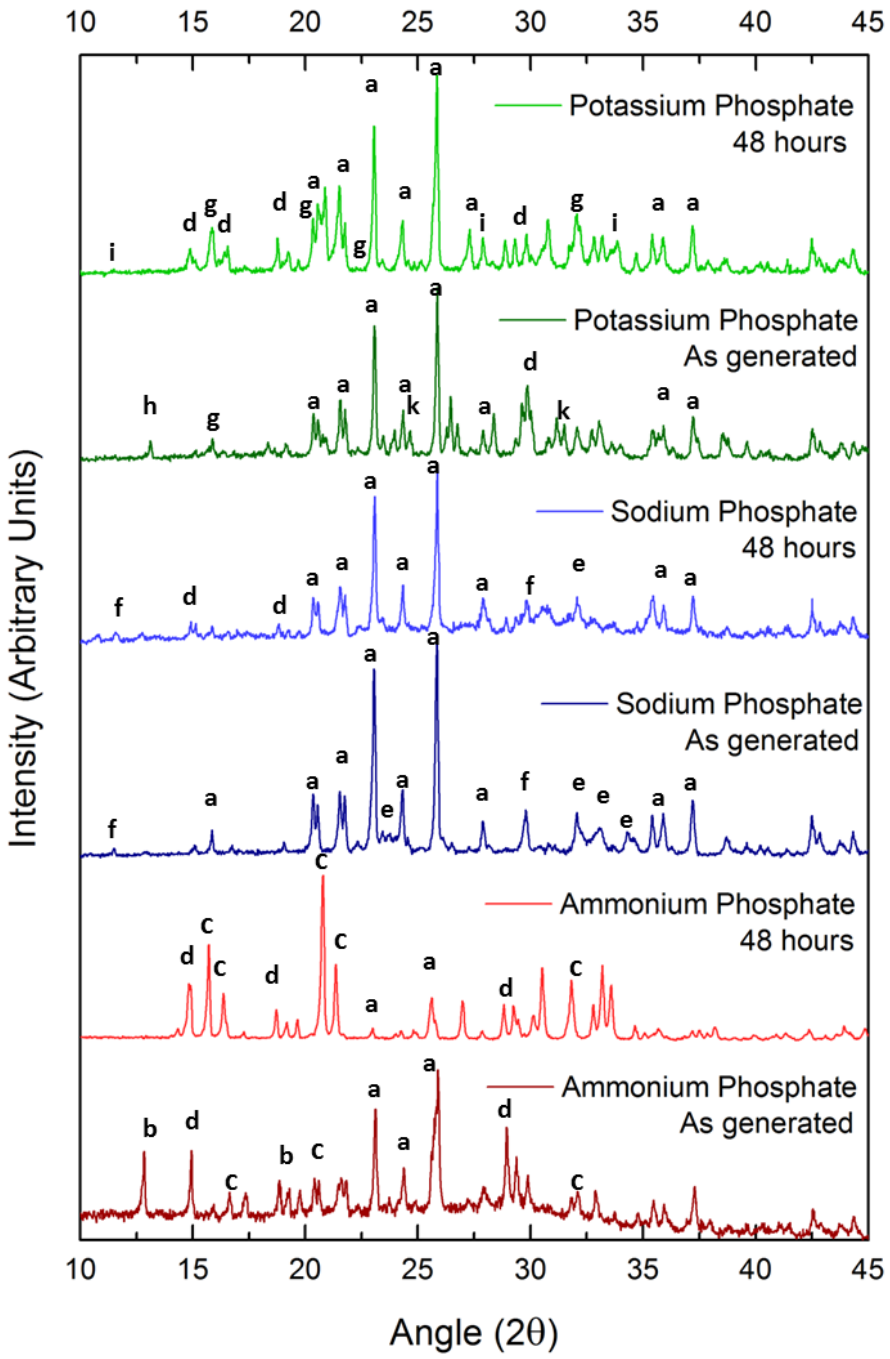

Figure 4-4 XRD spectra of cements as generated and after 48 hours of incubation in PBS at 37 °C Phases are (a) $Mg_3(PO_4)_2$, (b) $Mg_3(NH_4)_2H_4(PO_4)_4{\cdot}8H_2O$, (c) $MgNH_4PO_4{\cdot}6H_2O$ (d) $MgHPO_4{\cdot}3H_2O$ (e) $MgNa_3H(PO_4)_2$, (f) $Na_{1.05}Mg_{3.96}(PO_4)_3$, (g) $KMgPO_4{\cdot}6H_2O$, (h) $Mg_3(PO_4)_2{\cdot}8H_2O$, (i) $K_2Mg(PO_3)_4$, and (k) KH_2PO_4.

The density and x-ray diffraction data discussed above can provide some inferences as to why the setting times were not well controlled and consequently, the cement products were mechanically inferior for the sodium and potassium phosphate derived cements. When compared to the ammonium phosphate cementing reaction, the reaction for the sodium and potassium phosphate cements does not proceed nearly as far towards completion, indicated by the extremely high levels of unreacted TMP remaining in the cement products indicated by the XRD data. A change in morality or the liquid content also does not appear to significantly alter this fact. In actuality, at high liquid contents these cements tend to react to an even smaller degree resulting in a cement that readily falls apart. As a result, the rigid product formed can be attributed as much to the effect of drying as it is to any cementing reaction. Cements with lower liquid content, ammonium phosphate included, contain too little water to form a moldable product. It was not possible, for the sodium and potassium phosphate based cements to find a liquid ratio which resulted in a clinically relevant setting time in part because, under the conditions tested, the product is not ‘setting’ through the completion of the necessary dissolution/precipitation/crystal growth mechanism characteristic of cementing reactions. The high true density, low apparent density and high porosity observed for the sodium and potassium phosphate based cements can then be attributed to the same lack of incomplete cementing reaction. The higher true density results from the higher true densities of unreacted salts when compared to hydrated phosphate phases present in the ammonium phosphate product. Lower apparent density and higher porosity result from the drying and accompanying loss of water from the putty, instead of incorporation of the water into the structure. This leaves poorly reacted cement product and poorly adhered unreacted TMP powder and salt crystals remaining in the

structure. The systems nevertheless warrant more attention which can be the subject of future research.

4.3.2 Alternative Strategies

A variety of additional methods beyond altering the P:L can be used in order to accelerate the cementing reaction, including increasing the reacting salt concentration, changing the pH and adding an accelerant. In order to determine if the neutral pH of the solution reduced the reaction rate, similar 3 M solutions were created with only monoatomic ammonium or diatomic ammonium salts. The cement setting times with this series of 6 solutions at two different P:L can be found in Figure 4-5. For the ammonium phosphate solutions, the diatomic ammonium salt solution slowed the cementing reaction from 25 min 1^{st} setting time (ST) at P:L of 1:1 versus 9 min at P:L of 2:1. The monoatomic ammonium salt solution decreased the reaction time to 4 min. The opposite was seen with the sodium solutions. The diatomic sodium phosphate solution reduced the first setting time to 8 min at P:L of 1:1 while the monoatomic sodium phosphate solution increased the 1^{st} ST at 1:1 to beyond 60 min. The use of monoatomic or diatomic potassium salt did not serve to reduce the 1^{st} ST below 60 min. In all cases increasing the P:L to 2:1 reduced the setting time as in Figure 4-1. Cements were allowed to dry at 37 °C before removing them from the molds. Although the diatomic sodium phosphate solution reduced the setting time to within a reasonable range, the resulting pellet was not found to be durable similar to the successful ammonium phosphate solution embodiments comprising P:L of 2:1 and 1:1 when removed from the mold.

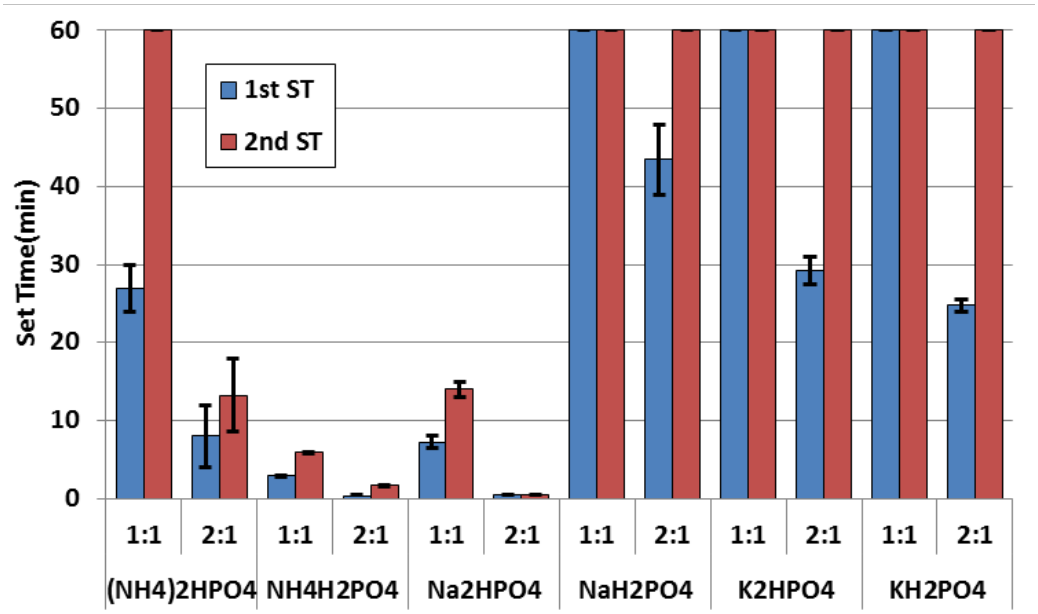

Figure 4-5 Cement setting times of 3M monoatomic or diatomic hydrogen salt solutions at two different P:L ratios of 1:1 and 2:1.

The inclusion of some form of amorphous calcium phosphate is frequently used to accelerate the reaction of CPCs and reduce the setting time [197]. As discussed in Chapter 3, amorphous phases are typically expected to react more quickly than crystalline analogs. For this reason, the testing methodology from Chapter 3 was revisited, utilizing amorphous TMP reacting with 3M pH 7.0 sodium and potassium solutions. Although this strategy did not yield durable cements with the ammonium phosphate solution, the slower reaction rate of the sodium and potassium cements reopens the possibility with these solutions. Similar to Chapter 3, powder-to-liquid ratios less than 1:1 were required to create a liquid putty due to the high surface area of the amorphous powder. While the putty slowly dried and satisfied the mechanical resilience for the 1st ST, these formulations did not result in the 2nd ST meeting the mechanical requirement for a hard and set product after 60 minutes. The formulation also failed to provide an acceptable cement product even after extended incubation in PBS at 37 °C for 48 hours.

A final strategy to increase the reaction rate of the cement, or induce other precipitation-controlled reactions, is to use a 'seed' phase. In this strategy, a portion of the product phase is included in the initial formulation as a 'seed' for the reacting material to grow a new product phase on the starting initial precursor. This strategy overcomes nucleation kinetic barrier, the greatest energy barrier to crystal growth in solution, and is frequently employed in a wide variety of industrial practices, including with struvite synthesis [206-208].

To create seed crystals, 1 gram of crystalline TMP was immersed in 10 mL of each of the three 3 M, pH 7.0 reacting solutions comprising of the desired mixture of diatomic and monoatomic ammonium sodium and potassium phosphate as described earlier. The extreme excess of the reacting salt should drive the chemical reaction towards completion. The highest possible salt concentration is desired for the same reason, however the sodium solution is super-saturated at room temperature at the 3 M concentration, thus higher concentrations could not be explored. Mixtures were incubated at 37 °C for 48 hours, stirring occasionally. At this point, the excess solution was decanted and the resulting powder was rinsed with DI water, then acetone and dried at 70 °C overnight. The powders were then analyzed through XRD to confirm the presence of the anticipated product phases: $MgNH_4PO_4$, $MgHPO_4$, $MgKPO_4$ and $MgNaPO_4$ or hydrated analogs of these phases. The XRD spectra of the seed powders as well as the spectra of matched phases can be found in Figure 4-6. Results indicate that the ammonium (NH_4H) solution reacted completely to form struvite over the more soluble newberyite. In stark contrast to this, the spectra of the sodium (NaH) and potassium (KH) seed powders are nearly identical to the unreacted TMP powder, indicating that even with extreme excess of the reacting solution, the proposed cementing reaction is not proceeding under the given conditions.

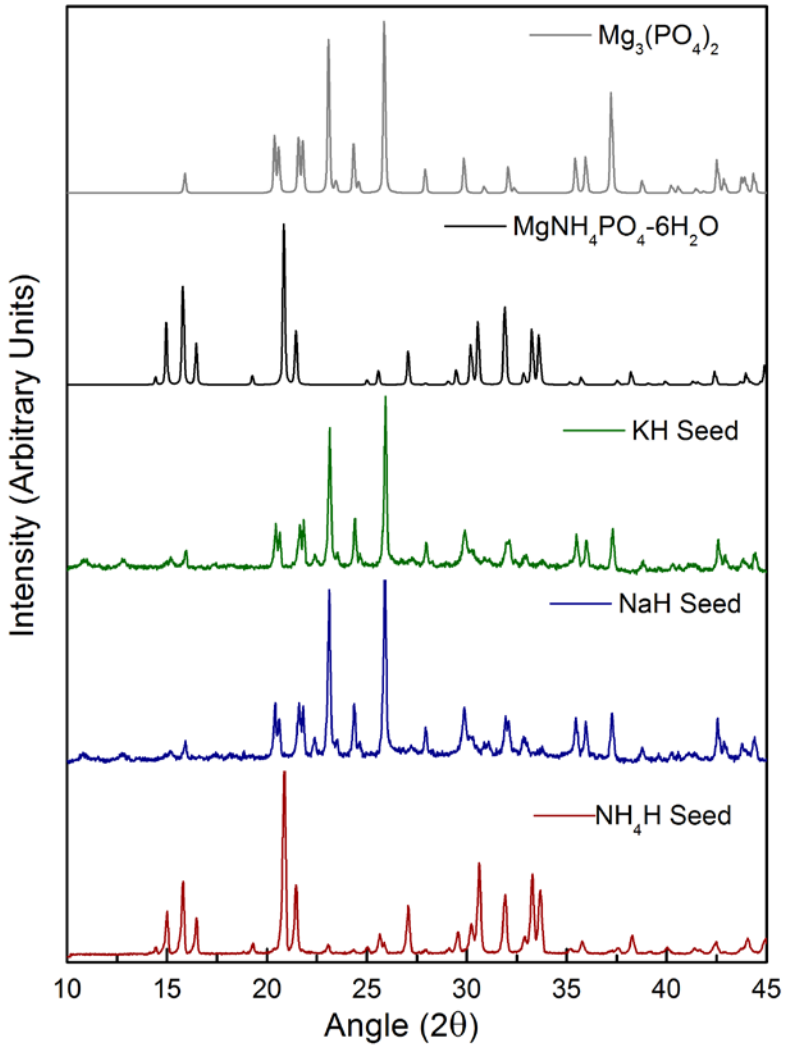

Figure 4-6 X-ray diffraction patters of generated seed crystals from ammonium, potassium and sodium solutions and matching phase spectra, $Mg_3(PO_4)_2$ and $MgNH_4PO_4 \cdot 6H_2O$.

Testing results of the numerous cement embodiments explored with sodium and potassium phosphate solutions clearly indicate that, while hypothetically possible, the driving force for these reactions is extremely weak. Numerous other researchers have successfully explored magnesium phosphate cement formulations with potassium and sodium phosphate reacting salts. Mestres et al have repeatedly shown a magnesium sodium phosphate cement formulation to be fast setting, strong and antibacterial while BSI Inc. has patented and is taking

into clinic the Osteocrete™ magnesium potassium phosphate cement formulation [28, 29, 38, 66, 67, 73]. The difference however between the cement formulations with these researchers and the cement studied here is with the magnesium source: both Mestres and the Osteocrete™ formulation use MgO while this study is based on the use of $Mg_3(PO_4)_2$ that is likely more stable requiring further activation. No studies could be found successfully using TMP and sodium or potassium phosphate salts or solutions. It is likely that the activation energy for the reactions proposed in Equations 4-1 and 4-2 is too high to ensure completion of the reaction with regularity.

4.4 CONCLUSIONS

Solutions of sodium phosphate, potassium phosphate and ammonium phosphate mixtures of the monoatomic and diatomic phosphate forms were created at a 3 M concentration and neutral pH and the cementing reaction of these solutions was tested with crystalline tri-magnesium phosphate powder. Under the tested parameters, the ammonium phosphate solution, as previously demonstrated, created a hard cement construct under clinically appropriate setting times. The sodium and potassium phosphate solutions on the other hand, did not obtain clinically appropriate setting times under any tested solution volumes or P:L ratios. X-ray diffraction results indicate only low levels of cement product phases in the set cements, with a bulk of the unreacted tri-magnesium phosphate remaining. Due to this lack of reaction completion, cement constructs made with sodium and potassium phosphate solutions were not mechanically durable. Alternative strategies, including altering the solution concentration, solution pH and reacting salt, and utilization of amorphous tri-magnesium phosphate all of which unfortunately, did not result

in increasing the reaction rate or completion of the reaction. Further studies were thus focused on optimizing cement formulations from the ammonium phosphate solution embodiment.

5.0 SPECIFIC AIM 4: EVALUATION OF THE EFFECT OF MANNITOL POROGEN ADDITION ON A MAGNESIUM AMMONIUM PHOSPHATE CEMENT FORMULATION

5.1 INTRODUCTION

Porosity is widely regarded as a necessary parameter for the generation of functionally integrated scaffolds for tissue engineering, including hard tissue implants. Pore structure should be integrated in order to permit cellular infiltration and migration as well as provide mass transport for cellular nutrition. Methods typically utilized to generate porosity include the addition of salt or sugar crystals, the use of degradable fibers, utilization of 3D printing or the use of gases to generate pores [109, 111, 209-215]. The pores generated should be inter-connected with macropore sizes in the 100-600μm range [111, 216]. In particular, in ceramic systems, the porous structure negatively impacts the strength of the scaffold, and thus it is necessary to optimize the porosity while also maximizing the strength of the scaffold. With CPCs, researchers have explored the addition of water soluble mannitol sugar as a porogen. The addition of mannitol is known to increase the cement macroporosity and dissolution rates while also resulting in significant loss of mechanical strength [210, 211, 213, 217-220]. Importantly, the addition of the soluble mannitol does not affect the cytocompatibility of the cement scaffolds.

Due to the hierarchical structure of HA mineral and collagen, natural bone displays high strengths, on average of 130-190MPa for cortical bone and 3.6-9.3 MPa for cancellous bone [97]. While highly dense (< 20 % porosity) HA cements may achieve strengths of up to 150MPa under laboratory conditions, commercially available HA cements generally display strengths below 30MPa at 40 % or more porosity [93, 221]. Brushite cements on the other hand, rarely display strengths above 20 MPa, and these cements display these characteristics without the incorporation of macropores [93]. Comparatively, MgP cements have routinely demonstrated strengths between 40-85MPa [36, 37, 56, 57]. Under these conditions, it is conceivable to develop MPCs with strengths comparable or greater than brushite cements while also introducing porosity to provide for cellular infiltration and scaffold resorption. The goal of this study is thus to evaluate the role of mannitol on the workability, mechanical durability and cytocompatibility of the magnesium ammonium phosphate cement system developed through the work already discussed in Chapters 3 and 4.

5.2 MATERIALS AND METHODS

5.2.1 Cement Preparation

Trimagnesium phosphate (TMP, $Mg_3(PO_4)_2$) powder was synthesized through an aqueous precipitation reaction as detailed in Chapter 2. The resulting powder was thermally treated to 800°C for 6 hours in air to form anhydrous crystalline TMP powder with a surface area less than 1 m^2/g, as detailed in Chapter 3. The powder was then lightly ground and sieved to below 500 µm to remove large agglomerates.

Cements were created by combining the synthesized TMP powder with 0, 10, 20, 30, 40 or 50 weight % mannitol sugar crystals (Sigma-Aldrich) then mixing the powder with the 3 M pH 7.0 ammonium phosphate reacting solution comprising a mixture of diammonium phosphate and ammonium dihydrogen phosphate solutions to create the cement via the reaction described in detail in Chapter 3. Cement powders were created by then mixing with the ammonium phosphate solution at a variety of powder-to-liquid ratios (P:L) wherein the powder is the combined TMP and mannitol. Cements were stirred for sixty seconds then filled into cylindrical molds, 6 mm diameter, 15 mm height for mechanical testing and 10 mm diameter, 2 mm height for cell culture. Samples were correspondingly stored overnight at 37 °C prior to testing.

5.2.2 Cement Characterization

Cement setting times were measured at room temperature utilizing the Gilmore needle test, as described in Chapter 3. Cement phases were identified using x-ray diffraction (XRD) as outlined in Chapters 2, 3 and 4. Fourier transform infrared spectroscopy (FTIR) was used to identify differences in molecular chemical linkages between the different cement systems. Cements were observed under scanning electron microscope (SEM). XRD, FTIR and SEM testing were performed as described in Chapter 2.

5.2.3 Mechanical Properties of Cements

Wet compressive strengths of the cements were analyzed with a 2 kN load cell at a cross head speed of 1.0 mm per minute (Instron, Norwood MA). Cement cylinders were incubated in phosphate buffered saline (PBS) at 37 °C prior to compression testing to determine the change in

strength due to aqueous conditions as well as the effect of mannitol dissolution. PBS incubation time points considered were 0, 1, 3, 5, 7 and 14 days, with 5 samples at each time point. Brunauer-Emmett-Teller method specific surface area (SSA) of cements was measured from N_2 adsorption-desorption isotherms on a Micrometrics ASAP 2020 instrument. The true density and % porosity of cements following PBS incubation was determined following Equations 4-3 and 4-4 outlined in Chapter 4.

5.2.4 *In Vitro* Dissolution Characteristics

Cement pellets were incubated in PBS, at a concentration of 10ml of PBS per 1.0 gram of cement, at 37 °C. The PBS was changed every 24 hours. At each time point (1, 3, 5, 7, 14 days) the pH of the PBS was measured and the wet weight of each sample was recorded. In order to determine ion concentrations, the collected PBS solution was diluted in 0.03 M Tris buffer solution and analyzed by inductively coupled plasma optical emission spectroscopy (ICP-OES, iCAP duo 6500, Thermo Fisher). Cement samples incubated in PBS were dried overnight at 37 °C then characterized using XRD, FTIR, SSA, density and SEM analyses to compare with the as-generated cement samples to determine if any changes occurred due to the saline incubation.

5.2.5 Cytocompatibility

Murine MC3T3−E1 preosteoblast cells were utilized for cell culture studies. The substrates were sterilized as previously described, soaked in culture media for 24 h, then seeded with MC3T3 cells at a density of 40,000 cells/well. The media was changed every other day throughout the

testing period. Live/Dead staining and MTT cellular activity assay were completed as described in Chapter 2. Cell number quantification was completed using the CyQuant cell proliferation assay according to the manufacturer's instructions. Briefly, at each time point, the media was fully removed from samples and the samples were placed in -70 °C for at least 24 hours. When ready to test, the samples were thawed to room temperature then incubated in 400 µl of CyQuant cell lysis buffer and the dye solution for 5 minutes away from light. Following this, 200 µl of each solution was pipetted into a 96 well plate and the fluorescence was read at an excitation wavelength of 480 nm and emission wavelength of 520 nm. Hydroxyapatite and brushite CPCs were created to compare with the MPC cements. Common formulations of each cement were employed. Apatite cements were created utilizing α-TCP (HIMED, USA) and a 2.5% Na_2HPO_4 (Sigma Aldrich) solution at a powder to liquid (P:L) ratio of 2.5:1. Brushite cements were created using β-TCP (HIMED, USA) and monocalcium phosphate monohydrate ($Ca(H_2PO_4)_2$ Sigma Aldrich) at a 1:1 mole ratio employing a 0.5 M citric acid solution at a powder to liquid (P:L) ratio of 3:1.

5.2.6 Statistics

Statistical calculations were performed using IBM SPSS Statistics 23 statistical analysis program. For appropriate quantitative assessments, including ionic content via ICP-OES, MTT viability assay and mechanical strengths, the mean and standard deviation was assessed for a sample size of four per sample. Statistically significant differences were assessed through one-way ANOVA with Tukey's post hoc testing where the significance was set at $p < 0.05$.

5.3 RESULTS

5.3.1 Cement Setting Times

In order to develop a series of cements with clinically appropriate setting times, powder mixtures with 0-50 wt% mannitol were mixed with a variety of powder-to-liquid ratios. Since the addition of the poor forming mannitol can change the setting times, Figure 5-1 shows the first and second setting times for each combination in the series. At each mannitol content, the P:L ratio with the first and second setting times of approximately 8-10 min and 15-20 minutes at room temperature were chosen for further assessment. Powder-to-liquid ratios chosen for further exploration are denoted with stars in Figure 5-1. The optimized P:L ratios were: 1:1 for 0%, 1.5:1 for 10% and 20%, 1.75:1 for 30% and 40% and 2:1 for 50%. Here, the chosen P:L ratios were not always statistically different than others for the first or second set time, hence the P:L averages closest to the stated goals were chosen.

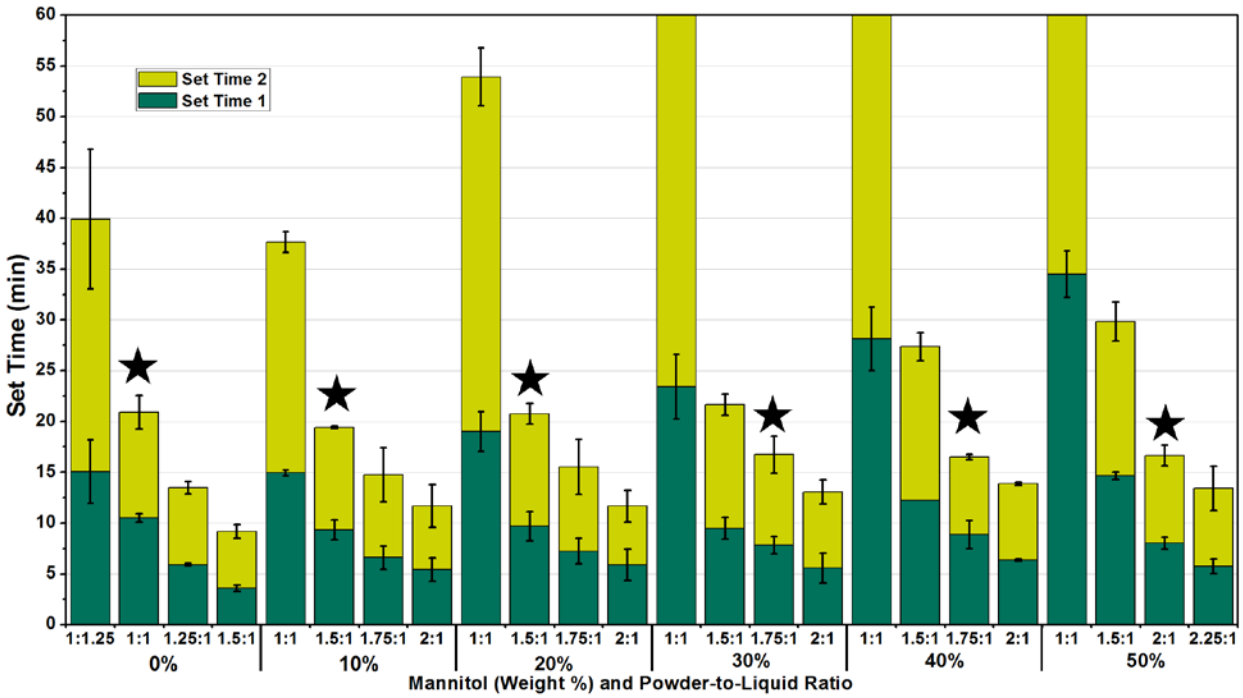

Figure 5-1 First and second setting times of mannitol-containing magnesium phosphate cements (n=4).

5.3.2 Cement Characterization

The cement embodiments chosen above were incubated in PBS, and initial properties as well as changes due to aqueous incubation were analyzed. Figure 5-2 displays the x-ray diffraction patterns collected from the as-prepared cements and after 14 days in PBS. Phases present in the as-reacted cement were correspondingly unreacted precursor TMP ($Mg_3(PO_4)_2$, +), hannayite ($Mg_3(NH_4)_2H_4(PO_4)_4 \cdot 8H_2O$, $), and mannitol (>). Following 14 days of incubation in PBS, struvite ($MgNH_4PO_4 \cdot 6H_2O$, *) and newberyite ($MgHPO_4 \cdot 3H_2O$, #) were the predominant phases, along with a small amount of unreacted TMP but no hannayite or mannitol was observed to be present.

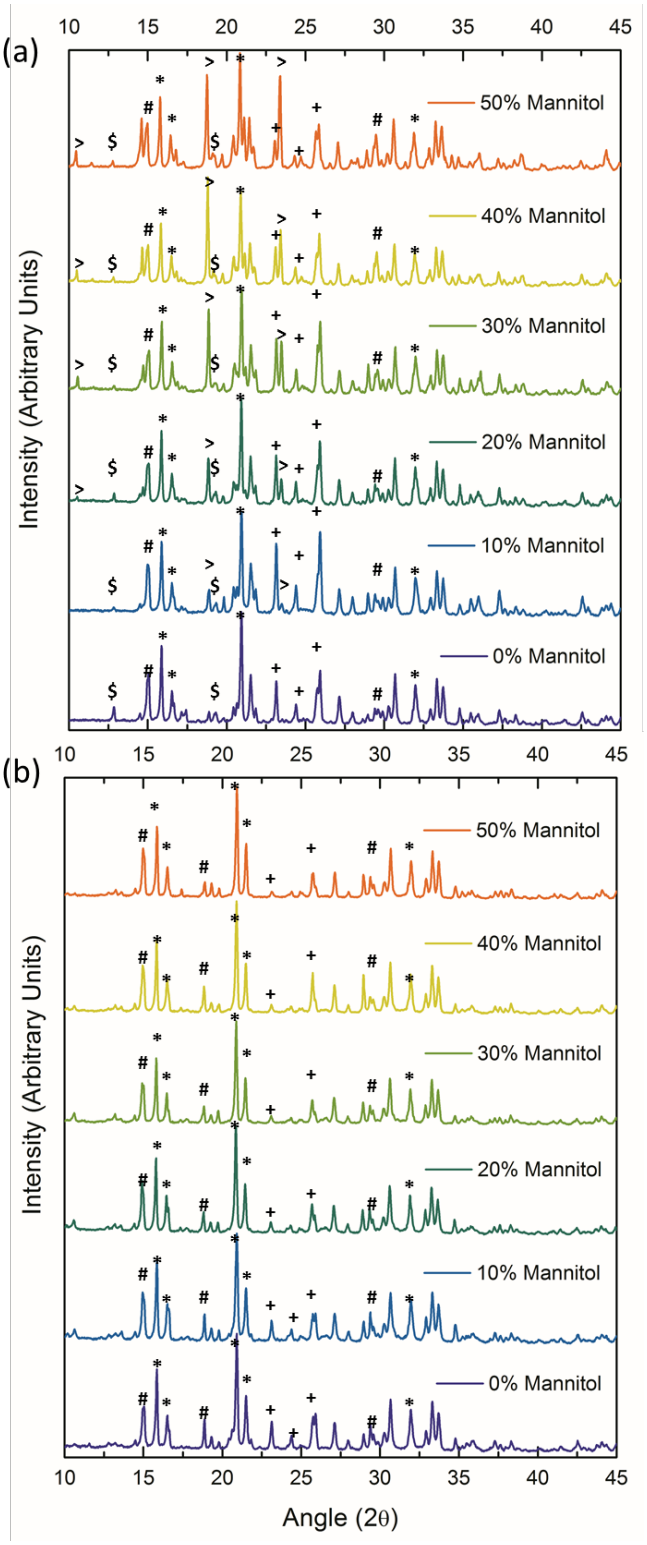

Figure 5-2 X-ray Diffraction patterns of mannitol-containing magnesium phosphate cements at (a) 0 days in PBS (as generated) and (b) 14 days in PBS. Phases present are denoted: struvite (*), newberyite (#), unreacted trimangesium phosphate (+), mannitol (>), and hannayite ($).

FTIR spectra analysis of the select mannitol containing cements as generated and following 14 days of incubation in PBS, as well as the spectra of pure mannitol for comparison, can be seen in Figure 5-3. The spectra of all the cements shows bands associated with the ammonium and phosphate bonds, including 1200-900 cm^{-1} and 700-450 cm^{-1} ranges which correspond to the PO_4 vibrational frequencies as well as peaks in the bands between 1600-1400 cm^{-1} which are attributed to NH_4 vibrations, as discussed in Chapter 2. Similarly, the broad hump from 3500-2000 cm^{-1} is due to adsorbed water, and NH_4 stretching vibrations observed at 2900 cm^{-1} and in the 1600-1400 cm^{-1} band range. Additionally, at Day 0, peaks associated with mannitol sugar can be seen in the mannitol-containing cements (50% shown in Figure 5-3). These peaks are associated with O-Hand C-H stretching vibrations in the range between 3700 and 2500 cm^{-1} as well as C-H vibrations between 1400and 1200 cm^{-1} [222]. The removal of mannitol from the cement structure is confirmed through FTIR as the bands associated with mannitol are no longer present after PBS incubation. While significant changes in crystal structure were observed through XRD, FTIR analysis shows no corresponding changes in the cement character after PBS incubation. This is attributed to the FTIR analysis primarily detecting changes in molecular linkages of infra-red active molecular bonds regardless of amorphous or crystalline state in comparison to the various characteristic crystallographic diffraction planes determined by XRD analysis for a particular crystalline phase as opposed to no significant diffraction observed for amorphous systems. FTIR assesses vibrational frequencies present in chemical moieties. The vibrational frequencies present in the cement do not change significantly within the specific crystallographic structure.

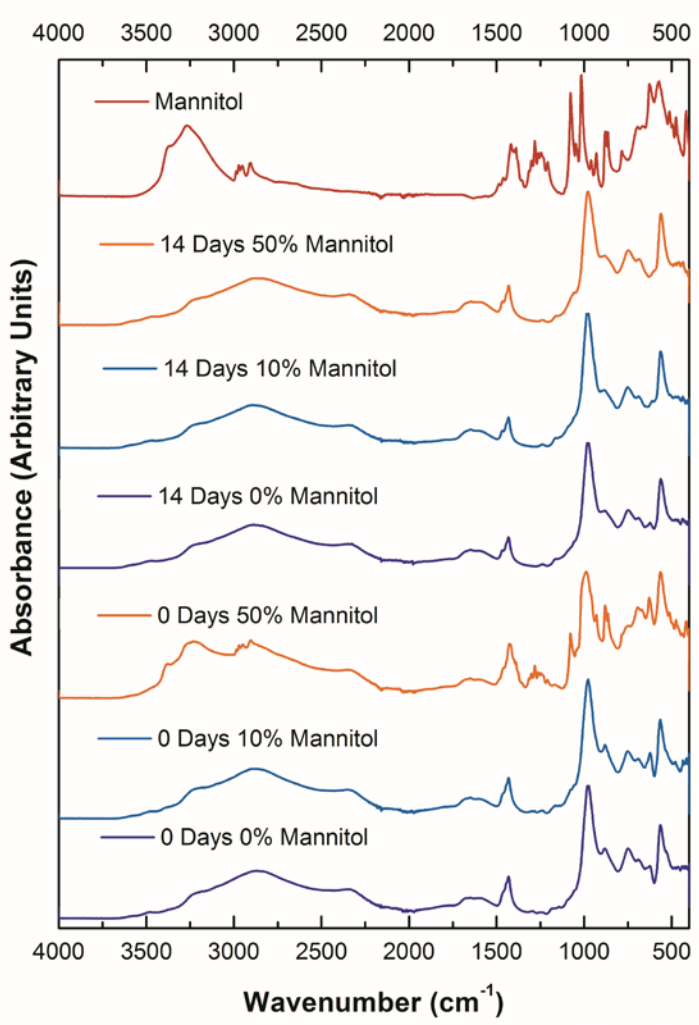

Figure 5-3 FTIR spectra of select mannitol containing cements as generated and after 14 days of incubation in PBS.

Figure 5-4 shows the pH values (a) and weight change (b) of mannitol containing cements through 14 days of incubation in PBS. After one day in PBS, pH values varied between ~7.0 and 7.5, with most cement embodiments becoming slightly more acidic than the PBS control with no statistical difference observed between cement samples or PBS. At 3 days in PBS, pH values of cements increased from 7.5-7.7, with pH increasing as the mannitol content increased. At further time points, the pH values of each cement embodiment displayed a slight

gradual decline, remaining slightly more basic than PBS. For time points 3 days and beyond, all the cements exhibited statistically higher pH than PBS. In general, the pH of 0% and 10% mannitol was statistically lower than 40% and 50% mannitol cements, with 20% and 30% not being statistically different than the others. Change in weight of mannitol containing cements, observed in Figure 5-4b, indicates that over the time period studied the main change in weight occurs within the first 24 hours in PBS. Weight change followed a linear relationship between weight loss and mannitol content, with 0% mannitol cements gaining on average 6% weight at Day 1 while 50% mannitol cements lost on average 2% of the starting weight. Weight change statistics followed a similar trend, with low mannitol content cements expectedly displaying statistically less weight loss than the high mannitol content cements.

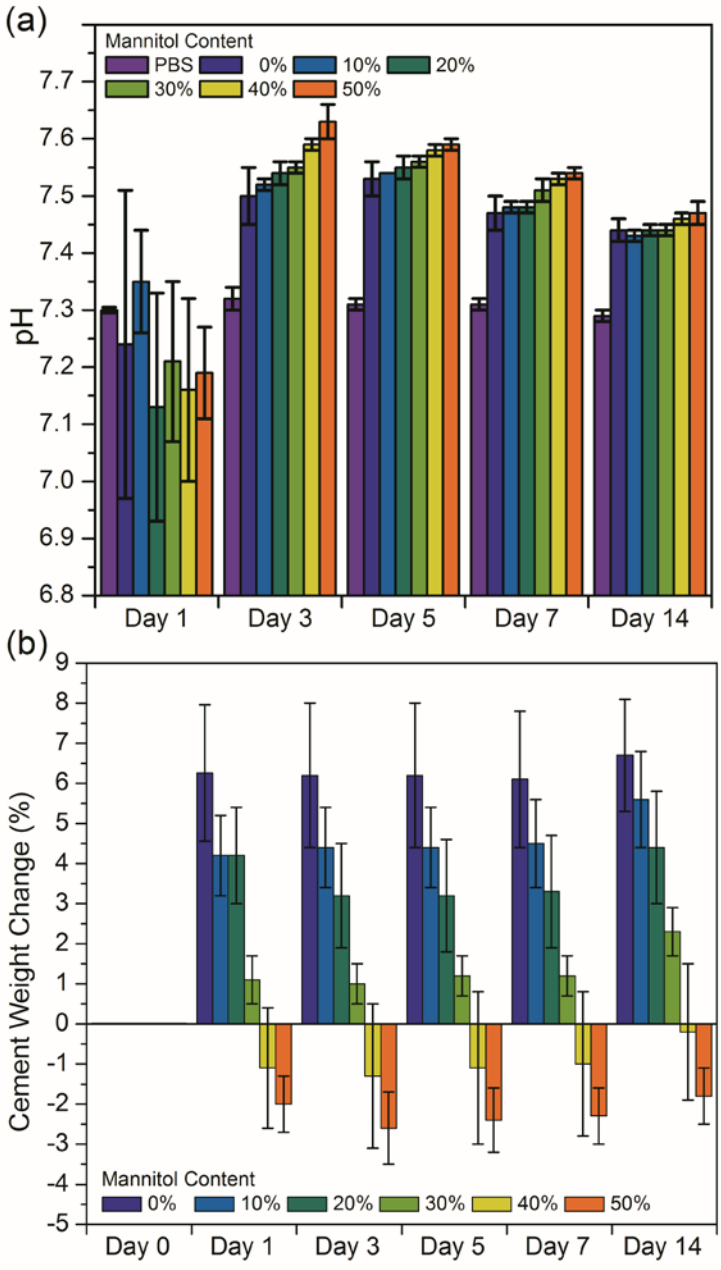

Figure 5-4 pH measurements (a) and weight change (b) of mannitol containing cements through 14 days of incubation in PBS (n=4).

In Figure 5-5 are displayed the daily ion concentrations of magnesium and phosphorous resulting from the cement dissolution. Results from ICP analysis indicate significantly elevated levels of magnesium and phosphorous in solution when compared with the PBS, which contains a

baseline of phosphorus but no magnesium. High variability is observed in the initial incubation time (Day 1) after which the cement dissolution appears to decline and stabilize. In both the magnesium and phosphorus ion concentration measurements the levels measured were significantly higher than PBS controls. Magnesium ion levels (at 3 days and beyond) were measured between 0.8 and 1.1 mMol concentrations, slightly reducing over time to range between 0.6 and 0.8 mMol at 14 days. Phosporous ion levels (at 3 days and beyond) were measured at 2.5-2.8 mMol. No statically significantly differences were observed between cement samples, although trends of increasing magnesium concentration with increasing mannitol content are seen.

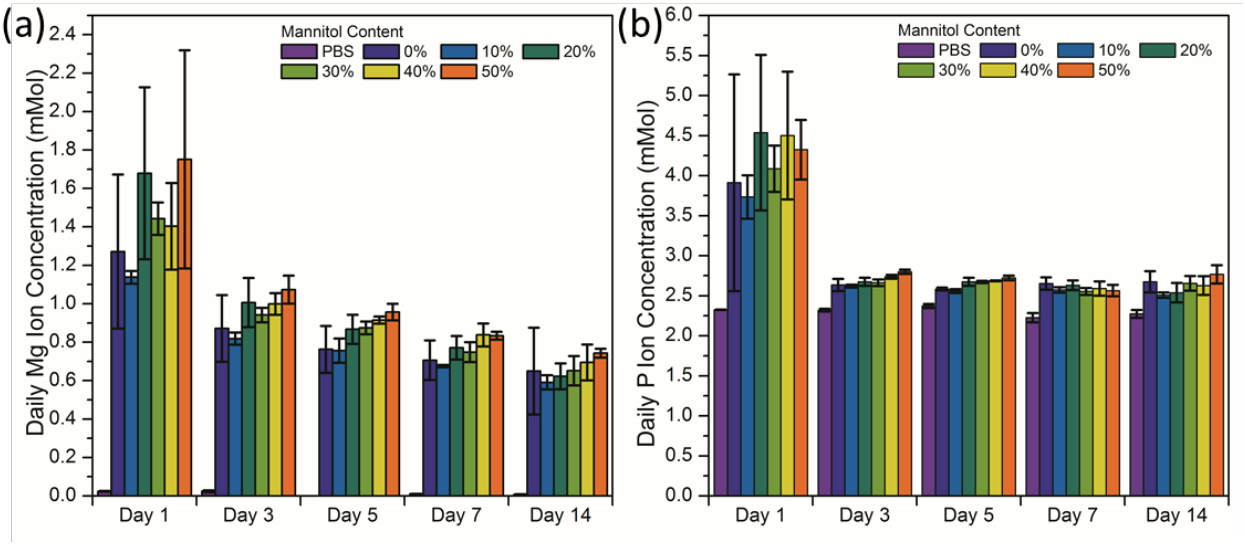

Figure 5-5 Daily magnesium (a) and phosphorus (b) ion concentration measure by ICP-OES through 14 days of incubation in PBS at 37°C (n=4).

5.3.3 Cement Strength and Porosity

Figure 5-6 shows the change in mechanical strength of mannitol cements as generated and with up to 14 days incubation in PBS. After generation, prior to PBS incubation, the cement compressive strengths of all cement embodiments ranged from 15-25 MPa with no statistical difference observed. Following PBS incubation, a loss of strength corresponded directly with an increase in mannitol content in the starting formulation as expected. After one day in PBS, the cement strength averages ranged from 19 MPa at 0% to 5 MPa at 30% to 1MPa at 50% mannitol content. This strength level remained constant for each cement embodiment through 7 days of testing. At 14 days in PBS, the mechanical strength slightly increased in many cement embodiments. (Not statistically significant.) At all time points, there is high variability of strength measurements, particularly with the 0% mannitol cements and as in the above measurements, statistically significant differences between incremental changes in mannitol content are generally not observed but statistically significant differences exist between further separated measurements following PBS incubation. For example, 0% mannitol is not statistically stronger than 10% mannitol at any PBS incubation time point but both are always statistically stronger than 40% and 50% mannitol containing cements at those identical time points.

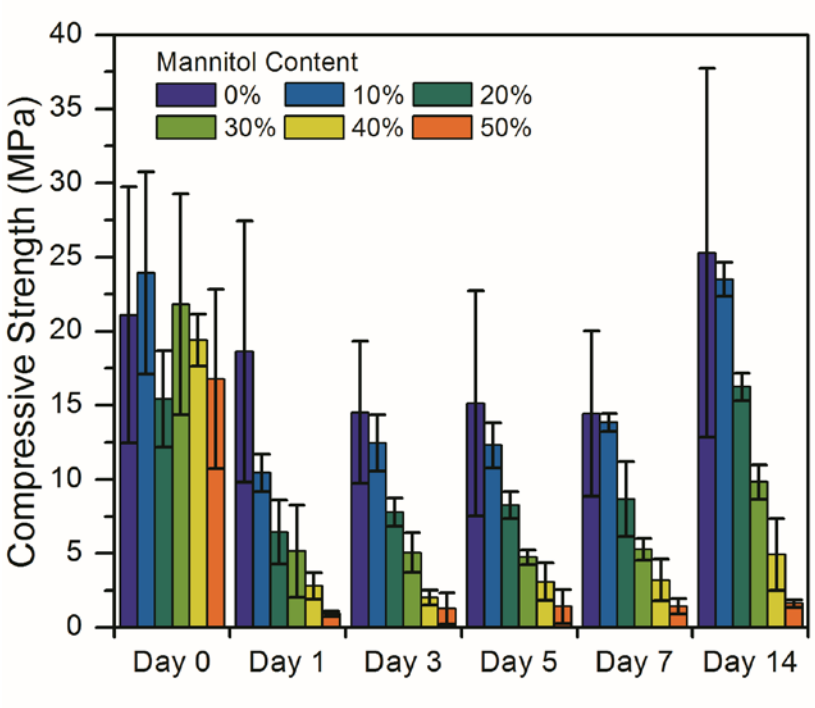

Figure 5-6 Compressive strength of magnesium ammonium cements, with up to 50 weight % mannitol porogen addition, through 14 days of incubation in PBS (n=4).

In Figure 5-7 can be observed the true density (a), apparent density (b), SSA (c), and %porosity (d) of cements observed through 14 days in PBS. With the as generated cements, the true density followed a linear trend decreasing from 2.35 to 1.90 g/cm^3, each with increasing mannitol content significantly lowering the measurement values. At day one there is still a similar trend of reduction in true density, from 2.35 to 2.25 g/cm^3, but to less of an extent, with 40% and 50% mannitol showing lower values than the other embodiments. At further time points, the true density of all cements was the same. For comparison, the true density of mannitol is 1.49 g/cm^3.

The apparent density of the as generated cements and cements after 1 day in PBS averaged between 1.3-1.6 g/cm^3 with the 0% mannitol cement slightly higher in density than the mannitol containing cements. Following further PBS incubation, the apparent density of the 0%

mannitol cement slightly decreases to 1.4 g/cm^3 while the densities of the mannitol containing cements drop much more drastically, to an average of 1.2 g/cm^3 at 5 days and near 1.0 g/cm^3 at 14 days in PBS. There is no consistent trend or statistically significant differences in apparent density observed between the various mannitol containing cements.

The BET measured surface area of the 0% mannitol cement was 125 m^2/g in the as generated cement while the mannitol containing cements displayed a specific surface area between 93 for the 10% cement declining to 80 for the 50% cement. While there was a trend of reduced surface area with increased mannitol content, the samples were not statistically different from each other. Following incubation in PBS, the specific surface area of all cements drastically increased. The 0% cement increased to greater than 150 m^2/g while the mannitol containing cements increased to between 135-175 m^2/g. The 0% mannitol cement notwithstanding, the cements displayed a general trend of increased surface area with increasing mannitol content. However, as with the above measurements, the incremental increase in porogen content did not result in a statistically significant change but a large difference in mannitol content was generally statistically different, specifically the SSA of 10% mannitol was always lower than the SSA of 50% mannitol. For comparison, the average surface area of mannitol was 0.29 m^2/g.

Finally, for porosity measurements, the as generated cements averaged porosity between 35-40%, with the 10% and 30% samples statically being higher than the 20% and 40% samples, respectively. Following PBS incubation, the porosity of the 0% cement remained steady between 30-35% while the porosity of the mannitol-containing cements rose significantly, increasing at each time point, to an average value between 55-60% at 14 days. Interestingly, there was no consistent trend of increased porosity observed with increasing mannitol content as would be expected for each time point of PBS incubation.

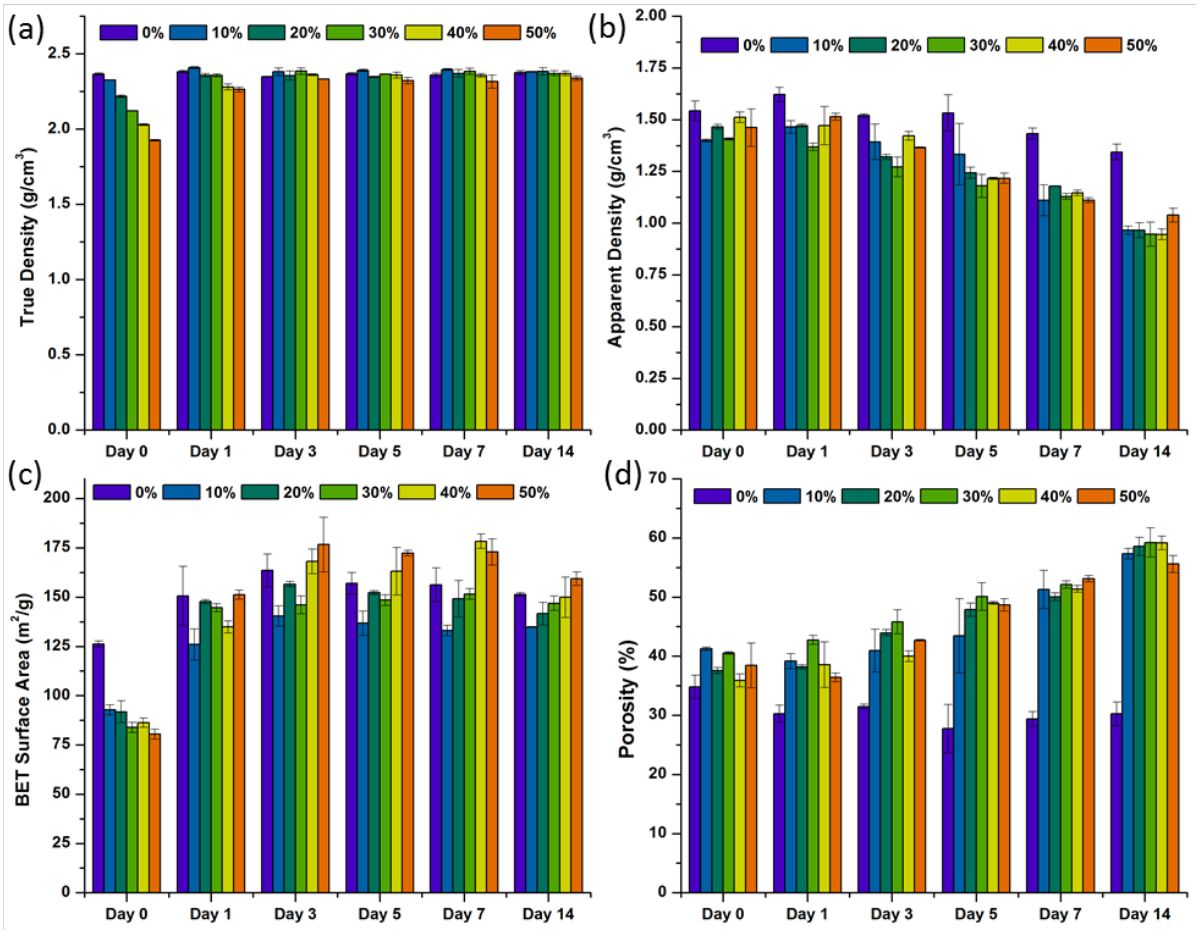

Figure 5-7 Measurements of true density (a), apparent density (b), surface area (c) and porosity (d) of mannitol containing cements through 14 days of incubation in PBS at 37 °C (n=4).

In Figure 5-8 can be seen representative mercury intrusion porosimetry results for the mannitol cements. In order to gain an understanding of the pore size distribution, samples of the cement were tested in the as generated and after 3 days of incubation in PBS to allow for mannitol dissolution. Figures 5-8a and 5-8b depict the differential intrusion at 0 and 3 days, respectively, while plots 5-8c and 5-8d depict the cumulative intrusion at the same time points. Mercury intrusion results show that the pore size distribution of the cements at day 0 (a) was quite similar, with a small amount of macropores around 100 µm and a significant portion of

micropores between 2.0-0.2 μm. A slight increase in micropore volume and size is seen with increasing mannitol content, from 0.11 mL/g peaking at 0.9 μm for the 0% to 0.19 mL/g peaking at 1.1 μm for the 50% mannitol cement. Cumulative intrusion at day 0 (c) indicates that the increased micropore volume results in a slight increase in cumulative intrusion as well, from 0.09 mL/g at 0% to 0.13 mL/g at 50%. Differential intrusion after 3 days of incubation indicated an increase in mid level (10 μm) pores as well as micropores (less than 1 μm), particularly for the 50% mannitol sample. Cumulative intrusion indicates a moderate increase in intrusion volume for the 0, 10, and 30% mannitol samples (up to 0.2 mL/g) but a large increase in intrusion volume for the 50% mannitol sample is observed as would be expected. It is important to note that mercury intrusion porosimetry measurements are of one individual sample and used to observe only general trends in pore structure but are not stastically measured.

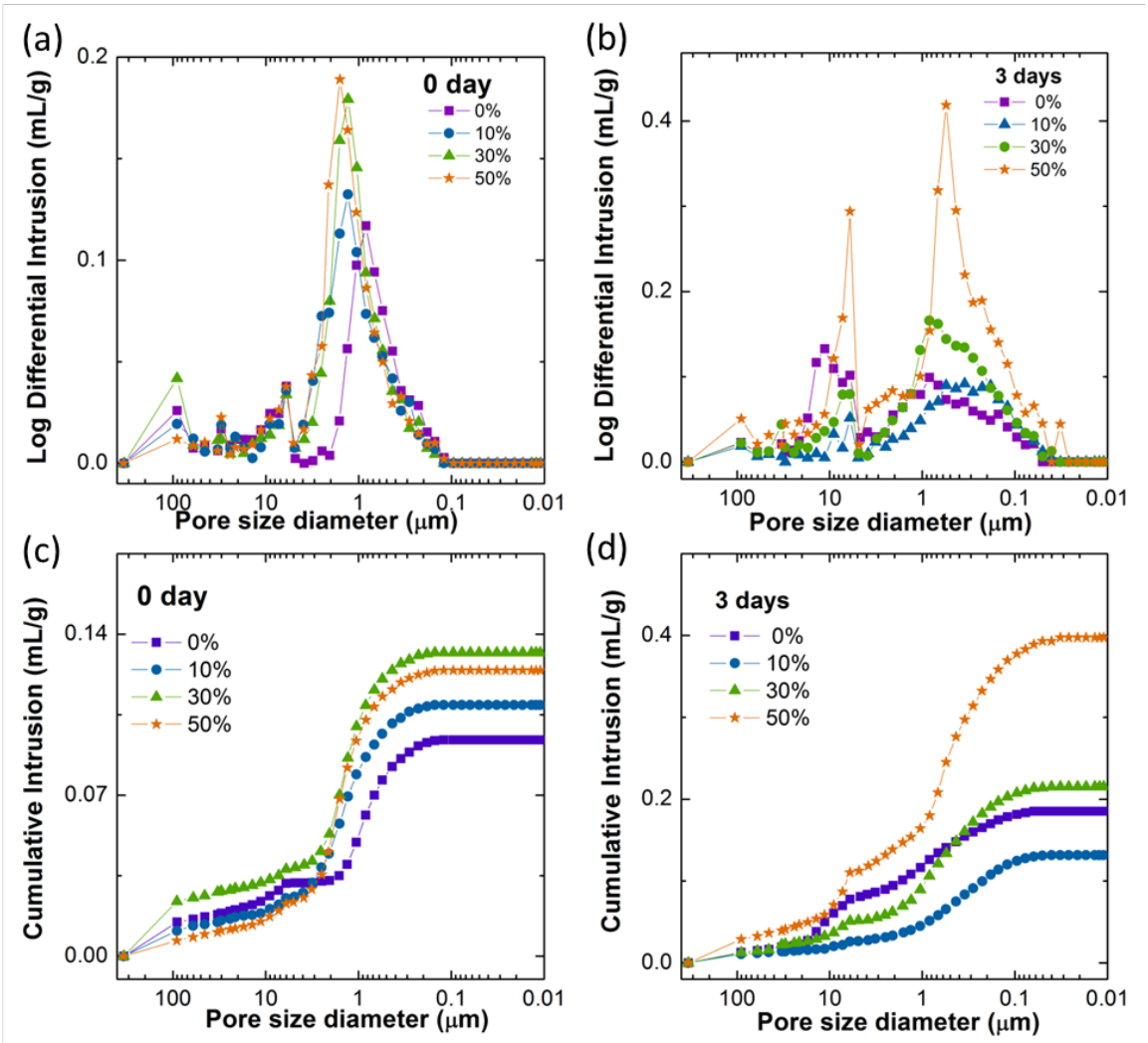

Figure 5-8 Mercury intrusion porosimetry measurements of mannitol supplemented cements. In (a) and (b) are the log differential intrusion volumes at 0 and 3 days of PBS incubation, respectively. In (c) and (d) are the cumulative intrusion volumes at 0 and 3 days of PBS incubation, respectively (n=1, representative only)

In Figures 5-9 and 5-10 are displayed the SEM images of cement pressed and fracture surfaces, respectively, at 0 and 14 days incubation in PBS with a scale bar of 50 μm. In Figure 5-9 the pressed (external) surface of the as generated cements shows a generally smooth surface with consistent cement morphology grain size. The presence of mannitol is particularly

noticeable in the 40% and 50% samples, seen as smooth, elongated, darker gray grains in the images. After 14 days in PBS the surface of the cement is less smooth, with the cement pellets covered in new crystal growth. These crystals are larger and of a more oblong morphology than the grains seen on the surface of the as generated cement. The morphology of mannitol crystals is not seen in any samples, and obvious macroporosity resulting from the removal of the mannitol is not observed.

In Figure 5-10, the internal fracture surface of the cements as generated is similar to the external surface, showing a consistent grain size and morphology of the cements with significant presence of long, smooth mannitol crystals in higher content cements. Crystals appear to of the size ranging from 10-200 μm, however the mercury porosimetry indicates additional particles below 10 μm. After 14 days of PBS incubation the internal cement microstructure shows significant portions of macropores 50-100 μm in size as well as noticeable porosity below 10 μm in size. Cement grain structure is more similar to that of the as-generated cement, showing the growth of some fine crystals but not the growth of large oblong crystals as seen on the surface of the cement. The surface crystal growth is then likely due to reprecipitation on the surface from the cements sitting in a stagnant (non-continuous flow) salt media for an extended period of time.

In Figure 5-11 can be seen the internal surface of the cements at higher magnification after 1 day in PBS, with a scale bar of 10 μm. These images indicate the cement microstructure is very similar to that of the 800 °C crystalline TMP- ammonium phosphate solution cement studied in Chapter 3. The higher magnification images show the same block and elongated crystal type in all cements, regardless of the original mannitol content.

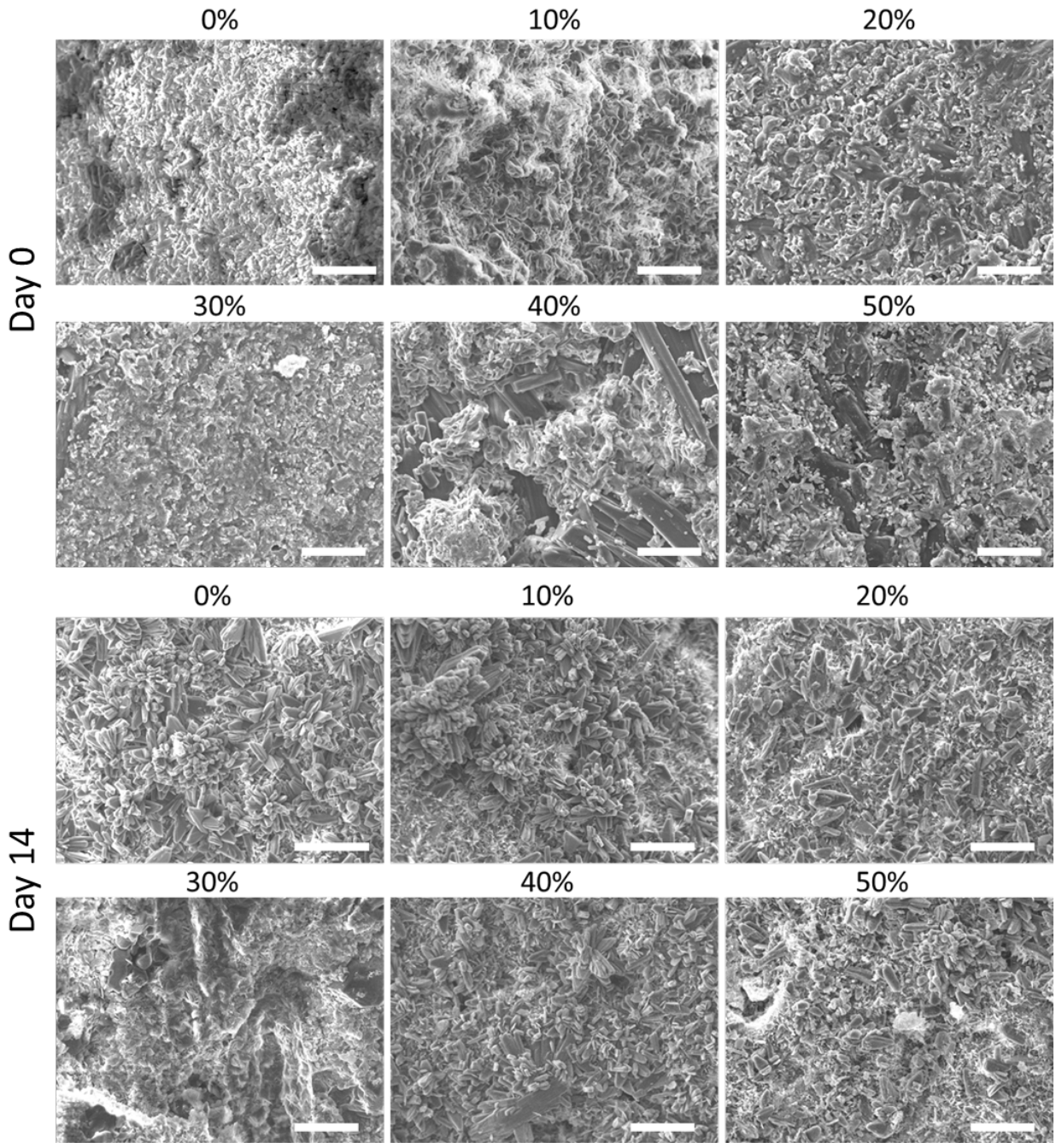

Figure 5-9 SEM images of the exposed cement surface as generated (Day 0) and after 14 days of PBS incubation (Scale bar is 50 µm).

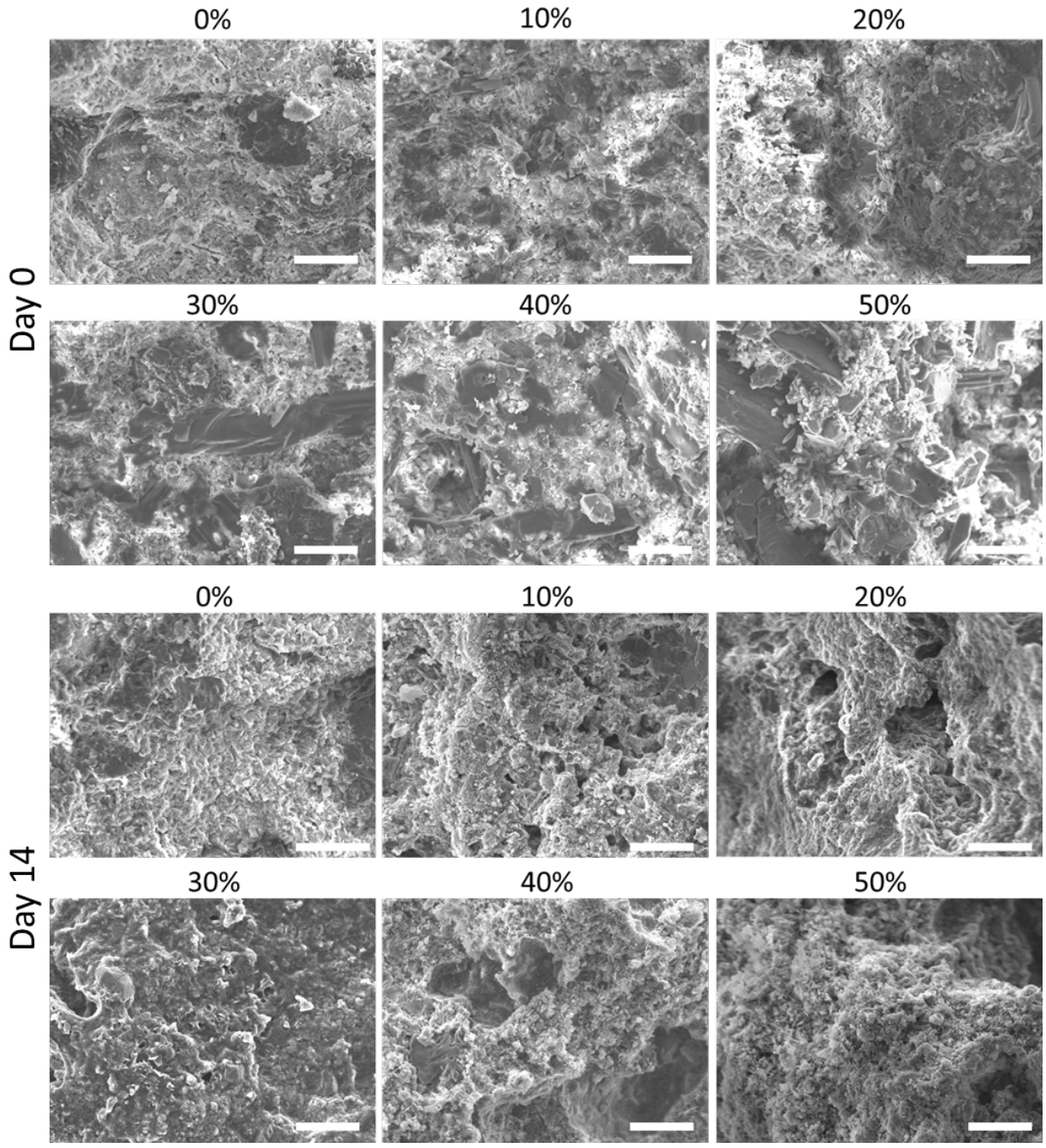

Figure 5-10 SEM images of the fracture (internal) cement surface as generated (Day 0) and after 14 days of PBS incubation (Scale bar is 50 µm).

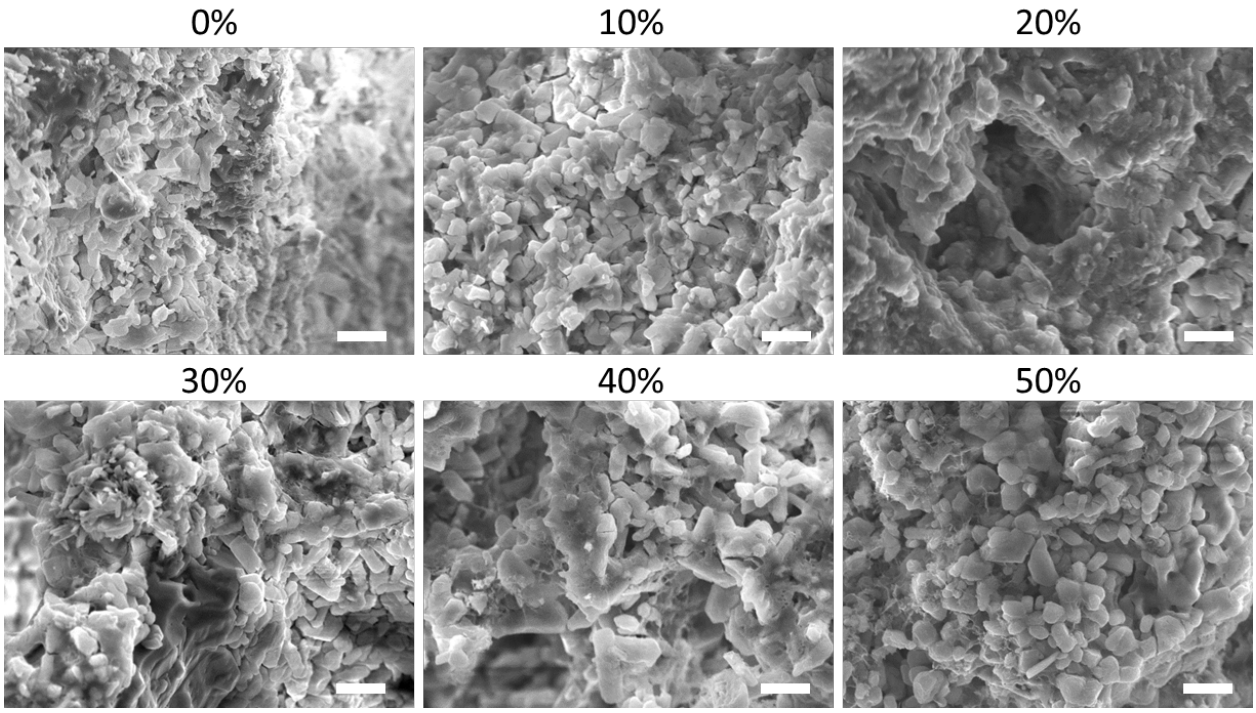

Figure 5-11 SEM images of internal cement surface after 1 day in PBS at 1500x magnification (Scale bar is 10 µm).

5.3.4 Cytocompatibility

In Figure 5-12 are displayed the Live/Dead staining of MC3T3 cells at 0 and 7 days of culture on cement pellets. Images at days 1 and 7 indicate that the addition of mannitol does not visibly improve nor harm the cytocompatibility of the cement. All cements, including hydroxyapatite and brushite controls, demonstrated lower cell viability and cell numbers than the tissue culture plastic control. Day 7 results indicate that the cell proliferation from day 7 was low, and brushite cements appear to have an increased level of dead cells.

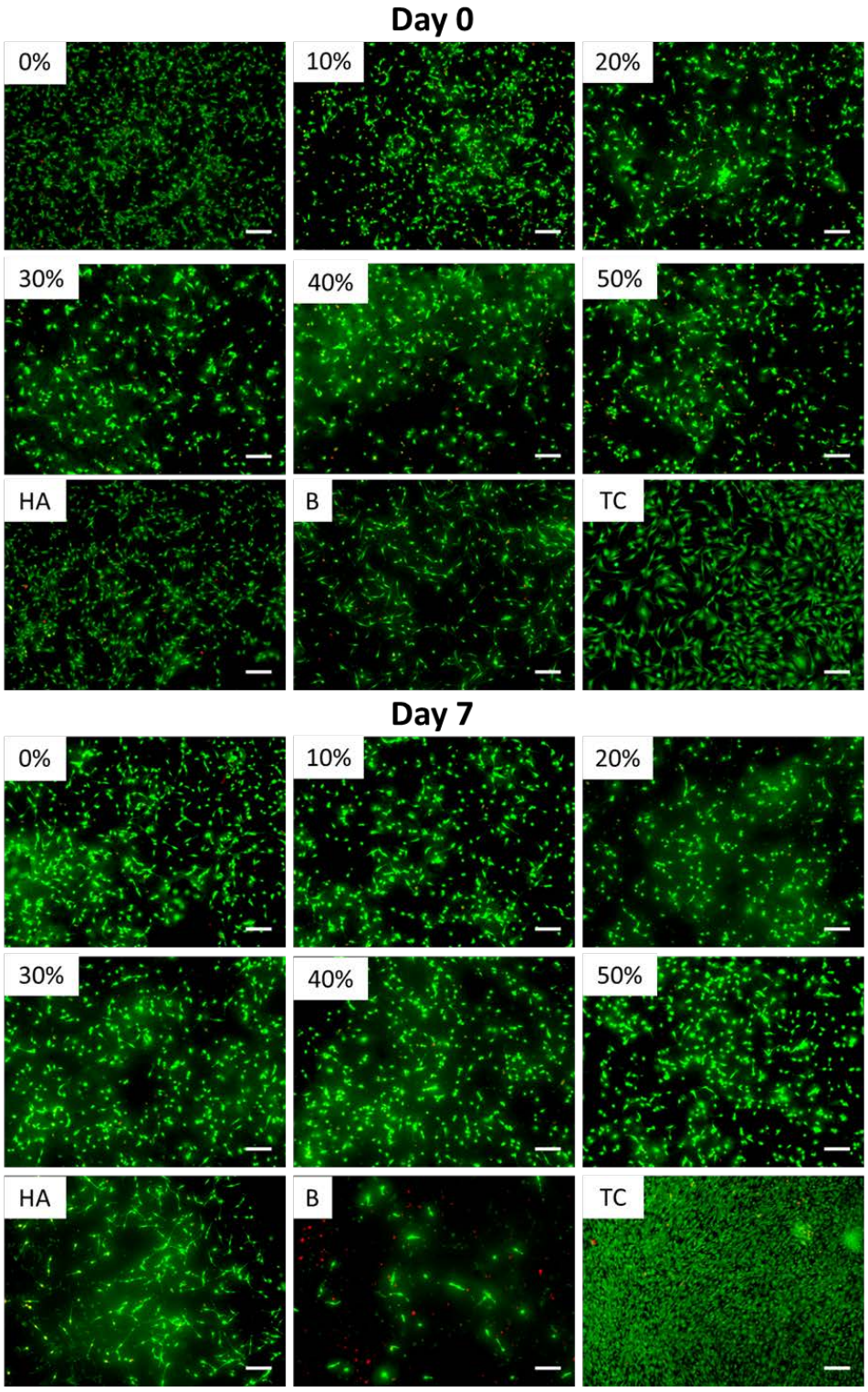

Figure 5-12 Live/Dead staining of MC3T3s on cements at 1 and 7 days of culture (Scale bar is 200 µm).

Figure 5-13 contains the MTT cellular activity (a) and cell number quantification (b) results tested with MC3T3 pre-osteoblast cells. Globally there were not significant trends between cement samples for MTT or cell number. At day 3, MTT indicated high activity for 0% mannitol samples and brushite samples than others. At day 7, the tissue culture control had higher MTT cell activity. Activity levels for cement constructs did not appear to change with time.

Cell number results indicate drastically more cells on the tissue culture control samples than on any of the cement constructs. Cell numbers on cement constructs increased slightly from day 1 to day 3, and cell number on the apatite cement increased significantly at day 7. It is important to note that MTT and cell number measurements were conducted on the cement construct alone. Tissue culture measurements were normalized to the cement construct surface area, from 1.9 cm^2 on the well plate to 0.785 cm^2 for the cement sample. The number of cells seeded on pellet surface (normalized from 40,000 cells/well) was about 16,000 cells per pellet. Thus the total cell number on cements was significantly lower than the original seeding density.

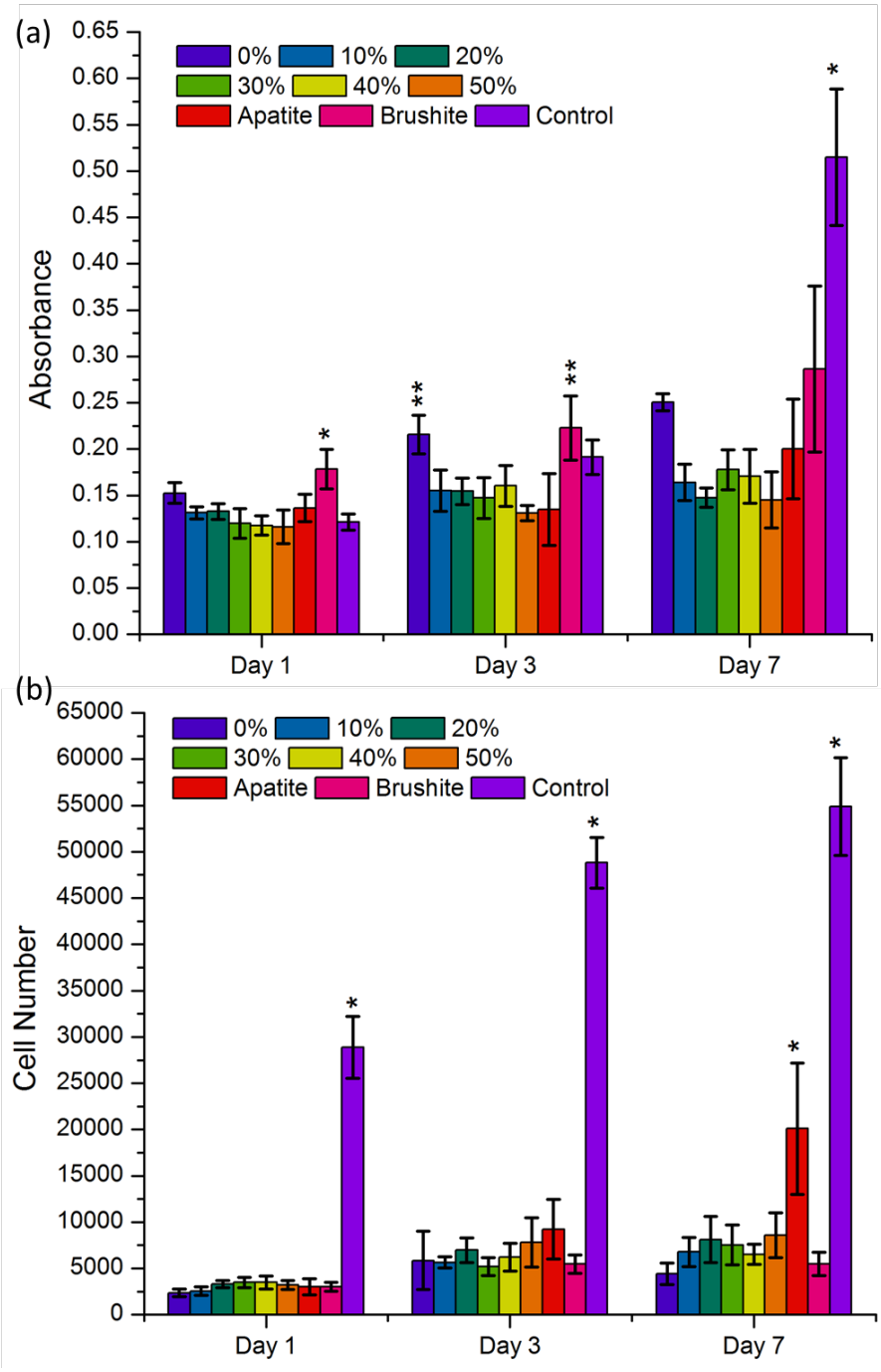

Figure 5-13 MTT (a) and cell number (b) data for MC3T3s grown on cements at 1, 3 and 7 days culture (n=4, p<0.05 indicated with *).

5.4 DISCUSSION

For the development of the next generation of synthetic bone graft substitutes a wide variety of properties are desired, including ease of use, mechanical strength, degradability and osteoconductivity. Porosity is near the top of this list because it is known to improve the implant integration with the host tissue and allows for nutrient flow and cellular ingrowth. Experience has shown that dense constructs may not integrate well with the patient's native bone, even resulting in long term implant infection and likely rejection. Mannitol has frequently been employed as a porogen in calcium phosphate cements because it dissolves quickly and does not cause biocompatibility issues nor disrupts the cementing reaction [111, 217, 218].

The addition of mannitol to the magnesium ammonium phosphate cement (MPC) resulted in longer setting times at a given powder-to-liquid ratio (Figure 5-1) which is to be expected as the sugar crystal does not participate in the cementing reaction. For this reason, a variety of P:L were tested to optimize the setting time of each cement formulation, with the optimized P:L to be used for the remainder of the study. XRD (Figure 5-2) and FTIR (Figure 5-3) test analyses shows the cementing reaction proceeded the same way as observed in Chapters 2 and 3, with the mannitol not affecting the phase formation of the as generated cement nor the phase evolution following the PBS incubation. This is supported as well by the SEM results in Figures 5-9, 5-10 and especially 5-11, which show the presence of mannitol and resulting porosity but no change in cement crystal microstructure with the mannitol addition. Results indicate that the mannitol is fully dissolved at the 14 day time point, evidenced by the lack of mannitol peaks in the XRD or FTIR plots. This is also supported by the changes in weight, surface area and true density shown in Figure 5-7, which show a significant change between the as generated cement and cements after 1 day in PBS, but little or no change beyond this point.

Major changes in weight (Figure 5-4b) occurred only after initial PBS exposure, with the 0% mannitol sample gaining 6% of its initial weight, trending downwards to 2% weight loss with the 50% mannitol sample. While these weight changes are not at the 10-50% change of the original mannitol inclusion, this level of weight change would not be expected. The measurements were taken as wet weight, where the samples are not dried after PBS incubation, so liquid is present as filled in many of the pores as well as the crystals of the cement holding associated water molecules. Additionally, the mannitol content was a weight percentage of the dry powder, to which a significant volume of solution was added and consumed.

Elevated magnesium and phosphate ion levels (Figure 5-5), slightly elevated pH measurements (Figure 5-4a) and reduced apparent density and increase porosity at longer PBS incubation time points (Figure 5-7) indicate that the cement scaffolds are continuing to dissolve over the time frame studied, even if that dissolution is not distinctly observable in the wet weight measurements. It is interesting to note that the apparent density and porosity level of the 0% mannitol cement remained unchanged while the mannitol containing cements changed. It is possible that, even the small amount of mannitol addition, resulted in enough additional interconnected porosity to change the dissolution/precipitation kinetics within the micropores of the mannitol-containing cement structures. This could result in more dissolution within the micropores of mannitol cements while the 0% cement dissolution could only occur in more poorly connected pores and from the surface of the sample, which would not change the porosity level.

Although the compressive strength of cements (Figure 5-6) after PBS incubation drastically decreased with increasing mannitol content, the increasing porosity observed at longer incubation times did not further decrease the cement strength. Failure of ceramic materials is

catastrophic, not a process of deformation as observed in polymers and metallic materials, and the strength is controlled or dictated by the largest defect in the material [223]. As every pore in a cement is structurally a defect, it holds to bare then that the failure of the cement is controlled by the largest defects present in the material. The native cement, with 0% mannitol, naturally contains pores in a variety of sizes, including occasional macropores introduced during mixing. Although the surface images do not appear macroporous, SEM images of the internal cement structures in Figure 5-10 confirm significant porosity, including some 50 μm+ sized pores and channels. Mercury porosimetry (Figure 5-8) results indicate however that the introduction of mannitol did not drastically increase the amount of macropores as anticipated. The addition of mannitol introduces more porosity to the structure until the material has more defects than the cement construct. The addition of more sub-micron sized porosity through mannitol dissolution would not result in significant further reduction in strength because the strength is controlled by the larger pores, which were already present. However, the introduction of more microporosity may result in more interconnected porosity yielding a larger over-all defect with increasing mannitol content. The trends in strength and porosity observations are further complicated by the fact that cement structures are composed of unique grains and crystals held together through some bonding and mechanical interference, as demonstrated in Figure 5-11 as well as in Chapter 3, and not dense as typically observed in sintered ceramic constructs.

Cytocompatibilty results from live/dead staining (Figure 5-12) and MTT and cell number assays (Figure 5-13) indicate that the addition of mannitol does not appear to improve or harm the MC3T3 osteoblast cell viability. Cell viability on all cement constructs is lower than on the tissue culture plastic, which is not unexpected as the cements are a dynamic system, with continuous dissolution of the various phases and the sugar crystals and changing the media pH

combined with ion concentrations changing constantly. It is encouraging that the magnesium ammonium cement embodiments are comparable to hydroxyapatite and brushite CPCs which are considered the industry standard in bone cements. However, mannitol was added to the magnesium phosphate cement with the intent to improve fluid flow and cellular infiltration into the constructs. The fluid flow objective was met, evidenced by the increasing porosity and magnesium and phosphorous ion levels. Cell number and activity levels however, did not seem to increase with increasing mannitol content. Indeed, although the overall porosity increased, the mannitol did not introduce significant additional macroporosity to the cement structure, indicated through mercury porosimetry results (Figure 5-8). While some macroporosity may have increased, the level does not appear to be enough to create interconnected macropores, preventing thorough cellular infiltration of the construct. There is also the potential that pH and ion levels within the cement porosity were more extreme than the levels measured in the media and this too reduced the driving force for inducing cellular infiltration. As some cells can be seen within the near-surface pores in the live/dead images (appearing round and out of focus), the lack of cellular infiltration is likely a combination of these two factors. The true effects of the addition of mannitol can only be observed in-vivo when the pre-molded constructs are implanted into a relevant animal model which is a likely direction to be continued in the near future to ascertain the true efficacy of the MPC derived by the ammonium phosphate solution approach.

5.5 CONCLUSION

Magnesium ammonium phosphate cements were successfully created with up to 50 weight % mannitol pore formers. Optimized powder-to-liquid ratios were chosen to yield clinically

appropriate handling characteristics and setting times of 10-15 minutes. All embodiments maintained a balanced pH and moderate cytocompatibility. Addition of even 10 weight % mannitol resulted in significantly increased porosity of the cement. The porosity of mannitol containing cements increased with increasing aqueous incubation, and the majority of this porosity was below 10 um, which prevented significant cellular infiltration. The addition of mannitol significantly reduced the compressive strength of the cement after aqueous solution incubation, with increasing mannitol content decreasing the strength. Given these results, it is recommended that a low level of mannitol addition (10-20%) positively improves porosity, while only moderately affecting the strength of the cement. The true efficacy of the system will however, be assessed only following in-vivo studies in suitable and relevant animal models.

6.0 SPECIFIC AIM 5: EFFECT OF FIBER REINFORCEMENT OF A MAGNESIUM AMMONIUM PHOSPHATE CEMENT WITH WETSPUN POLYCAPROLACTONE FIBERS

6.1 INTRODUCTION

While calcium phosphate cements have been the obvious choice as a repair scaffold because the chemical composition of these cements mimics that of native bone mineral, magnesium phosphate cement (MPC) formulations are an alternative to calcium phosphate forming cements [10]. MPCs have frequently been reported to display greater control over clinically appropriate setting times, greater compressive strength, and more rapid resorption and bone growth than their calcium phosphate counterparts [28-34]. Compressive strength for these cements often range up to 85 MPa [36-38, 56-59]. Ginebra et al recently explored MPCs for dental applications, showing pushout strengths greater than 20 MPa, intrinsic antibacterial capabilities and no foreign body response, inflammation or necrosis [28, 36]. Magnesium plays a vital role in bone calcification and density, metabolism of bone mineral and increasing bone cell adhesion and stability [19, 34, 42].

Although calcium and magnesium phosphate cements have become highly engineered medical devices, their use is ultimately limited to void filling and non-load-bearing applications due to the intrinsically brittle nature of the ceramic. While the compressive strength of these

cements are often greater than cortical bone and close to trabecular bone, the flexural strength leaves much to be desired [128]. Typical flexural strengths of calcium phosphate cements range from 5-15 MPa, compared to the 200 MPa flexural strength of cortical bone [26, 224, 225]. To improve the flexural strength and reduce the brittleness, reinforcement strategies may include compaction of the wet body, introducing bimodal particle size distributions, creating a dual-setting cement system and introducing fibrous reinforcement [226]. The concept of reinforcement through fibrous inclusions is widely utilized in the commercial cement industry to improve the fracture toughness and reduce catastrophic brittle failure of concrete [227]. The same principle, only at a smaller scale, is under exploration for ceramic bone cements. Use of polymer fibers may improve the toughness, decrease brittle fracture and improve the ability of the cement systems to withstand drilling stresses [228]. Reinforcement of calcium phosphate bone cements has been examined with poly(lactide-co-glycolide), chitosan, carbon nanotubes and bioglass as the fibrous inclusions [118, 119, 161, 226, 229-233]. The inclusion of biodegradable fibers can also serve as a mechanism to create porosity following *in vivo* implantation, which improves the implant's cellular influx and new bone growth [128].

In addition to creating porosity for cellular infiltration, the utilization of a biodegradable polymer such as polycaprolactone (PCL) provides the potential to deliver drugs or biologics during the degradation process. Osteomyelitis is a significant complication of orthopedic surgery, often resulting in secondary surgery to remove the infected implant [234]. Sustained, long-term delivery of antibiotics from the implant reduces or eliminates these concerns [235]. Antiobiotic loaded calcium phosphate cements have been explored in a variety of modalities, including mixing the antibiotic into the powder or liquid phase, and the addition of drug-loaded degradable microspheres or fibers [132, 134, 236-238]. Finally, the use of a biodegradable

polymer such as polycaprolactone (PCL) or poly(lactide-co-glycolide) (PLGA) may allow the degradation profile to be tailored to achieve optimal porosity evolution, allowing for exploring drug release, inducing cellular infiltration and ultimately causing bone ingrowth [239-242].

Wet spinning is one of the several synthesis techniques which can be used to create fibers for these applications [243-247]. Wet spinning involves dissolving the polymer of choice in a good solvent for the polymer then injecting this solution into a non-solvent coagulating bath, which leaches out the solvent leaving behind a pure, solidified polymer fiber [246, 248]. Similar to electrospinning, numerous factors affect the final morphology and materials properties of resulting fibers, including solvent and coagulant choices and draw ratio [243, 245, 246].

To date, fiber reinforcement of magnesium phosphate bone cements (MPBC) has not been explored. In this study, fibers of polycaprolactone (PCL) were generated through a wet-spinning mechanism. These fibers were then characterized and subsequently added to a magnesium phosphate cement (MPC) embodiment and the effect of these fibers on the cement properties was further explored.

6.2 MATERIALS AND METHODS

6.2.1 Fiber Generation and Characterization

Polycaprolactone (PCL, 70,000-90,000 MW, Sigma Aldrich) was dissolved in a 1:1 ratio of acetone and tetrahydrofuran at a concentration of 2.0 g/mL. The polymer solution was incubated at 37 °C and stirred for 24 hours prior to wet spinning. Wet-spinning was performed by injecting the PCL solution through a 16 gauge blunt-tip needle into a double coagulation bath of 98%

ethanol at a rate of 5 mL/hour. Ethanol is a poor solvent for PCL, thus serves as a coagulation bath, extracting the acetone and tetrahydrofuran and leaving the polymer fiber behind. Dual coagulation baths were used because this resulted in better solvent extraction and fiber drying. The linear collection rate of the PCL fibers was set to 250 cm/min to generate approximately 100 micron diameter fibers. A schematic of the wet-spinning set-up can be found in Figure 6-1. The fibers were dried in a desiccator for at least 24 hours, then cut into 1.5 mm long pieces using a scalpel and stored in a desiccator until use. Generated fibers were imaged through digital optical microscopy (Keyence VHX-600K) to measure the diameter and length of fiber pieces. The mechanical strength of the fibers was tested through tensile testing of individual fibers (MTS Insight 1SL) at a rate of 25 mm/min to rupture.

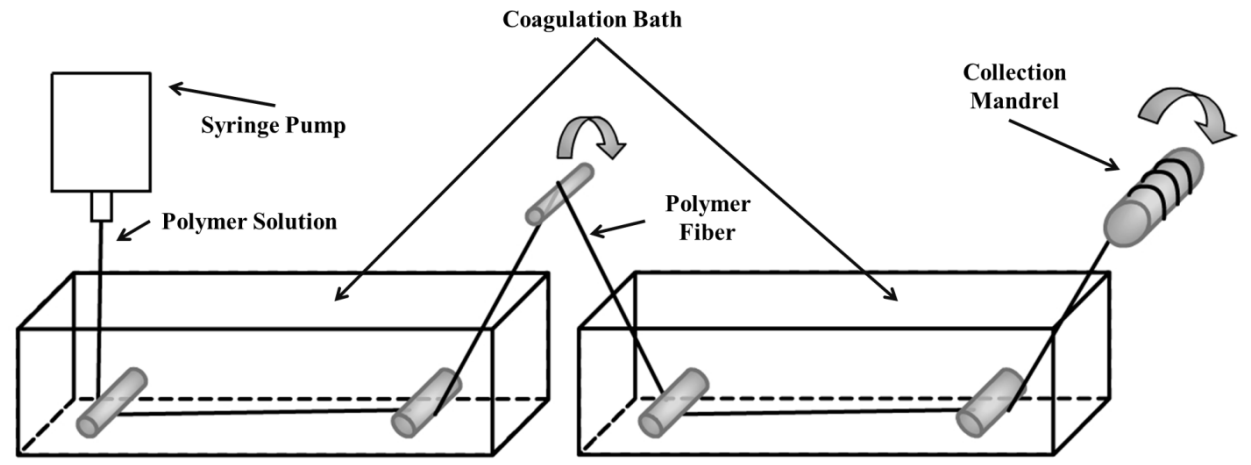

Figure 6-1 Schematic of the wet spinning set up.

6.2.2 Cement Generation

The cement formulation consisted of $Mg_3(PO_4)_2$ (TMP, Sigma Aldrich) combined with the as-prepared PCL fibers and a pH 7.0 ammonium phosphate solution. The commercially obtained

TMP powder was thermally treated for 6 hours at 1000 °C under air in order to decrease the powder surface area below 1.0m^2/g thus reducing the powder reactivity. The 3.0 M, pH 7.0 ammonium phosphate solution was made by combining appropriate amounts of monoatomic and diatomic ammonium phosphate salts at a ratio of 2:7 monoatomic:diatomic salt in deionized water. The thermally-treated TMP powder was gently mixed with the PCL fibers, at 0 %, 5 %, 7.5 %, 10 %, and 15 % fiber content by weight to create the cement powder. The cement powder was then mixed with the ammonium phosphate solution at 0.83 mL solution per 1 gram of TMP powder, maintaining a consistent powder-to-liquid ratio of 1:0.83 independent of the fiber content. Putties were mixed for 60 seconds, then lightly pressed into molds, and dried at 37 °C overnight prior to further testing as outlined in Chapter 5 for the mannitol containing cements.

6.2.3 Cement Characterization and *In Vitro* Dissolution

First and second setting times of cement pastes were determined using the Gilmore needle test at room temperature following the ASTM standard C266-13 at room temperature and handling characteristics were qualitatively assessed based on consistency and handling ease as for the mannitol containing cements discussed in Chapter 5 and for non-mannitol containing cements in Chapter 3. Cement phases were identified through x-ray diffraction. Fourier transform infrared (FTIR) spectroscopy was used to identify or analyze any differences in molecular linkages between cements. Cements were also observed under scanning electron microscope as introduced in Chapter 2. Specific surface area (SSA) was measured as well as true density and apparent density, which were used to calculate percent porosity as outlined in the earlier chapters. The percent porosity is then calculated from the envelope and true densities following Equations 4-3 and 4-4 as previously described in Chapter 4.

Cement strengths were analyzed in compression and 3 point bending modalities. For compression testing, cement cylinders, nominally 6mm diameter by 13 mm height, were utilized and for 3 point bend testing, rectangular cement constructs 4.5 mm by 4.5 mm by 16 mm long were utilized. Compression testing was completed following modified ASTM D 695 and ASTM C39 methods employing a 2 kN load cell at a crosshead speed of 1.0 mm per minute (Instron, Norwood MA). Bend testing was completed following modified ASTM C1609 method, employing a 500 N load cell, with a span between contact points of 13.5 mm and a crosshead speed of 0.05 mm per minute to 0.15 mm displacement then 0.10 mm per minute to 0.30 mm displacement. For both sets of mechanical testing, cements were incubated in phosphate buffered saline (PBS) at 37 °C prior to testing to determine the change in strength due to aqueous incubation. PBS incubation time points were 0, 1, 5, 15 and 30 days with 4 samples considered for each time point for each test. Strength measurements were calculated following Equation 6-1:

Equation 6-1

$$f=PL/bd^2$$

Where f is the strength in Mpa, P is the load in N, L is the span length (13.5 mm), b is the sample width and d is the sample height, both in mm. Peak strength was calculated using Equation 6-1 with the maximum strength obtained before initial failure of the sample. L/50 residual strength was calculated following Equation 6-1 using the load at a displacement of L/50, or 0.27 mm. Fracture toughness was determined by integrating the stress-strain plot to determine the area under the curve at the peak strength displacement and at L/50 displacement. The area

under the curve, recorded as toughness, is in Joules (J). Samples of the post-fracture cements were then imaged under SEM in order observe the fracture-surface morphology.

Cement pellets were incubated in PBS at 37 °C at a concentration of 10 mL of PBS per 1 gram of cement. The PBS was changed every 24 hours, and the pH and sample weight was measured at east time point (1, 3, 5, 7, 15, 30 days) during the study. Samples incubated in PBS were dried overnight at 37 °C and characterized through XRD, FTIR, SSA, density and SEM, under the conditions outlined above, in order to assess changes in the cement from the as-generated stage due to the aqueous solution incubation.

6.2.4 Cell viability

MC3T3 cells were grown on cement substrates, following THF incubation to remove the fibers, to demonstrate cell viability and short-term ingrowth into pores. Fiber removal was confirmed through visual inspection. Cells were cultured and seeded as previously described in Chapter 5 for the mannitol containing cements. After 24 hours, live/dead staining was completed after which samples were fixed, dehydrated and sputter coated for SEM observation using the procedure described in Chapter 2.

6.3 RESULTS

6.3.1 Fiber Characterization

The use of a dual ethanol coagulation bath wet spinning system to create PCL fibers reliably generated opaque fibers of approximately 100 µm diameter under the conditions stated above. The arithmetic mean was 101.3 ± 15.5 µm while the geometric mean was 100.1 ± 1.7 µm. The cut fibers averaged a length of approximately 1.45 µm, with the arithmetic mean 1.45 ± 238 mm and the geometric mean 1.426 ± 0.012 mm. A total of 150 fibers were measured for each diameter and length calculations. An example image of the fibers can be seen in Figure 6-2.

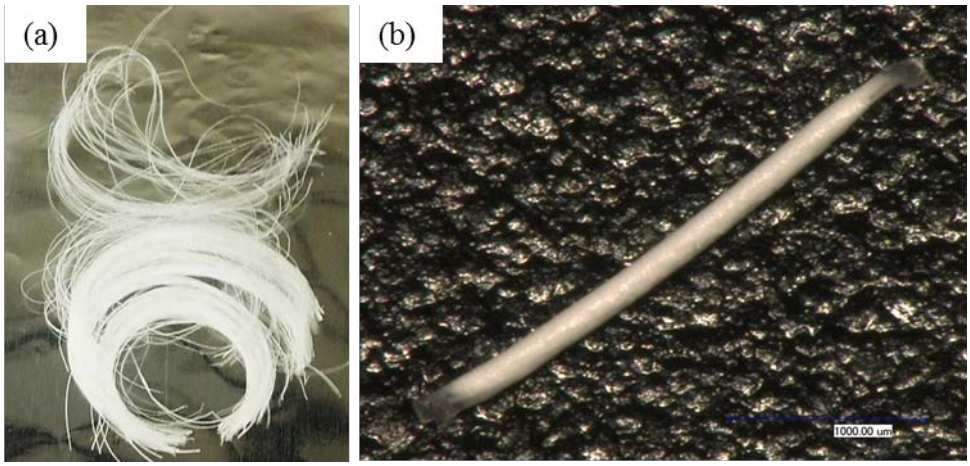

Figure 6-2 Macroscopic (a) and optical microscopy (b) image of the PCL fibers derived by wet-spinning.

Table 6-1 shows the mechanical properties of the individual fibers tested in tension to failure (average of 14) and an example of the representative stress-strain curve can be seen in Figure 6-3. The fibers were able to undergo a large amount of plastic elongation prior to rupture

as expected, on average more than 600%. Engineering and True stress and strain are reported due to the large amount of deformation the fibers experience before failure. This level of deformation is expected to improve the flexibility and toughness of the cement while reducing the ultimate strength of the cement.

Table 6-1 Mechanical properties of fibers at failure.

Max Load (N)	Engineering Stress (MPa)	True Stress (MPa)	Engineering Strain	True Strain	Elongation (%)
0.21± 0.045	19.3 ± 4.9	119.0 ± 45.0	5.21 ± 2.47	1.91 ± 0.33	637 ± 119

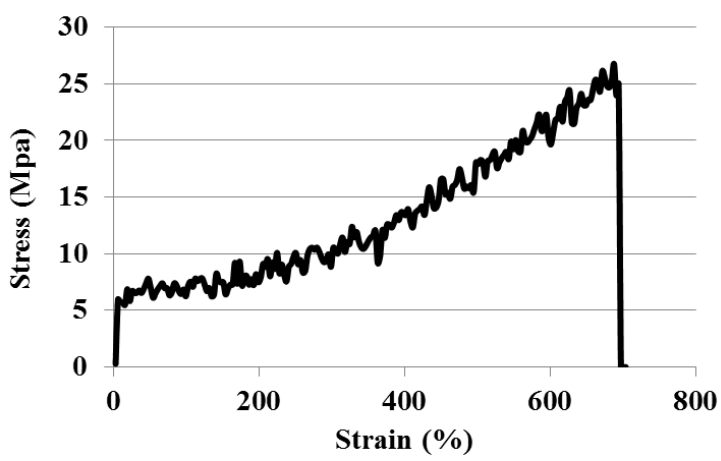

Figure 6-3 Example Fiber Stress-Strain Curve.

6.3.2 Cement Characterization

Cements were generated with up to 15 weight % PCL fiber and resulted in setting times (ST) of 6:30-9:00 minutes 1st ST and 12:30-15:00 minutes 2nd ST, as depicted in Figure 6-4. A general trend of reduced set time with increasing fiber content was observed. No statistically significant differences exist between the 1st ST of the samples. However, significant differences exist

between the 2nd STs of the cements, specifically 0% and 7.5% fiber content are significantly larger than 5%, 10% and 15% fiber containing cements. Up to 10 % fiber resulted in a putty which was moldable but not flow-able at the given liquid content. At 15 % fiber, the cement consistency during mixing was sponge-like and difficult to handle. After final setting however, all embodiments resulted in cement bodies which were durable to the touch and easy to handle.

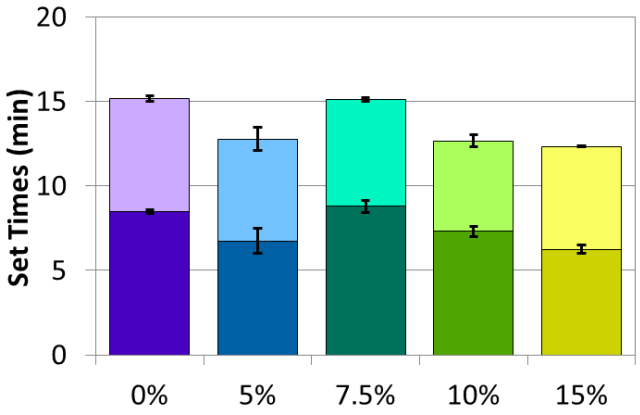

Figure 6-4 First and second setting times of fiber containing cements

The cements were incubated in PBS at 37 °C, and initial properties as well as changes due to aqueous incubation were analyzed. In Figure 6-5 are shown the XRD patterns obtained from the as prepared cements and after 30 days immersion in PBS. Phases present in the initial cement resulting after reaction and setting were unreacted precursor TMP ($Mg_3(PO_4)_2$, ICCD 00-033-0876, +), struvite ($MgNH_4PO_4 \cdot 6H_2O$, ICCD 98-002-2086, *) and newberyite ($MgHPO_4 \cdot 3H_2O$, ICCD 00-035-0780, #) in addition a small amount of hannayite ($Mg_3(NH_4)_2H_4(PO_4)_4 \cdot 8H_2O$, ICCD 98-000-6099, $). Following 30 days of incubation in PBS, struvite and newberyite were the dominant phases, with a significant amount of unreacted TMP

remaining but with no hannayite similar to the trend observed in mannitol containing cements discussed in Chapter 5.

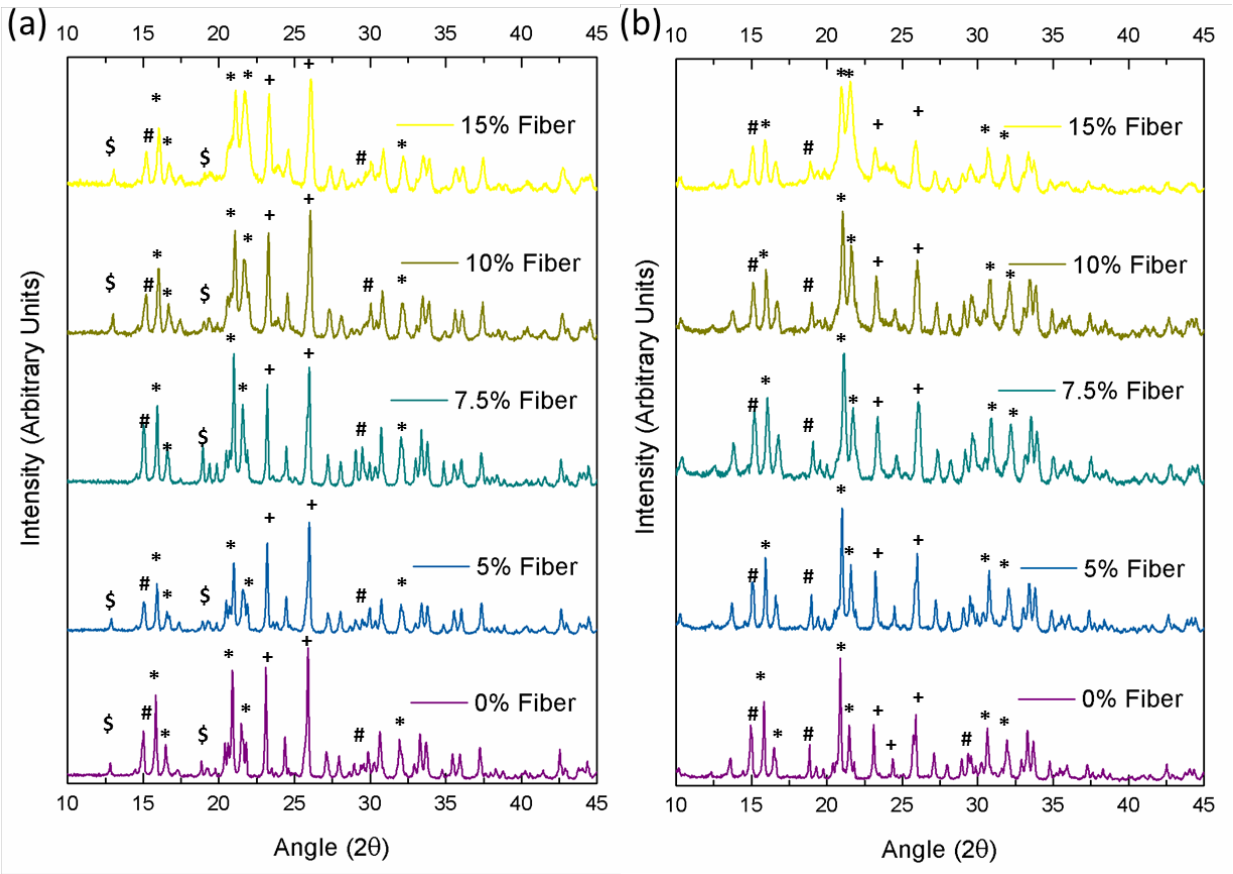

Figure 6-5 X-ray diffraction spectra of cements at (a) 0 days and (b) 30 days of incubation in PBS. Phases present are denoted: struvite (*), newberyite (#), unreacted trimangesium phosphate (+), and hannayite ($).

Figure 6-6 shows the FTIR spectra of cements at 0 (a) and 30 (b) days of incubation in PBS at 37 °C, as well as the FTIR spectra of the PCL fiber for comparison. PCL fiber is occasionally detected in the cement spectra, such as the 10 % fiber sample at 0 days, particularly notable around the 1750 cm^{-1} wavenumber. However, given the composite nature of the cement,

the fiber is not observed in all samples. Beyond the bands indicative of PCL, no differences are seen between sample types or time point measurements. Typical bands corresponding to PO_4, water, OH and NH_4 vibrations are also seen in all samples as is the case for the cements discussed in Chapter 5. As these bands are identical to previous analysis, a more detailed discussion of specific FTIR band wavelengths of the magnesium ammonium cement formulation can found in Section 3.3.3 with corresponding Figures 3-10 & 3-11.

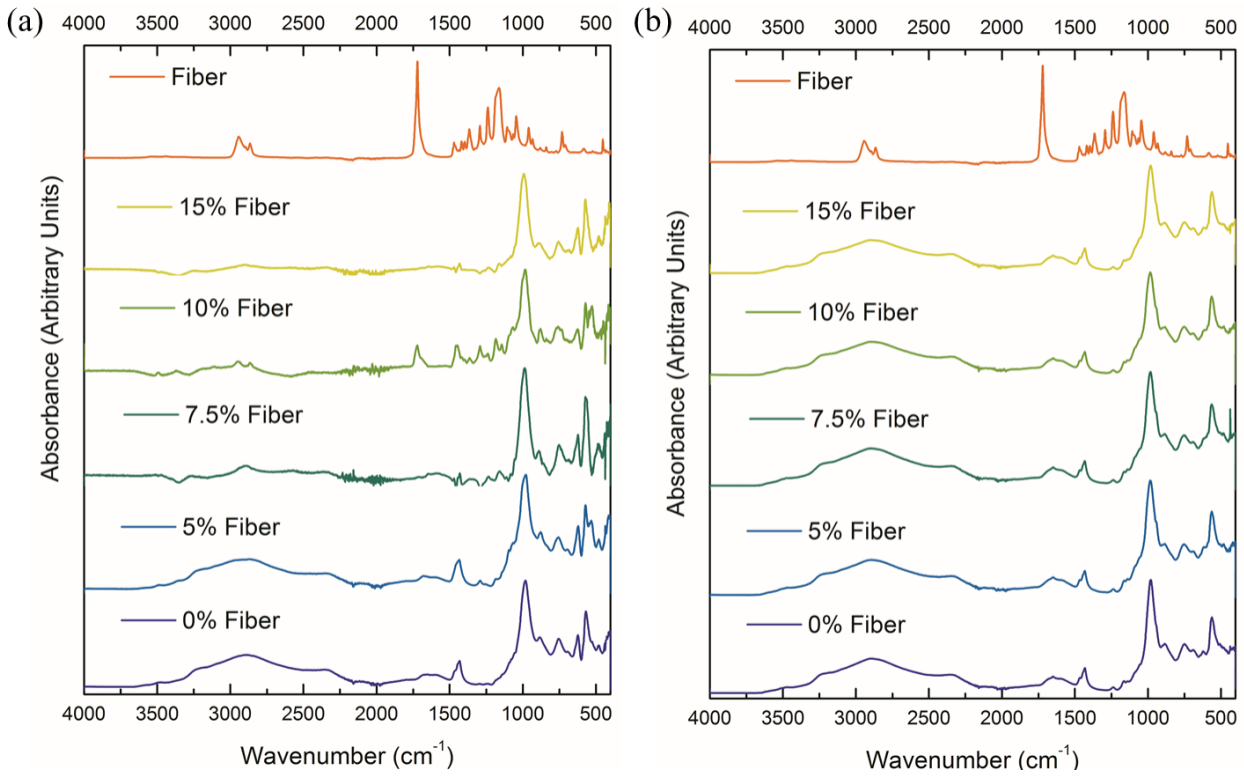

Figure 6-6 FTIR spectra of cements at 0 days (a) and 30 days (b) incubation in PBS at 37 °C.

In Figure 6-7 is displayed the pH and weight change measured through 30 days in PBS. Measurements of PBS (6-7a) throughout cement incubation indicates that there is an initial mild drop in pH to 7.0-7.25, likely due to any unreacted solution dissolving, followed by an increase in pH to approximately 7.50-7.75 for all the samples. This measurement plateaus after 3 days,

with only slight variations seen through 30 days of incubation in PBS. Figure 6-7b shows the change in weight of samples through the same 30 day period. These measurements, collected on the wet samples at each time point, indicate an initial increase in cement weight of 6-7%, a value which remains constant throughout the times points observed. There is no significant difference between conditions at any time point, or between time points for each condition.

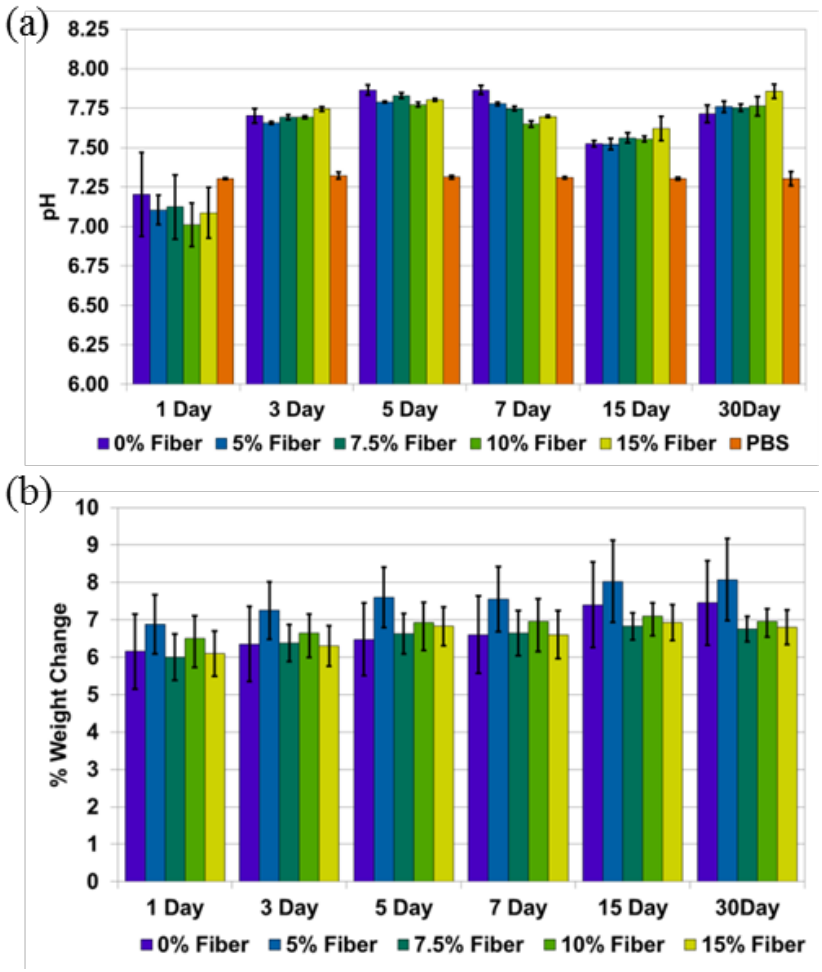

Figure 6-7 pH (a) and weight change (b) of cements through 30 days of incubation in PBS.

In Figure 6-8 are the density trends of the magnesium phosphate fiber reinforced cements (MPFRC) cements incubated in PBS through 30 days at 37 °C. These measurements are of n=1

and are used only as an indication of the expected trends. True density measurements (a) show a decrease with increasing fiber content, from 2.5 g/cm^3 at 0% fiber to 2.0 g/cm^3 at 15% fiber, which is to be expected as the polymer true density is lower than the cement true density. Following THF immersion inducing dissolution of the PCL, true density of all samples is nearly the same (2.4 g/cm^3), indicating the complete removal of the PCL from the cement structure. There is a mild trend of decreasing true density with PBS incubation, which may be caused by water incorporation and cement product hydration as well as through new crystal growth within the porous structure of the cement.

Envelope density (b), or apparent density, shows a similar trend of lower density with increasing fiber content, from 1.62 g/cm^3 at 0% fiber to 1.45 g/cm^3 at 15% fiber. The apparent density following THF incubation is quite similar to the initial apparent density after cement generation for each sample, indicating that the apparent density is heavily influenced by the innate porosity of the cement. Here there is a mild trend of increasing apparent density with increasing PBS incubation time, which may similarly be a result of cement hydration or new crystal growth during incubation.

Porosity measurements (c) indicate some decreasing porosity of the as-generated cement with increasing fiber content, from 38% at 0% fiber to 29% with 15% fiber. As the wet-spun fiber are by nature mostly dense constructs and the cement is innately porous, this trend is anticipated; the higher over-all cement content yields a higher initial porosity value. Porosity levels decrease slightly with increased PBS incubation, corresponding well to the decreased true density and increased apparent density seen in (a) and (b). Less expected, porosity measurements following THF incubation indicate all samples contained 50-55% porosity, which is a large increase event especially for the 0% fiber cements. This may be attributed in part

dehydration of the cement scaffold from the solvent incubation resulting in loss of water and adsorbed solvents.

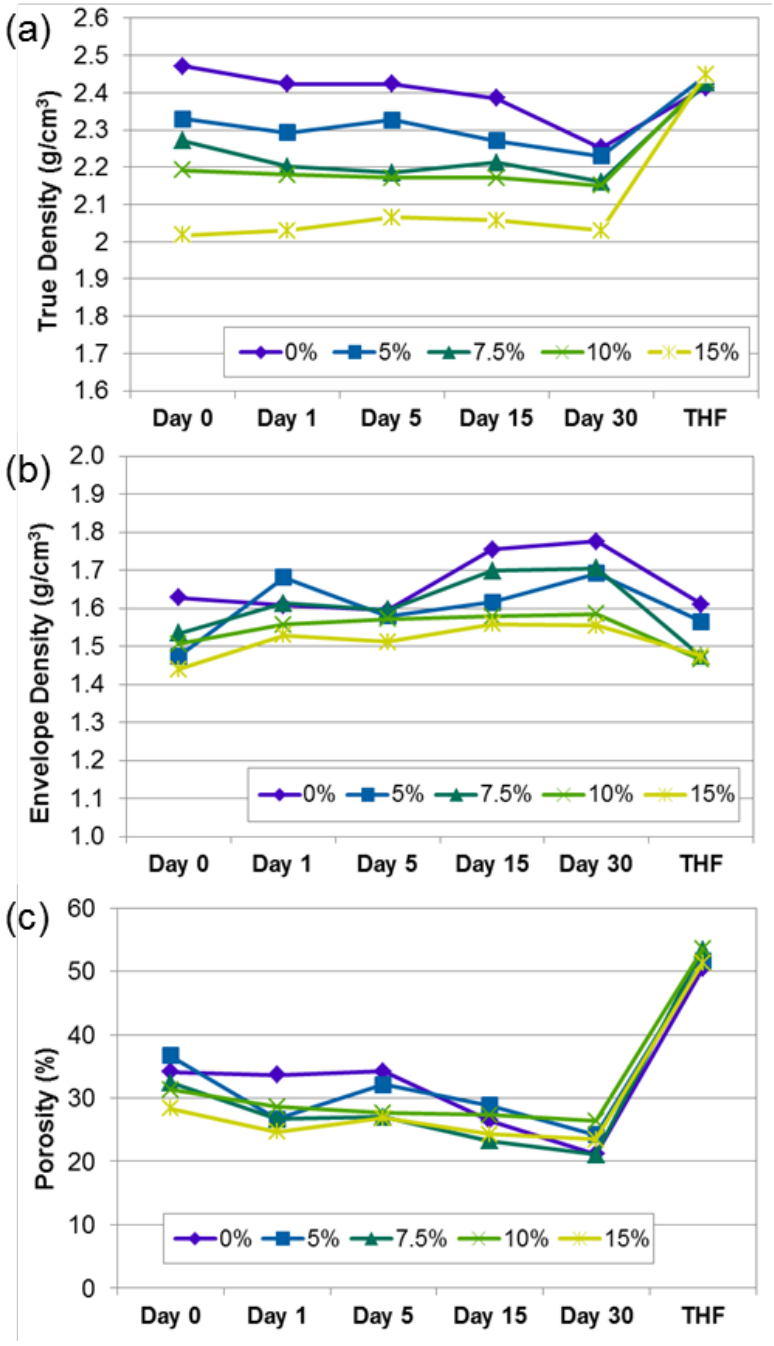

Figure 6-8 Density trends of cements through PBS incubation and with the PCL fibers removed (labeled THF) showing the true density (a), envelope density (b) and porosity (c).

In Figure 6-9 is plotted representative log differential (instantaneous) and cumulative mercury intrusion porosimetry of cement samples as generated and following THF incubation to remove the fibers. Mercury intrusion is utilized to assess pore size distribution of the cement. Results of instantaneous intrusion of the as generated cement (a) indicate all samples contain some level of macroporosity (around 100 μm in size) as well as a significant amount of microporosity (3 μm and below). Following THF immersion (b) to remove PCL fibers, the level of macroporosity increases with increasing fiber content. These macropores range from 50-100 μm in size matching the fiber diameter in general. Cumulative mercury intrusion indicates slight differences in porosity in the as generated cements (c) while the THF incubated samples (d) indicate the increased macroporsity of fiber containing cements.

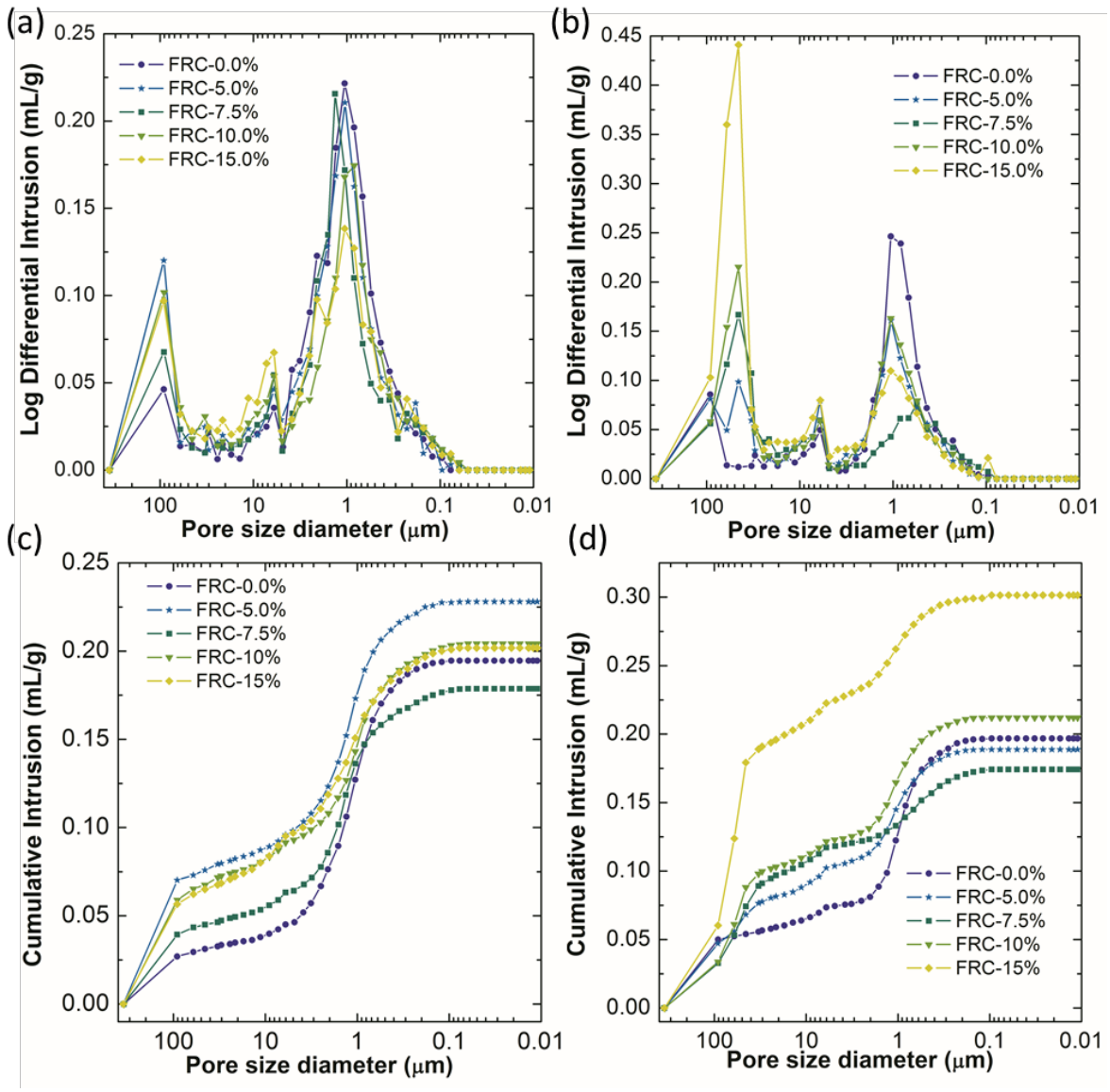

Figure 6-9 Mercury intrusion porosimetry depicting the log differential (or instantaneous) intrusion volume of cements as generated (a) and with PCL fibers removed (b) and cumulative intrusion volume of cements as generated (c) and with PCL fibers removed (d).

In Figure 6-10 are representative force-displacement curves obtained following the 3 point bending modality of cements with varying amounts of fiber content. These representative images demonstrate increasing residual strength following peak fracture with increasing fiber content in the cement, indicated by arrows in each image. These plots point to the fact that,

through with the inclusion of up to 15 weight % wet-spun PCL fibers, the cement failure remains within the pseudo-strain hardening modality.

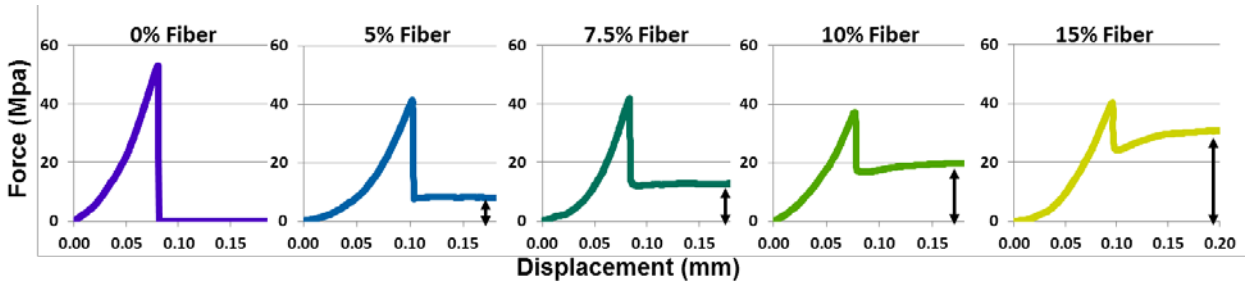

Figure 6-10 Representative force-displacement curves in 3-point bending of fiber reinforced cements.

In Figure 6-11 are 3 point bend strength of the cement samples at (a) the peak strength and (b) L/50 residual strength through 30 days of incubation in PBS. L/50 is indicative of a measurement at a fracture displacement distance of the sample length/50 as an indication of 'residual' strength or toughness following initial peak strength measurements. At Days 0, 1 and 5 there are no statistical differences in the peak strength values (a) of the cements, however there is a very high level of variability in several of the sample sets. At Day 15 and 30 the 0% fiber samples are significantly stronger than all of the fiber containing cements and the 5% fiber cements are significantly stronger than the 15% cements. A trend of decreasing strength with increasing fiber content at longer incubation times is thus observed. Additionally, while this study lacks the statistical power to confirm, there appears to be an increase in cement strength at longer PBS incubation time points, particularly with the 0% fiber cement samples. The residual strength measurements (b) indicate increasing residual strength with increasing fiber content. At all the time points, all fiber-containing cements demonstrated non-zero residual strengths, in comparison to the complete failure and resulting zero residual strength of the 0% fiber cement.

Within each time point, lower fiber content results in statistically lower residual strength broadly, but may not be statistically different than one step change in fiber content. For example, 5% fiber samples are never significantly lower than 7.5% samples, but are nearly always significantly lower than 10% (Day 30 notwithstanding) and always significantly lower than 15% samples. Cements with 15% fiber demonstrated high residual strengths than all other samples at 0, 1, 15 and 30 days of PBS incubation, but were not significantly higher than 10% fiber cements at Day 15.

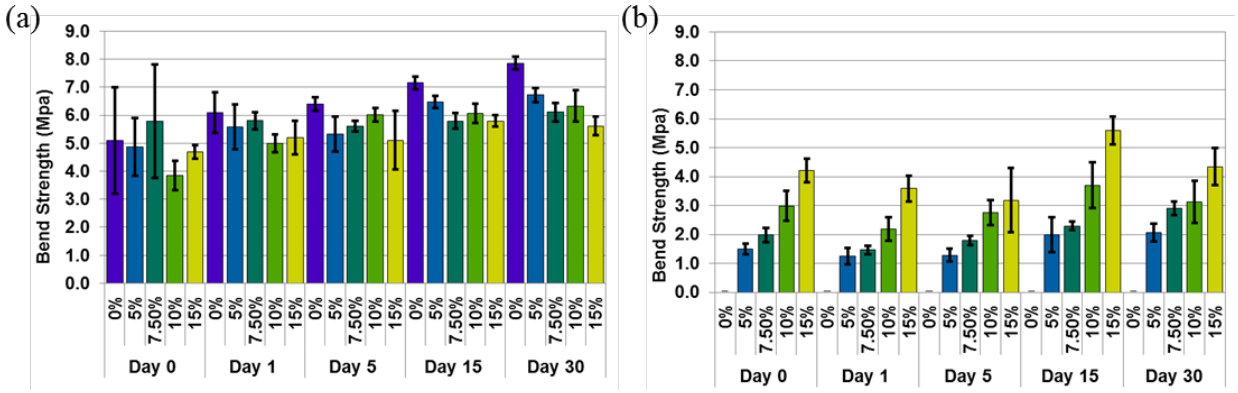

Figure 6-11 3 point bend strength of cement samples at (a) the peak strength and (b) L/50 residual strength through 30 days of incubation in PBS.

Toughness under 3 point bending of cement samples is shown in Figure 6-12 at (a) the peak strength point and (b) L/50 residual point through 30 days of incubation in PBS. Through all the tested time points, there is no significant difference in measured peak toughness of samples at any given time point. The initial peak toughness did increase in the 30 day measurement over the earlier time points, from an average of nearly 2 J to 3 J in all samples. Residual toughness is a measure of the total energy absorbed during testing through a facture displacement of L/50. Here again the influence of fiber content can be seen, with all fiber-

containing samples demonstrating significantly high toughness than the 0% fiber cement at every time point studied. Similar to 6-11b above, the increasing fiber content increases the toughness measurement globally, but one step in increased fiber content generally does not lead to a statistically significant increase in toughness. Cements containing 5% fiber demonstrated statistically lower toughness values than 10 and 15% fiber cements at day 0 and lower strengths than 15% fiber cements at each other time point. Cements containing 15% fiber demonstrated statistically higher residual toughness than 5 and 7.5% and 10% fiber cements at days 0, 1, 15 and 30.

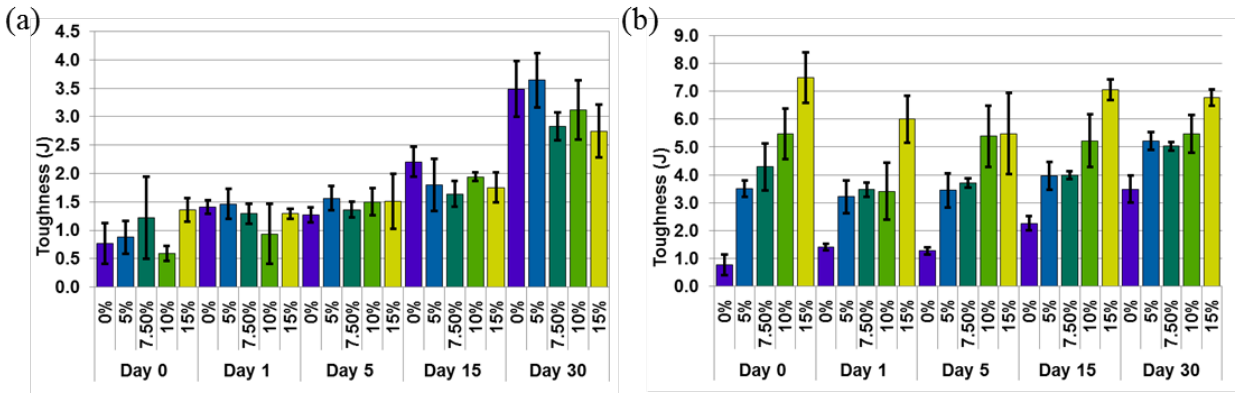

Figure 6-12 Toughness under 3-point bending of cement samples at (a) the peak strength point and (b) L/50 residual point through 30 days of incubation in PBS.

For comparison purposes, compressive strength of cements at the same PBS incubation time points were measured, the results of which can be found in Figure 6-13. Here there is a high level of variability in each sample set, and there is nearly no statistically significant differences among the compressive strengths measured. Only the 15% fiber cements demonstrate statistically a gradual (not statistically significant) decrease and then increase in strength throughout the 30 days of PBS incubation.

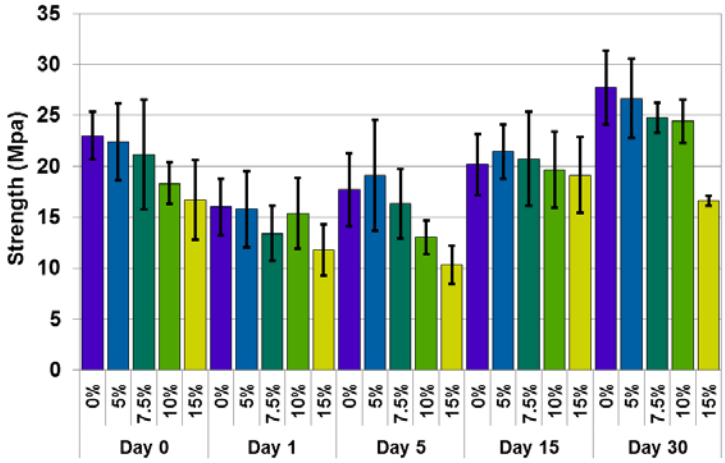

Figure 6-13 Compressive strength of fiber reinforced cements through 30 days of incubation in PBS.

Figure 6-14 and 6-15 contain SEM images of the external surface (6-14) and internal fracture surface (6-15) of cements at 0, 1 and 30 days of incubation in PBS. The scale bar here is 100 µm. Figure 6-14 indicates a smooth pressed surface with PCL fibers emerging from the surface of those cements which contain them. Following only one day in PBS the cement surface morphology demonstrates the evolution of new crystal growth on the surface. These crystals are of a hexagonal morphology. At 30 days in PBS, this crystal growth is more wide spread, as crystals appear to have grown over the surface of the polymeric fibers as well, a distinct difference from the smooth fiber morphology observed in the day 0 images. The additional crystals grown at extended PBS incubation are smaller in size and of a more rounded morphology. Figure 6-15 depicts the fracture surface morphology of the cements which were tested beyond L/50 displacement in mechanical testing discussed above, with the scale bar at 50 µm, showing a more zoomed in picture of the internal surface. These images show a fine crystal size within the as-generated cement and a smooth interface between the cement and polymer

fiber. Following PBS incubation similar hexagonal crystals are observed in many of the cement images.

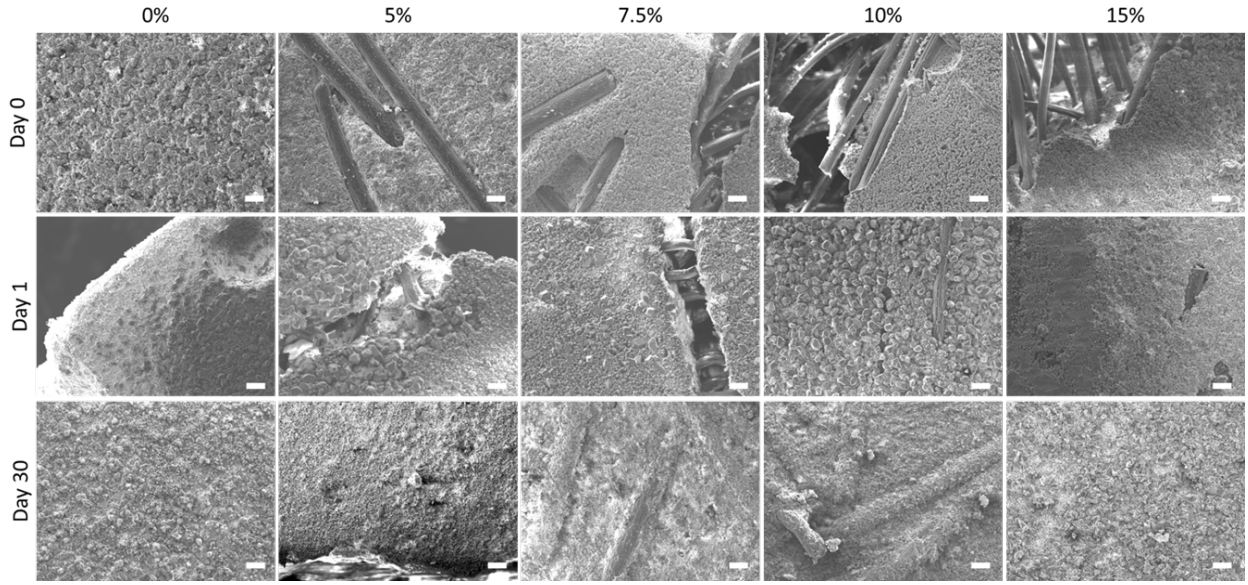

Figure 6-14 SEM images of the external (pressed) surface of fiber containing cements as generated and at 1 and 30 days of incubation in PBS at 37 °C (100µm scale bar).

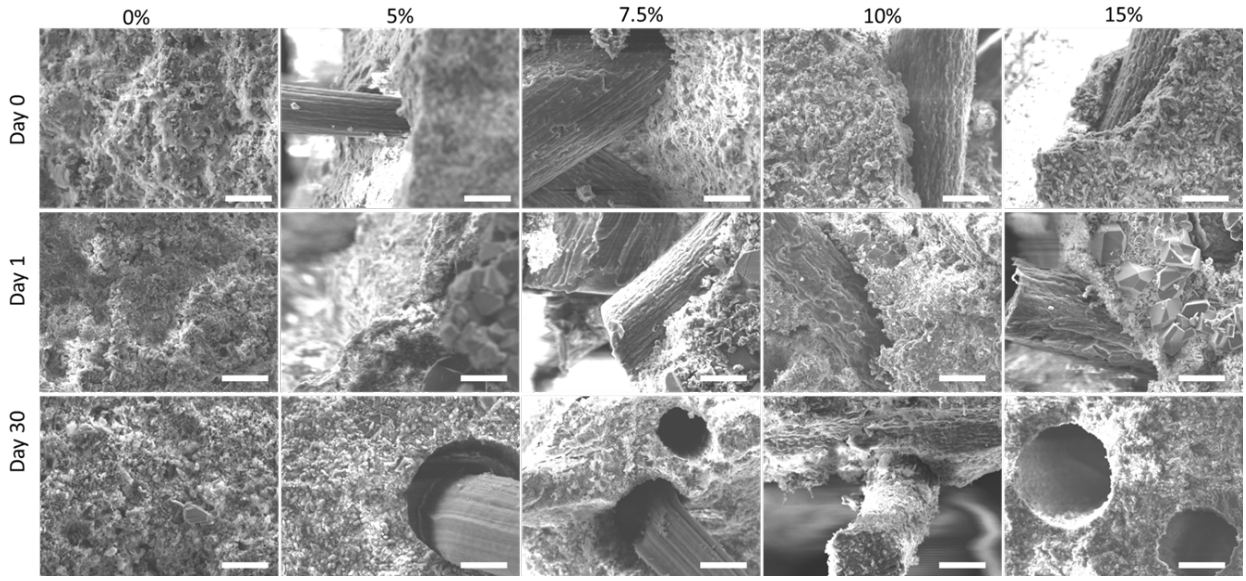

Figure 6-15 SEM images of the internal (fracture) surface of fiber containing cements as generated and at 1 and 30 days of incubation in PBS at 37 °C (50um scale bar).

Figures 6-16 and 6-17 show representative live/dead staining and SEM images (respectively) of MC3T3 osteoblast cells growing within the macroporous structure created after the PCL fibers had been removed through THF incubation. Live/dead images show consistent cell viability, independent of pore former content, as well as cell growth within the pores, seen as spherical shaped cells significantly out of focus. SEM images indicate the cells are well attached within the pore structure, not merely deposited or floating within the pores.

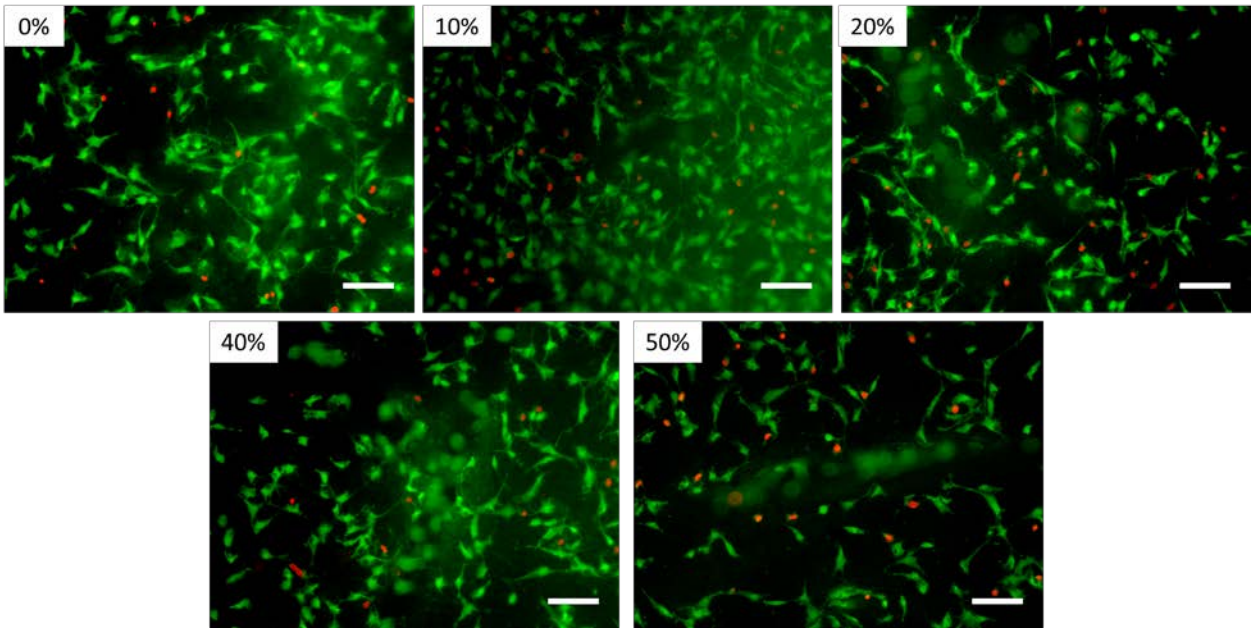

Figure 6-16 Live/dead staining of MC3T3 cells on magnesium ammonium cement scaffolds after fiber leaching (Scale bar is 100 μm).

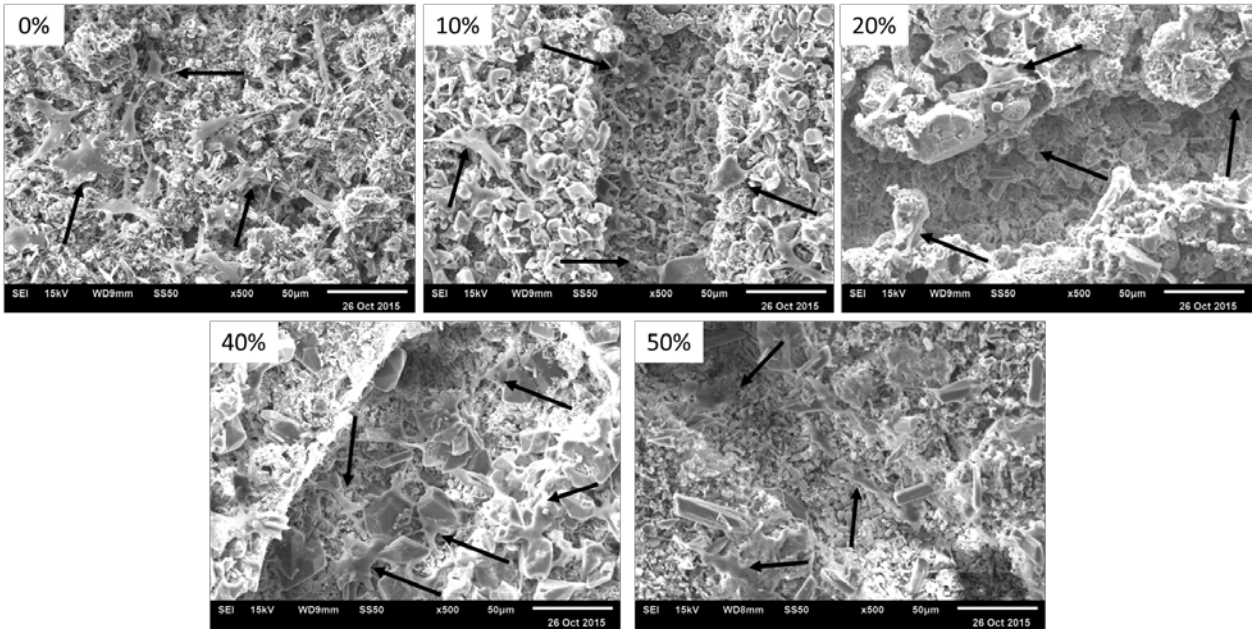

Figure 6-17 SEM images of MC3T3 cells on magnesium ammonium cement scaffolds after fiber leaching (Scale bar is 50 μm).

6.4 DISCUSSION

The use of fiber reinforcement in cement and concrete materials has its roots in common industrial practices, particularly the use of steel rebar to toughen concrete for building construction. The use of fiber reinforcement for calcium phosphate bone cements (CPCs) has been the subject of both academic and industrial investigation, exploring natural and synthetic polymers as well as ceramics [128, 249]. Fiber reinforced cement (FRC) is a general term which can refer to the use of short fibers, long fibers, short bundles of fibers, yarns of twisted fibers and woven structures and these fiber constructs can be randomly oriented or intentionally directional in their orientation [249]. In this study, individual 100 μm diameter fibers of polycaprolactone cut to a short length (1.5 mm) are utilized in a random orientation. In published studies, short lengths individual fibers or yarns are most commonly used, with fiber diameter ranging from 30 nm to 350 μm and length ranging from 30 nm to 200 mm. These properties, in addition to several others shown in Figure 6-18a play a significant role in mechanical behavior of FRCs and ultimately control the failure modality of the cement, from brittle to quasi-brittle (tension softening) to ductile (strain hardening), the stress stain curves and failure depictions of which are shown in Figure 6-18b [249].

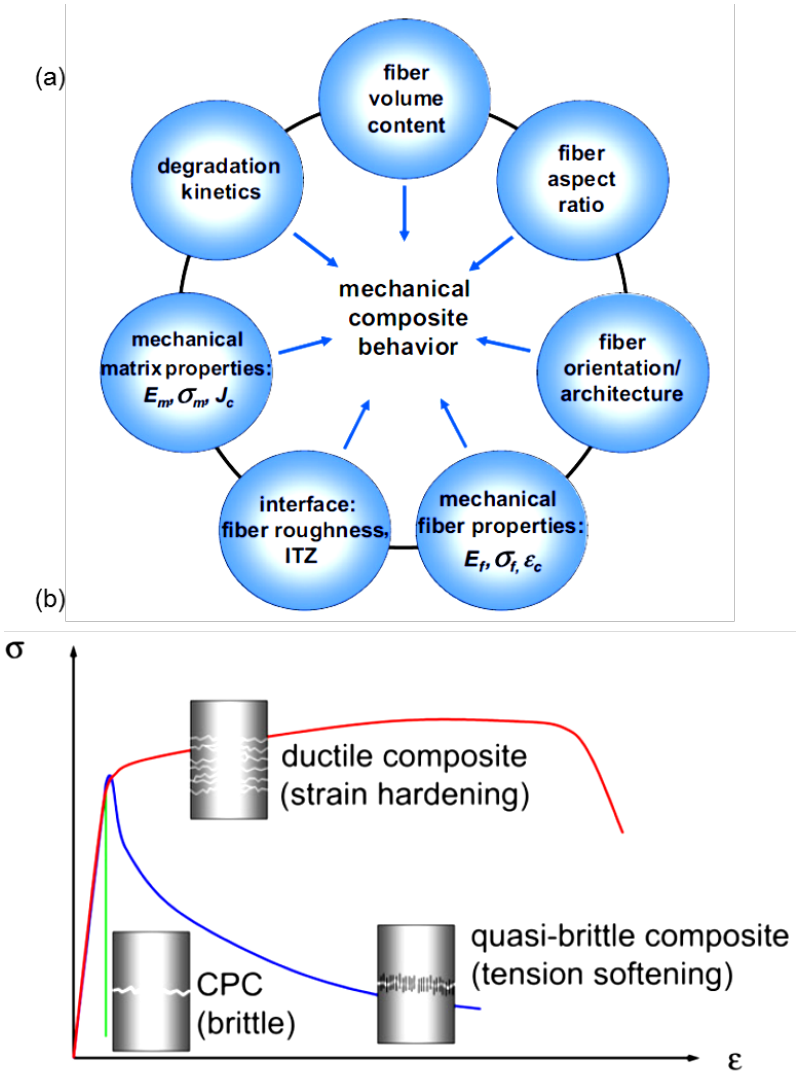

Figure 6-18 Material parameters affecting mechanical behavior of FRCs (a) and representative stress-strain curves of FRCs failing through brittle, tension softening or strain hardening modalities, taken from Krueger et al. [249].

Wet spinning was used to create the PCL fibers used in this study. As previously described, wet spinning is a relatively simple, inexpensive, small scale process to create polymeric fibers of diameters larger than electrospinning [245, 246]. It also lends the capability to incorporate drugs and biologics, particularly heat-sensitive drugs, into the fiber construct [243-245]. Wet spinning does have its disadvantages, including lower tensile strength than melt-

extruded fibers of the same diameter and the use of significant volume of solvents in the coagulation bath.

In order to create the polymer fibers, a “good” solvent formulation and “poor” solvent were chosen for PCL with the aid of the thorough work of Luo et al evaluating the effect of solvent-polymer solubility and dielectric constant on the electrospinning of PCL [248]. Numerous parameters required optimization, include solvent ratios (acetone:THF), volume content of polymer, flow rate and needle gauge size, collection speed and coagulation bath configuration. Altering a variety of these parameters including solution concentration, polymer molecular weight, solvent and coagulant bath chemicals and collection rate yielded a wide variety of fiber diameters and morphologies. For the sake of brevity of the thesis, the details of the various optimization parameters studied and tested are not presented here, but several authors have evaluated the role of these and other parameters on the resulting wet-spun fiber product [243-245, 247].

The fibers created with the described set up were smooth and opaque (Figure 6-2), with a reliable diameter of 100 μm, optimized to allow for cellular infiltration after fiber degradation. Fibers experienced very little elastic deformation before undergoing massive plastic deformation (Table 6-1 and Figure 6-3), greater than 600%, under tensile testing to failure. Deformation induced a visual change from being opaque to transparent in the visual examination of the optical transparency of the fibers, noticeable on the cut ends of the fiber in Figure 6-2b. Fibers were added at 5, 7.5, 10 and 15 weight % to the TMP. Studied concentrations in the literature range from 0.2-30 weight % fiber addition however fiber content greater than 3 volume % typically result in poor workability and injectability of the cement [128, 249]. The length of the fibers was

chosen based on Krueger et al to meet the critical length requirement based on the desired 100 μm diameter.

The addition of PCL fibers to the magnesium ammonium cement matrix slightly reduced the cement setting time (Figure 6-3). No statistically significant differences exist between the 1st ST of the samples, however significant differences exist between 2nd STs of the cements, specifically 0% and 7.5% are significantly larger than 10% and 15% similar to what has been reported by others. It did not however affect the cementing reaction, demonstrated through XRD (Figure 6-5) and FTIR (Figure 6-6). Similarly, the addition of the fibers did not significantly affect the pH or weight change of the cement constructs through 30 days in PBS. The addition of polymeric fibers reduces the true density of the bulk cement (Figure 6-8a) and following fiber leaching, leaves behind a large increase in porosity as expected (Figure 6-8c). The removal of fibers results in substantially more macropores (> 50 um), increasing with increasing fiber content. Live/dead staining (Figure 6-16) and SEM imaging (Figure 6-17) of MC3T3 cells grown on cement constructs with the fibers removed indicate that, unlike mannitol porogen cements studied in Chapter 5, the 100 μm PCL fibers leave behind well formed macropores which can facilitate cellular in-growth. Cells are seen as spherical and out of focus in live/dead staining, indicating that they are within the fiber channels, and SEM imaging confirms that the cells within the channels are well adhered to the cement, not floating. As discussed in Chapter 5 however, proper fluid flow and interconnected porosity are required for optimal cement integration and remain concerns with these cements as well.

The inclusion of fibers in cements is intended to reduce or eliminate the catastrophic brittle failure which these materials undergo. Including fibers improves the toughness of the material through a complex set of mechanical interactions between the fibers and cement matrix.

Depending on the design, mechanical failure can transition from brittle failure to tension softening (quasi brittle) failure to strain hardening behavior [249]. Quasi-brittle failure demonstrates a maximum fracture strength through the matrix material followed by reduced residual ductility and strength through the fiber pullout, fracture or plastic deformation. In contrast, strain hardening behavior demonstrates initial matrix failure but greater yet maximum fracture strength through the energy dissipation of the fibers, resulting in hardening through additional strain. Energy adsorption through the fiber-matrix interactions can result from several mechanisms including interface debonding, fiber pullout and fiber deformation. The tensile strength and elastic modulus of fiber play an important role in the reinforcement. A high tensile strength and elastic modulus facilitate stress transfer to the fiber from the matrix as a whole at large failure strain levels giving the cement high extensibility [128]. Compared to melt-extruded fibers, the wet spun fibers created here demonstrate low tensile strength and long, low modulus plastic deformation but high strain to failure.

Evaluating the effect of fiber reinforcement on cement mechanical properties requires evaluating not only compressive testing but flexural testing. Compressive testing cannot be used to evaluate changes in toughness and is not sensitive to the effects of fiber addition [249]. This is confirmed with compression testing of the MPC-FRCs (Figure 6-13) which showed no significant change as a function of fiber content. Instead, failure in bending is required to properly evaluate the effect of fiber reinforcement on the cement matrix. Figure 6-10 clearly demonstrates classic quasi brittle failure modality of the MPC-FRC composites, with increasing fiber content not affecting the peak strength of the as generated cement, but reducing the peak strength with increasing incubation time in PBS (Figure 6-11). The failure interface seen in Figure 6-14 image of 7.5% fiber cement at day 1 looks remarkably similar to the quasi-brittle

failure depiction in Figure 6-18b. Residual strength measurements (6-11b) and toughness measurements (6-12b) at L/50 displacement in bending furthermore clearly show the improvement in mechanical properties of the cement with fiber incorporation.

While the inclusion of fibers improved mechanical toughness, further improvements to the designed system can still be implemented. Mechanical testing of the fibers indicates immense plastic deformation, but at the expense of the elastic modulus of the fiber. Low modulus fibers may impart toughness through moderate load transfer from the cement matrix, however this is only done effectively at high volume content of fibers, such as the 10 and 15 weight % fiber cements in this study. Improving the elastic modulus is known to significantly improve the load transfer, increasing the residual strength of the cement [249]. Improving the elastic modulus is frequently done through drawing of the spun fibers, but would result in reduced fiber diameter. Visual evaluation of the cement as generated and after PBS incubation through SEM imaging confirms significant deformation of fibers, particularly Figure 6-14 image of Day 1 7.5 % and Figure 6-15 images of Day 30, 5% and 7.5% cements. In addition to this, numerous images show the ends of fiber or smooth round holes left behind where fibers have been pulled out. These images indicate that there is poor interface bonding between the fiber and cement. Improving the interfacial bonding would result in significantly more energy adsorption during deformation. This may be done by increasing the surface roughness of the fibers as well as altering the surface chemistry [249]. An improvement in these two parameters could allow for reducing the volume fraction of fiber content while improving the cement failure modality to strain hardening instead of tension softening, while also improving the workability of the cement in clinical settings. These are some avenues that could be explored in the near future as the system is further developed.

6.5 CONCLUSION

Wet spinning of high molecular weight polycaprolactone solution through a dual ethanol coagulation bath system results in reliably produced, 100 μm diameter PCL fibers. These fibers were introduced into a magnesium ammonium phosphate cement system to test the handling and mechanical resilience of the resulting cement. Increasing fiber content increased residual strength and toughness of the cements while not affecting the initial peak strength of the cements. Due to the low modulus of the wet-spun fibers, cements failed in a tension-softening modality, and high volumes of fiber was required to retain the majority of the initial strength value. The high-fiber content cements performed well through the entire aqueous incubation period studied but were difficult to handle when forming do to the fiber content. Additional processing of the wet-spun fibers to increase the tensile strength and module is recommended, which would improve the bending failure of the cements while allowing for reduced fiber content to improve handling characteristics. Cytocompatibility studies showed cellular infiltration into pores formed from fiber removal. This confirms that the design of polycaprolactone wet-spun fiber-reinforced magnesium ammonium phosphate cement with degradable fibers imparts improved mechanical performance of the cement construct while allowing for cellular infiltration through fiber degradation.

7.0 CONCLUSIONS AND FUTURE WORK

Calcium phosphate cements (CPCs) have received considerable attention as bone void fillers. However, for the past decade, magnesium phosphate based ceramic implants and cements have been gradually gaining interest as a faster-degrading alternative to CPCs with a unique combination of observed properties including high strength, controlled setting time and pH including intrinsic anti-bacterial and adhesive properties. The work reported here expands upon the currently limited knowledge of magnesium phosphates particularly, exploring the effect of amorphous or crystalline of trimagnesium phosphate (TMP) powder as a bulk scaffold. Additionally, the work investigated the use of TMP as a starting cement precursor, evaluating the potential of a variety of reacting salts applied in neutral pH solution as well as exploring the effect of the addition of a fast-dissolve porogen and slowly degrading biocompatible and biodegradable polymer fiber.

This work has shown that, in bulk scaffold form, the amorphous TMP demonstrated unique mineralization potential leading to improved osteoclast cytocompatibility when compared to the more inert crystalline trimagnesium phosphate pellet scaffold. The high mineralization potential of the amorphous scaffolds are attributed to the high surface area as well as the amorphous nature of the synthesized TMP generated through aqueous precipitation and the high dissolution of this amorphous material as well as the rapid growth of calcium-rich crystals and influence of serum present in the culture media. While the amorphous scaffold improved

osteoblast cytocompatibility, both amorphous and crystalline scaffolds suspended the formation of mature osteoclasts from monocytes. The growth of calcium-rich rosette crystals on the amorphous trimagnesium phosphate pellet however, did not seem to affect the osteoclast culture.

When explored as the precursor ceramic in a cementing reaction with a 3.0 M, neutral pH ammonium phosphate solution, amorphous and semi-crystalline embodiments of the synthesized trimagnesium phosphate resulted in poor cements, with uncontrolled set time, poor putty consistency and low mechanical strengths, due to the highly reactive nature of the amorphous and semi-crystalline trimagnesium phosphate powder. This reactivity was however, insurmountable utilizing traditional reaction retardant methods. In comparison, the crystalline trimagnesium phosphate resulted in a malleable putties with clinically relevant setting times and resulting products that were strong as well as exhibiting good handling characteristics.

The crystalline trimagnesium phosphate was also used to explore the cementing reactions with salt solutions of sodium phosphate, potassium phosphate or ammonium phosphate, all at a concentration of 3.0 M and pH of 7.0 as before. The sodium and potassium salts formed workable putties, but resulted in exceedingly long setting times and mechanically poor cements. This was attributed to a low chemical driving force for the reaction to proceed to completion. The effect was also not overcome with variations in powder-to-liquid ratio, changes in reaction temperature, the use of amorphous trimagnesium phosphate in lieu of the crystalline counterpart, or the use of sodium and potassium solutions of different pH. In comparison, the ammonium phosphate solution reaction proceeded rapidly enough propelling the reaction forward towards completion to a larger extent, resulting in mechanically strong cements.

This optimized magnesium ammonium phosphate cement formulation was next used to explore the effect of added porosity through the inclusion of quickly dissolving mannitol sugar

crystals as a porogen. Using the same synthesized crystalline trimagnesium phosphate powder and 3.0 M, pH 7.0 ammonium phosphate solution, mannitol content up to half of the total powder weight was added, and ammonium phosphate solution volume was optimized based on mannitol content. The inclusion of mannitol did not however, affect the crystallinity, pH or cytocompatibility of the resulting cement. Increasing mannitol resulted in progressively decreased compressive strengths. The addition of mannitol indeed expectedly resulted in increased microporosity and total porosity greater than 60% of the cement volume.

In order to explore the effect of fiber reinforcement on magnesium phosphate cement, highly deformable fibers of polycaprolactone (PCL) were created through a wet-spinning method, resulting in fibers 100 μm in diameter and 1.5 mm in length. Using commercially available crystalline trimagnesium phosphate as the cement precursor and the same 3.0 M, pH 7.0 ammonium phosphate reacting solution, cements with up to 15 weight % fiber content were created. Increasing fiber content resulted in increasing residual strength and cement toughness determined by 3-point bending failure tests. Low fiber containing cements displayed better workability than high fiber containing cements. Removal of fibers through dissolution resulted in large increases in macroporosity and visible cellular infiltration into the porous channels created by the fibers.

Based on the work conducted so far and the promising results obtained, it would be reasonable to continue the work into the future. An obvious missing link that would be relevant to explore would be investigating clinically crucial properties including cement injectability and cohesion in blood and aqueous environments. Unique properties of some magnesium cements, including bone-bone and bone-tendon adhesion and inherent antibacterial activity should be evaluated with the various formulations explored in this work. The use of the neutral pH solution

was designed in order to allow for the incorporation of drugs, biologics or cells for delivery *in vivo*, which has not yet been explored with this or other magnesium phosphate cements. Similarly, with additional optimization and processing design, the wet-spun fibers could impart even more mechanical resilience while also serving as an excellent platform as a delivery agent for controlled release of drugs or biologics during degradation. Moving expeditiously towards exploring these systems in relevant animal model studies will be particularly useful to fully understand the complex relationship between porosity, dissolution and bone tissue growth with these novel magnesium phosphate systems. The knowledge gained throughout the work reported here combined with the potential future work will likely expand the fundamental understanding of magnesium cements even more for bone repair applications. These advances in turn, can lead the way for exploring even further the wide possibilities within the realm of magnesium cement systems. Possibilities include comparisons between magnesium oxide and trimagnesium phosphate based formulations as well as formulations including other magnesium ceramics such as magnesium hydroxide. Additional studies will include expanding the system to include other ions and compounds such as calcium, strontium, silicates and carbonates into the magnesium bone cements. The field is therefore filled with expanding possibilities with tremendous potential for advancing the knowledge base of resorbable inorganic cement systems.

APPENDIX A

EXPLORATION OF CALCIUM AND STRONTIUM SUBSTITUTION INTO TRIMAGNESIUM PHOSPHATE THROUGH AQUEOUS PRECIPITATION

A.1 INTRODUCTION

The study of magnesium phosphates for bone cements is a relatively new field of study compared to traditional calcium phosphates. Calcium phosphate bone cements have been exploited to a large extent because the composition closely mimics mineralized bone matrix, although the mechanical strength and resorption rate of these cements are not ideal. In addition to calcium, many other ions such as magnesium, silicon, zinc, potassium and copper play important roles in bone regeneration, from regulating the metabolic processes and osteoblastic differentiation genes to promoting angiogenesis and increasing bone cell adhesion [167, 250] . With regards to bone formation and dissolution, magnesium has been shown to play a major role in calcification and bone density, mineral metabolism, hydroxyapatite crystal formation and increased bone cell adhesion and stability [19, 34, 41, 43]. Phosphate is not only a main component of bone growth, but has also been shown to stimulate expression of matrix gla protein which is involved in bone formation [167]. Strontium consumption on the other hand has been shown to increase bone density in low doses and is frequently given as a supplement to patients

with osteoporosis in Europe, albeit excessive doses have been shown to result in defective mineralization in bone and rickets disease [125]. Strontium has been shown to support osteoblast differentiation through enhancing Wnt/β- catenin signaling while inhibiting the formation of osteoclasts [251, 252].

Substitutions between magnesium, calcium and strontium in phosphate apatite type ceramics have been widely explored because all three are divalent cations with positive biological functions reported in bone [253-263]. Magnesium substitution into β-TCP scaffolds is known to increase the temperature at which the β-TCP to α-TCP phase transformation occurs, enabling improved sintering and densification [120, 134]. Magnesium substitution also stabilizes β-TCP scaffolds allowing significantly more control over particle size and crystallinity. Magnesium substitution, especially at high levels, has been shown frequently to improve cytocompatibility of calcium phosphate materials. Strontium substitution into calcium phosphates on the other hand, has been shown to increase the material solubility [264]. While the substitution of calcium and strontium into magnesium phosphate through aqueous synthesis has not been explored, Zhou et al recently explored microwave-assisted synthesis with magnesium and calcium substituted into strontium phosphate, showing that the magnesium-strontium phosphate improved cytocompatibility compared to strontium-calcium phosphate and pure strontium phosphate while also increasing the solubility [265]. The objective of this study is to essentially investigate the effects of calcium and strontium substitution on the crystal structure and phase evolution of tri-magnesium phosphate powders under simple aqueous synthesis conditions that was explored in detail in Chapter 2.

A.2 MATERIALS AND METHODS

A.2.1 Materials synthesis

Calcium and strontium substituted trimagnesium phosphate powders were synthesized through a modification of the aqueous precipitation synthesis method introduced and described in Chapter 2. Strontium chloride ($SrCl_2$) or calcium chloride ($CaCl_2$) were added to the magnesium chloride solution during synthesis, to achieve hypothetical nominal substitutions amounts following Equation A-1 which follows Equation 2-1 modified with x as the substituted ion level. Amount of substitutions considered and evaluated were 0, 5, 10, 25 and 50 mole % of magnesium content.

Equation A-1

$$2PO_4^{3-} + 3(xY^{2+} + (1\text{-}x)Mg^{2+}) \rightarrow (Y_xMg_{1-x})_3(PO_4)_2 \text{ ;}$$

Y = Sr, Ca and the phosphate solution was Na_3PO_4 similar to what is described in Chapter 2

Sodium phosphate solution remained the same as in Chapter 2. Phosphate solution was pipetted into the magnesium/calcium/strontium salt solution, resulting in a white precipitate which was then centrifuged, washed and dried according to the protocol established in Chapter 2.

A.2.2 Materials Characterization

To assess the efficacy of calcium or strontium substitution into the TMP crystal structure, powders were thermally treated to a variety of temperatures: no treatment, 500 °C, 600 °C, 700 °C and 800 °C for 6 hours and subjected to XRD and FTIR analysis as described in the earlier chapters. TGA/DSC analysis was completed on the synthesized powders to determine the level of hydration and onset temperature of bulk crystallization as in Chapter 3. The synthesized powders were dissolved in 8% nitric acid solution and then evaluated for their elemental contents using ICP-OES as previously described, measuring the magnesium, calcium, strontium and phosphorous levels for each sample. The powders were coated in palladium and observed under SEM to evaluate morphological changes due to doping.

A.2.3 Cytocompatibility

The synthesized powders were thermally treated to 200 °C and 800 °C for 6 hours to obtain amorphous, partially dehydrated powder and fully crystalline powders as in Chapter 2. Pellets were created using a Carver press as described, with powders thermally treated, pressed and then the pellets were thermally treated again to the same temperature (200 °C or 800 °C) to help bond the powder in the pellet. Pellets were sterilized using UV radiation. MC3T3 osteoblasts were seeded on pellets at a cell density of 40,000 cells/well and cultured as previously described in Chapter 2. After 48 hours, cells were subjected to live/dead staining.

A.3 RESULTS AND DISCUSSION

Figure A-1 shows the x-ray diffraction patterns collected on calcium and strontium doped trimagnesium phosphate following synthesis to examine the structural state of the as-prepared doped materials. These results indicate that all powders were initially amorphous similar to the unsubstituted TMP previously studied.

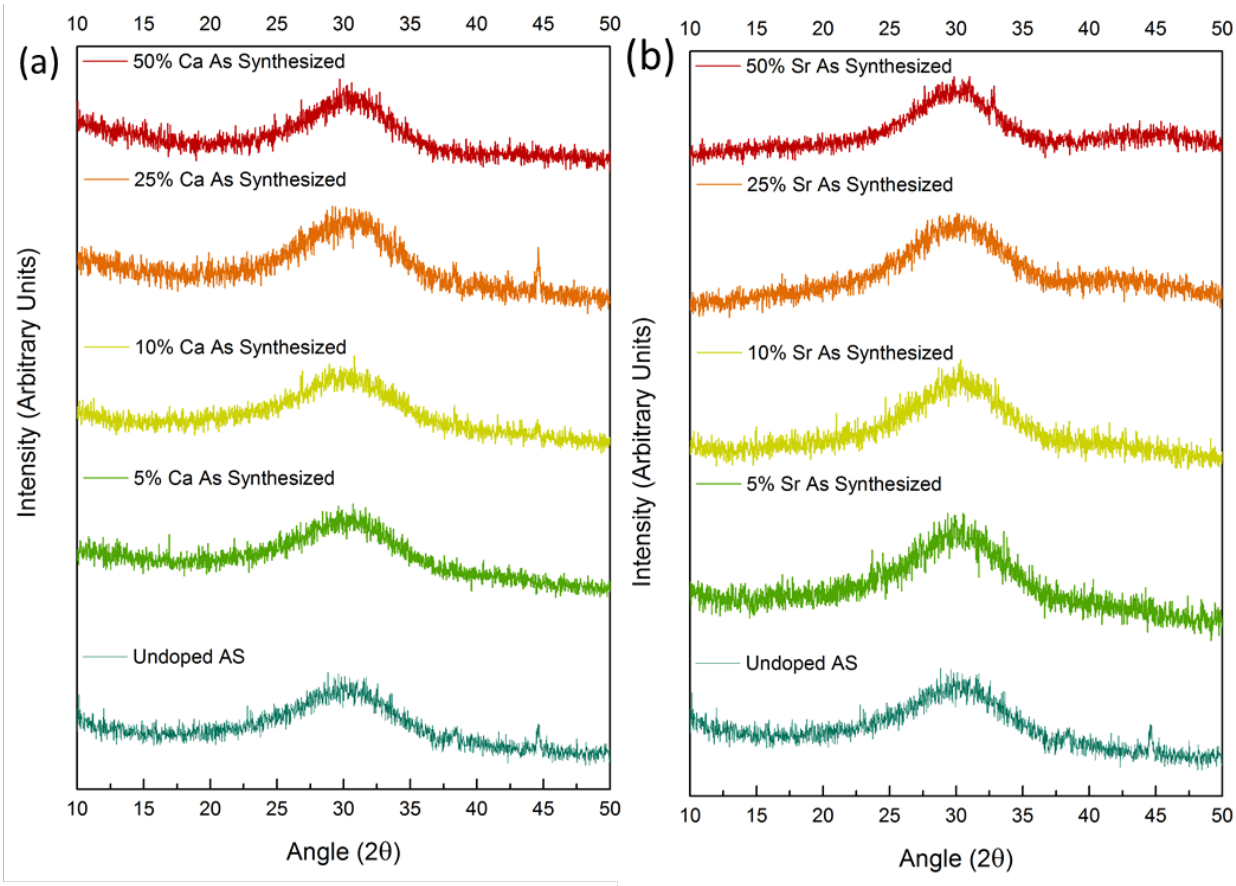

Figure A-1 X-ray diffraction patterns of the as synthesized calcium and strontium doped tri-magesnium phosphate powder indicating that all the as-prepared powders were amorphous.

Figures A-2 and A-3 display the XRD patterns of calcium and strontium doped TMP, respectively, after thermal treatment to 800 ^{o}C for 6 hours in air to crystallize the powders. Phases are identified as: (a) $Mg_3(PO_4)_2$ (farringtonite, ICCD 98-001-7103), (b) $Na_{1.05}Mg_{3.96}(PO_4)_3$ (sodium magnesium phosphate, ICCD 00-054-0072), (c) $Ca_4Mg_5(PO_4)_6$ (stanfieldite, ICCD 00-011-0231), (d) $Ca_3(PO_4)_2$ (tricalcium phosphate, ICCD 00-003-0713), (e) $Mg_{21}Ca_4Na_4(PO_4)_{18}$ (magnesium calcium sodium phosphate, 01-073-0020), (f) $SrMg_2(PO_4)_2$ (magnesium strontium phosphate, ICCD 00-014-0206), (g) $NaMg(PO_4)$ (sodium magnesium phosphate, ICCD 00-032-1123), (h) $Sr_9Mg(PO_3OH)(PO_4)_6$ (ICCD 00-048-1855), (i) $Sr(PO_3)_3$ (ICCD 01-076-4588), (k) $Sr_2P_2O_7 \bullet ½H_2O$ (ICCD 00-012-0369) and (x) for as of yet unidentified peaks. XRD of attempted calcium or strontium substitution indicates that ionic substation into the TMP crystal structure was generally not achieved through the aqueous precipitation method utilized. A doped crystal structure would demonstrate peak broadening and shifting of the 2θ peak positions, which can then be analyzed through Reitveld refinement to determine the amount of substitution [266]. Diffraction patterns of 800 °C calcium substituted TMP show multiphasic materials at even 5 mole % addition. TMP 5% Ca showed the presence of $Na_{1.05}Mg_{3.96}(PO_4)_3$ (b) as well as a small amount of $Mg_{21}Ca_4Na_4(PO_4)_{18}$ (e) mixed in with the $Mg_3(PO_4)_2$ (a) phase. Increasing substitution to TMP 10% Ca showed the removal of $Na_{1.05}Mg_{3.96}(PO_4)_3$ (b) and a large increase in $Mg_{21}Ca_4Na_4(PO_4)_{18}$ (e) as well as a reduction in $Mg_3(PO_4)_2$ (a). Increasing the calcium level to 25% further reduced $Mg_3(PO_4)_2$ (a), maintaining a high level of $Mg_{21}Ca_4Na_4(PO_4)_{18}$ (e) and showed the development of $Ca_4Mg_5(PO_4)_6$ (c). Finally at 50% calcium/ 50% magnesium, $Mg_3(PO_4)_2$ (a) is a minor phase, along with $Ca_4Mg_5(PO_4)_6$ (c). A significant portion of $Mg_{21}Ca_4Na_4(PO_4)_{18}$ (e) is present, with the most intense peaks corresponding to the development of $Ca_3(PO_4)_2$ (d).

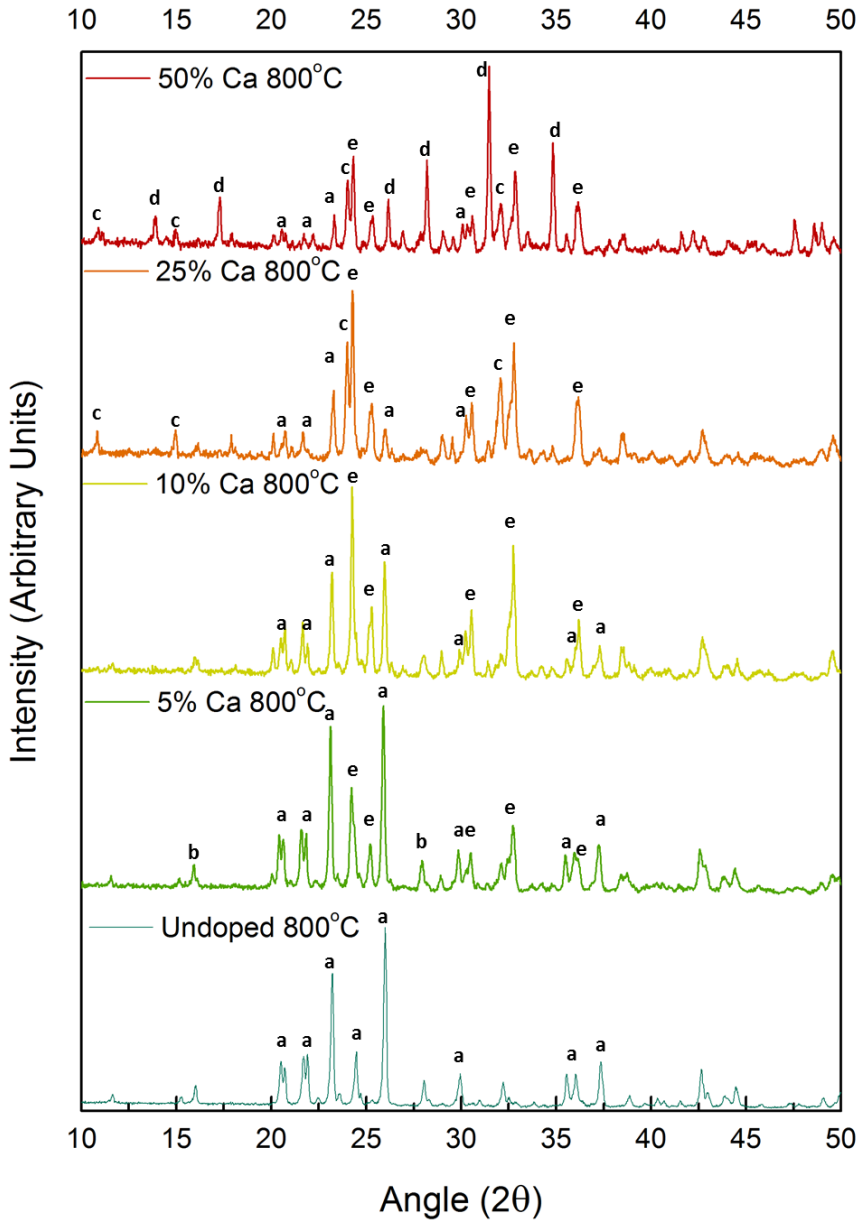

Figure A-2 X-ray diffraction results of calcium doping into tri-magnesium phosphate through aqueous co-precipitation and thermal treatment to 800 °C for 6 hours in air, phases are (a) $Mg_3(PO_4)_2$, (b) $Na_{1.05}Mg_{3.96}(PO_4)_3$, (c) $Ca_4Mg_5(PO_4)_6$, (d) $Ca_3(PO_4)_2$, and (e) $Mg_{21}Ca_4Na_4(PO_4)_{18}$.

A similar trend is seen in the strontium substituted phosphate as seen for the phosphate with the corresponding calcium substitution, with all strontium-containing powders developing into multiphase materials. TMP with even 5% Sr similar to Ca showed multi-phases mainly $Mg_3(PO_4)_2$ (a) with a small amount of $SrMg_2(PO_4)_2$ (f) and $NaMg(PO_4)$ (g). Increasing the strontium amount to 10% resulted in increasing levels of $SrMg_2(PO_4)_2$ (f), the evolution of $Sr(PO_3)_3$ (i) and a low level of $NaMg(PO_4)$ (g). Increasing further to 25% Sr, the level of $SrMg_2(PO_4)_2$ (f) and $Sr(PO_3)_3$ (i) increase while the amount of $Mg_3(PO_4)_2$ (a) and $NaMg(PO_4)$ (g) continue to decrease. An additional phase, $Sr_9Mg(PO_3OH)(PO_4)_6$ (h) evolves. At 50% Sr, (h) $Sr_9Mg(PO_3OH)(PO_4)_6$ becomes a major phase, with low levels of $Sr(PO_3)_3$ (i) and a small amount of (k) $Sr_2P_2O_7 \bullet ½H_2O$. In addition to this, XRD spectra of 10, 25 and 50% Sr powders exhibit major peaks which currently remain unidentified, marked with an x at approximately 23°, 33° and 47° 2θ, respectively further serving as an indicator of the phase instability of the system at 800^{o}C. Several other minor peaks are not explicitly identified in Figure A-3 and are likely attributed to small amounts of (a), (g) or minor peaks of (h), (i) and (k), however the spectra is heavily complex with overlapping peaks and these minor peaks cannot be readily identified requiring deconvolution that was not conducted for this study.

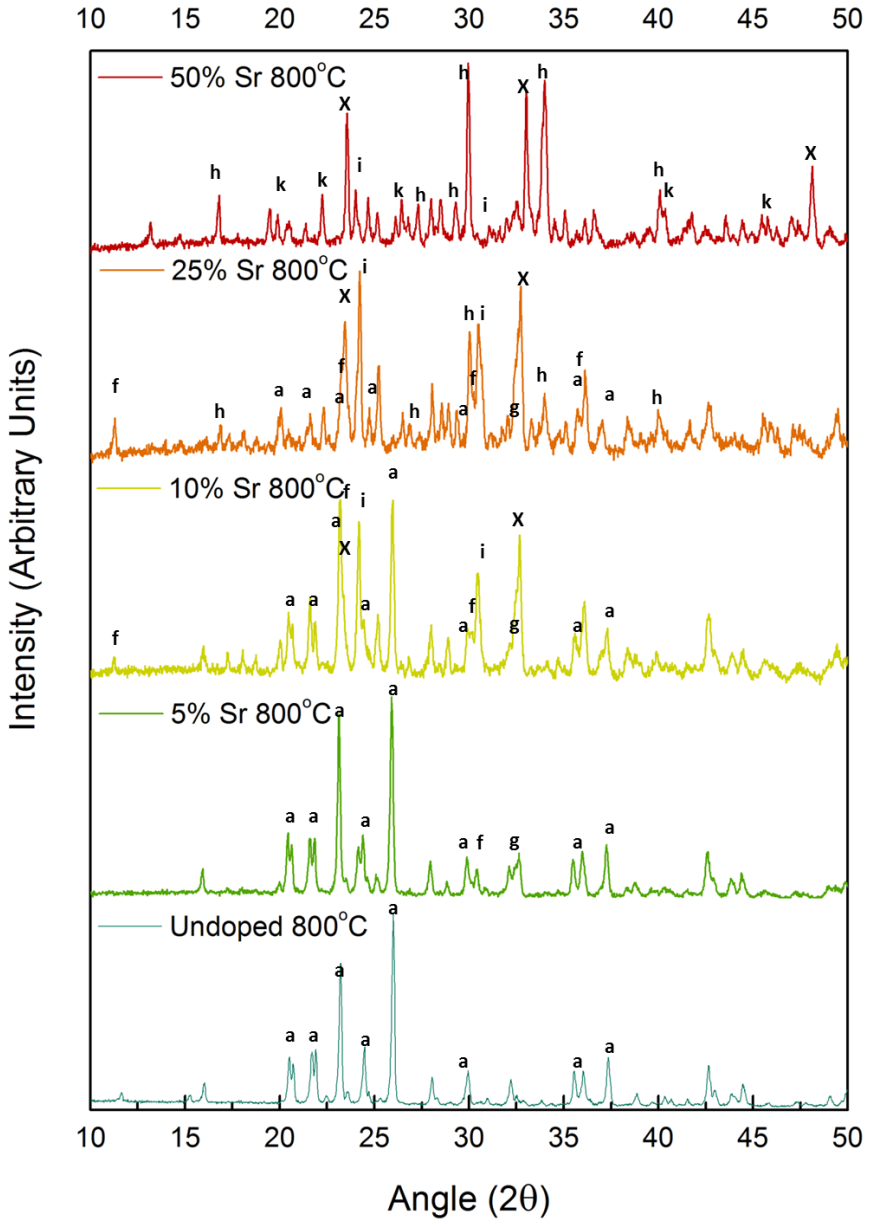

Figure A-3 X-ray diffraction results of strontium doping into tri-magnesium phosphate through aqueous co-precipitation and thermal treatment to 800 °C for 6 hours in air. Phases are identified as (a) Farringtonite (f) Magnesium strontium phosphate, (g) Sodium magnesium phosphate, (h) 00-048-1855, (i) 01-076-4588, (k) 00-012-0369 and (x) for as of yet unidentified peaks.

Figure A-4 shows the SEM images of calcium and strontium substituted powders as well as the unsubstituted powder in the as-synthesized and following thermal treatment to 800 °C for 6 hours in air. SEM images indicate that there is no significant change in the bulk particle morphology following thermal treatment for the unsubstituted phosphate. However, there is significant change in particle morphology with calcium or strontium addition. Increasing substitution amounts results in the particle shape morphing from the flat, hexagonal plates of pure TMP into agglomerates of somewhat spherical irregular, globular particles. Low strontium and calcium levels (5 and 10%) show retention of some hexagonal particle morphology, while higher strontium and calcium levels (25 and 50%) do not show these particles. This trend is consistent with the XRD results, indicating significant portions of TMP remaining at low substitution levels but those levels reducing with increasing ion substitution.

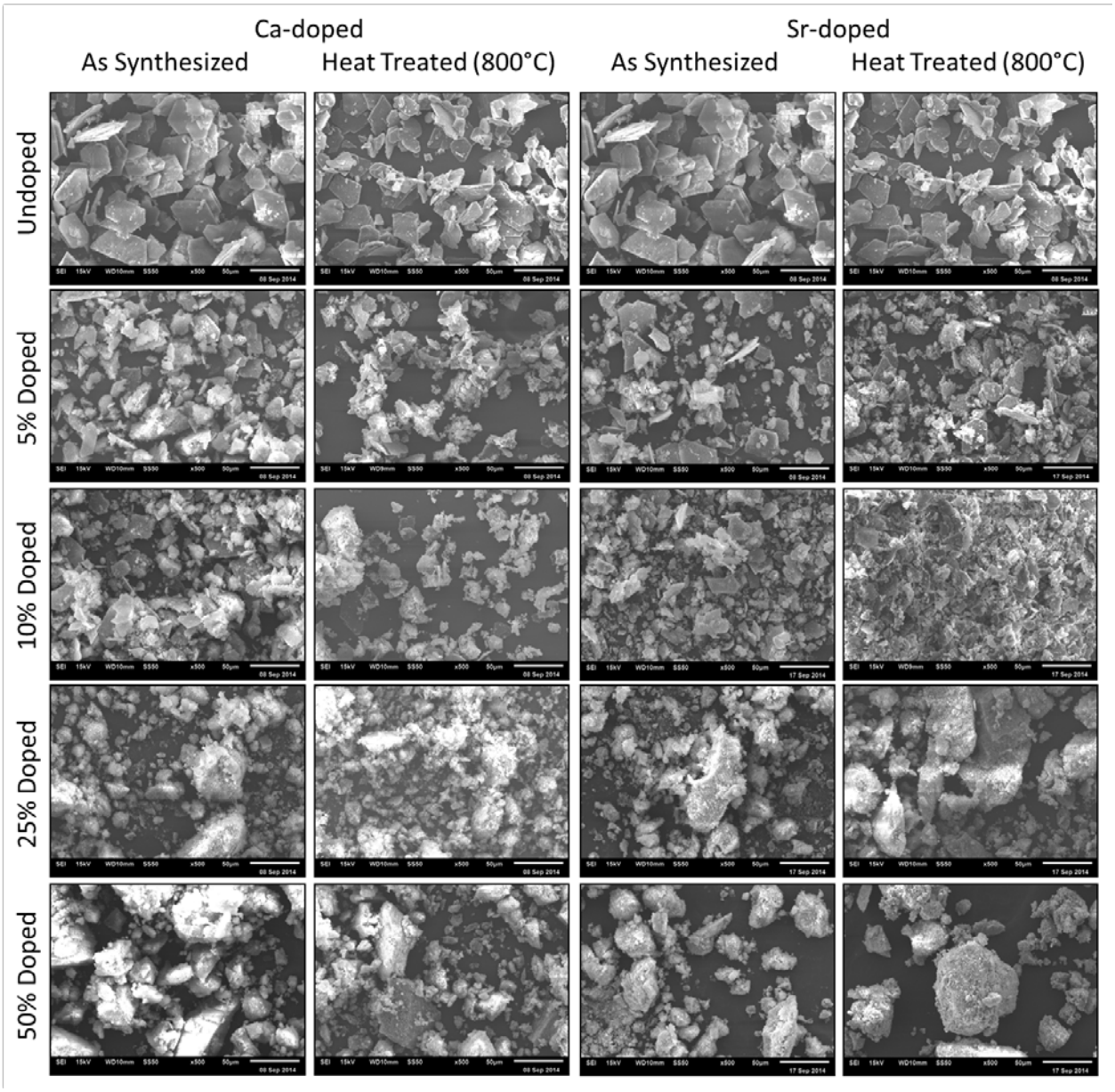

Figure A-4 SEM images of calcium and strontium doped TMP powders as synthesized and after thermal treatment to 800 °C for 6h in air. Scale bar 50 microns.

TGA/DSC of the amorphous powder was conducted to ascertain phase transition and crystallization temperatures in an attempt to isolate whether the materials are initially doped within the amorphous structure since the powders were perceived to be amorphous when synthesized and multiphase following thermal treatment to 800 °C. Several dynamic situation

could arise such as the materials may be doped but tend to crystallize into single-phase doped material and/or phase separate at high temperature thermal treatment, or the material may phase separate as part of the crystallization process. Table A-1 shows the results of mass loss and temperature of the crystallization peak measured through TGA/DSC. In Figure A-5 are representative plots of (a) undoped TMP, (b) TMP 50% Ca and (c) TMP 50% Sr showing the mass loss profile and heat flow profiles of these powders. Results in Figure A-5 and Table A-1 show that the hydration level of calcium substitution TMP was similar to that of undoped TMP (27%), ranging from 25% for 5% Ca to 21% for 50% Ca. Strontium substituted powders showed slightly lower hydration levels at higher strontium content, dropping from 27% at 5% Sr to 15% at 50% Sr. The crystallization or phase evolution peak temperature decreased with increasing substitution for both calcium and strontium, dropping from 688 °C at 5% Ca to 645 °C at 50% Ca and 687 °C at 5% Sr to 657 °C at 50% Sr. While there were gradual shifts in the hydration level and crystallization or phase evolution temperature, the DSC plots show similar patterns of hydration loss below 200 °C and crystallization around 675 °C. Calcium and strontium substituted plots do not show any additional inflection point which may be indicative of a two-step crystallization followed by a phase separation process.

Table A-1 TGA/DSC mass loss and crystallization change peak temperature measurements of calcium and strontium doped TMP precipitates.

TGA/DTA Results	Control	5% Ca	10% Ca	25% Ca	50% Ca	5% Sr	10% Sr	25% Sr	50% Sr
Total mass % lost	27.14	24.98	25.02	32.51	21.28	26.75	23.48	20.08	14.45
Temp. of second peak (°C)	676.6	687.9	670.1	657.7	645.5	687	687.7	652.9	657.1

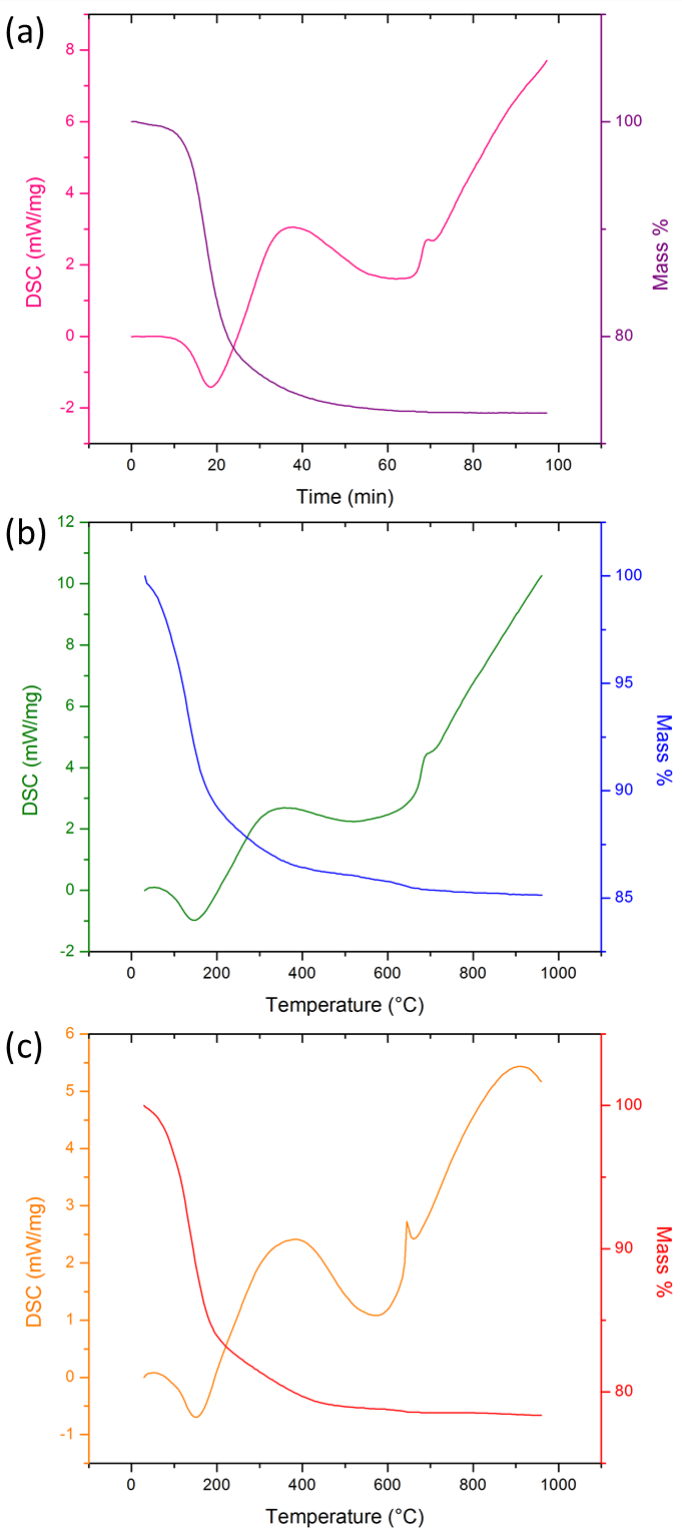

Figure A-5 TGA/DSC plots of un-doped TMP (a), 50% calcium doped TMP (b) and 50% strontium doped TMP (c).

XRD results of calcium and strontium substituted TMP powders thermally treated to 500 °C, 600 °C and 700 °C can be seen in Figures A-6, A-7 and A-8, respectively. Spectra indicate progressively increased crystallization for both ions. Powders treated to 500 °C remained amorphous similar to the as synthesized powder (Figure A-6). Powders treated to 600 °C however, showed partial crystallization (Figure A-7). Increasing the level of calcium or strontium appears to slow the crystallization of the powder, evidenced by the less defined peaks seen in both calcium (a) and strontium (b) at higher doping levels. The addition of strontium in particular stabilized the amorphous phase for a longer period. This seems contradictory to the DCS results which indicated a reduction in crystallization temperature, however the reduction was minor and the DSC plot of the 50% strontium substituted TMP shows this crystallization 'peak' to be less well defined than seen often seen with TMP. The less definition in the peak may indicate a more gradual change that does not yield a significant energy peak in DSC. Furthermore, DSC is more indicative of dynamic changes while the heat treatment is conducted for a period of 6h allowing enough time for diffusion processes to occur.

XRD results of the powders treated to lower thermal temperatures also confirm that the powders transition into multiphase materials upon crystallization and at no point form truly doped, single-phase materials, even at low (5%) substitution levels. Figure A-7 demonstrates the first instance of crystallization (600 ^{o}C thermal treatment) and the substituted materials show additional peaks not present in the baseline TMP spectra. These peaks match well with the phases identified in Figure A-2 and A-3, however the identification is more difficult with the presence of amorphous content at lower temperatures.

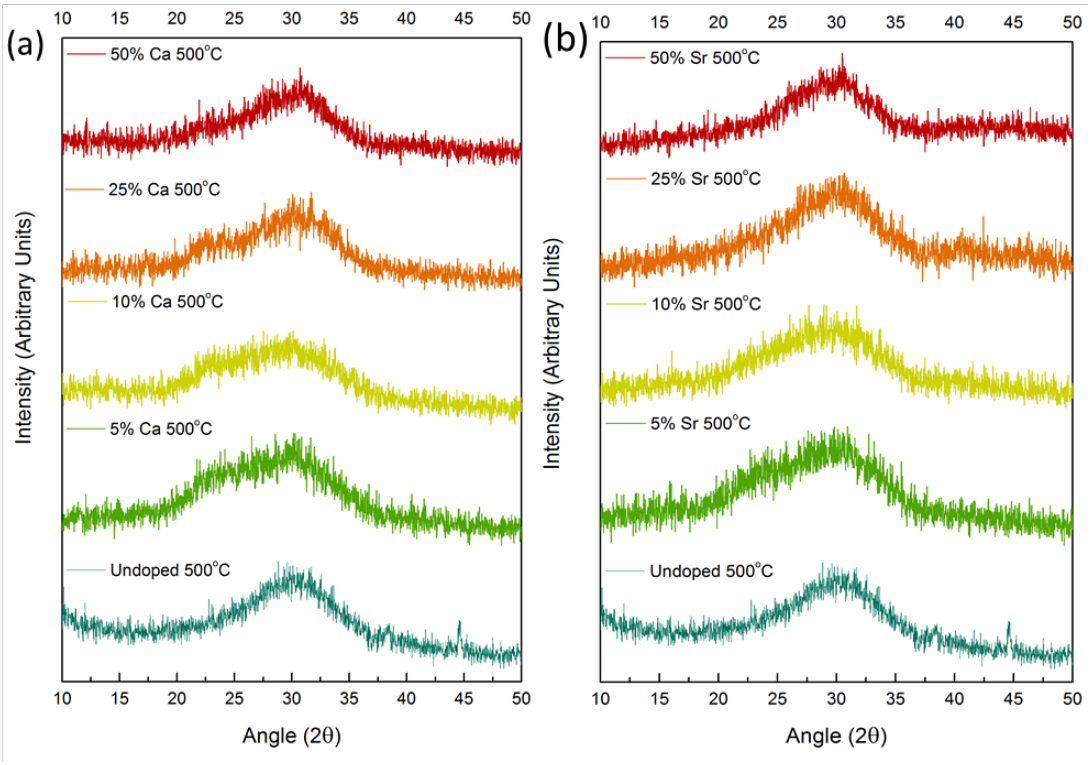

Figure A-6 **XRD of calcium and strontium doped TMP thermally treated to 500 °C for 6 hours.**

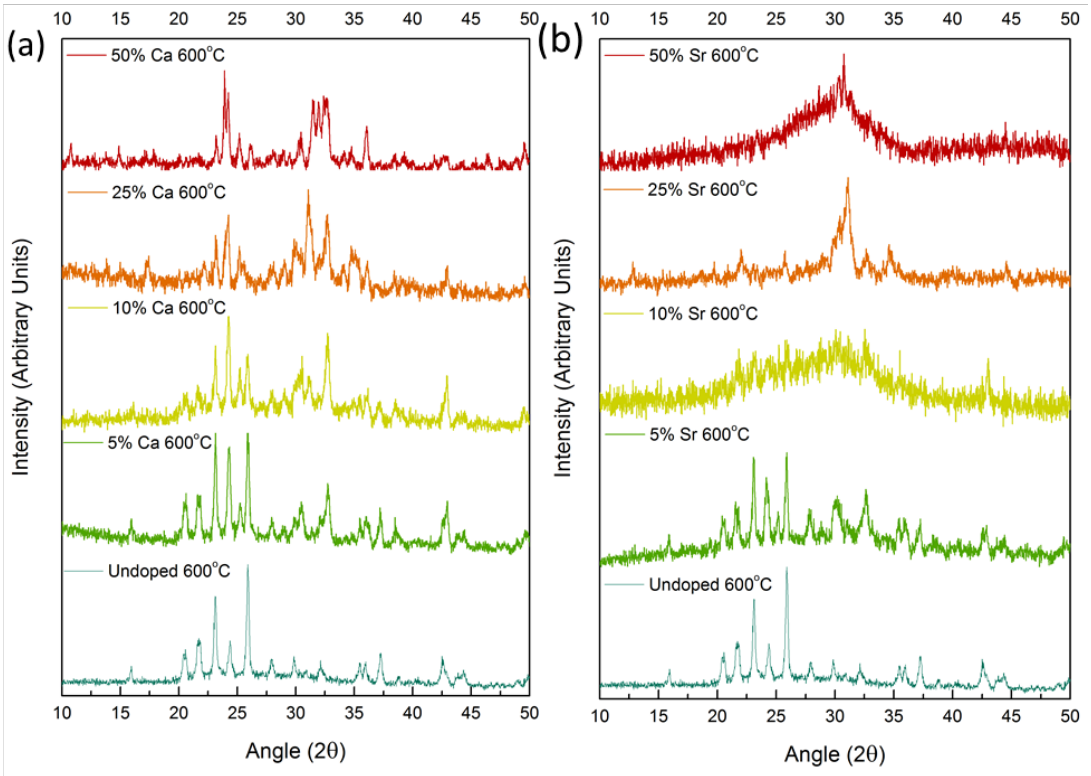

Figure A-7 **XRD of calcium and strontium doped TMP thermally treated to 600 °C for 6 hours.**

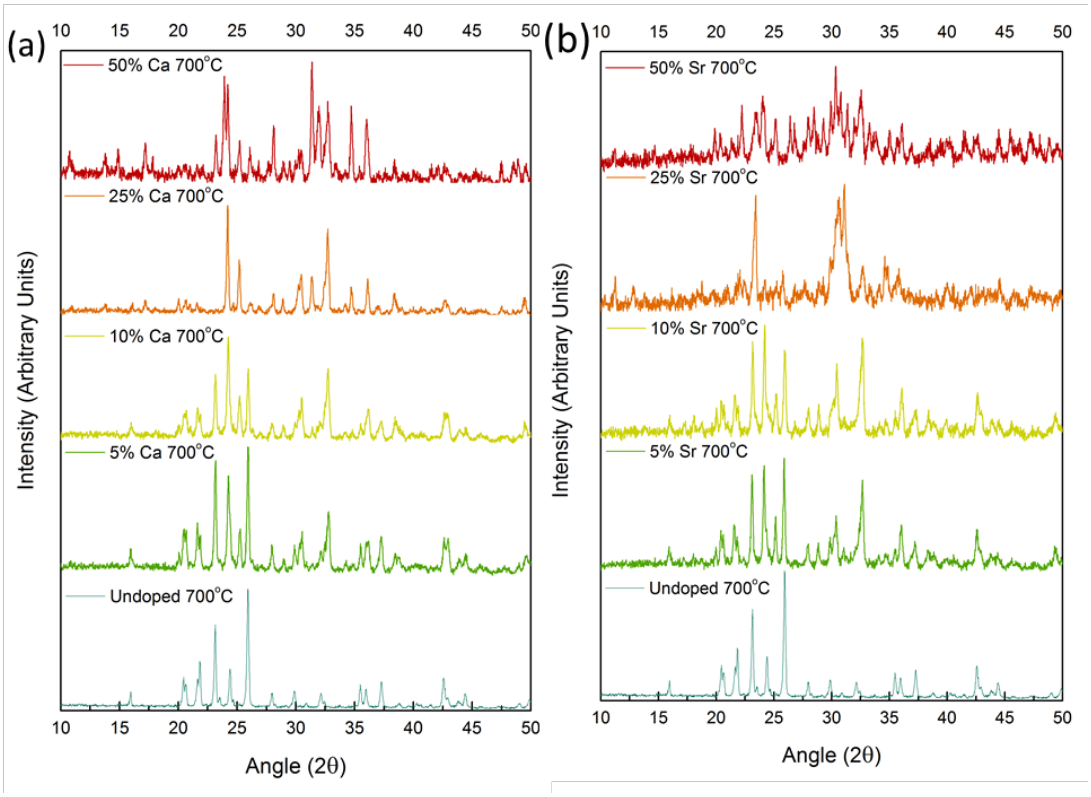

Figure A-8 XRD of calcium and strontium doped TMP thermally treated to 700 °C for 6 hours.

Similar trends of water loss and crystallization are seen through FTIR of the doped materials. Figure A-9 shows the spectra of calcium doped TMP as synthesized (a), and thermally treated to 500 °C (b), 600 °C (c) and 800 °C (d) while Figure A-10 shows the same for strontium doped TMP. As discussed in the FTIR of pure TMP in Chapter 2, FTIR spectra here show that all synthesized powders (A-9a and A-10a) are amorphous, indicated by the non-descript phosphate peaks at 1000 and 500 cm^{-1}, and are heavily hydrated, evidenced by the large hump between 2500-3500 cm^{-1} and the peak around 1600 cm^{-1}. Thermal treatment to 500 °C results in removal of the water hump and peak (A-9b and A-10b), while the phosphate peaks remain broad. Thermal treatment to 600 °C indicates (A-9c and A-10c) the beginnings of crystallization shown

by the peak separation of the phosphate peaks, as discussed in Chapter 2. Similar to results from XRD, FTIR indicates reduced crystallization with increasing dopant content, evidenced by less peak separation of the phosphate peaks. This conclusion however is convoluted by the multiphase nature of the materials. Thermal treatment to 800 °C (A-9d and A-10d) indicates differences in the phosphate peak number and position, particularly evident in the 50% strontium sample (A-10d). The multiple peaks and lack of peak distinction (A-9d, Ca 50%) can be attributed to the multitude of phosphate compounds present, each with its own specific bond configurations and vibrational patterns.

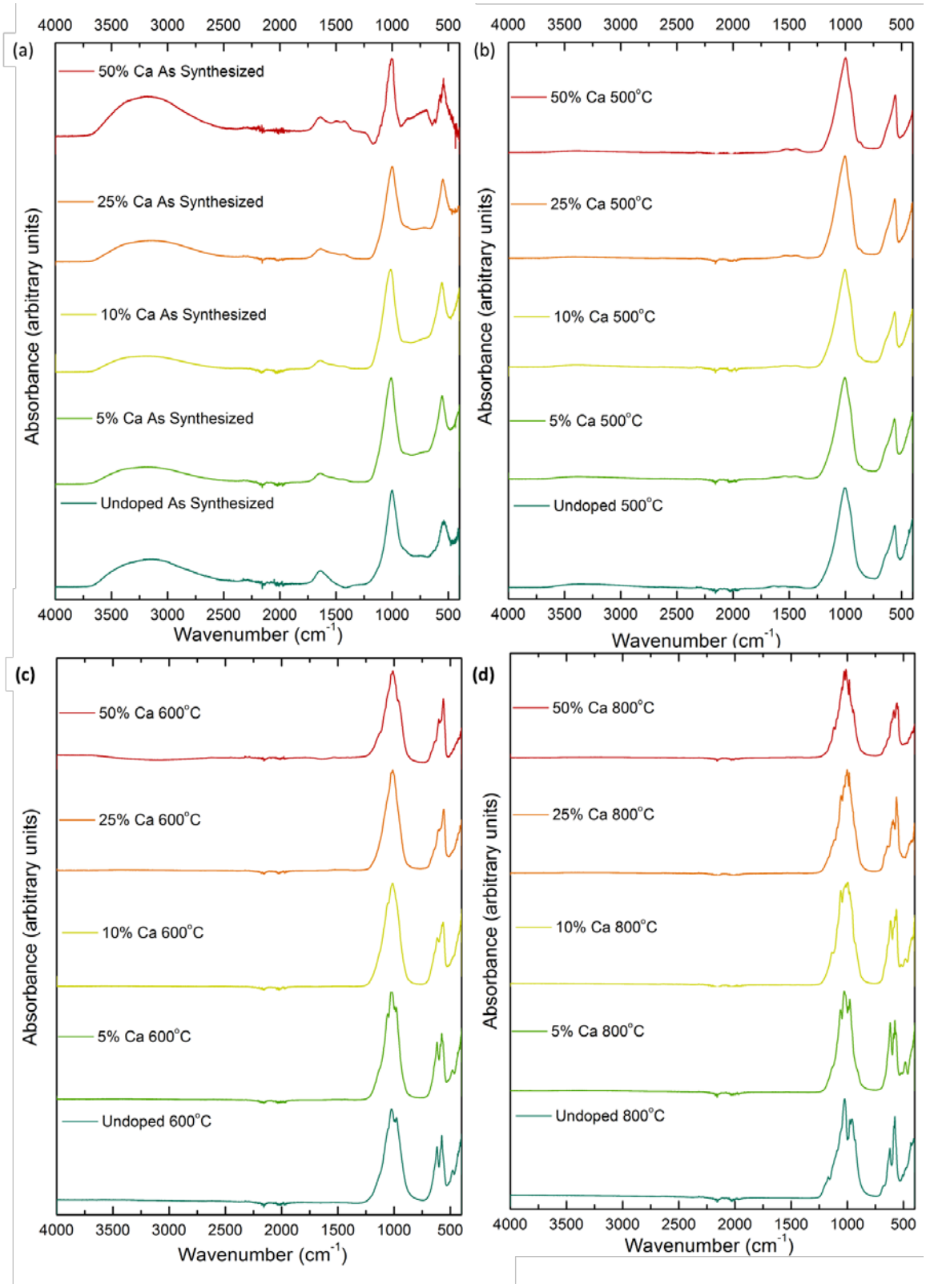

Figure A-9 FTIR spectra of calcium doped TMP as synthesized and thermally treated to 500, 600 and 800 °C for 6 hours each in air.

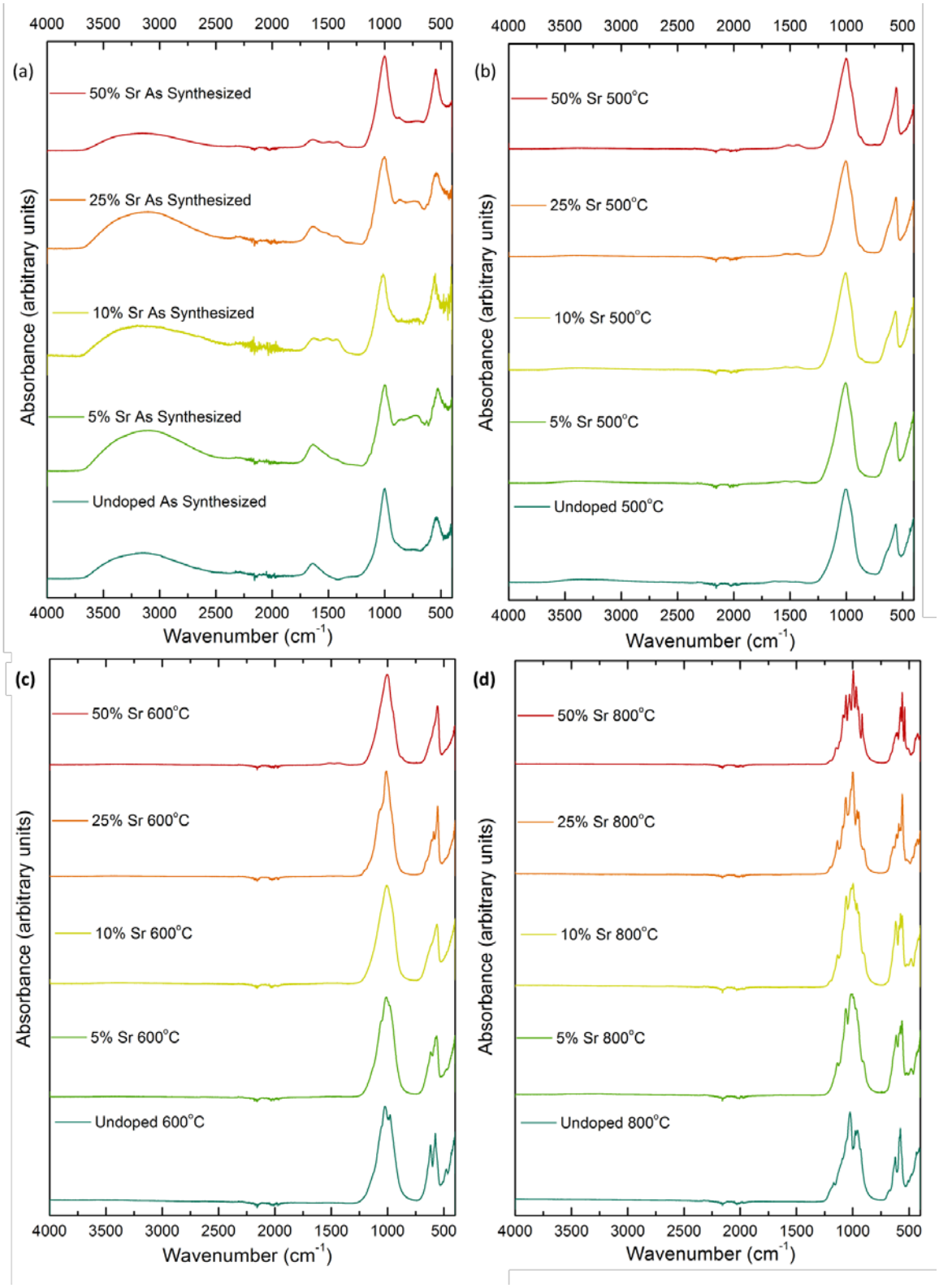

Figure A-10 FTIR spectra of strontium doped TMP as synthesized and thermally treated to 500, 600 and 800 °C for 6h in air.

ICP was utilized to determine ion content from which ion molecular ratios were calculated, the results of which can be seen in Table A-2. The calcium to substituent element ratios were close to the intended substitution levels for both calcium and strontium substitution. This indicates that although the resulting powders were multiphasic, calcium, strontium and magnesium ions were not disproportionately removed in solution during synthesis. Theoretically the molar concentration of Mg in TMP is 60%, experimentally this value was measured at 55% in pure TMP. This value should be the total cation concentration across all the samples. However, measurements showed an increase in molar cation concentration with increasing substitute ion concentration. This increase was more marked in the strontium substituted samples. This is consistent with the phases seen in XRD in that there were frequently phases present which included more than three cations per every two phosphate groups.

Table A-2 Molecular ion ratios of magensium, calcium, strontium and phosphorous measured through ICP-OES.

	Ca/Ca+Mg	Sr/Sr+Mg	Ca+Mg+Sr/ (P+Mg+Ca/Sr)
TMP AS			0.550
TMP 5pCa AS	0.041		0.559
TMP 10pCa AS	0.087		0.563
TMP 25pCa AS	0.234		0.565
TMP 50pCa AS	0.442		0.604
TMP 5pSr AS		0.054	0.571
TMP 10pSr AS		0.088	0.599
TMP 25pSr AS		0.251	0.658
TMP 50pSr AS		0.456	0.719

Finally, live/dead staining results shown in Figure A-11 indicate increased calcium and strontium substitution on 800°C thermally treated samples promoted improved cell viability as compared to the TMP baseline material, achieving viability levels close to β-TCP controls.

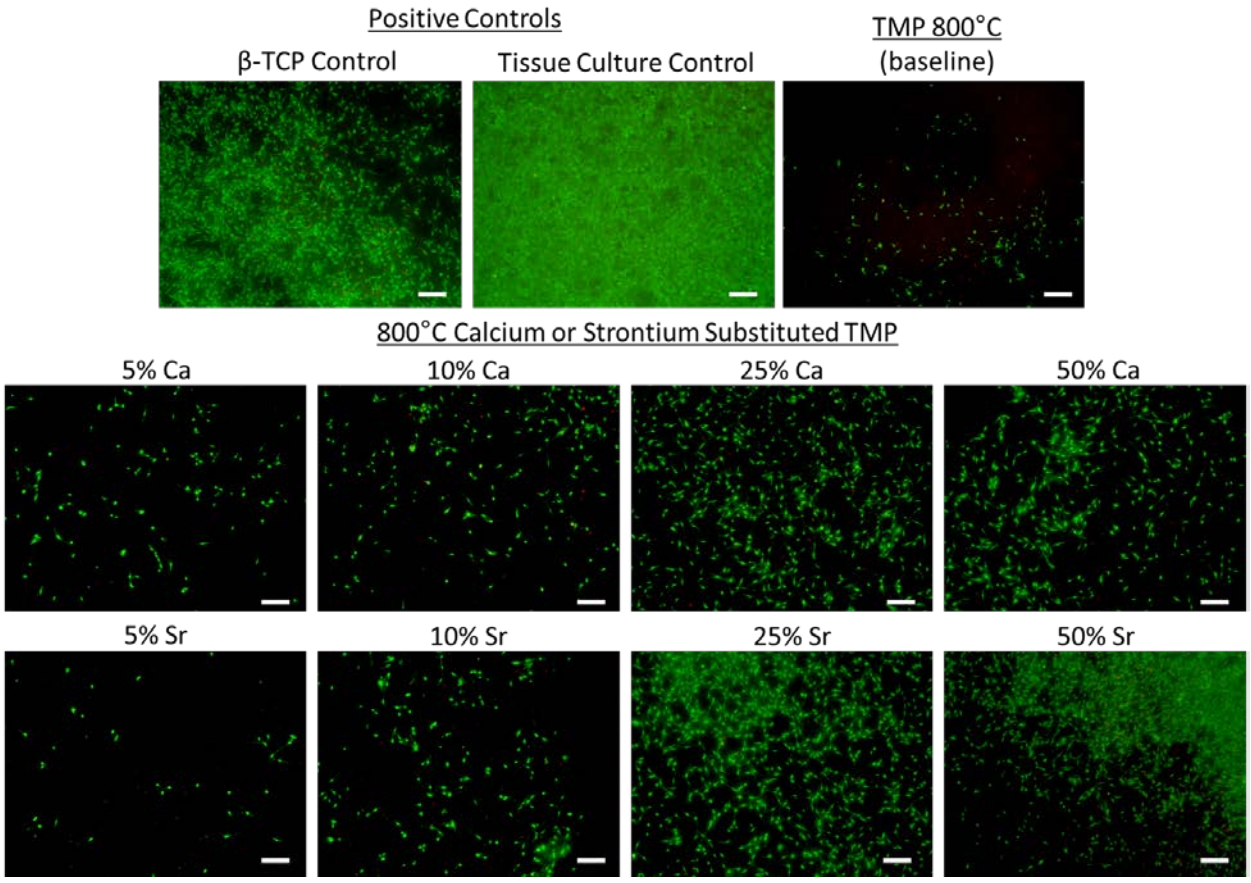

Figure A-11 Live/dead staining of MC3T3 cells grown on calcium and strontium substituted TMP pellets thermally treated to 800 °C for 6 hours in air. Scale bar is 200 µm.

A.4 CONCLUSION

This study investigated the feasibility and effects of calcium and strontium substitution on the time-temperature-transformation of trimagnesium phosphate powder through modifications to the aqueous precipitation reaction introduced in Chapter 2. The phases present in and the crystal structure of the doped samples were determined using XRD, FTIR, and SEM. Additionally ICP was used to determine the composition of the samples. The findings indicate that true substitution of the substitute ion into the TMP structure did not occur to a large extent. Instead

the introduction of substitute ions resulted in phase separation even at low substitution concentrations of 5 mole%. An increase in the substitute ion concentration increased the stability of the amorphous phase, as evidenced by the increasing presence of this phase in samples with a higher substitute ion concentration. Morphologically, there is a shift in powder form from a plate like structure to a more spherical shape with increasing doping concentrations. Cytocompatibility was improved with substitute ion addition, especially through the addition of strontium to the chemical structure. As these substituted materials were to be used in place of pure tri-magnesium phosphate for a cementing reaction, alternative synthesis methods, such as refluxing or thermal treatment, will be explored in the future or even the use of the amorphous Ca and Sr substituted TMP as the starting cement precursors will also likely be explored.

APPENDIX B

BIODEGRADABLE POLY(LACTIDE-CO-GLYCOLIDE) COATINGS ON MAGNESIUM ALLOYS FOR ORTHOPEDIC APPLICATIONS

In addition to the work done surrounding fundamental analysis and practical improvements to magnesium-based cementitious materials, research was conducted to study the effect of polymeric coatings on metallic magnesium biomaterial substrates, which will be the subject of Appendices B and C. In Appendix B polymeric film coatings were applied by dip coating on two magnesium alloy systems, AZ31 and Mg4Y, in an attempt to slow the degradation of these alloys under *in vitro* conditions. Poly(lactic-co-glycolic acid) polymer in solution was explored at various concentrations, yielding coatings of varying thicknesses on the alloy substrates. Electrochemical corrosion studies indicate that the coatings initially provide some corrosion protection. Degradation studies showed reduced degradation over three days, but beyond this time point do not maintain a reduction in corrosion rate. Scanning electron microscopy indicates inhomogeneous coating durability, with gas pocket formation in the polymer coating, resulting in eventual detachment from the alloy surface. *In vitro* studies of cell viability utilizing mouse osteoblast cells showed improved biocompatibility of polymer coated substrates over the bare AZ31 and Mg4Y substrates. Results demonstrate that while challenges remain for long term

degradation control, the developed polymeric coatings nevertheless provide short term corrosion protection and improved biocompatibility of magnesium alloys for possible use in orthopedic applications. Results of these studies are described herein.

B.1 INTRODUCTION

Historically, within the orthopedic market, fixation and repair have been limited to implantation of inert alloys, such as titanium and stainless steel, to immobilize and heal damaged bone [267-269]. Magnesium and magnesium-based alloys pose a bright prospect for use in orthopedic and craniofacial repair applications since these alloys not only display physical properties strikingly similar to natural bone but also exhibit the unique ability to degrade *in vivo* [267, 270-272]. As a result, these alloys are potentially promising candidates for orthopedic fixation plates and screw device. Such implants that degrade on demand *in vivo* following completion of their primary function to providing support to the underlying fractured bone or healing of the non-union are indeed desirable because this type of implant reduces the chance of long term complications associated with permanent implants, including foreign body response, delayed type hypersensitivity, and secondary removal surgery [267, 273]. Consequently, research into the potential of magnesium-based alloys for implants that degrade in this manner has increased exponentially in the past five years. The current barrier to clinical implementation for magnesium alloys is the aggressive degradation rate, accompanying hydrogen gas evolution, and limited bioactivity [273, 274]. This hydrogen gas evolution results in undesirable gas pocket formation near the site of implantation. The corrosion of magnesium *in vivo* results in hydrogen gas evolution per the general reaction in Equation B-1:

Equation B-1

$$Mg + 2H_2O \rightarrow Mg^{2+} + 2(OH)^- + H_2$$

It can be seen from Equation B-1 that the dissolution of one atom of magnesium generates one molecule of hydrogen gas [275]. It is also generally accepted that magnesium and the hydroxide ions will react to form $Mg(OH)_2$ passivation layer on the surface of the implant. However, this layer is not highly stable and that magnesium alloys are susceptible to pitting corrosion [268].

Strategies to limit degradation rate *in vivo* include exploring unique alloying elements, processing strategies and applying surface coatings. Alloying and improvements in processing methodologies may obtain slower degradation rates, but are not likely to drastically improve surface bioactivity of the implant, which can ultimately affect osseo-integration and new bone growth [274, 276]. The utilization of surface coating is thus of great interest, as coatings have the potential to both slow degradation and increase the biocompatibility of implants. Specifically of interest are calcium-phosphate based coatings due to their structural similarity to the mineralized component of natural bone, and degradable polymeric coatings [272, 277-281]. Coatings of degradable polymers can not only act as a corrosion barrier, but can be used to deliver drugs, genes and growth factors at the body-implant interface [282]. Among the many natural and synthetic polymers explored poly (lactide-co-glycolide) (PLGA) has numerous justifications for use as a coating owing to their high biocompatibility, clearance through FDA for numerous devices, well explored drug delivery capabilities and ability to tailor *in vivo* degradation rates with metabolically digestible degradation products [283-286]. The integration of PLGA on the surface of magnesium alloys could therefore potentially serve to inhibit corrosion and

additionally act as a scaffold to elude antibiotic agents, such as cefoxitin sodium, or growth factors, such as BMP-2 [287, 288]. Previously, Li et al explored a high molecular weight 90:10 PLGA on a magnesium 6 wt% zinc alloy, and showed some corrosion protection of the alloy, as demonstrated by polarization curves and electrochemical impedance spectroscopy [289]. Surprisingly, the authors determined that a thinner coating would provide more protection against corrosion than a thicker coating. The authors speculated that the thinner coating is sufficient to passivate the alloy surface and that a thicker coating would contains more defects than the thinner coating while providing no additional passivation, thus leading to an inferior corrosion protection profile for the thicker coating. Xu et al and Lu et al have recently reported the incorporation of PLGA, films or spheres, into composite coatings for drug-release purposes [290, 291].

In this study, a mid-range molecular weight 50:50 PLGA is coated on to two magnesium alloy systems, AZ31 (96 % Mg, 3 % Al and 1 % Zn by weight) and Mg4Y (96 % Mg and 4 % Y, by weight). It should be noted that this is the first report of PLGA coatings on AZ31 or Mg-Y alloy systems to the best of our knowledge. The present study was conducted in order to evaluate the potential of PLGA coatings to slow the corrosion and increase the biocompatibility of the AZ31 and Mg4Y alloys. The successful implementation of PLGA for this purpose could lead to the use of PLGA as a one-step, multifunctional coatings for magnesium-based alloys for use in orthopedic applications requiring biocompatibility and time dependent corrosion protection.

B.2 MATERIALS AND METHODS

B.2.1 Materials and Sample Preparation

Hot rolled AZ31 alloy was acquired from Alfa Aesar (Ward Hill, MA, USA) and was used as received. Mg4Y was acquired from GKSS Research Institute (Geesthacht, Germany) in ingot form, graciously provided by Dr. Norbert Hort, and further homogenized by heat treating to 525 °C in ultra-high purity Argon (UHP-Ar)under inert atmosphere for 8 h. Samples were cut into squares 1.25 x 1.25 x 0.08 cm in size and cleaned by etching in 3 % nitric acid solution. The samples were then rinsed with acetone, polished to 1200 grit (5 μm) SiC polishing paper, and sonicated for 30 minutes in acetone. Cleaned and polished samples were stored in acetone until application of the polymer coatings. Poly(D,L-lactide-co-glycolide), Mw 30,000-60,000, (Sigma-Aldrich) was dissolved in dichloromethane at 10 and 20 % weight/volume, from here on referred to as AZ31-PLGA 10 %, AZ31-PLGA 20 %, Mg4Y-PLGA 10 % and Mg4Y-PLGA 20 %, respectively, depending on the alloy and polymer concentration utilized. The polished substrates were subsequently dipped into the respective polymer solution at room temperature, allowed to reside for 1 minute, withdrawn at a speed of 200 μm/s using a dip coater (Desktop Dip Coater, Model No EQ-HWTL-01-A, MTI Corporation, USA), and then finally allowed to dry at room temperature. This dip coating process was repeated in triplicate on each sample for each test completed.

B.2.2 Characterization of Coatings

The coating thickness of the films was calculated by measuring the weight gain from dip coating in polymer solutions and the sample dimensions. Thickness measurements were taken in triplicate and averaged. The presence of the coatings was further confirmed by attenuated total reflectance Fourier transform infrared spectroscopy (ATR-FTIR, Nicolet 6700 spectrophotometer, Thermo Electron Corporation) using a diamond ATR Smart orbit. Spectra were obtained at 1.0 cm^{-1} resolution averaging 32 scans in the 400 – 2500 cm^{-1} frequency range.

B.2.3 *In vitro* Degradation and Corrosion

Electrochemical corrosion characterization studies of the coated alloy samples were performed using CH604A (CH Instruments Inc) electrochemical work station. Following sample preparation as described in the previous section, one side of each sample was connected to a wire with silver epoxy and then electrically insulated, so that only one side is exposed for conducting the electrochemical tests. The length and width measurements were taken for corrosion current calculations. Ag/AgCl and a platinum wire were employed as the reference and counter electrodes, respectively. Testing was carried out utilizing a 3-neck jacketed flask (ACE Glassware) filled with 125 mL Dulbecco's Modified Eagle's Medium (DMEM) containing 10 % fetal bovine serum (FBS, Atlanta Biologicals, Lawerenceville, GA) and 1 % penicillin/streptomycin antibiotics (P/S, Gibco, Grand Island,NY), equilibrated to 37 °C. All the specimens were allowed to equilibrate to reach a stable open circuit potential (OCP), before initiating the polarization tests at a scan rate of 1.0 mV/s. The corrosion current was determined using the Tafel extrapolation of the polarization curve and normalized by the exposed surface

area to yield a measurement of corrosion current density. The software program Origin with a Tafel packet was used to perform the Tafel extrapolation and plot the data.

Corrosion profile up to 21 days was assessed by analyzing the magnesium ion concentration in media extracted after sample incubation. The coated substrates were sterilized by UV light exposure for 1 h per side. Each substrate was then soaked in 2 mL of DMEM containing 10 % FBS and 1 % P/S under standard growth conditions of 37 ºC, 5 % CO_2 and 95 % relative humidity for 21 days. The media was changed and collected every 24 h to monitor the degradation rate under *in vitro* conditions. The collected media was diluted in 0.03 M Tris buffer solution and analyzed using inductively coupled plasma optical emission spectroscopy (ICP-OES, iCAP duo 6500 Thermo Fisher). Magnesium ion concentrations in solution were compared to media and uncoated substrate controls. The coatings were characterized post-corrosion using a digital optical microscope (Keyence VHX-600K) and a scanning electron microscope at 10 kV (SEM, Philips XL30 FEG ESEM). Samples were sputter coated with palladium (Cressington sputter coater 108A) for observation of the surface morphology post corrosion using SEM.

B.2.4 Cell Culture

Murine MC3T3 –E1 pre-osteoblast cells obtained from ATCC (Manassas, VA) were utilized for cell culture studies. Cells were cultured in minimum essential medium alpha (α-MEM, Gibco, Grand Island, NY) containing 10 % fetal bovine serum (FBS, Atlanta Biologicals, Lawerenceville, GA) and 1 % penicillin/streptomycin antibiotics (P/S, Gibco, Grand Island, NY) at 37 ^{o}C, 5 % CO_2 and 95 % relative humidity. Substrates were placed in 12 well plates and sterilized using UV radiation for 40 minutes on each side. The substrates were then seeded with

MC3T3 cells, after third to seventh passage, at a density of 60,000 cells/well, with a total media volume of 2 mL/well. Media was changed every other day throughout the testing period.

B.2.5 Live/Dead Assay and Cytoskeletal Imaging

Cell viability was assessed using Live/Dead staining (Invitrogen, Live/Dead Staining Kit). The assays were performed on day 1 and day 3 substrate cell cultures. The coated alloy substrates were rinsed with phosphate buffered saline (PBS, Lonza BioWhittaker Buffers and Buffered Salines, 1x, 0.0067 M(PO_4) without calcium or magnesium) and then incubated for 30 minutes in live/dead stain, calcein AM and ethidium homodimer-1, diluted in PBS. After incubation, the samples were again washed with PBS and then imaged using fluorescence microscopy (Olympus CKX41, Olympus DP25 Microscope Camera).

Following fluorescence imaging, cells were fixed using a 2.5 % glutaraldehyde solution for 15 minutes. Fixed samples were then subjected to alcohol dehydration and mounted for SEM imaging. Samples were coated with palladium in order to observe the cell morphology using SEM.

B.3 RESULTS AND DISCUSSION

B.3.1 Coating Characterization

The thickness of the coatings was calculated by measuring the sample dimensions and the gain in weight following dip coating, assuming a fully dense, nonporous coating and the manufacturer-provided material density of 1.34 g/ml using the Equation B-2

Equation B-2

Thickness = 10^4 * weight gain / [density * surface area]

where thickness is in µm, weight gain in g, density in g/cm^3 and surface area in cm^2. Resulting thicknesses indicate that there is a large increase in coating thickness with a higher solution concentration, Table B-1. There is no statistical difference however between the coating thickness on AZ31 or Mg4Y alloy with either polymer concentrations, indicating similar interaction occurring between the alloy surface and the polymer solution for both alloys.

Table B-1 Coating thicknesses on magnesium substrates.

Sample Type	Thickness (µm)
AZ31-PLGA 10%	~1.6
AZ31-PLGA 20%	~41.8
Mg4Y-PLGA 10%	~1.6
Mg4Y-PLGA 20%	~62.1

FT-IR was used to confirm the presence of the polymer coatings on the alloy. Figure B-1 shows the FT-IR spectrum of uncoated Mg alloys, PLGA and PLGA coated samples. The

characteristic bonds at numerous wave numbers, such as the carbonyl stretching at 1750 cm^{-1}, C–O–C stretching at ~1080 $cm^{-1}$are indicative of the presence of the PLGA polymer [292]. No such peaks are expectedly seen on the bare metal substrates devoid of the polymer. Differences between the coating thicknesses, as expected, did not appear to influence and cause any changes to the obtained spectra.

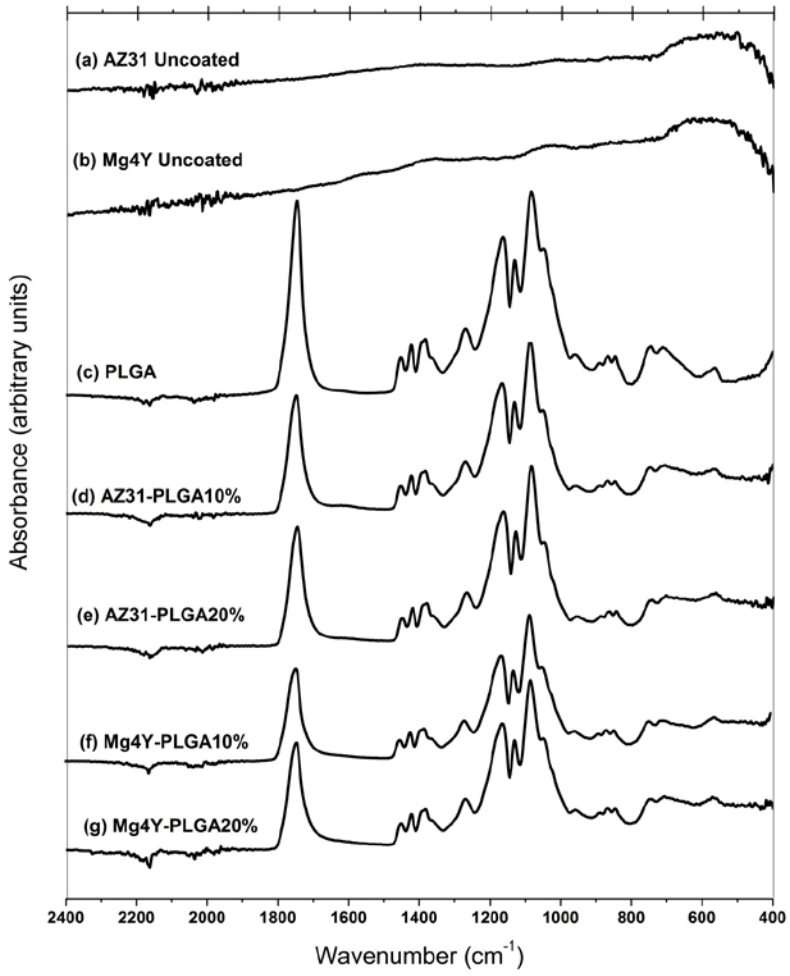

Figure B-12 FTIR spectra of Uncoated AZ31 (a), Uncoated Mg4Y (b), pure PLGA (c) and coated samples AZ31-PLGA 10 % (d), AZ31-PLGA 20 % (e), Mg4Y-PLGA 10 % (f) and Mg4Y-PLGA 20 % (g), showing clear presence of PLGA on all coated substrates.

B.3.2 *In Vitro* Degradation

Polarization curves for the coated and uncoated substrates can be seen in Figure B-2 for AZ31 substrates (a) and Mg4Y substrates (b). Table B-2 gives a summary of the corrosion potential and corrosion current densities as calculated from extrapolation of the Tafel plots. For the AZ31 alloy, PLGA coatings on the substrates resulted in an E_{corr} that is less negative than the uncoated alloy, indicating that the coating did provide a barrier for corrosion. Increase in polymer thickness further yielded an increase in E_{corr} indicating the beneficial influence of the thicker polymer coating. The presence of the polymer coatings on AZ31 visibly also lowered the i_{corr} values compared to the uncoated AZ31 alloy substrate, although there was no significant variation between the two different polymer concentrations and thickness of the polymer coatings. The addition of PLGA coatings on Mg4Y alloy substrates also resulted in E_{corr} values which are less negative than the uncoated substrates as well as reductions in i_{corr} values similar to the coatings on AZ31. Similar to the coatings on the AZ31 substrate, there was no perceivable difference in the i_{corr} values between the two polymer concentrations and consequent thickness of the polymer coatings. Additionally, unlike the coatings on AZ31increasing the thickness of the PLGA coating on Mg4Y substrates did not offer much change in the E_{corr} or i_{corr} values. It should be however noted that the corrosion potential of the uncoated Mg4Y is more negative compared to the uncoated commercial AZ31 alloy indicative of a more reactive alloy surface, which is not consistent with predictions reported by previous researchers [286]. This is possibly a consequence of the difference in the processing conditions of the alloys. AZ31 is a commercial product that has been likely processed with better precision and impurity control than the laboratory-generated Mg4Y that was not subjected to any further processing modifications following casting other than the standard homogenization treatments. Despite these differences

between the two alloy substrates to begin with, overall however, the polarization curves of the polymer coated AZ31 and Mg4Y substrates do exhibit corrosion protection of the bare AZ31 and Mg4Y alloys as demonstrated by less negative E_{corr} as well as a reduction in i_{corr} for all the coated substrates regardless of the thickness and the polymer concentration.

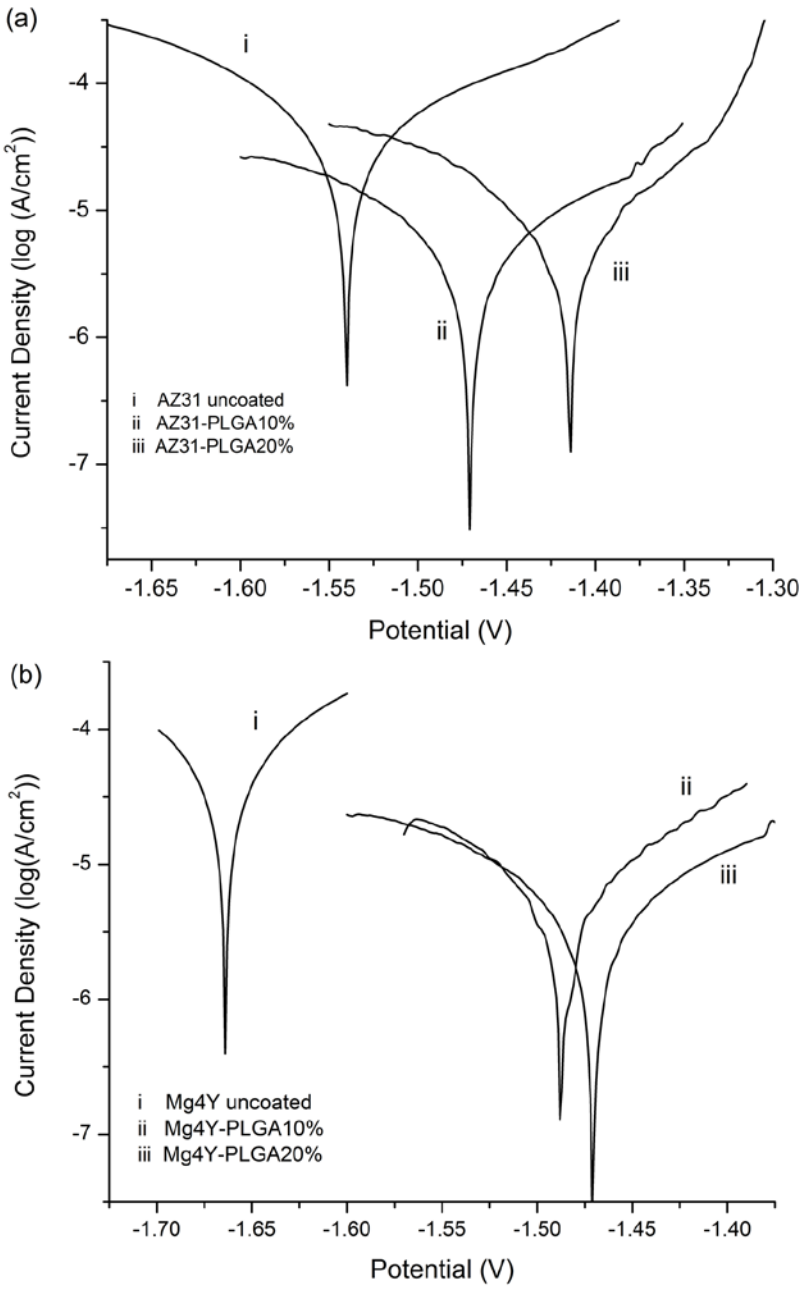

Figure B-2 Polarization curves of substrates AZ31 (a) uncoated (i), PLGA 10 % (ii) and PLGA 20 % (iii) coatings and Mg4Y (b) uncoated (i), PLGA10 % (ii) and PLGA 20 % (iii) coatings.

Table B-2 Corrosion potential (E_{corr}) and current density (i_{corr}) values for coated and uncoated substrates.

	E_{corr} (V)	i_{corr} (A/cm^2)
AZ31-Uncoated	-1.54	3.10E-05
AZ31-PLGA10%	-1.469	5.20E-06
AZ31-PLGA20%	-1.415	6.05E-06
Mg4Y-Uncoated	-1.664	4.42E-05
Mg4Y-PLGA10%	-1.485	8.09E-06
Mg4Y-PLGA20%	-1.469	6.85E-06

Coated and uncoated substrates were further immersed in DMEM with FBS and P/S which was changed daily and maintained under *in vitro* conditions to qualitatively determine the effect of polymeric coatings on the stability and degradation rate of the alloys. SEM images of the coated substrates of AZ31 and Mg4Y are shown in Figures B-3 and B-4 respectively, at three time points namely, 3, 12 and 15 or 21 days. At day 3, microscopic inspection indicates that coatings on all substrates are present; however noticeable changes to the substrate surface begin to appear particularly with the coatings corresponding to higher polymer concentration and higher thickness. Coatings of PLGA 10 % show the onset of corrosion under the surface, as indicated by the plate-like morphology typical of magnesium corrosion product which is also seen in the AZ31 and Mg4Y uncoated substrates. Comparing the PLGA 10 % coated substrates with the uncoated substrates, the coatings appear to slow the corrosion for shorter time points. The corrosion however progresses with increase in incubation time. Coatings of PLGA 20 % show the formation of gas bubbles, likely of trapped hydrogen gas, forming underneath the polymeric surface during 3 days of incubation. As the incubation time progresses, these bubbles appear to grow with increasing volume of gas generated reaching the maximum pressure leading to collapse of the gas bubbles, consequently leaving the unprotected substrate fully exposed in some areas to the liquid environment while the polymer remains intact in other non-specific

areas. The same plate-like corrosion product can be seen on the exposed areas of the substrate. This effect appears to be especially aggravated on the Mg4Y-PLGA 20 % surface. The Mg4Y alloy appears to undergo more aggressive corrosion in the presence of PLGA in contrast to the AZ31 alloy. Previous research indicates that opposite effect should be true in the uncoated alloys [286]. However, to the authors knowledge, these two alloys, with or without coatings, have not been directly compared. For all polymer coatings, the polymer provides partial protection of the alloy surface initially, but the stability of the coating appears to break down with incubation time leading to eventual swelling, deformation, and delamination of the polymer from the alloy surface.

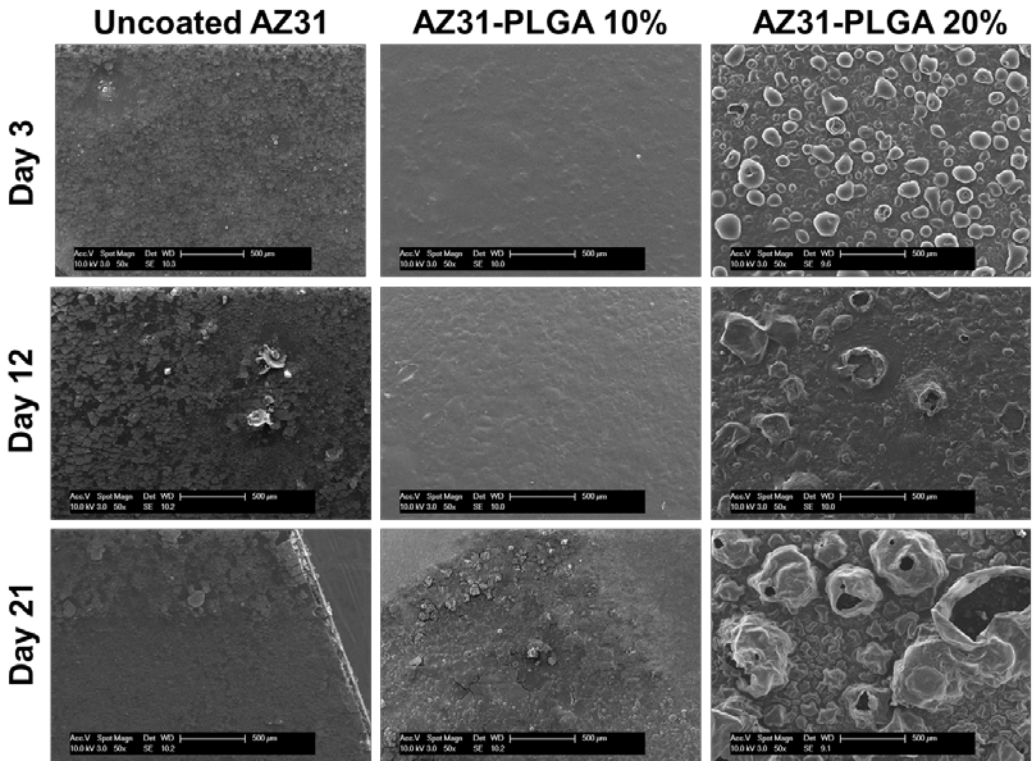

Figure B-3 SEM Images of uncoated and PLGA coated AZ31 substrates post incubation in media (Scale bar is 500 µm).

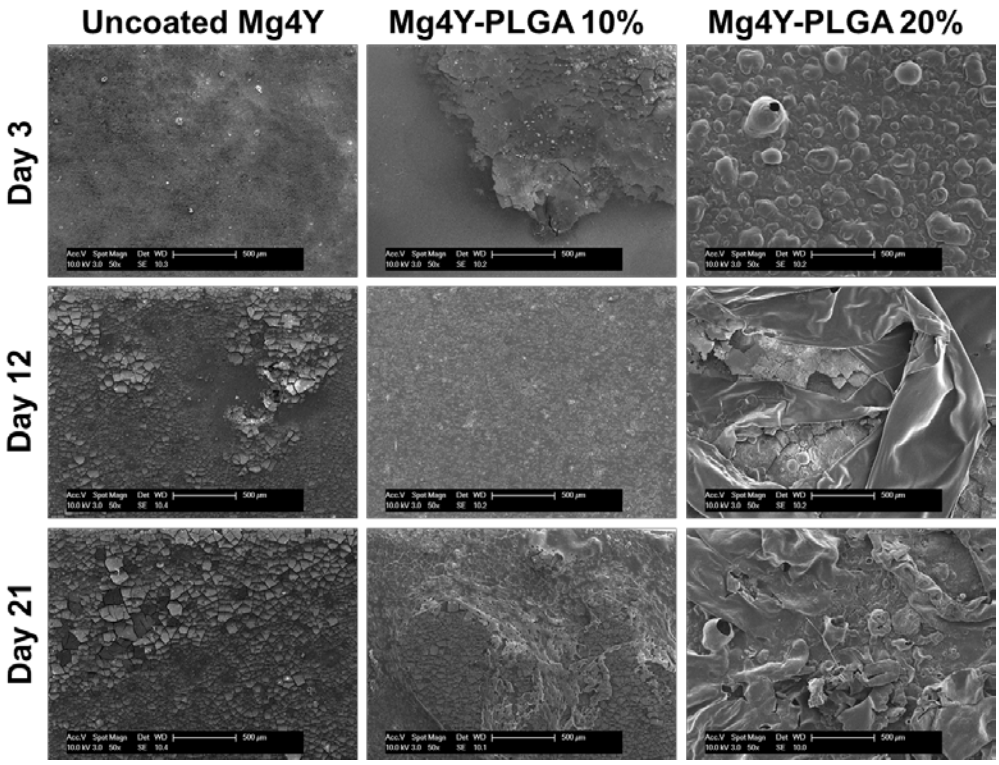

Figure B-4 SEM Images of uncoated and PLGA coated Mg4Y substrates post incubation in media (Scale bar is 500 µm).

ICP was used to determine ionic concentrations of magnesium in the DMEM collected in order to further evaluate the degradation of the AZ31 and Mg4Y substrates when coated with the protective PLGA polymer (Figures B-5 a & b). For all samples, including uncoated substrates, there is an increase in magnesium ion concentration above pure media baseline. Both AZ31-PLGA 10 % and Mg4Y- PLGA 10 % coatings show some reduction in magnesium ion release at day 3, and at subsequent time points AZ31-PLGA 10 % coatings yield magnesium concentrations similar to the uncoated substrate for subsequent time points until day 12 beyond which the magnesium ion concentration appear to be slightly elevated compared to the uncoated AZ31 alloy. For AZ31-PLGA 20 % and Mg4Y- PLGA 20 %, there is again a reduction in magnesium ion release in comparison to the uncoated substrates at day 3. However, at later time

points this reduction is not maintained. The PLGA 20 % coatings on both substrates appear antagonistic, with the daily ion release rate increasing rapidly until day 9 above that of the uncoated substrates with the Mg4Y-PLGA 20 % exhibiting almost two-fold higher dissolution of Mg compared to the corresponding coating on AZ31. This is unexpected because as corrosion of the metal alloy underneath the PLGA coating proceeds, pH should increase, pushing the surface closer to passivation [268]. This would in turn reduce the corrosion because the buildup of the more robust magnesium hydroxide layer would lead to some corrosion protection for the alloy surface [293].

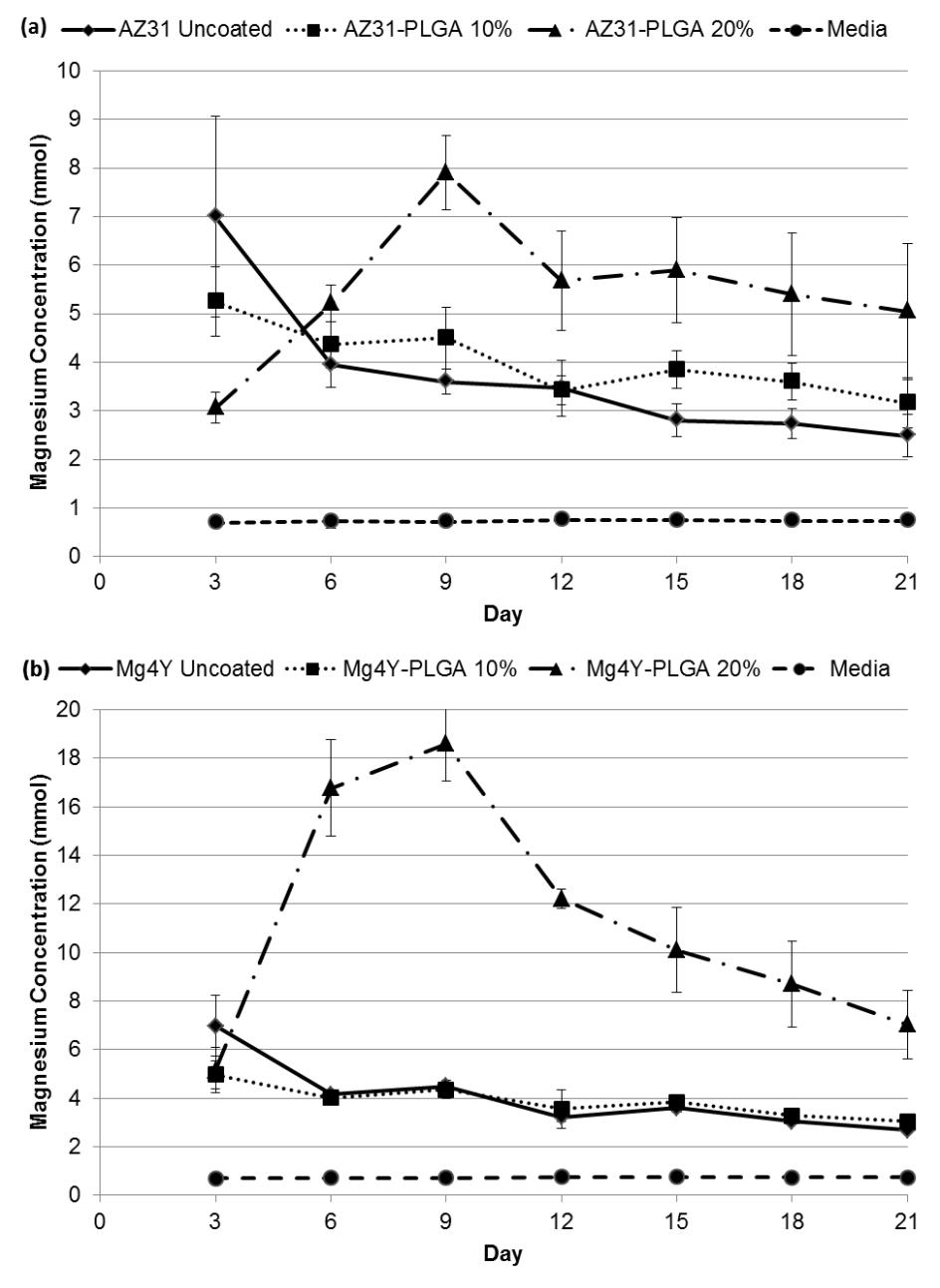

Figure B-5 ICP measurements of daily magnesium ion concentration in extracted incubation media for AZ31 coated and uncoated samples (a) and Mg4Y coated and uncoated samples (b).

It is also important to note that PLGA is considered semi-permeable to water, as the water penetration into the bulk of the polymer occurs faster than surface hydrolytic degradation of the polymer [294]. It is well known that the hydrolytic degradation within the bulk of the

PLGA coating would result in the formation of acidic byproducts. These byproducts could react with the magnesium corrosion ions or magnesium hydroxide, forming soluble magnesium lactates or magnesium glycolates. The formation of lactates and glycolates will prevent the formation and growth of dense and thick corrosion protective magnesium hydroxide layer. It is therefore very unlikely that the reaction products of magnesium lactate and glycolate can form dense corrosion protective layers as these salts are more soluble than magnesium hydroxide [295, 296]. The local increase in pH as well as absence of any corrosion protective layer will therefore lead to the rapid corrosion of the underlying bare surfaces. The effect is expected to be greater with the thicker coating, thus explaining the greater corrosion seen with the PLGA 20 % coatings.

The corrosion results observed by us compare well with the observation of the coating tests reported by Chen et al, wherein PCL and PLA coatings on pure magnesium displayed a "special interaction" [280]. The authors observed that the individual degradations of the polymer coating and the magnesium alloy were each antagonistic of the other and that this reciprocity ultimately undermined the corrosion resistance of the material under dynamic degradation tests. The hypothesized effect reported by Chen et al correlates well with the ICP results of day 3 reported here as well as the electrochemical corrosion results, which asses that the corrosion protection by the PLGA coating on AZ31 and Mg4Y is only observed at very early time points, demonstrating that the PLGA coatings regardless of the concentration only serve to provide a physical barrier to corrosion, through day 3, but that protection is not maintained beyond six days of incubation, presumably due to the penetration of water into the PLGA bulk coating and the subsequent degradation of both the polymer coating and the magnesium alloy substrate. The discussed mechanism is also consistent with the SEM observations, which clearly show the

formation of large number of hydrogen gas bubbles in AZ31 PLGA 20 % and Mg4Y PLGA 20 % coatings in contrast with the corresponding AZ31and Mg4Y substrates containing PLGA 20 % coatings (see Figures B-3 & B-4).

Figure B-6 shows the digital optical images of the incubated substrates at the same three time points as shown in the SEM images. These images also support the previous observations of coating protection and durability, including the formation of bubbles beneath the polymer (day 3 PLGA 20 % on AZ31 and Mg4Y), the separation of the thicker coatings from the alloy surface (especially PLGA 20 % on Mg4Y) and the more aggressive corrosion of Mg4Y in comparison to AZ31.

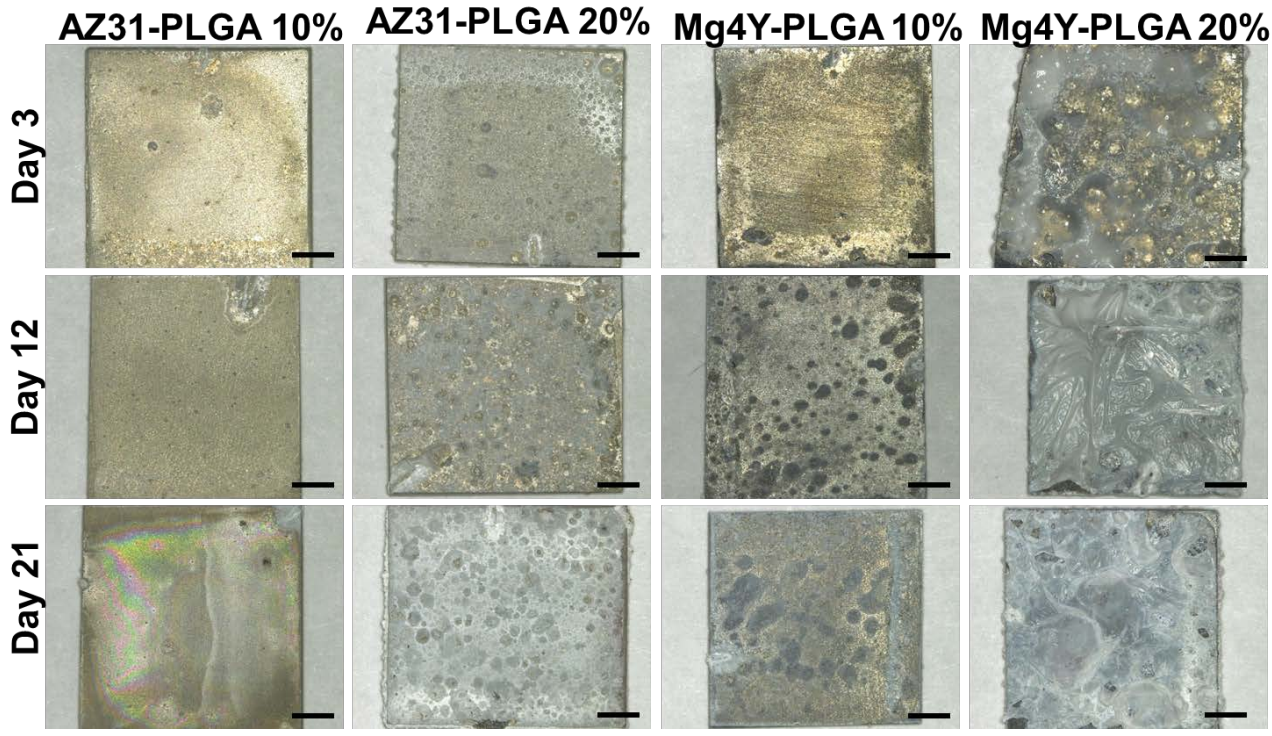

Figure B-6 Digital Optical Images of PLGA coated AZ31 and Mg4Y substrates post incubation in media (Scale bar is 2 mm).

B.3.3 Cytocompatibility

SEM images of cells fixed on the surface of the alloys 24 h following seeding can be seen in Figure B-7 and the Live/Dead staining of osteoblasts at 1 and 3 days post seeding can be seen in Figure B-8. These SEM images show the cell cytoskeletons, indicated by the arrows, flattened and extended on the polymeric surface, indicating good adhesion of the osteoblasts validating the polymer coated surface being favorable for cell attachment. Staining of cells at one and three days (Figure B-8) shows an increase in cell number at day 3 over day 1, indicating no inhibition for cell proliferation, especially for the polymer coated AZ31 substrates. It appears therefore that the formation of gas bubbles in the polymer plays a direct role in the location and the manner in which the cells grow. For example, AZ31-PLGA 20 % at day 3 shows open regions where the hydrogen bubbles resulting from corrosion have burst open preventing attachment of the cells. Surrounding the gas pocket are areas of high density of cells, but within the spherical gas bubble pocket regions no cells have proliferated. Additionally, as seen in Mg4Y-PLGA 10 % at day 3, where cells may have proliferated within the spherical gas pocket region following collapse of the gas bubbles or underneath the polymeric coating, those cells do not survive. This is likely due to the change in local ion concentrations as discussed above. The application of PLGA coatings on the surface of AZ31 and Mg4Y alloys despite the time dependent corrosion protection demonstrated in Figure B- 3 and B-4, has a clear improvement on the biocompatibility of the uncoated alloy surface showing improved cell viability and proliferation over the uncoated substrates.

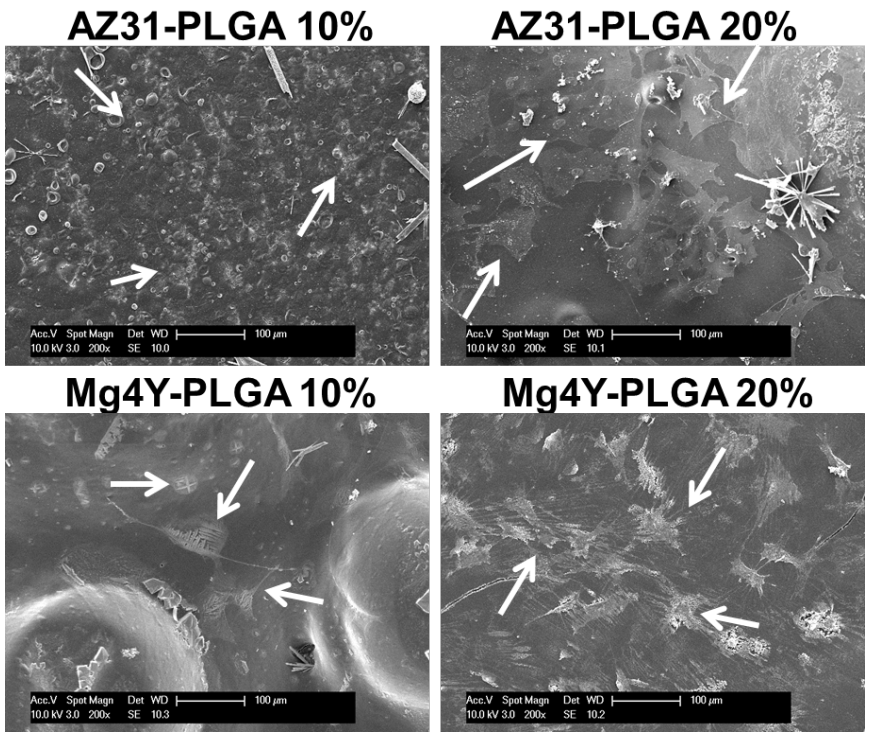

Figure B-7 Morphology of MC3T3 osteoblasts at 24 hrs post-seeding, indicating better cell adhesion for thicker PLGA coatings (Scale bar is 100 µm).

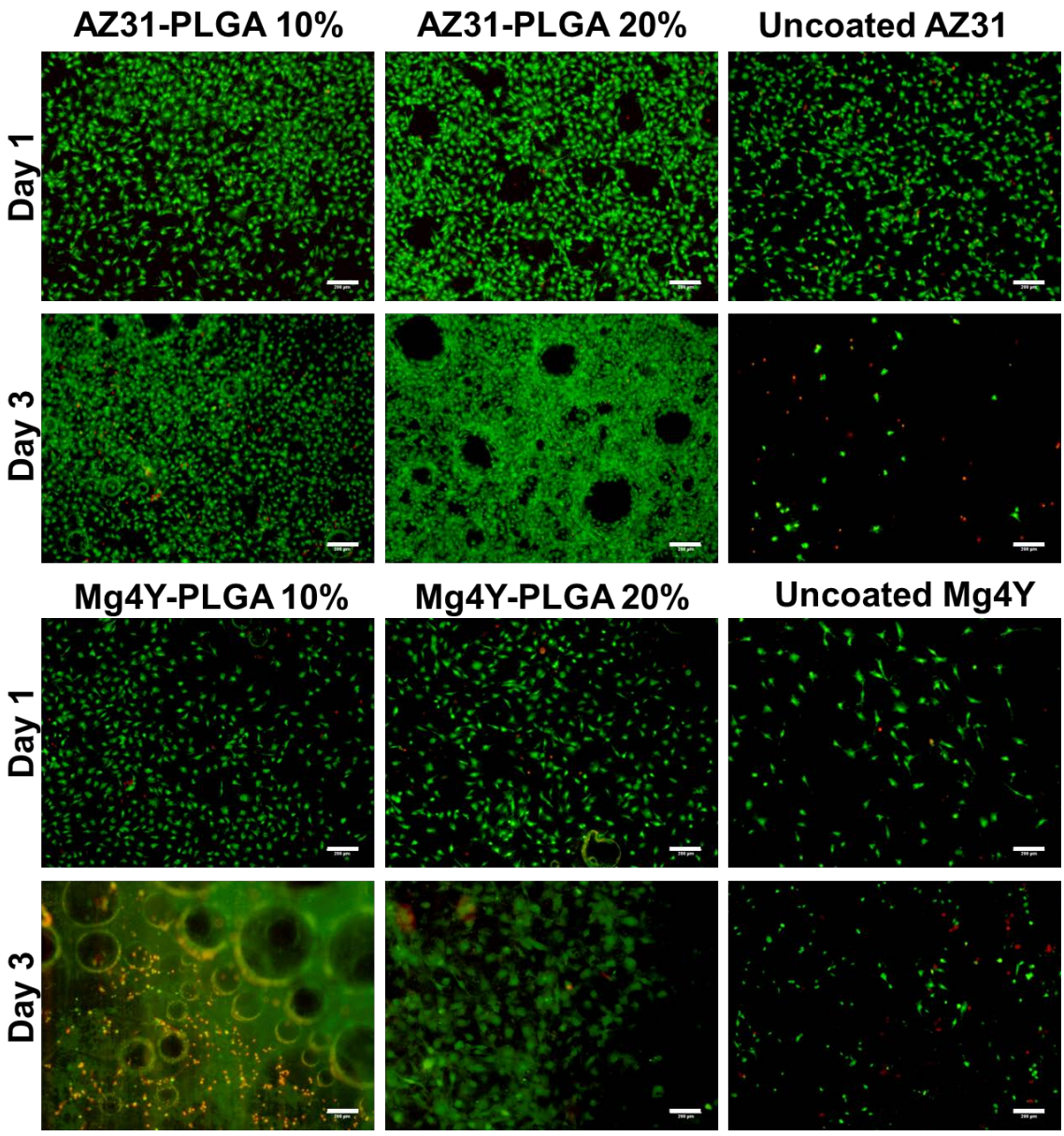

Figure B-8 Live/Dead Staining of MC3T3 osteoblasts on coated and uncoated substrates indicating improved biocompatibility of coated substrates over uncoated substrates (Scale bar is 100 µm).

Compiling the various corrosion and cell adhesion, viability and proliferation results, it is clear that although the biocompatibility of the PLGA coating is better, the corrosion protective nature of PLGA coatings on the surface of magnesium alloys however is inconsistent. While numerous factors affect the degradation rate of poly(lactide-co-glycolide) polymers, the crucial

issue with utilizing PLGA (and many other degradable polymers) as a temporary tool for corrosion protection is the mechanism of PLGA degradation. PLGA is known to undergo bulk erosion *in vivo*, wherein the full body of the material is simultaneously attacked by water, as opposed to surface erosion, where only the surface of the material is degraded [294]. In the context of protecting metallic surfaces from corrosion, the bulk erosion of the polymeric coating leads to rapid exposure of the surface to water and acidic erosion byproducts. Thus, the amount of water exposure to the underlying bare metal surfaces is limited but not fully prevented. This appears to be exaggerated by the evolution of hydrogen gas upon initiation of corrosion. The gas is trapped below the polymeric coating, forming gas pockets which burst and expose larger areas of the metallic substrate to aqueous attack. Further studies and optimized coating strategies to increase the alloy surface-polymer coating adhesion may yield improved corrosion resistance because an increased adhesion would reduce or eliminate gas pocket formation between the polymer and alloy. These studies are currently in progress and will be reported subsequently.

B.4 CONCLUSION

A 50:50 poly(lactide-co-glycolide) polymer with two different concentrations was coated onto the surface of both AZ31 and Mg4Y alloys through a solution dip-coating method. The implementation of PLGA yielded homogeneous and reliable coatings on AZ31 and Mg4Y alloy substrates offering some level of immediate corrosion protection over a limited time period. However, once the aqueous corrosion attack is initiated, the polymer offers little protection over subsequent time periods although dramatic improvements in osteoblast adhesion and proliferation are observed on the surface of both alloy substrates. Between the two alloys, Mg4Y

substrates, both coated and uncoated, appear less resistant to corrosion than AZ31 substrates, which is in direct contrast with results from previous studies. Preventing the formation of gas pockets below the polymeric coatings, through increased alloy-polymer adhesion, may lead to improved corrosion resistance rendering the implementation of these coated Mg alloy substrates for possible use in orthopedic fixation plate application while also permitting the utilization of PLGA for additional biotechnological applications such as drug delivery.

APPENDIX C

CORROSION PROTECTION AND IMPROVED CYTOCOMPATIBILITY OF BIODEGRADABLE POLYMERIC LAYER-BY-LAYER COATINGS ON AZ31 MAGNESIUM ALLOYS

Composite coatings of electrostatically assembled layer-by-layer anionic and cationic polymers combined with an $Mg(OH)_2$ surface treatment serve to provide a protective coating on AZ31 magnesium alloy substrates. This ceramic conversion coating and layer-by-layer polymeric coating combinations reduced the initial and long term corrosion progression of the AZ31 alloy. X-ray diffraction and Fourier transform infrared spectroscopy confirmed the successful application of coatings. Potentiostatic polarization tests indicate improved initial corrosion resistance. Hydrogen evolution measurements over a two week period and magnesium ion levels over a one week period indeed indicate longer range corrosion protection and retention of the $Mg(OH)_2$ passivation layer in comparison to uncoated substrates. Live/Dead staining and DNA quantification were thus used as measures of biocompatibility and proliferation while actin staining and scanning electron microscopy were used to further observe cellular morphology and integration with the coated substrates. The coatings simultaneously provided improved cytocompatibility, cellular adhesion and proliferation in comparison to the uncoated alloy surface

utilizing both murine pre-osteoblast MC3T3 cells and human mesenchymal stem cells. The implementation of such coatings on magnesium alloy implants could serve to improve the corrosion resistance and cellular integration of these implants with the native tissue while delivering vital drugs or biological elements to the site of implantation. Results of these studies are reported herein.

C.1 INTRODUCTION

The utilization of stainless steel or titanium biomedical implants is favorable for clinical applications requiring load-bearing capacities. Necessary as these products may be in today's medical procedures, these inert implants are far from ideal, lacking beneficial characteristics seen in many polymeric and ceramic implants, especially biodegradability [267, 270, 271, 297]. Alternatively, for the past decade there has been a renewed interest in replacing these implants with magnesium-based alloys, which are degradable *in vivo* through simple corrosion and display mechanical properties similar to native bone [269, 275]. The body innately requires magnesium to function and at low levels is able to absorb the hydrogen gas released, however, at faster rates the corrosion can result in hydrogen gas pocket formation and implant failure [268, 273, 274, 298]. As the interest in degradable magnesium alloys for biomedical applications escalates, the uncontrolled degradation remains a major challenge. For clinically relevant magnesium devices, the rates of corrosion must be controlled to ensure functionality and to avoid the accumulation of the hydrogen gas formed during corrosion. In general, two approaches have been adopted to tailor alloy degradation. The first is by modifying the alloy itself through appropriate alloy design, and the second is via the surface modification, such as the application

of coatings [293]. Implementation of suitable coatings can not only serve to delay the initial degradation of the alloy, but may also improve biocompatibility enabling enhanced osseointegration between the coated implant to the surrounding tissue [279, 281, 293, 299, 300]. Coatings of metal-based implants typically fall into two general classes: conversion coatings and deposition coatings. Coatings of these two archetypes, with a variety of techniques and compositions, have been employed by researchers to prevent or slow the corrosion of magnesium [293]. In conversion coatings, the coating is formed *in situ*, through a reaction between the substrate and its environment, and is typically inorganic [293]. For magnesium alloys these coatings are often oxides, phosphates or fluorides. Although conversion coatings exhibit good adhesion to the substrate, there remain concerns with respect to the mechanical durability and biocompatibility of these coatings [293]. The most highly studied conversion coatings calcium phosphate based, especially hydroxyapatite due to its similarity to native mineralized tissues. Although the biocompatibility of calcium phosphate coatings is generally higher than other conversion coatings, the corrosion protection of conversion coatings are shown to be low because these coatings often display cracks or pores which result in unfavorable corrosion levels [293] It is surmised that the most effective conversion coating, plasma electrolytic anodization (PEO) coating application. These coatings show the greatest corrosion protection due to the physical technique of application not the chemical stability of the coating applied. For deposition coatings, a coating is applied through physical interactions with the metal surface. These coatings are typically organic or ceramic, and for magnesium alloys will often require a conversion coating pre-treatment to improve the adhesion of the coating to the alloy [293, 301]. Inorganic deposition coatings are typically hydroxyapatite-based and tend to show high biocompatibility but poor corrosion protection due to the porous nature of the coating [277].

Organic deposition coatings have been widely studied with varying conclusions. Typically 'one-step' organic coatings applied without a primary conversion coating do not show good adhesion or protection of the surface. Organic coatings in 'two-steps' which combine apply a conversion coating prior to the deposited coating show better adhesion and corrosion protection [293].

A more complex coating process, known as layer-by-layer deposition, has the potential to improve upon the disadvantages of other coating techniques. Layer-by-layer assembly of polymer layers resulting in polyelectrolyte multilayer (PEM) film was introduced only 20 years ago by Decher and Lvov and relies on static interactions positively charged and negatively charged polymer chains dissolved in solutions [302-306]. By incubating a substrate in alternating solutions of positive and negatively charged polymers, thin well-adhered film layers are formed. With this technique, a wide variety of solution parameters, such as concentration, pH, molecular weight and additives can be tailored to manipulate the final properties of the coating, including stiffness, hydrophobicity, protein adhesion, degradation rate and drug elusion, surface charge and cell attachment and interactions [307-310]. Additionally, the coating layer assembly can be manipulated to incorporate drugs, biological molecules and nanoparticles into the coatings [307]. These coatings have been widely explored for biomedical applications [307, 311]. The implementation of the layer-by-layer coating technique for biomedical magnesium alloys was first attempted recently by Cai et al, exploring the combination of poly(ethylene imine) and poly(styrene sulfonate) with 8-hydroxyquinoline on a AZ91 magnesium alloy [299]. Very recently Liu et al explored the corrosion resistance of chitosan/poly(styrene sulfonate) multilayers on a mirco-arc oxidized magnesium surface [312]. In both cases the researchers showed improved corrosion resistance of the coated alloy however the exploration into the biocompatibility of these surfaces is minimal or non-existent, respectively.

This work demonstrates the implementation of a combination of coating techniques, utilizing an $Mg(OH)_2$ passivation layer formed through chemical conversion *in situ* in conjunction with the layer-by-layer (LbL) deposition of a degradable PEM coating, to form a protective, biocompatible coating on a commercially available AZ31 magnesium alloy. The anionic polymers explored in this study were polycaprolactone (PCL) and two different poly(lactide-go-glycolide) (PLGA) formulations. These polymers were selected since they have been widely used both in research and clinically. They are also biocompatible and biodegradable with metabolically digestible degradation products, and are currently utilized in FDA-approved medical devices [283, 284]. The cationic polymers explored were polyethylenimine (PEI) and polyallylamine hydrochloride (PAH). These polymers have been studied for applications such as gene delivery, antibacterial uses and cell encapsulation [310, 313-315]. The resulting coated substrates were characterized for immediate and long term corrosion protection to understand the roles of the resultant PEM on the degradation behavior of the underlying AZ31 alloy. Furthermore, the cytocompatibility of the PEM coated substrates was tested with murine osteoblasts and human mesenchymal stem cells.

C.2 MATERIALS AND METHODS

C.2.1 Materials and Sample Preparation

Hot rolled AZ31 alloy was acquired from Alfa Aesar (Ward Hill, MA, USA) and was used without further thermal or mechanical treatment. Samples were cut into 1.25 x 1.25 x 0.08 cm

pieces and cleaned by etching in 3% nitric acid solution in ethanol. Samples were then polished to 1200 grit (5 μm) using SiC polishing paper and sonicated for 30 minutes in acetone. Following sonication, samples were incubated in a 5M NaOH solution for 2 hours at 60 °C to form an $Mg(OH)_2$ surface layer, then dried in air at 60 °C for 1 hour. Samples were subsequently rinsed in deionized water for 5 minutes, then again dried at 60 °C for 30 minutes. Layer-by-layer coatings were created via a dip-coating method (Desktop Dip Coater, Model No EQ-HWTL-01-A, MTI Corporation, USA), wherein for each coating the substrates were dipped into the polymer solution, incubated for 1 minute, withdrawn at 200 μm/s and dried in air. Layers were generated with the following sequence, "ABCBCBCBCB". Solutions A and C contain cationic polymers, polyethylenimine (PEI, MW 25,000) at 10 mg/ml in DI water and poly(allylamine hydrochloride) (PAH, MW 58,000) at 5 mg/ml in 4-(2-hydroxyethyl)piperazine-1-ethanesulfonic acid buffer (HEPES buffer), respectively. Solution B consists of a synthetic anionic polymer, 50:50 poly(lactide-co-glycolide) (PLGA 50:50, MW 30,000-60,000) 75:25 poly(lactide-co-glycolide) (PLGA75:25, MW 76,000-115,000) or polycaprolactone (PCL, MW 70,000-90,000) each at 50 mg/ml in dichloromethane. All five polymers were acquired from Sigma-Aldrich. Three different variations of layer-by-layer coatings were generated, depending on the anionic polymer used, subsequently termed PLGA50:50, PLGA75:25 or PCL depending on the anionic polymer utilized for the 'B' layer.

C.2.2 Characterization of Coatings

The formation of the $Mg(OH)_2$ layer was confirmed utilizing glancing angle x-ray diffraction (GA-XRD, Philips PWI830 Diffractometer) using copper Kα radiation with a 2θ range of 10-80º, 0.02º step size and an ω angle of 1º offset. The chemical nature of the coatings was confirmed by

Attenuated Total Reflectance Fourier Transform Infrared spectroscopy (ATR-FTIR, Nicolet 6700 spectrophotometer, Thermo Electron Corporation) using a diamond ATR Smart orbit. Spectra were obtained at 1.0 cm^{-1} resolution averaging 64 scans in the 400 – 2500 cm^{-1} frequency range. The surface morphology of the coating was studied using scanning electron microscopy (SEM, Joel JSM-6610LV) at 10 kV operating voltage. Prior to imaging samples were sputter coated with palladium (Cressington sputter coater 108A).

C.2.3 Electrochemical Corrosion

Electrochemical corrosion characterization of the coated alloy samples was performed using a CH604A (CH Instruments Inc) electrochemical work station. Following sample preparation as described previously, length and width were measured and then one side of each sample was connected to a wire with silver epoxy and then electrically insulated with polymeric epoxy, such that only one side is exposed for electrochemical testing. Ag/AgCl reference electrode (4.0M KCl, Accument) and a platinum wire counter electrode were employed. Testing was carried out utilizing a 3-neck jacketed flask (ACE Glassware) filled with 125mL Dulbecco's Modified Eagle's Medium (DMEM) containing 10 % fetal bovine serum (FBS, Atlanta Biologicals, Lawerenceville, GA) and 1 % penicillin/streptomycin antibiotics (P/S, Gibco, Grand Island,NY), equilibrated to 37 °C. All the specimens were allowed to equilibrate to reach a stable open circuit potential (OCP), before initiating the potentiostatic polarization tests at a scan rate of 1.0 mV/s. The corrosion current was determined using the Tafel extrapolation of the polarization curve and normalized by the exposed surface area to yield a measurement of corrosion current density. The Tafel extrapolation was taken at potential values 50 mV below and above the corrosion potential

value to ensure proper extrapolation. The software program Origin with a Tafel extrapolation packet was used to perform the analysis and plot the data.

C.2.4 *In Vitro* Degradation

Corrosion profile up to 7 days was assessed by analyzing the magnesium ion concentration in media extracted after sample incubation. The coated substrates were sterilized by UV light exposure for 1 hour per side. Each substrate was then soaked in 2 mL of DMEM containing 10 % FBS and 1 % P/S under standard growth conditions of 37 ºC, 5 % CO_2 and 95 % relative humidity for 7 days. The media was changed and collected every 24 hours to monitor the dissolution rate under *in vitro* conditions. The collected media was diluted in 0.03 M Tris buffer solution and analyzed using inductively coupled plasma optical emission spectroscopy (ICP-OES, iCAP duo 6500 Thermo Fisher). Magnesium ion concentrations in solution were compared to media and uncoated substrate controls. Samples were prepared in triplicate for each condition. Statistically significance differences were assessed daily through ANOVA with Dunnett's 1-tailed t-test post-hoc testing, assuming AZ31 control values to be higher than coated substrates. Significance was set at the $p<0.05$ level. IBM-SPSS statistical analysis software was used for calculations.

C.2.5 Hydrogen Evolution

The evolution of hydrogen was tested by placing the substrates in Hank's solution (Sigma Aldrich) at 37 °C and measuring the evolved hydrogen over a two week time span. Sample dimensions were recorded prior to sterilizing under UV radiation, 1 hour each side. Samples

were placed in individual mesh bags and suspended within 1 liter beakers of Hank's solution, underneath an inverted funnel. A burette was placed over-top of the funnel above the samples to capture hydrogen released. Three samples were suspended for each condition to account for the low hydrogen evolution anticipated from the coated samples. To the greatest extent possible, difficulties and concerns associated with measurement of hydrogen evolution have been addressed [275]. All beakers, funnels and burettes are glass so as to prevent hydrogen permeation. The samples were suspended to ensure full surface exposure and the inverted funnels were elevated to prevent ion accumulation within the funnel volume. Solution level in each burette was measured intermittently for two weeks. The coatings were characterized post-corrosion using a scanning electron microscopy.

C.2.6 Cell culture

Murine MC3T3 –E1 pre-osteoblast cells and Human Mesenchymal Stem Cells (hMSC, Lonza USA) were utilized for cell culture studies. Cells were cultured in minimum essential medium alpha (α-MEM, Gibco, Grand Island, NY) containing 1 % penicillin/streptomycin antibiotics (P/S, Gibco, Grand Island, NY) and either 10 % fetal bovine serum, for MC3T3, or 20 % fetal bovine serum, for hMSC (FBS, Atlanta Biologicals, Lawerenceville, GA) at 37 ^{o}C, 5 % CO_2 and 95 % relative humidity. Substrates were placed in 12-well plates and sterilized using UV radiation for 40 minutes on each side. The substrates were then seeded with cells with a total media volume of 2 ml/well. Media was changed every other day throughout the testing period.

C.2.7 Cytocompatibility

Cell viability was assessed using Live/Dead staining, as previously described. Cellular adhesion and morphology was observed using actin and nucleus staining. MC3T3 and hMSC cells were seeded on sterilized substrates at a concentration of 20,000 cells/ml and cultured in appropriate media for 24 hours. Cells were then rinsed with PBS, fixed using a 4 % paraformaldehyde solution then permeabilized with a 0.2 % Tween20 solution (Bio-Rad, USA). Following this cellular actin was stained using phalloidin (Sigma Aldrich) and nuclei were stained using dapi (Applichem) according to manufacturer's instructions. Cells were imaged using fluorescence microscopy. Following fluorescence imaging, fixed samples were then subjected to alcohol dehydration and mounted for SEM imaging.

Quantification of cellular DNA levels as a measure of proliferation was assessed with MC3T3 cells. Cells were seeded at a density of 80,000 cells/ml and cultured for 1, 3 and 7 days. Substrates were rinsed with PBS then cells were lysed (CellLytic, Sigma Aldrich). The Quan-It PicoGreen dsDNA Reagent and Kit (Invitrogen) was used to measure cellular DNA according to manufacturer's instruction. Lamda dsDNA was used for the standard curve and the fluorescence level was measured using Synerge2 Multi-Mode Microplate Reader (Biotek, USA). Statistically significant differences were assessed through ANOVA with Dunnett's 1-tailed t-test post-hoc testing, assuming AZ31 control values to be lower than coated substrates. Significance was set at the $p<0.05$ level. IBM-SPSS statistical analysis software was used for calculations.

C.3 RESULTS

C.3.1 Coating Characterization

Glancing angle x-ray diffraction (GA-XRD) was used to confirm the formation of the $Mg(OH)_2$ layer on the surface of the AZ31 substrates. Following sodium hydroxide treatment and rinsing in DI water, the substrate was dried and kept in a desiccator until the diffraction measurement was completed. Figure C-1 shows the collected GA-XRD spectra along with simulated spectra for pure magnesium and magnesium hydroxide. The collected spectra shows minor peaks associated with major peaks of $Mg(OH)_2$ spectra, particularly at approximately 18.5º and 38º 2θ angles.

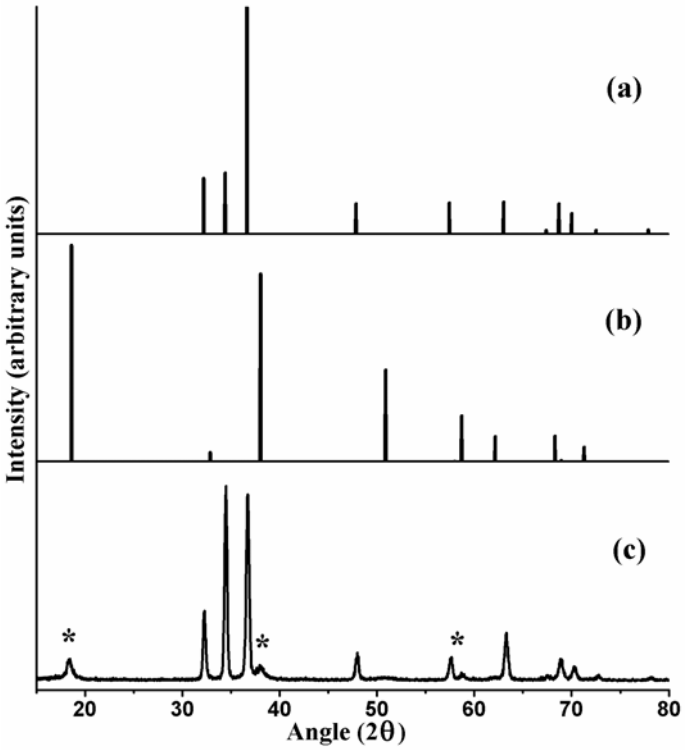

Figure C-1 Simulated x-ray diffraction patterns of pure magnesium [JCPDS 35-0821] (a) and $Mg(OH)_2$ [JCPDS 7-239] (b) with glancing angle x-ray diffraction of (c) NaOH-treated AZ31 substrate showing growth of $Mg(OH)_2$ layer, indicated by the asterisk *.

FT-IR was used to follow the development of the layer-by-layer coatings on the AZ31 substrates. Figure C-2 shows the FT-IR spectrum of the PCL (i), PLGA50:50(ii) and PLGA75:25 (iii) coated samples after all 5 cationic/anionic layer pairs were applied, respectively. Further FT-IR testing of individual layer assembly shows small peaks of cationic polymers when these polymers are the top coat (Results not shown.) For each coating type, the coated substrate is compared to FTIR spectra of $Mg(OH)_2$-treated substrate and pure spectra of each utilized polymer component. The characteristic bonds at numerous wave numbers, especially the C=O stretching at 1750 cm^{-1} and the numerous C–O–C and C-H bending peaks between near 1080 cm^{-1} and 1500 cm^{-1}, are indicative of the presence of the PCL and PLGA polymers.

Additionally, there are minor peaks around 1625 cm $^{-1}$ visible which match the pattern for PAH and are likely associated with C=C bonds of unreacted ends of the PAH chains. No carbon or nitrogen-based peaks are seen on the bare metal substrates devoid of the polymer, though the peak at around 3600 cm $^{-1}$ is associated with free –OH bonds. The coated substrate spectra shown are after completing the coating process and the presence of the thicker, top-coating anionic polymers (PCL, PLGA50:50 and PLGA75:25) mask most bond peaks characteristic of the cationic PEI and PAH polymers.

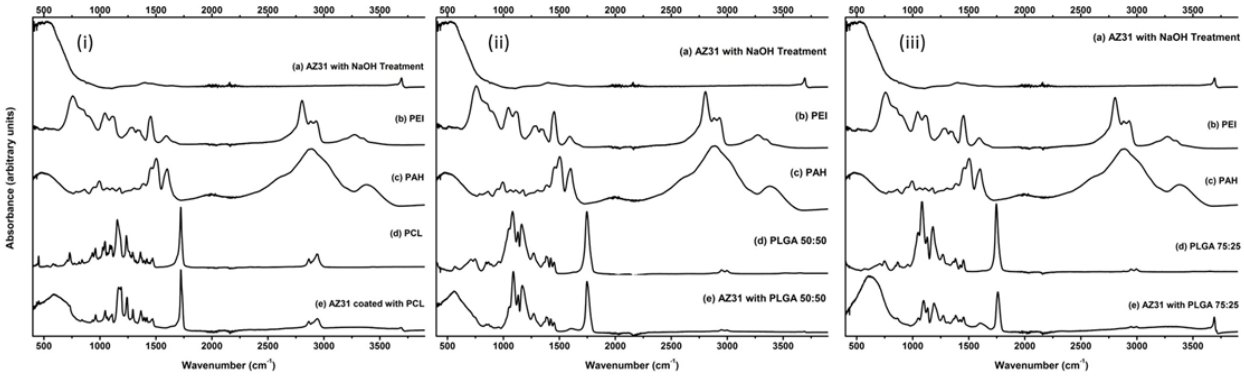

Figure C-2 FTIR spectra of coated substrates and individual components. In each set of spectra, (a) is AZ31 with NaOH treatment, (b) is pure PEI and (c) is pure PAH while (d) is the utilized anionic polymer and (e) is the fully coated substrate. Spectra set (i) presents the PCL coatings, (ii) presents the PLGA50:50 series and (iii) presents the PLGA75:25 series, each showing clear presence of the anionic polymers on coated substrates. The presence of the cationic polymers is obscured by thick top coating.

Scanning electron microscopy was used to observe the morphology of the substrates after the coating process. Figure C-3 shows images of the substrates as-polished (a) and after layer-by-layer coatings (b-d). The as-prepared AZ31 substrate shows a flat but imperfect surface with grooves remaining from the final 5 μm polishing paper. The sodium hydroxide-treated surface, not shown, displays slightly altered morphology of the substrate, reducing the visibility of

residual grooves from polishing. The PCL (b), PGLA50:50 (c) and PLGA75:25 (d) layer-by-layer coated substrates show smoother, muted surfaces with only slight remnants of the polishing artifacts remaining. The coatings are non-porous and do not show any signs of delamination from the alloy surface. Qualitatively, this reinforces the confirmation of the successful $Mg(OH)_2$ treatment and anionic-cationic layer-by-layer assembly to the surface of AZ31 substrates.

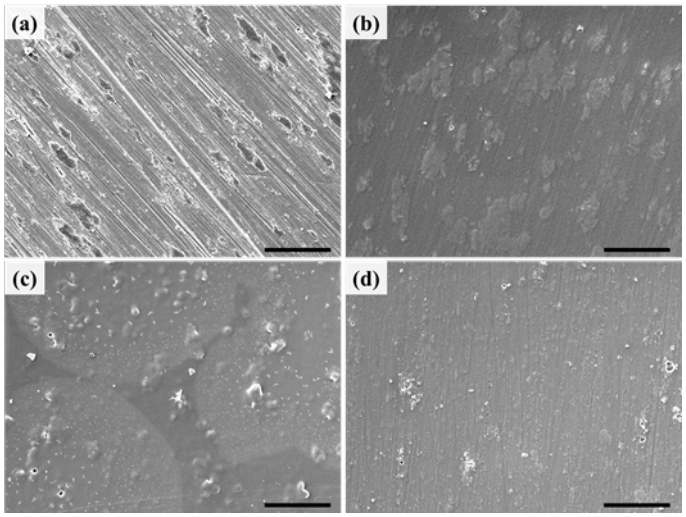

Figure C-3 SEM images of uncoated AZ31(a), PCL (b), PLGA 50:50 (c) and PLGA 75:25 (d). Scale bar is 50 µm.

C.3.2 Corrosion Characterization

Polarization curves (a) and impedance spectra (b) for the uncoated and coated substrates can be seen in Figure C-4. Table C-1 gives a summary of the corrosion potential and corrosion current densities as calculated from extrapolation of the Tafel plots. All three coatings, PCL (ab), PLGA50:50 (ac) and PLGA75:25 (ad) as well as solely the $Mg(OH)_2$ conversion coating (ae) on the substrates resulted in i_{corr} values lower than the uncoated AZ31 alloy substrate (aa) as well as E_{corr} values that are more anodic than the uncoated AZ31 alloy. PCL offered the greatest

reduction in corrosion current over the uncoated alloy, which was measured at $2.75E^{-05}$, with an i_{corr} value of $3.35E^{-07}$, followed by PLGA50:50 and PLGA75:25, which were similar at i_{corr} values of 1.12 E^{-06} and 1.56 E^{-06} respectively which was also quite similar to the $Mg(OH)_2$ coating, which measured at $1.02E^{-06}$. Both PGLA50:50 and PLGA75:25 show a breakdown in the anodic corrosion current at lower potential values. EIS results correspond with polarization measurements, indicating that PCL coating is the most protective and that all coatings provide increased corrosion impedance over the uncoated alloy.

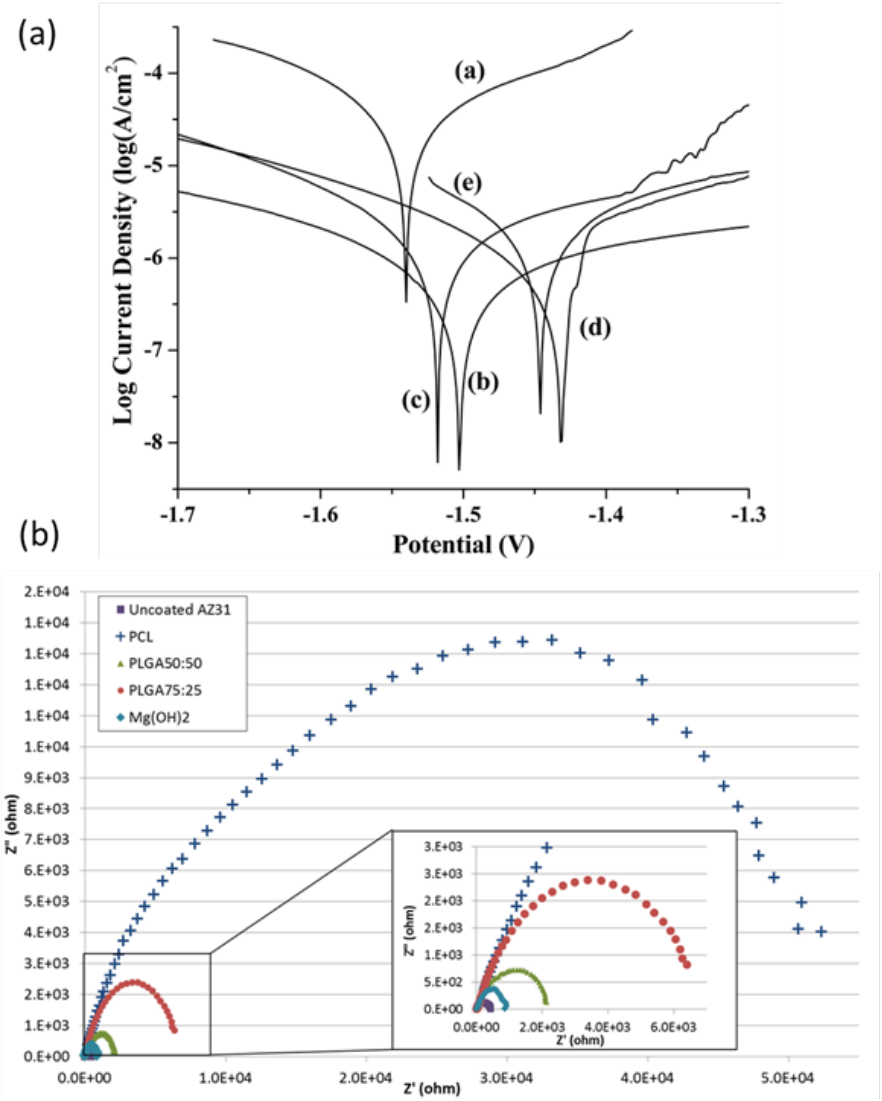

Figure C-4 Polarization curves (a) of uncoated AZ31 (aa), PCL (ab), PLGA50:50 (ac), PLGA75:25 (ad) and $Mg(OH)_2$ (ae) showing less negative corrosion potential and reduced corrosion current for all coated substrates over the uncoated alloy. Electrochemical Impedance Spectroscopy (EIS) measurements of the coated and uncoated substrates are shown in (b). Measurements were taken in the frequency range of 1000-0.01 Hz with an amplitude of 0.005 V.

Table C-1 Corrosion potential (E_{corr}) and current density (i_{corr}) values for coated and uncoated substrates.

	E_{corr} (V)	i_{corr} (A/cm^2)
Uncoated AZ31	-1.54	2.75E-05
PCL	-1.50	3.35E-07
PLGA5050	-1.52	1.12E-06
PLGA7525	-1.44	1.56E-06
$Mg(OH)_2$	-1.45	1.02E-06

Daily released magnesium ion concentration in media for coated and uncoated substrates can be seen Figure C-5. This data shows the dissolution profile as a function of soluble magnesium ion release over a one week period under *in vitro* culture conditions. Although connected more directly with passivation coating dissolution, or here $Mg(OH)_2$ dissolution, than magnesium corrosion, the localized ion concentrations are an important consideration for biocompatibility of the substrate. At each time point the magnesium level in media for coated samples is significantly lower ($p<0.05$) than the uncoated AZ31 substrates. Though not calculated, it appears that magnesium ion levels of coated substrates remaining higher than basal media levels for all time points. This indicates that the coatings provide some corrosion protection but do not fully passivate the substrate from corrosion.

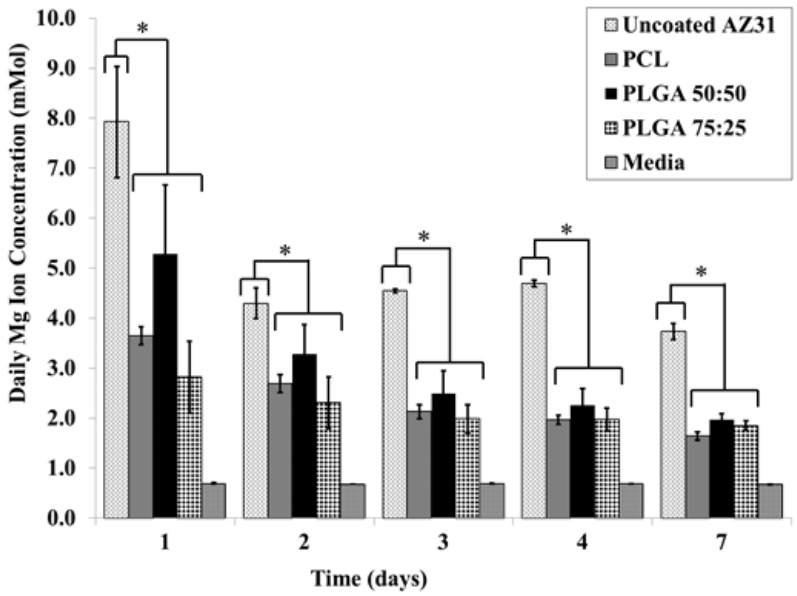

Figure C-5 ICP measurements of daily released magnesium ion concentration in extracted incubation media for AZ31 coated and uncoated samples. For every time point, all coated samples show statistically lower ion concentrations ($p<0.05$) than the uncoated AZ31, indicated by the *asterisk.

Cumulative hydrogen gas evolution plots for the uncoated and coated substrates can be seen in Figure C-6. Measurements indicate that cumulative hydrogen released from uncoated AZ31 is much higher than that of coated substrates. Uncoated AZ31 shows a characteristically high corrosion rate initially, through about the first 12 hours, followed by slower, relatively constant corrosion rate through the remaining period of the study. All coated substrates showed a slow rate of hydrogen release initially, through the first 48 hours of testing. The corrosion then plateaued, showing no additional measurable release after this 48 hour period. Figure C-7 shows the SEM images of samples post corrosion in Hanks solution. Electron microscopy of these samples at the end of the corrosion period shows the presence of surface cracks on the uncoated AZ31 (a), characteristic of magnesium corrosion morphology. The polymer-coated substrates show various levels of corrosion progression. PLGA50:50 (c) shows the most aggressive

progression of corrosion, with cracking morphology similar to the uncoated substrate and nearly no visible polymer remaining. PLGA75:25 (d) shows some underlying cracking beginning to form, with the bulk of the sample still coated in polymer. PCL (b) shows the least amount of corrosion, displaying some defects in the polymer coating but no visible cracking morphology.

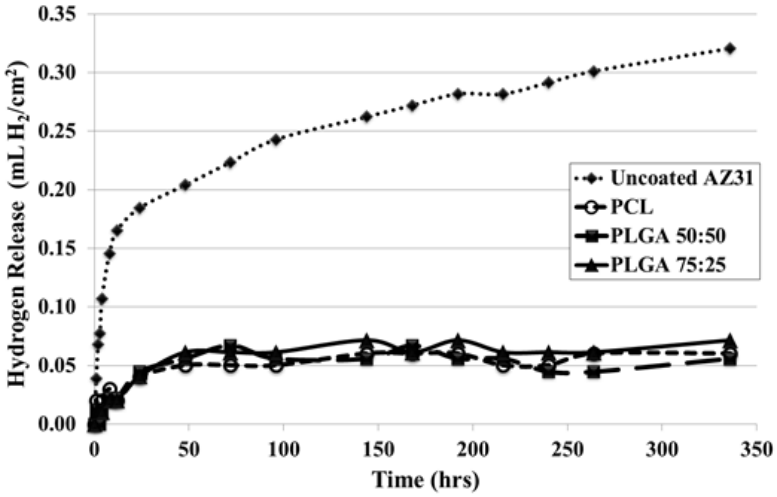

Figure C-6 Cumulative hydrogen evolution in Hanks solution over a two-week period, showing a marked reduction in hydrogen release with coated samples in comparison to uncoated AZ31.

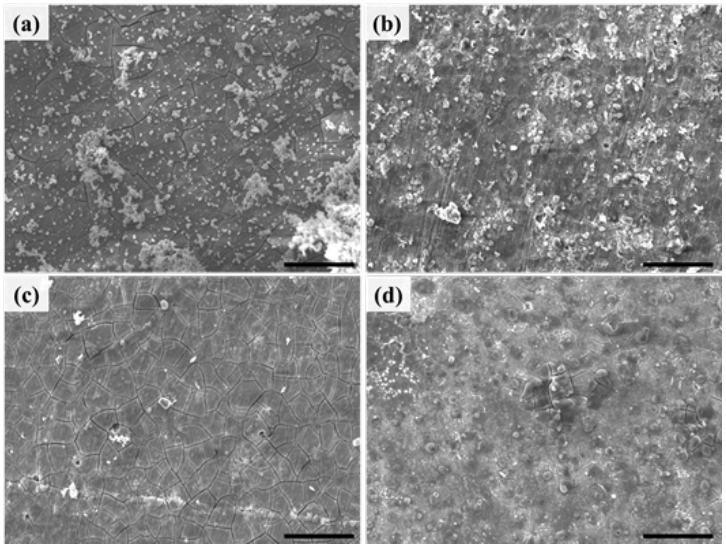

Figure C-7 SEM images of substrates Uncoated AZ31(a), PCL(b), PLGA 50:50 (c) and PLGA 75:25 (d) following two week incubation for hydrogen-evolution testing. Scale bar is 50 µm.

C.3.3 Cytocompatibility

Live/Dead staining of osteoblasts and hMSCs 3 days post seeding can be seen in Figure C-8, respectively. For both MC3T3 and hMSC cell cultures, live/dead staining indicates improved cell viability and proliferation on coated substrates over the uncoated AZ31 alloy. No discernible difference can be seen between the three types of polymer coatings. Actin staining of osteoblasts and hMSCs 24 hours post seeding can be seen in Figure C-9. For MC3T3 cells (a-d), cellular morphology is circular and poorly defined on the uncoated AZ31 (a), without strong actin fiber staining, indicating that the cells are likely poorly adhered to the substrate. On the PCL-coated substrate (b) cells appear elongated while on the PLGA50:50 (c) and PLGA75:25 (d) coated substrates cells appear well spread out, showing strong actin filaments extended in numerous directions. For hSMCs (e-h), cells cultured on uncoated AZ31 (e) appear extremely elongated, though better adhered than the MC3T3s under the same conditions. On the PCL (f) coated substrates hMSCs appear somewhat elongated, but less than the MC3T3s did under the same condition. The hMSCs grown on the PLGA50:50 (g) and PLGA75:25 (h) coated substrates appear very healthy and well adhered with strong actin fibers extending in various directions on the substrates.

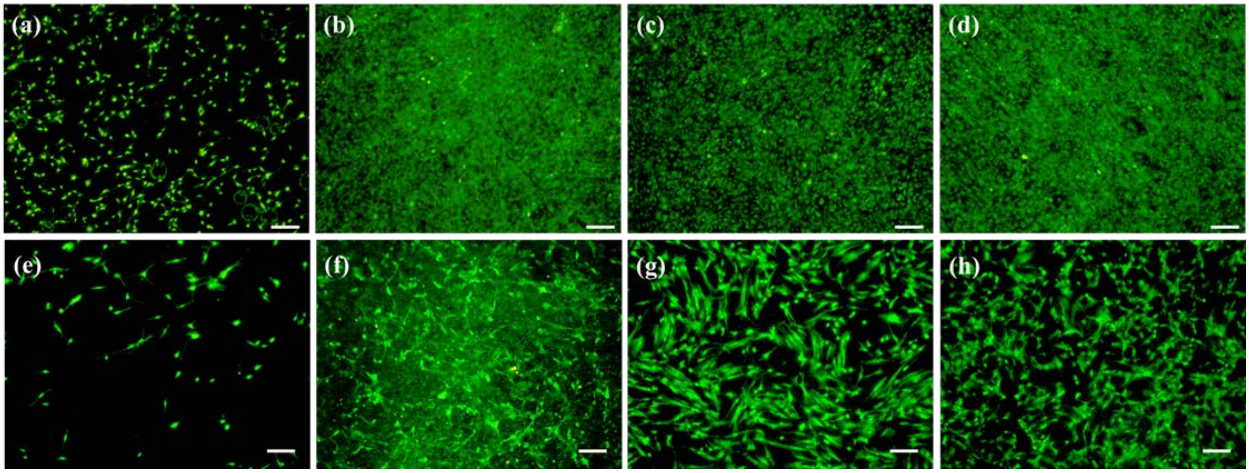

Figure C-8 Live/Dead staining of MC3T3 osteoblasts (a-d) and hMSCs (e-h) on day 3 of culture post seeding on uncoated AZ31 (a & e), PCL (b & f), PLGA 50:50 (c & g) and PLGA 75:25 (d & h) indicating improved biocompatibility of coated substrates over uncoated substrates. Scale bar is 200 µm.

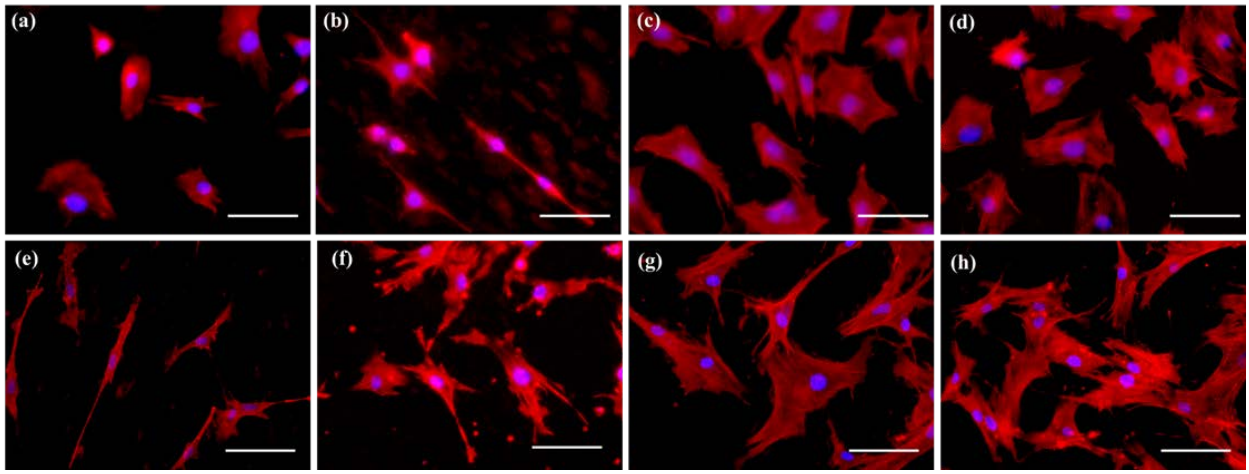

Figure C-9 Cell morphology of MC3T3 osteoblasts (a-d) and hMSCs (e-h) observed at 24 hours post seeding through actin-nucleus co-staining on uncoated AZ31 (a & e), PCL (b & f), PLGA 50:50 (c & g) and PLGA 75:25 (d & h). Scale Bar is 100 µm.

In Figure C-10 can be seen the same substrates from the cell morphology study, dehydrated and mounted for electron microscopy examination, which allows simultaneous observation of the coatings, the cells and the interaction between the two. Fixed MC3T3 cells are

barely visible on the corroded AZ31 substrate (a). Morphologies of MC3T3s on the polymeric coatings (b-d) are similar to those observed through actin staining: the cells grown on the PCL (b) coated substrate appear more elongated while the cells grown on the PGLA50:50(c) and PLGA75:25 (d) substrates appear more spread out. The cells on PCL substrates do not appear to be as fully adhered as those on the PLGA substrates, with some portions of the cytoskeleton rising up above the surface of the polymer. SEM images of hMSCs fixed on the coated and uncoated substrates show similar trends. Cells on the uncoated AZ31 (e) are thin and very elongated, cells on the PCL (f) are also elongated but to a lesser extent while cells on PLGA50:50 (g) and PLGA75:25 (h) are spread out and well adhered to the substrates.

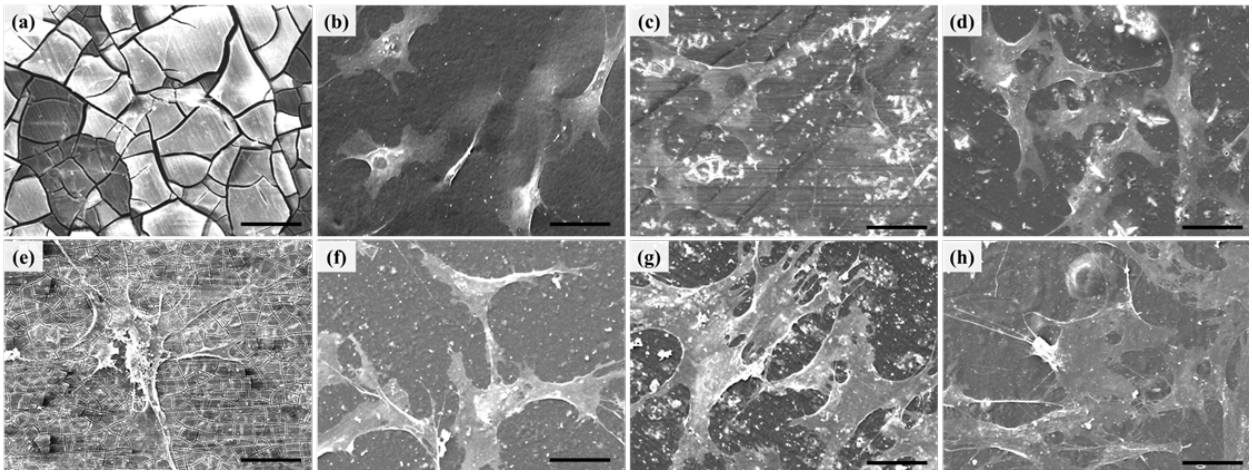

Figure C-10 SEM morphology of fixed MC3T3 osteoblasts (a-d) and hMSCs (e-h) at 24hrs post-seeding on Uncoated AZ31 (a & e), PCL (b & f), PLGA 50:50 (c & g) and PLGA 75:25 (d & h). Scale Bar is 100 µm.

The quantification of total DNA content from MC3T3 cells can be seen in Figure C-11. Grown over the period of 1, 3 and 7 days, DNA quantification studies support what was seen qualitatively in the live/dead staining, that the cell viability and proliferation is higher on the coated substrates in comparison to the uncoated substrate. Although there was no statistical

difference after day 1, days 3 and 7 samples coated with PCL, PLGA50:50 and PLGA75:25 show significantly higher DNA levels than the uncoated substrates, indicated by the asterisks in the figure. High DNA levels are correlated with higher numbers of cells on the substrates.

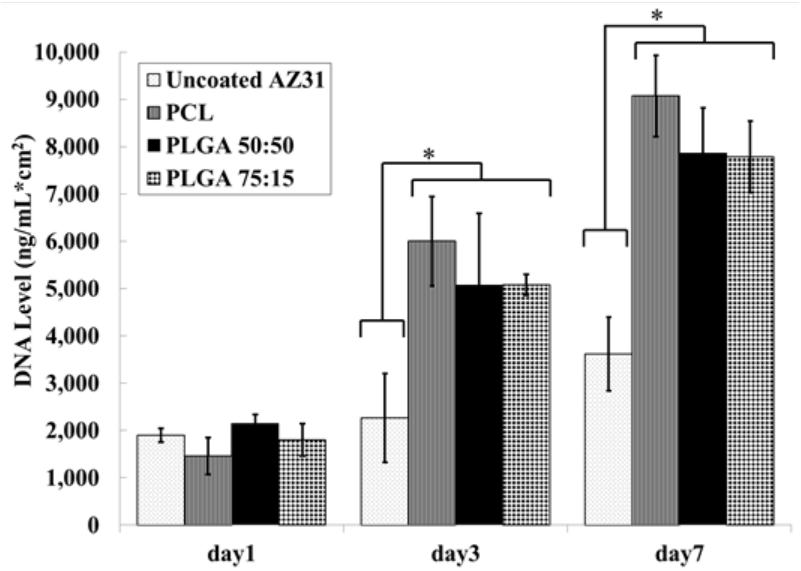

Figure C-11 Quantification of total DNA content, using MC3T3 osteoblasts, on substrates at various time points. On day 3 and day 7 all coated substrates showed statistically higher ($p<0.05$) levels of DNA than the uncoated substrate, indicated by the *asterisk.

C.4 DISCUSSION

The application of coatings to the surface of implants is an accepted technique to improve the initial corrosion resistance and biocompatibility of magnesium-based alloys. Degradable polymeric coatings can be used to provide localized drug and gene delivery to the implant site accelerating the regeneration process. With the intent of both slowing corrosion and facilitating the delivery of biological agents, the coatings explored in this study combine a passivating

conversion coating with a layer-by-layer deposition coating of polymers. The choice of polymers is designed to utilize those polymers known for their drug and gene delivery functionality as well as their biocompatibility. The conversion coating consists of a $Mg(OH)_2$ passivation layer, which reduces the initial magnesium surface reactivity as a stand-alone coating. The spontaneous formation of a magnesium oxide/magnesium hydroxide layer on magnesium exposed to humidity, as well as the increased thickness of the hydroxide layer when immersed in water, has been previously studied [293]. Studies have shown that this passivation coating, while it provides initial protection, is not stable in ionic solutions, where chlorine in culture media aids in breaking down the hydroxide layer. More importantly, a recent study showed that while the hydroxide layer improves corrosion resistance, the coating was able to delay cell death but resulted in reduced cell densities and abnormal cellular morphology, thus making it a poor choice as a stand-alone protective layer against corrosion [316].

The deposition coating is formed through the layer-by-layer assembly of anionic and cationic polymers. The anionic polymers explored in this study were polycaprolactone and two different poly(lactide-go-glycolide) formulations. These polymers are biodegradable and are frequently studied for drug delivery [283, 284, 317]. The three anionic polymers used in this study were chosen based on the variety of anticipated degradation rates, from PLGA50:50 degrading the most rapidly to PCL degrading the most slowly [318, 319]. The cationic polymers explored were polyethylenimine and polyallylamine hydrochloride. These polymers have been studied for applications such as gene delivery, antibacterial uses and cell encapsulation [310, 313-315]. Cationic polymers function in such capacities due to the cell-membrane-disrupting potential charge. For the same reason, these polymers can be toxic in bulk quantities [320]. Recently, PEI was studied as a protective coating on magnesium. It was shown that the imide

rings of PEI interact with the magnesium hydroxide corrosion product and that the PEI coating shows general improvement to the corrosion resistance of the alloy [321, 322]. Importantly, it has been seen that the coupling of cationic and anionic polymers significantly reduces the cytotoxicity of the cationic polymers [315]. Cationic polymers such as these are largely not degradable *in vivo* thus lower molecular weight options are favorable, as these are both more water soluble and typically shower lower toxicity [323]. Some evidence indicates that these non-degradable polymers can accumulate in critical organs [314]. Although the specific PEI and PAH polymers in this study are not biodegradable, much research has focused on tailoring such polymers to facilitate degradation *in vivo* [324, 325].

XRD and FTIR techniques used to characterize the passivation and layer-by-layer coatings in Figures C-1 and C-2 have confirmed that coating synthesis was completed as intended. Electron microscopy in Figure C-3 additionally confirmed that the coatings are homogenous over the surface of the substrate.

The corrosion studies carried out in this work are sufficiently complimentary in their depiction of the protective nature of these coatings on the magnesium substrate. The protective nature of the coatings shown in the electrochemical corrosion studies is supported by the lower hydrogen evolution and magnesium ion release of these samples at initial incubation in solution. Overall the level of protection from the three different coatings is somewhat varied when comparing them in both the polarization testing in Figure C-4 and magnesium ion release in Figure C-5. Polarization studies showed PCL to be most protective, while ion release studies indicate that PLGA75:25 is most protective upon initial incubation in media, while PCL is intermediate and PLGA50:50 is the least protective. It should be noted however that polarization curves are of only one representative sample and the statistical significance between coated

samples in the ion concentration study is not computed due to low sampling power. In these studies the intent was to show the protective nature of the composite $Mg(OH)_2$-layer-by-layer coatings over uncoated substrates and only the qualitative differences between the types of coatings can be discussed. Magnesium ion concentrations, Figure C-5, of coated samples for the first 48 hours of testing appear to be similar to hydrogen evolution results, Figure C-6, however, the ion concentration curves predict some corrosion that is not seen as additional hydrogen release beyond this time period. This is likely due to the difference between corrosion, and thus hydrogen production, and corrosion product dissolution. Because the coated substrates begin with an exaggerated 'passivation' layer, initial corrosion is minimal and likely due to defects in the samples. The magnesium ion release is due to the slow dissolution of the $Mg(OH)_2$ layer. The initial spike in ion concentration and hydrogen evolution for uncoated AZ31 is due to the total sample surface area being exposed. Once a passivation layer is formed, the corrosion rate is reduced. However it is not halted all together due to the instability of the passivation layer and the solubility of this layer in chloride-containing solutions. The application of the initial conversion layer ($Mg(OH)_2$) coating prevents this immediate spike in corrosion for the coated as well as stabilizing the substrate surface for subsequent layer-by-layer coating. The application of polymeric coatings additionally prevents the fragmentation of the conversion layer, which is quite similar to a natural passivation layer in nature and thus not fully stable. Visibly, the corrosion progression seen through SEM in Figure C-7 appears to confirm the anticipated rates of polymer degradation, with PLGA50:50 showing the least remaining polymer, PLGA75:25 showing some remaining polymer and PCL showing the most intact polymer remaining. All three anionic polymers undergo bulk hydrolytic degradation, allowing aqueous penetration as the degradation progresses. The access of water to the $Mg(OH)_2$ layer, and subsequent partial

dissolution of this layer, explains the discrepancy between elevated magnesium ion levels and lack of hydrogen evolution at later time points. Once the polymer layer completely degrades away, the passivation layer can begin to break down or dissolve. Thus at short time points, the magnesium ion levels are dependent upon the polymer hydrolytic degradation rate and ion diffusion through the polymer and subsequent low level dissolution of the magnesium hydroxide. During this, the bulk breakdown of the base $Mg(OH)_2$ layer and subsequent magnesium alloy corrosion is halted until full degradation of the polymer occurs. When the polymer has completed dissolved, it is expected that the underlying alloy would corrode similar to a magnesium implant once it has reached a steady corrosion rate. Initially, upon implantation, magnesium alloys show a short-term burst of very active corrosion, as the native material builds a passivation layer. After this burst, the rate of corrosion decreases significantly, to a level which the hydrogen evolution is tolerable in vivo [281, 299, 326]. Following dissolution of the polymeric coating, it is expected that the hydroxide coating would behave as the passivation layer formed on native alloys, maintaining the corrosion rate at that of the passivated native alloy. This formed hydroxide layer would slowly break away, allowing fresh corrosion to occur before a new passivation layer forms in the way that typical magnesium corrosion occurs in vivo. Ideally, throughout the degradation of the polymers, cellular integration with the implant is achieved, which would help ensure that the implant maintains this comparatively slow and steady rate of hydrogen gas and magnesium release.

The corrosion results shown are in stark contrast to what has previously been seen in the application of PCL and PLGA-type polymers to magnesium alloys. Previously, it has been shown in our laboratory as well as by others that the application of such polymers results in bubbling of the water-penetrable polymer and poor corrosion protection beyond 24 hours of

incubation. In fact, many researchers have seen that these coatings have an antagonistic effect on corrosion, increasing corrosion rates of the coated samples over uncoated alloys [280, 289, 327]. It has been postulated that this effect is due to the bulk degradation exhibited by the polymers, allowing water to contact the alloy surface, and acidic polymer degradation products increasing the solubility of the passivation layer that would otherwise form on areas of the metal exposed to water. Additionally, the bubbling effect may create localized galvanic corrosion effects. Our results indicate that while the degradation of the polymers may prevent the formation of a $Mg(OH)_2$ passivation, it does not weaken or dissolve the pre-formed passivation layer, which would result in similar antagonistic corrosion as seen previously [280, 289, 328]. The combination of the water-soluble, but not degradable, PAH and PEI polymers layered in between the degradable PLGA or PCL polymers likely slows the penetration of water through the coating, thus further slowing the degradation of the coating in comparison to pure PLGA or PCL coatings.

Cytocompatibility studies show that the layer-by-layer coatings indeed improve the viability of osteoblast and hMSC cultures on magnesium substrates. Live/Dead staining C-3 days post seeding, Figure C-8, as well as total DNA quantification at 3 and 7 days, Figure C-11, show that cell numbers are markedly increased on coated samples in comparison to uncoated samples indicating cells are growing faster. Additionally, actin staining and SEM imaging at 24 hours post seeding, Figures C-9 and C-10, indicate that the adhesion of both osteoblasts and hMSCs is more favorable on the coated substrates than the native AZ31 surface in culture. Especially on the PLGA50:50 and PLGA75:25 surfaces, cells appear to favor the surface, extending in numerous directions and integrating well with the polymer. In comparison, the few cells on the native AZ31 surface appear elongated or rounded and not integrate well with the surface,

indicating that the cells are poorly attached to this surface. For magnesium alloys it is often difficult to separate the poor viability due to high magnesium levels with the poor viability due to the ever changing and corroding surface of the alloys, but the overall result is generally that the alloys need some way to improve the biocompatibility of the surface that facilitates cell adhesion, proliferation and ultimately differentiation on the surface of the metal. The intention of the $Mg(OH)_2$ and layer-by-layer coating presented here is to facilitate this, improving initial cellular adhesion, proliferation and integration with the implant. Morphology observations and viability and proliferation results have confirmed improved adhesion and proliferation over the native alloy. These results indicate that the intention lain out above, where-in the combination of layer-by-layer and conversion coating techniques allows for impeded degradation and improved cytocompatibility and cellular integration, can be achieved. The next step in coating design is to study long term cellular integration and differentiation as the polymer and underlying alloy degrade. Ultimately, the layer-by-layer coating will be further tailored to facilitate the delivery of drugs, growth factors or gene transfer particles to yield a coating specifically designed to provide the most beneficial aspects of biomedical engineering to the patient.

C.5 CONCLUSION

Electrostatically assembled layers of anionic biodegradable polymers PLGA or PCL and cationic polymers PEI and PAH combined with $Mg(OH)_2$ surface treatment serve to provide a protective coating on AZ31 magnesium alloy substrates. This ceramic conversion coating and layer-by-layer polymeric coatings combination were shown to reduce immediate and long term corrosion of the substrate. The coatings also provided improved biocompatibility, cellular adhesion and

proliferation in comparison to the uncoated alloy surface. The implementation of such coatings on magnesium alloy implants could serve to improve the corrosion resistance and perhaps contribute to cellular integration of these implants with the native tissue while also serving to deliver vital drugs or biological elements to the site of implantation.

BIBLIOGRAPHY

[1] Bauer TW, Muschler GF. Bone graft materials - An overview of the basic science. *Clinical Orthopaedics and Related Research* 2000:10-27.

[2] Giannoudis PV, Dinopoulos H, Tsiridis E. Bone substitutes: An update. *Injury-International Journal of the Care of the Injured* 2005;36:S20-S27.

[3] Kolk A, Handschel J, Drescher W, Rothamel D, et al. Current trends and future perspectives of bone substitute materials – From space holders to innovative biomaterials. *Journal of Cranio-Maxillofacial Surgery* 2012;40:706-718.

[4] Greenwald AS, Boden SD, Goldberg VM, Khan Y, et al. Bone-graft substitutes: facts, fictions, and applications. *The Journal of Bone and Joint Surgery American Volume* 2001;2:98-103.

[5] Frost&Sullivan. Report: U.S. Markets for Orthopedic and Dental Biomaterial Devices. 1998.

[6] Van der Stok J, Van Lieshout EMM, El-Massoudi Y, Van Kralingen GH, et al. X-Bone substitutes in the Netherlands – A systematic literature review. *Acta Biomaterialia* 2011;7:739-750.

[7] Nandi SK, Roy S, Mukherjee P, Kundu B, et al. Orthopaedic applications of bone graft & graft substitutes: a review. *Indian Journal of Medical Research* 2010;132:15-30.

[8] LeGeros RZ. Calcium phosphate materials in restorative dentistry: a review. *Advances in Dental Research* 1988;2:164-180.

[9] Schmitz JP, Hollinger JO, Milam SB. Reconstruction of bone using calcium phosphate bone cements: A critical review. *Journal of Oral and Maxillofacial Surgery* 1999;57:1122-1126.

[10] Low KL, Tan SH, Zein SH, Roether JA, et al. Calcium phosphate-based composites as injectable bone substitute materials. *Journal of biomedical materials research Part B, Applied biomaterials* 2010;94:273-286.

[11] Dorozhkin SV. Calcium orthophosphate cements for biomedical application. *Journal of Materials Science* 2008;43:3028-3057.

[12] Ishikawa K, Miyamoto Y, Takechi M, Ueyama Y, et al. Effects of neutral sodium hydrogen phosphate on setting reaction and mechanical strength of hydroxyapatite putty. *Journal of Biomedical Materials Research* 1999;44:322-329.

[13] No YJ, Roohani-Esfahani S-i, Zreiqat H. Nanomaterials: the next step in injectable bone cements. *Nanomedicine* 2014;9:1745-1764.

[14] Wynn-Jones G, Shelton RM, Hofmann MP. Injectable citrate-modified Portland cement for use in vertebroplasty. *Journal of Biomedical Materials Research Part B: Applied Biomaterials* 2014;102:1799-1808.

[15] Driessens FCM, Boltong MG, Bermúdez O, Planell JA, et al. Effective formulations for the preparation of calcium phosphate bone cements. *Journal of Materials Science: Materials in Medicine* 1994;5:164-170.

[16] Bohner M, Gbureck U, Barralet JE. Technological issues for the development of more efficient calcium phosphate bone cements: a critical assessment. *Biomaterials* 2005;26:6423-6429.

[17] Leroux L, Hatim Z, Frèche M, Lacout JL. Effects of various adjuvants (lactic acid, glycerol, and chitosan) on the injectability of a calcium phosphate cement. *Bone* 1999;25:31S-34S.

[18] Alves H, dos Santos L, Bergmann C. Injectability evaluation of tricalcium phosphate bone cement. *Journal of Materials Science: Materials in Medicine* 2008;19:2241-2246.

[19] Pina S, Ferreira JMF. Brushite-Forming Mg-, Zn- and Sr-Substituted Bone Cements for Clinical Applications. *Materials* 2010;3:519-535.

[20] Temenoff JS, Mikos AG. Injectable biodegradable materials for orthopedic tissue engineering. *Biomaterials* 2000;21:2405-2412.

[21] Constantz BR, Ison IC, Fulmer MT, Poser RD, et al. Skeletal repair by in situ formation of the mineral phase of bone. *Science* 1995;267:1796-1799.

[22] LeGeros RZ. Calcium Phosphate-Based Osteoinductive Materials. *Chemical Reviews* 2008;108:4742-4753.

[23] Vallet-Regi M, Gonzalez-Calbet JM. Calcium phosphates as substitution of bone tissues. *Progress in Solid State Chemistry* 2004;32:1-31.

[24] Hofmann MP, Mohammed AR, Perrie Y, Gbureck U, et al. High-strength resorbable brushite bone cement with controlled drug-releasing capabilities. *Acta Biomaterialia* 2009;5:43-49.

[25] Wong RK, Gandolfi BM, St-Hilaire H, Wise MW, et al. Complications of Hydroxyapatite Bone Cement in Secondary Pediatric Craniofacial Reconstruction. *Journal of Craniofacial Surgery* 2011;22:247-251.

[26] Ginebra MP, Rilliard A, Fernández E, Elvira C, et al. Mechanical and rheological improvement of a calcium phosphate cement by the addition of a polymeric drug. *Journal of Biomedical Materials Research* 2001;57:113-118.

[27] Qiao P-y, Li F-f, Dong L-m, Xu T, et al. Delivering MC3T3-E1 cells into injectable calcium phosphate cement through alginate-chitosan microcapsules for bone tissue engineering. *Journal of Zhejiang University Science B* 2014;15:382-392.

[28] Mestres G, Abdolhosseini M, Bowles W, Huang SH, et al. Antimicrobial properties and dentin bonding strength of magnesium phosphate cements. *Acta Biomaterialia* 2013;9:8384-8393.

[29] Mestres G, Ginebra M-P. Novel magnesium phosphate cements with high early strength and antibacterial properties. *Acta Biomaterialia* 2011;7:1853-1861.

[30] Tamimi F, Le Nihouannen D, Bassett DC, Ibasco S, et al. Biocompatibility of magnesium phosphate minerals and their stability under physiological conditions. *Acta Biomaterialia* 2011;7:2678-2685.

[31] Klammert U, Ignatius A, Wolfram U, Reuther T, et al. In vivo degradation of low temperature calcium and magnesium phosphate ceramics in a heterotopic model. *Acta Biomaterialia* 2011;7:3469-3475.

[32] Klammert U, Vorndran E, Reuther T, Mueller FA, et al. Low temperature fabrication of magnesium phosphate cement scaffolds by 3D powder printing. *Journal of Materials Science: Materials in Medicine* 2010;21:2947-2953.

[33] Zhou H, Luchini TJF, Bhaduri SB. Microwave assisted synthesis of amorphous magnesium phosphate nanospheres. *Journal of Materials Science: Materials in Medicine* 2012;23:2831-2837.

[34] Driessens FCM, Boltong MG, Zapatero MI, Verbeeck RMH, et al. In-Vivo Behaviour of 3 Calcium-Phosphate Cements and a Magnesium Phosphate Cement. *Journal of Materials Science: Materials in Medicine* 1995;6:272-278.

[35] Driessens FCM, Boltong MG, Bermudez O, Planell JA. Formulations and Setting Times of Some Calcium Orthophosphate Cements - A Pilot Study. *Journal of Materials Science: Materials in Medicine* 1993;4:503-508.

[36] Yu Y, Wang J, Liu C, Zhang B, et al. Evaluation of inherent toxicology and biocompatibility of magnesium phosphate bone cement. *Colloids and Surfaces, B: Biointerfaces* 2010;76:496-504.

[37] Wang A-j, Zhang J, Li J-m, Ma A-b, et al. Effect of liquid-to-solid ratios on the properties of magnesium phosphate chemically bonded ceramics. *Materials Science & Engineering C-Materials for Biological Applications* 2013;33:2508-2512.

[38] Mestres G, Aguilera FS, Manzanares N, Sauro S, et al. Magnesium phosphate cements for endodontic applications with improved long-term sealing ability. *International Endodontic Journal* 2014;47:127-139.

[39] Zhou H, Agarwal AK, Goel VK, Bhaduri SB. Microwave assisted preparation of magnesium phosphate cement (MPC) for orthopedic applications: A novel solution to the exothermicity problem. *Materials Science & Engineering C-Materials for Biological Applications* 2013;33:4288-4294.

[40] Hoppe A, Guldal NS, Boccaccini AR. A review of the biological response to ionic dissolution products from bioactive glasses and glass-ceramics. *Biomaterials* 2011;32:2757-2774.

[41] Yoshizawa S, Brown A, Barchowsky A, Sfeir C. Magnesium ion stimulation of bone marrow stromal cells enhances osteogenic activity, simulating the effect of magnesium alloy degradation. *Acta Biomaterialia* 2014;10:2834-2842.

[42] Feyerabend F, Witte F, Kammal M, Willumeit R. Unphysiologically high magnesium concentrations support chondrocyte proliferation and redifferentiation. *Tissue Engineering* 2006;12:3545-3556.

[43] Yoshizawa S, Brown A, Barchowsky A, Sfeir C. Role of magnesium ions on osteogenic response in bone marrow stromal cells. *Connective Tissue Research* 2014;55:155-159.

[44] Janning C, Willbold E, Vogt C, Nellesen J, et al. Magnesium hydroxide temporarily enhancing osteoblast activity and decreasing the osteoclast number in peri-implant bone remodelling. *Acta Biomaterialia* 2010;6:1861-1868.

[45] Roy M, Bose S. Osteoclastogenesis and osteoclastic resorption of tricalcium phosphate: Effect of strontium and magnesium doping. *Journal of Biomedical Materials Research Part A* 2012;100A:2450-2461.

[46] Ostrowski N, Lee B, Hong D, Enick PN, et al. Synthesis, Osteoblast, and Osteoclast Viability of Amorphous and Crystalline Tri-Magnesium Phosphate. *ACS Biomaterials Science & Engineering* 2014;1:52-63.

[47] Feyerabend F, Fischer J, Holtz J, Witte F, et al. Evaluation of short-term effects of rare earth and other elements used in magnesium alloys on primary cells and cell lines. *Acta Biomaterialia* 2010;6:1834-1842.

[48] Seehra SS, Gupta S, Kumar S. Rapid Setting Magnesium Phosphate Cement for Quick Repair of Concrete Pavements - Characterization and Curability Aspects. *Cement and Concrete Research* 1993;23:254-266.

[49] Yang Q, Wu X. Factors influencing properties of phosphate cement-based binder for rapid repair of concrete. *Cement and Concrete Research* 1999;29:389-396.

[50] Cenni R, Janisch B, Spliethoff H, Hein KR. Legislative and environmental issues on the use of ash from coal and municipal sewage sludge co-firing as construction material. *Waste Management* 2001;21:17-31.

[51] Li J, Xu G, Chen Y, Liu G. Multiple scaling investigation of magnesium phosphate cement modified by emulsified asphalt for rapid repair of asphalt mixture pavement. *Construction and Building Materials* 2014;69:346-350.

[52] Yang N, Shi C, Yang J, Chang Y. Research Progresses in Magnesium Phosphate Cement-Based Materials. *Journal of Materials in Civil Engineering* 2014;26.

[53] Thomopoulos S, Zampiakis E, Das R, Kim HM, et al. Use of a Magnesium-Based Bone Adhesive for Flexor Tendon-to-Bone Healing. *The Journal of Hand Surgery* 2009;34:1066-1073.

[54] Wagh AS, Jeong SY. Chemically Bonded Phosphate Ceramics: I, A Dissolution Model of Formation. *Journal of the American Ceramic Society* 2003;86:1838-1844.

[55] Yasukawa A, Ouchi S, Kandori K, Ishikawa T. Preparation and characterization of magnesium-calcium hydroxyapatites. *Journal of Materials Chemistry* 1996;6:1401-1405.

[56] Qian C-x, Yang J-M. Effect of Disodium Hydrogen Phosphate on Hydration and Hardening of Magnesium Potassium Phosphate Cement. *Journal of Materials in Civil Engineering* 2011;23:1405-1411.

[57] Wang A-j, Yuan Z-l, Zhang J, Liu L-t, et al. Effect of raw material ratios on the compressive strength of magnesium potassium phosphate chemically bonded ceramics. *Materials Science & Engineering C-Materials for Biological Applications* 2013;33:5058-5063.

[58] Wu F, Wei J, Guo H, Chen F, et al. Self-setting bioactive calcium-magnesium phosphate cement with high strength and degradability for bone regeneration. *Acta Biomaterialia* 2008;4:1873-1884.

[59] Wu F, Su J, Wei J, Guo H, et al. Injectable bioactive calcium-magnesium phosphate cement for bone regeneration. *Biomedical Materials* 2008;3.

[60] Klammert U, Reuther T, Blank M, Reske I, et al. Phase composition, mechanical performance and in vitro biocompatibility of hydraulic setting calcium magnesium phosphate cement. *Acta Biomaterialia* 2010;6:1529-1535.

[61] Klammert U, Gbureck U, Vorndran E, Rodiger J, et al. 3D powder printed calcium phosphate implants for reconstruction of cranial and maxillofacial defects. *Journal of cranio-maxillo-facial surgery : official publication of the European Association for Cranio-Maxillo-Facial Surgery* 2010;38:565-570.

[62] Moseke C, Saratsis V, Gbureck U. Injectability and mechanical properties of magnesium phosphate cements. *Journal of Materials Science: Materials in Medicine* 2011;22:2591-2598.

[63] Barralet JE, Tamimi MFA, Flynn AP. Magnesium Phosphate Biomaterials. Google Patents; 2013.

[64] Gbureck U. Preparation for magnesium ammonium phosphate cements. Google Patents; 2013.

[65] Ginebra MMP, Mestres BEÀG. Inorganic cement for biomedical uses, preparation method thereof and use of same. Google Patents; 2013.

[66] Lally TJ. Multi-Purpose Bio-Material Composition. Google Patents; 2008.

[67] Lally TJ. Bio-adhesive composition, method for adhering objects to bone. Google Patents; 2003.

[68] Tomic EA. Magnesium oxide powder for workable, rapid-setting phosphate-containing cement compositions. Google Patents; 1988.

[69] Wagh AS, Primus C. Method and product for phosphosilicate slurry for use in dentistry and related bone cements. Dentsply International Inc; University of Chicago; 2006.

[70] Weill E, Bradik LJ. Magnesium phosphate cement systems. Google Patents; 1988.

[71] Zimmermann M. Magnesium ammonium phosphate cement composition. Kyphon Inc; 2006.

[72] Zimmermann M. Magnesium ammonium phosphate cement composition. Google Patents; 2011.

[73] Bertone AL, Hackett, B., Litsky, A., Johnson, A., Kaeding, C. C., Lally, T. A magnesium injectable formulation adheres bone to bone and tendon to bone. 51st Annual meeting, Orthopaedic Research Society. Rosemont, III2004.

[74] Grossardt C, Ewald A, Grover LM, Barralet JE, et al. Passive and Active In Vitro Resorption of Calcium and Magnesium Phosphate Cements by Osteoclastic Cells. *Tissue Engineering Part A* 2010;16:3687-3695.

[75] Ostrowski N, Sharma V, Roy A, Kumta PN. Systematic Assessment of Synthesized Tri-magnesium Phosphate Powders (Amorphous, Semi-crystalline and Crystalline) and Cements for Ceramic Bone Cement Applications. *Journal of Materials Science & Technology*;31:437-444.

[76] Sarkar AK. Phosphate Cement-Based Fast-Setting Binders. *American Ceramic Society Bulletin* 1990;69:234-238.

[77] Antonijević D, Ilić D, Medić V, Dodić S, et al. Evaluation of conventional and digital radiography capacities for distinguishing dental materials on radiograms depending on the present radiopacifying agent. *Vojnosanitetski Pregled* 2014;71:1006-1012.

[78] Kanter B, Geffers M, Ignatius A, Gbureck U. Control of in vivo mineral bone cement degradation. *Acta Biomaterialia* 2014;10:3279-3287.

[79] Wagh AS. Chapter 9 - Magnesium Phosphate Ceramics. In: Wagh AS, editor. Chemically Bonded Phosphate Ceramics. Oxford: Elsevier; 2004. p. 97-111.

[80] Sugama T, Kukacka LE. Magnesium monophosphate cements derived from diammonium phosphate solutions. *Cement and Concrete Research* 1983;13:407-416.

[81] Sugama T, Kukacka LE. Characteristics of mangesium pholyphosphate cements derived from ammonium polyphosphate solutions *Cement and Concrete Research* 1983;13:499-506.

[82] Qiao F, Chau CK, Li Z. Calorimetric study of magnesium potassium phosphate cement. *Materials and Structures* 2012;45:447-456.

[83] Finch T, Sharp JH. Chemical reactions between magnesia and aluminium orthophosphate to form magnesia-phosphate cements. *Journal of Materials Science* 1989;24:4379-4386.

[84] Jia J, Zhou H, Wei J, Jiang X, et al. Development of magnesium calcium phosphate biocement for bone regeneration. *Journal of the Royal Society Interface* 2010;7:1171-1180.

[85] Tan Y, Liu Y, Zhao Z, Paxton JZ, et al. Synthesis and in vitro degradation of a novel magnesium oxychloride cement. *Journal of Biomedical Materials Research Part A* 2015;103:194-202.

[86] Ewald A, Helmschrott K, Knebl G, Mehrban N, et al. Effect of cold-setting calcium- and magnesium phosphate matrices on protein expression in osteoblastic cells. *Journal of Biomedical Materials Research Part B-Applied Biomaterials* 2011;96B:326-332.

[87] Vorndran E, Ewald A, Mueller FA, Zorn K, et al. Formation and properties of magnesium-ammonium-phosphate hexahydrate biocements in the Ca-Mg-PO4 system. *Journal of Materials Science: Materials in Medicine* 2011;22:429-436.

[88] Yang G, Liu J, Li F, Pan Z, et al. Bioactive calcium sulfate/magnesium phosphate cement for bone substitute applications. *Materials Science & Engineering C-Materials for Biological Applications* 2014;35:70-76.

[89] Yu T, Ye J, Gao C, Yu L, et al. Effect of biomedical organic compounds on the setting reaction of calcium phosphates. *Colloids and Surfaces, B: Biointerfaces* 2010;75:363-369.

[90] Pijocha D, Loj, G., Nocuri-Wczelik, W., Slosarczyk, A. Effect of retardants on the heat release during settting of bone cement-type composites. *Journal of Achievements in Materials and Manufacturing Engineering* 2011;49:204-209.

[91] Kumar R, Kalmodia S, Nath S, Singh D, et al. Phase assemblage study and cytocompatibility property of heat treated potassium magnesium phosphate-silicate ceramics. *Journal of Materials Science: Materials in Medicine* 2009;20:1689-1695.

[92] Khairoun I, Boltong MG, Driessens FCM, Planell JA. Limited compliance of some apatitic calcium phosphate bone cements with clinical requirements. *Journal of Materials Science: Materials in Medicine* 1998;9:667-671.

[93] Zhang J, Liu W, Schnitzler V, Tancret F, et al. Calcium phosphate cements for bone substitution: Chemistry, handling and mechanical properties. *Acta Biomaterialia* 2014;10:1035-1049.

[94] Musha Y, Umeda T, Yoshizawa S, Shigemitsu T, et al. Effects of blood on bone cement made of calcium phosphate: Problems and advantages. *Journal of Biomedical Materials Research Part B: Applied Biomaterials* 2010;92B:95-101.

[95] Bohner M, Doebelin N, Baroud G. Theoretical and experimental approach to test the cohesion of calcium phosphate pastes. *European Cells and Materials* 2006;12:26-35.

[96] Heinemann S, Rössler S, Lemm M, Ruhnow M, et al. Properties of injectable ready-to-use calcium phosphate cement based on water-immiscible liquid. *Acta Biomaterialia* 2013;9:6199-6207.

[97] Hing KA. Bone repair in the twenty-first century: biology, chemistry or engineering? *Philosophical transactions Series A, Mathematical, physical, and engineering sciences* 2004;362:2821-2850.

[98] Pittet C, Lemaître J. Mechanical characterization of brushite cements: A Mohr circles' approach. *Journal of Biomedical Materials Research* 2000;53:769-780.

[99] Yu T, Ye J, Gao C, Yu L, et al. Effect of Borax on Hydration and Hardening Properties of Magnesium and Pottassium Phosphate Cement Pastes. *Journal of Wuhan University of Technology-Materials Science Edition* 2010;25:613-618.

[100] Bohner M, Loosli Y, Baroud G, Lacroix D. Commentary: Deciphering the link between architecture and biological response of a bone graft substitute. *Acta Biomaterialia* 2011;7:478-484.

[101] Baroud G, Bohner M, Heini P, Steffen T. Injection Biomechanics of Bone Cements Used in Vertebroplasty. *Bio-Medical Materials and Engineering* 2004;14:487-504.

[102] Farrar DF. Bone adhesives for trauma surgery: A review of challenges and developments. *International Journal of Adhesion and Adhesives* 2012;33:89-97.

[103] Hirvinen LJ, Litsky AS, Samii VF, Weisbrode SE, et al. Influence of bone cements on bone-screw interfaces in the third metacarpal and third metatarsal bones of horses. *American Journal of Veterinary Research* 2009;70:964-972.

[104] Gulotta LV, Kovacevic D, Ying L, Ehteshami JR, et al. Augmentation of tendon-to-bone healing with a magnesium-based bone adhesive. *American Journal of Sports Medicine* 2008;36:1290-1297.

[105] Schendel SA, Peauroi J. Magnesium-Based Bone Cement and Bone Void Filler: Preliminary Experimental Studies. *Journal of Craniofacial Surgery* 2009;20:461-464.

[106] Waselau M, Samii VE, Weisbrode SE, Litsky AS, et al. Effects of a magnesium adhesive cement on bone stability and healing following a metatarsal osteotomy in horses. *American Journal of Veterinary Research* 2007;68:370-378.

[107] Zeng D, Xia L, Zhang W, Huang H, et al. Maxillary Sinus Floor Elevation Using a Tissue-Engineered Bone with Calcium-Magnesium Phosphate Cement and Bone Marrow Stromal Cells in Rabbits. *Tissue Engineering Part A* 2012;18:871-882.

[108] Samali A, Holmberg CI, Sistonen L, Orrenius S. Thermotolerance and cell death are distinct cellular responses to stress: dependence on heat shock proteins. *FEBS Letters* 1999;461:306-310.

[109] Butscher A, Bohner M, Hofmann S, Gauckler L, et al. Structural and material approaches to bone tissue engineering in powder-based three-dimensional printing. *Acta Biomaterialia* 2011;7:907-920.

[110] Chevalier E, Chulia D, Pouget C, Viana M. Fabrication of porous substrates: A review of processes using pore forming agents in the biomaterial field. *Journal of Pharmaceutical Sciences* 2008;97:1135-1154.

[111] Cama G, Barberis F, Botter R, Cirillo P, et al. Preparation and properties of macroporous brushite bone cements. *Acta Biomaterialia* 2009;5:2161-2168.

[112] Zhang Y, Xu HK, Takagi S, Chow L. In-situ hardening hydroxyapatite-based scaffold for bone repair. *Journal of Materials Science: Materials in Medicine* 2006;17:437-445.

[113] Takagi S, Chow LC. Formation of macropores in calcium phosphate cement implants. *Journal of Materials Science: Materials in Medicine* 2001;12:135-139.

[114] del Real RP, Wolke JGC, Vallet-Regí M, Jansen JA. A new method to produce macropores in calcium phosphate cements. *Biomaterials* 2002;23:3673-3680.

[115] Simon CG, Khatri CA, Wight SA, Wang FW. Preliminary report on the biocompatibility of a moldable, resorbable, composite bone graft consisting of calcium phosphate cement and poly(lactide-co-glycolide) microspheres. *Journal of Orthopaedic Research* 2002;20:473-482.

[116] Link DP, van den Dolder J, Jurgens WJFM, Wolke JGC, et al. Mechanical evaluation of implanted calcium phosphate cement incorporated with PLGA microparticles. *Biomaterials* 2006;27:4941-4947.

[117] Felix Lanao RP, Leeuwenburgh SC, Wolke JG, Jansen JA. In vitro degradation rate of apatitic calcium phosphate cement with incorporated PLGA microspheres. *Acta Biomaterialia* 2011;7:3459-3468.

[118] Xu HHK, Eichmiller FC, Giuseppetti AA. Reinforcement of a self-setting calcium phosphate cementwith different fibers. *Journal of Biomedical Materials Research Part A* 2000;52:107-114.

[119] Xu HHK, Quinn JB. Calcium phosphate cement containing resorbable fibers for short-term reinforcement and macroporosity. *Biomaterials* 2002;23:193-202.

[120] Guo H, Su J, Wei J, Kong H, et al. Biocompatibility and osteogenicity of degradable Ca-deficient hydroxyapatite scaffolds from calcium phosphate cement for bone tissue engineering. *Acta Biomaterialia* 2009;5:268-278.

[121] Liao H, Walboomers XF, Habraken WJEM, Zhang Z, et al. Injectable calcium phosphate cement with PLGA, gelatin and PTMC microspheres in a rabbit femoral defect. *Acta Biomaterialia* 2011;7:1752-1759.

[122] Kroese-Deutman HC, Wolke JGC, Spauwen PHM, Jansen JA. Closing capacity of cranial bone defects using porous calcium phosphate cement implants in a rabbit animal model. *Journal of Biomedical Materials Research Part A* 2006;79A:503-511.

[123] Pekkan G, Aktas A, Pekkan K. Comparative radiopacity of bone graft materials. *Journal of Cranio-Maxillofacial Surgery* 2012;40:e1-e4.

[124] Wang X, Ye J, Wang Y. Influence of a novel radiopacifier on the properties of an injectable calcium phosphate cement. *Acta Biomaterialia* 2007;3:757-763.

[125] Habibovic P, Barralet JE. Bioinorganics and biomaterials: Bone repair. *Acta Biomaterialia* 2011;7:3013-3026.

[126] Dorozhkin SV. Calcium orthophosphate-based biocomposites and hybrid biomaterials. *Journal of Materials Science* 2009;44:2343-2387.

[127] Habraken WJEM, Wolke JGC, Jansen JA. Ceramic composites as matrices and scaffolds for drug delivery in tissue engineering. *Advanced Drug Delivery Reviews* 2007;59:234-248.

[128] Canal C, Ginebra MP. Fibre-reinforced calcium phosphate cements: A review. *Journal of the Mechanical Behavior of Biomedical Materials* 2011;4:1658-1671.

[129] Polo-Corrales L, Latorre-Esteves M, Ramirez-Vick JE. Scaffold Design for Bone Regeneration. *Journal of Nanoscience and Nanotechnology* 2014;14:15-56.

[130] Venkatesan J, Bhatnagar I, Manivasagan P, Kang K-H, et al. Alginate composites for bone tissue engineering: A review. *International Journal of Biological Macromolecules* 2015;72:269-281.

[131] Ferreira AM, Gentile P, Chiono V, Ciardelli G. Collagen for bone tissue regeneration. *Acta Biomaterialia* 2012;8:3191-3200.

[132] Jansen JA, Vehof JWM, Ruhe PQ, Kroeze-Deutman H, et al. Growth factor-loaded scaffolds for bone engineering. *Journal of Controlled Release* 2005;101:127-136.

[133] Bose S, Tarafder S. Calcium phosphate ceramic systems in growth factor and drug delivery for bone tissue engineering: A review. *Acta Biomaterialia* 2012;8:1401-1421.

[134] Schnieders J, Gbureck U, Thull R, Kissel T. Controlled release of gentamicin from calcium phosphate—poly(lactic acid-co-glycolic acid) composite bone cement. *Biomaterials* 2006;27:4239-4249.

[135] Bohner M, Baumgart F. Theoretical model to determine the effects of geometrical factors on the resorption of calcium phosphate bone substitutes. *Biomaterials* 2004;25:3569-3582.

[136] Karageorgiou V, Kaplan D. Porosity of 3D biomaterial scaffolds and osteogenesis. *Biomaterials* 2005;26:5474-5491.

[137] Ooms EM, Wolke JGC, van de Heuvel MT, Jeschke B, et al. Histological evaluation of the bone response to calcium phosphate cement implanted in cortical bone. *Biomaterials* 2003;24:989-1000.

[138] Smartt JMJ, Karmacharya J, Gannon FH, Ong G, et al. Repair of the Immature and Mature Craniofacial Skeleton with a Carbonated Calcium Phosphate Cement: Assessment of Biocompatibility, Osteoconductivity, and Remodeling Capacity. *Plastic and Reconstructive Surgery* 2005;115:1642-1650.

[139] Hutmacher DW, Schantz JT, Lam CXF, Tan KC, et al. State of the art and future directions of scaffold-based bone engineering from a biomaterials perspective. *Journal of Tissue Engineering and Regenerative Medicine* 2007;1:245-260.

[140] Hutmacher DW. Scaffolds in tissue engineering bone and cartilage. *Biomaterials* 2000;21:2529-2543.

[141] Ginebra M-P, Canal C, Espanol M, Pastorino D, et al. Calcium phosphate cements as drug delivery materials. *Advanced Drug Delivery Reviews* 2012;64:1090-1110.

[142] Ginebra MP, Traykova T, Planell JA. Calcium phosphate cements as bone drug delivery systems: A review. *Journal of Controlled Release* 2006;113:102-110.

[143] Bouler J-M, Bujoli B, Janvier P, Khairoun I, et al. Injectable calcium-phosphate cement releasing a bone resorption inhibitor. Graftys; Centre National de la Recherche Scientifique (CNRS); 2014.

[144] Seki K, Sakka A, Tokushige A, Imagama T, et al. Treatment for Staphylococcus aureus infection following open wedge high tibial osteotomy using antibiotic-impregnated calcium phosphate cement. *Knee Surgery, Sports Traumatology, Arthroscopy* 2014;22:2614-2617.

[145] Canal C, Pastorino D, Mestres G, Schuler P, et al. Relevance of microstructure for the early antibiotic release of fresh and pre-set calcium phosphate cements. *Acta Biomaterialia* 2013;9:8403-8412.

[146] Sehlke BM, Wilson TG, Jones AA, Yamashita M, et al. The Use of a Magnesium-Based Bone Cement to Secure Immediate Dental Implants. *International Journal of Oral & Maxillofacial Implants* 2013;28:E357-E367.

[147] Zheng YF, Gu XN, Witte F. Biodegradable metals. *Materials Science and Engineering: R: Reports* 2014;77:1-34.

[148] Gruskin E, Doll BA, Futrell FW, Schmitz JP, et al. Demineralized bone matrix in bone repair: History and use. *Advanced Drug Delivery Reviews* 2012;64:1063-1077.

[149] Afzal A. Implantable zirconia bioceramics for bone repair and replacement: A chronological review. *Materials Express* 2014;4:1-12.

[150] Fu Q, Saiz E, Rahaman MN, Tomsia AP. Toward Strong and Tough Glass and Ceramic Scaffolds for Bone Repair. *Advanced Functional Materials* 2013;23:5461-5476.

[151] Kaur G, Pandey OP, Singh K, Homa D, et al. A review of bioactive glasses: Their structure, properties, fabrication, and apatite formation. *Journal of Biomedical Materials Research Part A* 2014;102:254-274.

[152] Liljensten E, Adolfsson E, Strid K-G, Thomsen P. Resorbable and nonresorbable hydroxyapatite granules as bone graft substitutes in rabbit cortical defects. *Clinical implant dentistry and related research* 2003;5:95-101.

[153] Yokogawa Y, Kawamoto Y, Toriyama M, Suzuki T, et al. Preparation of Trimagnesium Phosphate by Mechanochemical Reaction. *Journal of the Ceramic Society of Japan* 1991;99:150-152.

[154] Yang JM, Qian CX. Effect of Borax on Hydration and Hardening Properties of Magnesium and Pottassium Phosphate Cement Pastes. *Journal of Wuhan University of Technology-Materials Science Edition* 2010;25:613-618.

[155] Zhang X-J, Lin D-Y, Yan X-H, Wang X-X. Evolution of the magnesium incorporated amorphous calcium phosphate to nano-crystallized hydroxyapatite in alkaline solution. *Journal of Crystal Growth* 2011;336:60-66.

[156] Zhang X, Jiang FC, Groth T, Vecchio KS. Preparation, characterization and mechanical performance of dense beta-TCP ceramics with/without magnesium substitution. *Journal of Materials Science-Materials in Medicine* 2008;19:3063-3070.

[157] Wei J, Jia JF, Wu F, Wei SC, et al. Hierarchically microporous/macroporous scaffold of magnesium-calcium phosphate for bone tissue regeneration. *Biomaterials* 2010;31:1260-1269.

[158] Zhong C, Chu CC. Biomimetic mineralization of acid polysaccharide-based hydrogels: towards porous 3-dimensional bone-like biocomposites. *Journal of Materials Chemistry* 2012;22:6080-6087.

[159] Zhao J, Zhao YP, Guan QQ, Tang GW, et al. Crosslinking of Electrospun Fibrous Gelatin Scaffolds for Apatite Mineralization. *Journal of Applied Polymer Science* 2011;119:786-793.

[160] Zhao C, Ji W, Han P, Zhang J, et al. In vitro and in vivo mineralization and osseointegration of nanostructured Ti6Al4V. *Journal of Nanoparticle Research* 2011;13:645-654.

[161] Vakiparta M, Forsback AP, Lassila LV, Jokinen M, et al. Biomimetic mineralization of partially bioresorbable glass fiber reinforced composite. *Journal of Materials Science-Materials in Medicine* 2005;16:873-879.

[162] Thula TT, Rodriguez DE, Lee MH, Pendi L, et al. In vitro mineralization of dense collagen substrates: A biomimetic approach toward the development of bone-graft materials. *Acta Biomaterialia* 2011;7:3158-3169.

[163] Ma Z, Chen F, Zhu Y-J, Cui T, et al. Amorphous calcium phosphate/poly(D,L-lactic acid) composite nanofibers: Electrospinning preparation and biomineralization. *Journal of Colloid and Interface Science* 2011;359:371-379.

[164] Douglas TEL, Krawczyk G, Pamula E, Declercq HA, et al. Generation of composites for bone tissue-engineering applications consisting of gellan gum hydrogels mineralized with calcium and magnesium phosphate phases by enzymatic means. *Journal of Tissue Engineering and Regenerative Medicine* 2014:n/a-n/a.

[165] Fischer J, Prosenc MH, Wolff M, Hort N, et al. Interference of magnesium corrosion with tetrazolium-based cytotoxicity assays. *Acta Biomaterialia* 2010;6:1813-1823.

[166] Berzina-Cimdina L, Borodajenko N. Research of Calcium Phosphates Using Fourier Transform Infrared Spectroscopy. *Infrared Spectroscopy-Materials Science, Engineering and Technology* 2012;123-148.

[167] Jahnen-Dechent W, Ketteler M. Magnesium Basics. *Clinical Kidney Journal* 2012;5:i3-i14.

[168] Laurencin D, Almora-Barrios N, de Leeuw NH, Gervais C, et al. Magnesium incorporation into hydroxyapatite. *Biomaterials* 2011;32:1826-1837.

[169] Kolmas J, Jaklewicz A, Zima A, Bucko M, et al. Incorporation of carbonate and magnesium ions into synthetic hydroxyapatite: The effect on physicochemical properties. *Journal of Molecular Structure* 2011;987:40-50.

[170] Taylor AW, Frazier AW, Gurney EL, Smith JP. Solubility products of di- and trimagnesium phosphates and the dissociation of magnesium phosphate solutions. *Transactions of the Faraday Society* 1963;59:1585.

[171] Mousa S. Study on synthesis of magnesium phosphate minerals. *Phosphorus Research Bulletin* 2010;24:16-21

[172] Eanes ED, Posner AS. Division of Biophysics: Kinetics and Mechanism of Conversion of Noncrytsalline Calcium Phosphate to Crystalline Hydroxyapatite *Transactions of the New York Academy of Sciences* 1965;28:233-241.

[173] Matijevic E. Preparation and Properties of Uniform Size Colloids. *Chemistry of Materials* 1993;5:412-426.

[174] Matijevic E. Univorm Inorganic Colloid Dispersion-Achievements and Challenges. *Langmuir* 1994;10:8-16.

[175] Barrere F, van Blitterswijk CA, de Groot K. Bone regeneration: molecular and cellular interactions with calcium phosphate ceramics. *International Journal of Nanomedicine* 2006;1:317-332.

[176] Hallab NJ, Vermes C, Messina C, Roebuck KA, et al. Concentration- and composition-dependent effects of metal ions on human MG-63 osteoblasts. *Journal of Biomedical Materials Research* 2002;60:420-433.

[177] Bleek K, Taubert A. New developments in polymer-controlled, bioinspired calcium phosphate mineralization from aqueous solution. *Acta Biomaterialia* 2013;9:6283-6321.

[178] Zhang W, Wang G, Liu Y, Zhao X, et al. The synergistic effect of hierarchical micro/nano-topography and bioactive ions for enhanced osseointegration. *Biomaterials* 2013;34:3184-3195.

[179] Meng ZX, Li HF, Sun ZZ, Zheng W, et al. Fabrication of mineralized electrospun PLGA and PLGA/gelatin nanofibers and their potential in bone tissue engineering. *Materials Science and Engineering: C* 2013;33:699-706.

[180] Coelfen H. Biomineralization: A crystal-clear view. *Nature Materials* 2010;9:960-961.

[181] Sadat-Shojai M, Khorasani M-T, Dinpanah-Khoshdargi E, Jamshidi A. Synthesis methods for nanosized hydroxyapatite with diverse structures. *Acta Biomaterialia*.

[182] Lee D, Kumta PN. Chemical synthesis and characterization of magnesium substituted amorphous calcium phosphate (MG-ACP). *Materials Science and Engineering: C* 2010;30:1313-1317.

[183] Yang X, Xie B, Wang L, Qin Y, et al. Influence of magnesium ions and amino acids on the nucleation and growth of hydroxyapatite. *CrystEngComm* 2011;13:1153-1158.

[184] Tampieri A, Celotti G, Landi E, Sandri M. Magnesium doped hydroxyapatite: Synthesis and characterization. In: Mandal H, Ovecoglu L, editors. Euro Ceramics Viii, Pts 1-32004. p. 2051-2054.

[185] Sader MS, LeGeros RZ, Soares GA. Human osteoblasts adhesion and proliferation on magnesium-substituted tricalcium phosphate dense tablets. *Journal of Materials Science-Materials in Medicine* 2009;20:521-527.

[186] Zreiqat H, Howlett CR, Zannettino A, Evans P, et al. Mechanisms of magnesium-stimulated adhesion of osteoblastic cells to commonly used orthopaedic implants. *Journal of Biomedical Materials Research* 2002;62:175-184.

[187] Craciunescu O, Tardei C, Moldovan L, Zarnescu O. Magnesium substitution effect on porous scaffolds for bone repair. *Central European Journal of Biology* 2011;6:301-311.

[188] Li X, Senda K, Ito A, Sogo Y, et al. Effect of Zn and Mg in tricalcium phosphate and in culture medium on apoptosis and actin ring formation of mature osteoclasts. *Biomedical Materials* 2008;3:045002-045002.

[189] Detsch R, Mayr H, Ziegler G. Formation of osteoclast-like cells on HA and TCP ceramics. *Acta Biomaterialia* 2008;4:139-148.

[190] Dorozhkin SV. Bioceramics of calcium orthophosphates. *Biomaterials* 2010;31:1465-1485.

[191] Ginebra MP, Espanol M, Montufar EB, Perez RA, et al. New processing approaches in calcium phosphate cements and their applications in regenerative medicine. *Acta Biomaterialia* 2010;6:2863-2873.

[192] Combes C, Rey C. Amorphous calcium phosphates: synthesis, properties and uses in biomaterials. *Acta Biomaterialia* 2010;6:3362-3378.

[193] Dorozhkin SV. Amorphous calcium (ortho)phosphates. *Acta Biomaterialia* 2010;6:4457-4475.

[194] Posner AS, Betts F. Synthetic amorphous calcium phosphate and its relation to bone mineral structure. *Accounts of Chemical Research* 1975;8:273-281.

[195] Blumenthal NC, Betts F, Posner AS. Stabilization of amorphous calcium phosphate by Mg and ATP. *Calcified Tissue International* 1977;23:245-250.

[196] Ostrowski N. Synthesis and Characterization of Tri-Magnesium Phosphate (TMP)–Novel Precursors to Biocompatible Bone Void Fillers. presented in part at the 2012 AIChE Annual Meeting. Pittsburgh, PA2012.

[197] Hurle K, Neubauer J, Bohner M, Doebelin N, et al. Effect of amorphous phases during the hydraulic conversion of α-TCP into calcium-deficient hydroxyapatite. *Acta Biomaterialia* 2014;10:3931-3941.

[198] Zecchina A, Marchese L, Bordiga S, Pazè C, et al. Vibrational Spectroscopy of NH4+ Ions in Zeolitic Materials: An IR Study. *The Journal of Physical Chemistry B* 1997;101:10128-10135.

[199] Zhou H, Bhaduri S. Novel microwave synthesis of amorphous calcium phosphate nanospheres. *Journal of Biomedical Materials Research Part B-Applied Biomaterials* 2012;100B:1142-1150.

[200] Teucher B, Dainty JR, Spinks CA, Majsak-Newman G, et al. Sodium and bone health: impact of moderately high and low salt intakes on calcium metabolism in postmenopausal women. *Journal of Bone and Mineral Research* 2008;23:1477-1485.

[201] Karppanen H, Karppanen P, Mervaala E. Why and how to implement sodium, potassium, calcium, and magnesium changes in food items and diets? *J Hum Hypertens* 0000;19:S10-S19.

[202] Tylavsky FA, Spence LA, Harkness L. The importance of calcium, potassium, and acid-base homeostasis in bone health and osteoporosis prevention. *Journal of Nutrition* 2008;138:164s-165s.

[203] Motsei LE, Beighle DE. Bone mineral response to ammonium sulphate offered as a lick supplement in beef calves. *J S Afr Vet Assoc* 2006;77:19-23.

[204] Barzel US, Massey LK. Excess dietary protein can adversely affect bone. *Journal of Nutrition* 1998;128:1051-1053.

[205] Berg J, Tymoczko J, Stryer L. Section 23.4, Ammonium Ion Is Converted Into Urea in Most Terrestrial Vertebrates. Biochemistry. New York: W H Freeman; 2002.

[206] Liu Z, Zhao Q, Wei L, Wu D, et al. Effect of struvite seed crystal on MAP crystallization. *Journal of Chemical Technology & Biotechnology* 2011;86:1394-1398.

[207] Nikoobakht B, El-Sayed MA. Preparation and Growth Mechanism of Gold Nanorods (NRs) Using Seed-Mediated Growth Method. *Chemistry of Materials* 2003;15:1957-1962.

[208] Moriyama K, Kojima T, Minawa Y, Matsumoto S, et al. Development of Artificial Seed Crystal for Crystallization of Calcium Phosphate. *Environmental Technology* 2001;22:1245-1252.

[209] Tang M, Weir MD, Xu HHK. Mannitol-containing macroporous calcium phosphate cement encapsulating human umbilical cord stem cells. *Journal of Tissue Engineering and Regenerative Medicine* 2012;6:214-224.

[210] Xu HH, Burguera EF, Carey LE. Strong, macroporous, and in situ-setting calcium phosphate cement-layered structures. *Biomaterials* 2007;28:3786-3796.

[211] Xu HHK, Carey LE, Simon CG, Jr. Premixed macroporous calcium phosphate cement scaffold. *Journal of Materials Science-Materials in Medicine* 2007;18:1345-1353.

[212] Xu HHK, Simon CG. Self-hardening calcium phosphate cement-mesh composite: Reinforcement, macropores, and cell response. *Journal of Biomedical Materials Research Part A* 2004;69A:267-278.

[213] Xu HHK, Weir MD, Burguera EF, Fraser AM. Injectable and macroporous calcium phosphate cement scaffold. *Biomaterials* 2006;27:4279-4287.

[214] Zhang J, Zhou H, Yang K, Yuan Y, et al. RhBMP-2-loaded calcium silicate/calcium phosphate cement scaffold with hierarchically porous structure for enhanced bone tissue regeneration. *Biomaterials* 2013;34:9381-9392.

[215] Chen W, Zhou H, Tang M, Weir MD, et al. Gas-Foaming Calcium Phosphate Cement Scaffold Encapsulating Human Umbilical Cord Stem Cells. *Tissue Engineering Part A* 2012;18:816-827.

[216] Hollister SJ. Porous scaffold design for tissue engineering. *Nature Materials* 2005;4:518-524.

[217] Vazquez D, Takagi S, Frukhtbeyn S, Chow LC. Effects of Addition of Mannitol Crystals on the Porosity and Dissolution Rates of a Calcium Phosphate Cement. *Journal of Research of the National Institute of Standards and Technology* 2010;115:225-232.

[218] Shimogoryo R, Eguro T, Kimura E, Maruta M, et al. Effects of added mannitol on the setting reaction and mechanical strength of apatite cement. *Dental Materials Journal* 2009;28:627-633.

[219] Xu HHK, Takagi S, Quinn JB, Chow LC. Fast-setting calcium phosphate scaffolds with tailored macropore formation rates for bone regeneration. *Journal of Biomedical Materials Research Part A* 2004;68A:725-734.

[220] Xu HHK, Weir MD, Simon CG. Injectable and strong nano-apatite scaffolds for cell/growth factor delivery and bone regeneration. *Dental Materials* 2008;24:1212-1222.

[221] Van der Stok J, Van Lieshout EM, El-Massoudi Y, Van Kralingen GH, et al. Bone substitutes in the Netherlands - a systematic literature review. *Acta Biomaterialia* 2011;7:739-750.

[222] Burger A, Henck J-O, Hetz S, Rollinger JM, et al. Energy/temperature diagram and compression behavior of the polymorphs of D-mannitol. *Journal of Pharmaceutical Sciences* 2000;89:457-468.

[223] Munz D, Fett T. Ceramics: Mechanical Properties, Failure Behaviour, Materials Selection. Berlin Heidelberg: Springer-Verlag Berlin Heidelberg; 1999.

[224] Martin RI, Brown PW. Mechanical properties of hydroxyapatite formed at physiological temperature. *Journal of Materials Science: Materials in Medicine* 1995;6:138-143.

[225] Currey JD, Butler G. The mechanical properties of bone tissue in children. *J Bone Joint Surg Am* 1975;57:810-814.

[226] Geffers M, Groll J, Gbureck U. Reinforcement Strategies for Load-Bearing Calcium Phosphate Biocements. *Materials* 2015;8:2700.

[227] Zollo RF. Fiber-reinforced concrete: an overview after 30 years of development. *Cement and Concrete Composites* 1997;19:107-122.

[228] Vasconcellos LA, dos Santos LA. Calcium phosphate cement scaffolds with PLGA fibers. *Materials Science and Engineering: C* 2013;33:1032-1040.

[229] Zhao L, Tang M, Weir MD, Detamore MS, et al. Osteogenic Media and rhBMP-2-Induced Differentiation of Umbilical Cord Mesenchymal Stem Cells Encapsulated in Alginate Microbeads and Integrated in an Injectable Calcium Phosphate-Chitosan Fibrous Scaffold. *Tissue Engineering Part A* 2011;17:969-979.

[230] Xu HHK, Quinn JB, Takagi S, Chow LC, et al. Strong and macroporous calcium phosphate cement: Effects of porosity and fiber reinforcement on mechanical properties. *Journal of Biomedical Materials Research* 2001;57:457-466.

[231] Wu W, Yang W, Zhou D, Ma J, et al. A study on alpha-tricalcium phosphate bone cement carbon fiber-reinforced. *Sheng wu yi xue gong cheng xue za zhi = Journal of biomedical engineering = Shengwu yixue gongchengxue zazhi* 2006;23:569-572.

[232] Gorst NJ, Perrie Y, Gbureck U, Hutton AL, et al. Effects of fibre reinforcement on the mechanical properties of brushite cement. *Acta Biomaterialia* 2006;2:95-102.

[233] Ahern BJ, Harten RD, Gruskin EA, Schaer TP. Evaluation of a fiber reinforced drillable bone cement for screw augmentation in a sheep model--mechanical testing. *Clinical and translational science* 2010;3:112-115.

[234] Lew DP, Waldvogel FA. Osteomyelitis. *Lancet* 2004;364:369-379.

[235] Barth RE, Vogely HC, Hoepelman AI, Peters EJ. 'To bead or not to bead?' Treatment of osteomyelitis and prosthetic joint-associated infections with gentamicin bead chains. *International Journal of Antimicrobial Agents* 2011;38:371-375.

[236] Vorndran E, Geffers M, Ewald A, Lemm M, et al. Ready-to-use injectable calcium phosphate bone cement paste as drug carrier. *Acta Biomaterialia* 2013;9:9558-9567.

[237] Zilberman M, Elsner JJ. Antibiotic-eluting medical devices for various applications. *Journal of Controlled Release* 2008;130:202-215.

[238] Watts AE, Nixon AJ, Papich MG, Sparks HD, et al. In Vitro Elution of Amikacin and Ticarcillin from a Resorbable, Self-Setting, Fiber Reinforced Calcium Phosphate Cement. *Veterinary Surgery* 2011;40:563-570.

[239] Li WJ, Cooper JA, Jr., Mauck RL, Tuan RS. Fabrication and characterization of six electrospun poly(alpha-hydroxy ester)-based fibrous scaffolds for tissue engineering applications. *Acta Biomaterialia* 2006;2:377-385.

[240] Patlolla A, Collins G, Arinzeh TL. Solvent-dependent properties of electrospun fibrous composites for bone tissue regeneration. *Acta Biomaterialia* 2010;6:90-101.

[241] Kim K, Yu M, Zong X, Chiu J, et al. Control of degradation rate and hydrophilicity in electrospun non-woven poly(d,l-lactide) nanofiber scaffolds for biomedical applications. *Biomaterials* 2003;24:4977-4985.

[242] Göpferich A. Mechanisms of polymer degradation and erosion. *Biomaterials* 1996;17:103-114.

[243] Lavin DM, Zhang L, Furtado S, Hopkins RA, et al. Effects of protein molecular weight on the intrinsic material properties and release kinetics of wet spun polymeric microfiber delivery systems. *Acta Biomater* 2013;9:4569-4578.

[244] Lavin DM, Harrison MW, Tee LY, Wei KA, et al. A novel wet extrusion technique to fabricate self-assembled microfiber scaffolds for controlled drug delivery. *J Biomed Mater Res A* 2012;100:2793-2802.

[245] Nelson KD, Romero A, Waggoner P, Crow B, et al. Technique paper for wet-spinning poly(L-lactic acid) and poly(DL-lactide-co-glycolide) monofilament fibers. *Tissue Eng* 2003;9:1323-1330.

[246] Rissanen M, Puolakka A, Hukka T, Ellä V, et al. Effect of hot drawing on properties of wet-spun poly(L,D-lactide) copolymer multifilament fibers. *Journal of Applied Polymer Science* 2010;115:608-615.

[247] Lavin DM, Stefani RM, Zhang L, Furtado S, et al. Multifunctional polymeric microfibers with prolonged drug delivery and structural support capabilities. *Acta Biomater* 2012;8:1891-1900.

[248] Luo CJ, Stride E, Edirisinghe M. Mapping the Influence of Solubility and Dielectric Constant on Electrospinning Polycaprolactone Solutions. *Macromolecules* 2012;45:4669-4680.

[249] Krueger R, Groll J. Fiber reinforced calcium phosphate cements - On the way to degradable load bearing bone substitutes? *Biomaterials* 2012;33:5887-5900.

[250] Paul W, Sharma CP. Effect of calcium, zinc and magnesium on the attachment and spreading of osteoblast like cells onto ceramic matrices. *Journal of Materials Science-Materials in Medicine* 2007;18:699-703.

[251] Zhang W, Shen Y, Pan H, Lin K, et al. Effects of strontium in modified biomaterials. *Acta Biomater* 2011;7:800-808.

[252] Caudrillier A, Hurtel-Lemaire AS, Wattel A, Cournarie F, et al. Strontium ranelate decreases receptor activator of nuclear factor-KappaB ligand-induced osteoclastic differentiation in vitro: involvement of the calcium-sensing receptor. *Molecular Pharmacology* 2010;78:569-576.

[253] Alkhraisat MH, Cabrejos-Azama J, Rodriguez CR, Jerez LB, et al. Magnesium substitution in brushite cements. *Mater Sci Eng C Mater Biol Appl* 2013;33:475-481.

[254] Cabrejos-Azama J, Hamdan Alkhraisat M, Rueda C, Torres J, et al. Magnesium substitution in brushite cements for enhanced bone tissue regeneration. *Materials Science & Engineering C-Materials for Biological Applications* 2014;43:403-410.

[255] Dou Y, Cai S, Zhou W, Lu S, et al. Effect of Trace Element Doping on the Hydration Properties of Calcium Phosphate Bone Cement. *Rare Metal Materials and Engineering* 2011;40:59-62.

[256] Kalita SJ, Bhatt HA. Nanocrystalline hydroxyapatite doped with magnesium and zinc: Synthesis and characterization. *Materials Science & Engineering C-Biomimetic and Supramolecular Systems* 2007;27:837-848.

[257] Lu J, Wei J, Yan Y, Li H, et al. Preparation and preliminary cytocompatibility of magnesium doped apatite cement with degradability for bone regeneration. *Journal of Materials Science-Materials in Medicine* 2011;22:607-615.

[258] Yu T, Ye J, Zhang M. Effect of Magnesium Doping on Hydration Morphology and Mechanical Property of Calcium Phosphate Cement Under Non-Calcined Synthesis Condition. *Journal of the American Ceramic Society* 2013;96:1944-1950.

[259] Choi D, Kumta PN. An Alternative Chemical Route for the Synthesis and Thermal Stability of Chemically Enriched Hydroxyapatite. *Journal of the American Ceramic Society* 2006;89:444-449.

[260] Alkhraisat MH, Moseke C, Blanco L, Barralet JE, et al. Strontium modified biocements with zero order release kinetics. *Biomaterials* 2008;29:4691-4697.

[261] Kannan S, Goetz-Neunhoeffer F, Neubauer J, Pina S, et al. Synthesis and structural characterization of strontium- and magnesium-co-substituted beta-tricalcium phosphate. *Acta Biomaterialia* 2010;6:571-576.

[262] Landi E, Uggeri J, Medri V, Guizzardi S. Sr, Mg cosubstituted HA porous macro-granules: Potentialities as resorbable bone filler with antiosteoporotic functions. *Journal of Biomedical Materials Research Part A* 2013;101:2481-2490.

[263] Singh SS, Roy A, Lee BE, Banerjee I, et al. MC3T3-E1 proliferation and differentiation on biphasic mixtures of Mg substituted β-tricalcium phosphate and amorphous calcium phosphate. *Materials Science and Engineering: C* 2014;45:589-598.

[264] Boanini E, Gazzano M, Bigi A. Ionic substitutions in calcium phosphates synthesized at low temperature. *Acta Biomaterialia* 2010;6:1882-1894.

[265] Zhou H, Nedley M, Bhaduri SB. The impacts of Mg2+ on strontium phosphate: A preliminary study. *Materials Letters* 2013;113:63-66.

[266] McCusker LB, Von Dreele RB, Cox DE, Louer D, et al. Rietveld refinement guidelines. *Journal of Applied Crystallography* 1999;32:36-50.

[267] Staiger MP, Pietak AM, Huadmai J, Dias G. Magnesium and its alloys as orthopedic biomaterials: A review. *Biomaterials* 2006;27:1728-1734.

[268] Zeng R, Dietzel W, Witte F, Hort N, et al. Progress and challenge for magnesium alloys as biomaterials. *Advanced Engineering Materials* 2008;10:B3-B14.

[269] Witte F. The history of biodegradable magnesium implants: A review. *Acta Biomaterialia* 2010;6:1680-1692.

[270] Witte F, Hort N, Vogt C, Cohen S, et al. Degradable biomaterials based on magnesium corrosion. *Current Opinion in Solid State & Materials Science* 2008;12:63-72.

[271] Xin Y, Hu T, Chu PK. In vitro studies of biomedical magnesium alloys in a simulated physiological environment: A review. *Acta Biomaterialia* 2011;7:1452-1459.

[272] Wang Y, Wei M, Gao JC. Improve corrosion resistance of magnesium in simulated body fluid by dicalcium phosphate dihydrate coating. *Materials Science & Engineering C-Biomimetic and Supramolecular Systems* 2009;29:1311-1316.

[273] Witte F, Fischer J, Nellesen J, Crostack HA, et al. In vitro and in vivo corrosion measurements of magnesium alloys. *Biomaterials* 2006;27:1013-1018.

[274] Zberg B, Uggowitzer PJ, Loeffler JF. MgZnCa glasses without clinically observable hydrogen evolution for biodegradable implants. *Nature Materials* 2009;8:887-891.

[275] Kirkland NT, Birbilis N, Staiger MP. Assessing the corrosion of biodegradable magnesium implants: A critical review of current methodologies and their limitations. *Acta Biomaterialia* 2012;8:925-936.

[276] de Jonge LT, Leeuwenburgh SCG, Wolke JGC, Jansen JA. Organic-inorganic surface modifications for titanium implant surfaces. *Pharmaceutical Research* 2008;25:2357-2369.

[277] Roy A, Singh SS, Datta MK, Lee B, et al. Novel sol-gel derived calcium phosphate coatings on Mg4Y alloy. *Materials Science and Engineering B-Advanced Functional Solid-State Materials* 2011;176:1679-1689.

[278] Kannan MB. Enhancing the performance of calcium phosphate coating on a magnesium alloy for bioimplant applications. *Materials Letters* 2012;76:109-112.

[279] Wong HM, Yeung KWK, Lam KO, Tam V, et al. A biodegradable polymer-based coating to control the performance of magnesium alloy orthopaedic implants. *Biomaterials* 2010;31:2084-2096.

[280] Chen Y, Song Y, Zhang S, Li J, et al. Interaction between a high purity magnesium surface and PCL and PLA coatings during dynamic degradation. *Biomedical Materials* 2011;6:025005.

[281] Guo M, Cao L, Lu P, Liu Y, et al. Anticorrosion and cytocompatibility behavior of MAO/PLLA modified magnesium alloy WE42. *Journal of materials science Materials in medicine* 2011;22:1735-1740.

[282] Langer R. Drug delivery and targeting. *Nature* 1998;392:5-10.

[283] Jain RA. The manufacturing techniques of various drug loaded biodegradable poly(lactide-co-glycolide) (PLGA) devices. *Biomaterials* 2000;21:2475-2490.

[284] Park TG. Degradation of Poly(Lactic-co-Glycolic Adic) Microspheres - Effect of Copolymer Composition *Biomaterials* 1995;16:1123-1130.

[285] Valimaa T, Laaksovirta S. Degradation behaviour of self-reinforced 80L/20G PLGA devices in vitro. *Biomaterials* 2004;25:1225-1232.

[286] Drynda A, Deinet N, Braun N, Peuster M. Rare earth metals used in biodegradable magnesium-based stents do not interfere with proliferation of smooth muscle cells but do induce the upregulation of inflammatory genes. *Journal of Biomedical Materials Research Part A* 2009;91A:360-369.

[287] Kim K, Luu YK, Chang C, Fang DF, et al. Incorporation and controlled release of a hydrophilic antibiotic using poly(lactide-co-glycolide)-based electrospun nanofibrous scaffolds. *Journal of Controlled Release* 2004;98:47-56.

[288] Jeon O, Song SJ, Kang SW, Putnam AJ, et al. Enhancement of ectopic bone formation by bone morphogenetic protein-2 released from a heparin-conjugated poly(L-lactic-co-glycolic acid) scaffold. *Biomaterials* 2007;28:2763-2771.

[289] Li JN, Cao P, Zhang XN, Zhang SX, et al. In vitro degradation and cell attachment of a PLGA coated biodegradable Mg–6Zn based alloy. *Journal of Materials Science* 2010;45:6038-6045.

[290] Xu X, Lu P, Guo M, Fang M. Cross-linked gelatin/nanoparticles composite coating on micro-arc oxidation film for corrosion and drug release. *Applied Surface Science* 2010;256:2367-2371.

[291] Lu P, Fan H, Liu Y, Cao L, et al. Controllable biodegradability, drug release behavior and hemocompatibility of PTX-eluting magnesium stents. *Colloids and surfaces B, Biointerfaces* 2011;83:23-28.

[292] Paragkumar N T, Edith D, Six J-L. Surface characteristics of PLA and PLGA films. *Applied Surface Science* 2006;253:2758-2764.

[293] Hornberger H, Virtanen S, Boccaccini AR. Biomedical coatings on magnesium alloys - A review. *Acta Biomaterialia* 2012.

[294] von Burkersroda F, Schedl L, Gopferich A. Why degradable polymers undergo surface erosion or bulk erosion. *Biomaterials* 2002;23:4221-4231.

[295] Liu S-T, Nancollas GH. The Crystallization of Magnesium Hydroxide. *Desalination* 1973;12:75-84.

[296] Manzurola E, Apelblat A. Solubilities of l-glutamic acid, 3-nitrobenzoic acid, p-toluic acid, calcium-l-lactate, calcium gluconate, magnesium-dl-aspartate, and magnesium-l-lactate in water. *The Journal of Chemical Thermodynamics* 2002;34:1127-1136.

[297] Moravej M, Mantovani D. Biodegradable Metals for Cardiovascular Stent Application: Interests and New Opportunities. *International Journal of Molecular Sciences* 2011;12:4250-4270.

[298] Song G. Control of biodegradation of biocompatable magnesium alloys. *Corrosion Science* 2007;49:1696-1701.

[299] Cai K, Sui X, Hu Y, Zhao L, et al. Fabrication of anticorrosive multilayer onto magnesium alloy substrates via spin-assisted layer-by-layer technique. *Materials Science and Engineering: C* 2011;31:1800-1808.

[300] Hiromoto S, Yamamoto A. Control of degradation rate of bioabsorbable magnesium by anodization and steam treatment. *Materials Science and Engineering: C* 2010;30:1085-1093.

[301] Dong H. Surface engineering of light alloys: aluminum, magnesium and titanium Alloys. Oxford, UK: Woodhead Publishing; 2010.

[302] Decher G, Lvov Y, Schmitt J. Proof of Multilayer Structural Organization in Self-Assembled Polycation Polyanion Molecular Films *Thin Solid Films* 1994;244:772-777.

[303] Lvov Y, Decher G, Haas H, Mohwald H, et al. X-ray Analysis of Ultrathin Polymer-Films Self-Assembled onto Substrates *Physica B* 1994;198:89-91.

[304] Decher G, Hong JD. Buildup of Ultrathin Multilayer Films by a Self-Assembly Process 1: Consecutive Adsorption of Anionic and Cationic Bipolar Amphiphiles on Charged Surfaces *Makromolekulare Chemie-Macromolecular Symposia* 1991;46:321-327.

[305] Decher G, Hong JD. Buildup of Ultrathin Multilayer Films by a Self-Assembly Process. 2: Conseuctive Adsorption of Anionic and Cationic Bipolar Amphiphiles and Polyelectrolytes on Charged Surfaces *Berichte Der Bunsen-Gesellschaft-Physical Chemistry Chemical Physics* 1991;95:1430-1434.

[306] Decher G, Hong JD, Schmitt J. Buildup of Ultrathin Multilayer Films by a Self-Assembly Process. 3: Consecutively Alternating Adsorption of Anionic and Cationic Polyelectrolytes on Charged Surfaces. *Thin Solid Films* 1992;210:831-835.

[307] Gribova V, Auzely-Velty R, Picart C. Polyelectrolyte Multilayer Assemblies on Materials Surfaces: From Cell Adhesion to Tissue Engineering. *Chemistry of Materials* 2012;24:854-869.

[308] Flessner RM, Jewell CM, Anderson DG, Lynn DM. Degradable Polyelectrolyte Multilayers that Promote the Release of siRNA. *Langmuir* 2011;27:7868-7876.

[309] Kreke MR, Badami AS, Brady JB, Michael Akers R, et al. Modulation of protein adsorption and cell adhesion by poly(allylamine hydrochloride) heparin films. *Biomaterials* 2005;26:2975-2981.

[310] Chien H-W, Tan S-F, Wei K-L, Tsai W-B. Modulation of the functions of osteoblast-like cells on poly(allylamine hydrochloride) and poly(acrylic acid) multilayer films. *Colloids and Surfaces B-Biointerfaces* 2011;88:297-303.

[311] Detzel CJ, Larkin AL, Rajagopalan P. Polyelectrolyte Multilayers in Tissue Engineering. *Tissue Engineering Part B-Reviews* 2011;17:101-113.

[312] Liu P, Pan X, Yang W, Cai K, et al. Improved anticorrosion of magnesium alloy via layer-by-layer self-assembly technique combined with micro-arc oxidation. *Materials Letters* 2012;75:118-121.

[313] Godbey WT, Wu KK, Mikos AG. Poly(ethylenimine) and its role in gene delivery. *Journal of Controlled Release* 1999;60:149-160.

[314] Kunath K, von Harpe A, Fischer D, Peterson H, et al. Low-molecular-weight polyethylenimine as a non-viral vector for DNA delivery: comparison of physicochemical properties, transfection efficiency and in vivo distribution with high-molecular-weight polyethylenimine. *Journal of Controlled Release* 2003;89:113-125.

[315] Martinez JS, Keller TCS, III, Schlenoff JB. Cytotoxicity of Free versus Multilayered Polyelectrolytes. *Biomacromolecules* 2011;12:4063-4070.

[316] Lorenz C, Brunner JG, Kollmannsberger P, Jaafar L, et al. Effect of surface pre-treatments on biocompatibility of magnesium. *Acta Biomaterialia* 2009;5:2783-2789.

[317] Sill TJ, von Recum HA. Electrospinning: applications in drug delivery and tissue engineering. *Biomaterials* 2008;29:1989-2006.

[318] Alexis F. Factors affecting the degradation and drug-release mechanism of poly(lactic acid) and poly[(lactic acid)-co-(glycolic acid)]. *Polymer International* 2005;54:36-46.

[319] Gunatillake PA, and Adhikari, Raju Biodegradable Synthetic Polymers for Tissue Engineering. *European Cells and Materials* 2003;5:1-16.

[320] Brunot C, Ponsonnet L, Lagneau C, Farge P, et al. Cytotoxicity of polyethyleneimine (PEI), precursor base layer of polyelectrolyte multilayer films. *Biomaterials* 2007;28:632-640.

[321] da Conceicao TF, Scharnagl N, Dietzel W, Kainer KU. On the degradation mechanism of corrosion protective poly(ether imide) coatings on magnesium AZ31 alloy. *Corrosion Science* 2010;52:3155-3157.

[322] da Conceicao TF, Scharnagl N, Dietzel W, Kainer KU. Corrosion protection of magnesium AZ31 alloy using poly(ether imide) [PEI] coatings prepared by the dip coating method: Influence of solvent and substrate pre-treatment. *Corrosion Science* 2011;53:338-346.

[323] Lv H, Zhang S, Wang B, Cui S, et al. Toxicity of cationic lipids and cationic polymers in gene delivery. *Journal of Controlled Release* 2006;114:100-109.

[324] Arote R, Kim T-H, Kim Y-K, Hwang S-K, et al. A biodegradable poly(ester amine) based on polycaprolactone and polyethylenimine as a gene carrier. *Biomaterials* 2007;28:735-744.

[325] Dubas ST, Schlenoff JB. Polyelectrolyte multilayers containing a weak polyacid: Construction and deconstruction. *Macromolecules* 2001;34:3736-3740.

[326] Razavi M, Fathi MH, Meratian M. Microstructure, mechanical properties and bio-corrosion evaluation of biodegradable AZ91-FA nanocomposites for biomedical applications. *Materials Science and Engineering: A* 2010;527:6938-6944.

[327] Ostrowski NJ, Lee B, Roy A, Ramanathan M, et al. Biodegradable poly(lactide-co-glycolide) coatings on magnesium alloys for orthopedic applications. *J Mater Sci Mater Med* 2013;24:85-96.

[328] Ostrowski NJ, Lee B, Roy A, Ramanathan M, et al. Biodegradable poly(lactide-co-glycolide) coatings on magnesium alloys for orthopedic applications. *Journal of Materials Science-Materials in Medicine* 2013;24:85-96.